Simulation Techniques for the Study of the Manoeuvring of Advanced Rotorcraft Configurations

by

Stephen Rutherford, M.Eng.

Dissertation submitted to the Faculty of Engineering, University of Glasgow, for the Degree of Doctor of Philosophy.

March, 1997

Contents

Acknowledgements viii

Abstract x

Nomenclature xi

Chapter 1 Introduction 1
1.1 Existing Inverse Simulation at Glasgow 2
1.2 Limitations of Existing Inverse Simulation 3
1.2.1 Limitations of the Inverse Algorithm 3
1.2.1.1 Example of Differentiation Based Inverse Simulation Algorithm 4
1.2.2 Limitations of the Helicopter Mathematical Model 7
1.2.2.1 Helicopter Mathematical Models 7
1.2.2.2 Limitations of Disc Models 8
1.3 Aims of Research and Structure of Dissertation 8
1.3.1 Research Aims 8
1.3.2 Summary of Research Aims 10
1.3.3 Research Conclusions 11
1.3.4 Appendices 11
Table 1.1 Levels of Helicopter Rotor Mathematical Modelling 12

Chapter 2 Methods of Inverse Simulation 13
2.1 Introduction 13
2.1.1 The Inverse Problem and Inverse Simulation 13
2.1.2 History of Inverse Simulation 14
2.2 A Comparison of Inverse Simulation Techniques 17
2.2.1 General State Space Description of Methods of Inverse Simulation 18
2.2.1.1 Instantaneous Description of System 18
2.2.1.2 Conventional Simulation 18
2.2.1.3 Numerical Integration Based Inverse Simulation 19
2.2.1.4 Numerical Differentiation Based Inverse Simulation 19
2.2.2 Numerical Differentiation Approach 21
2.2.3 Numerical Integration Approach 22

2.3 Structure of the Algorithms 22
2.4 Numerical Stability 24
2.4.1 Numerical Differentiation Approach (Helinv) 24
2.4.2 Numerical Integration Algorithms 25
2.5 Chapter Summary 26

Chapter 3 Genisa: Generic Inverse Simulation Algorithm 27
3.1 The Genisa Algorithm 27
3.1.1 Overview 27
3.1.2 State Space Representation of the Genisa Algorithm 28
3.1.3 Evaluation of the Jacobian 30
3.2 Verification of the Genisa Algorithm 31
3.2.1 Concept of Verification 31
3.2.2 Genisa Algorithm Applied to HGS Model 32
3.2.3 Inverse Simulation of a Hurdlehop Manoeuvre 33
3.2.4 Comparison Between Genisa and Helinv 35
3.3 Examples of Numerical Instability 36
3.4 Chapter Summary 37

Chapter 4 An Investigation of the Stability, Flexibility and Robustness of the Genisa Algorithm 38
4.1 Stability of Genisa 38
4.2 A Demonstration of the Flexibility of Genisa 41
4.3 Alternative Manoeuvre Constraints 43
4.4 Changing Algorithm Parameters 44
4.5 Chapter Summary 47

Chapter 5 Development of a Helicopter Individual Blade Model: Hibrom 49
5.1 Introduction: Disc Model vs. Individual Blade Model 49
5.2 Main Rotor Modelling Assumptions 51
5.3 Individual Blade Model for Helicopter Main Rotor 58
5.3.1 Kinematics of a Blade Element 59
5.3.1.1 Velocity of a Blade Model 59
5.3.1.2 Acceleration of a Blade Element 63
5.3.2 Rotor Forces and Moments 65

5.3.2.1 Aerodynamic Forces Acting Upon a Blade Element 65
5.3.2.2 Inertial Force Acting Upon a Blade Element 68
5.3.2.3 Forces and Moments at Hub due to Blade Forces 69
5.3.2.4 Main Rotor's Contribution to External Forces and Moments 70
5.4 Equations Governing the Blade Flapping Dynamics 71
5.5 Chapter Summary 73

Chapter 6 Verification and Validation of the Helicopter Individual Blade Rotor Model: Hibrom 75
6.1 Verification of Hibrom 75
6.1.1 Inspection of Results 76
6.1.1.1 Hover 76
6.1.1.2 Forward Flight 78
6.1.2 Trim Controls and Attitudes 79
6.1.3 Open Loop Responses 81
6.1.3.1 Hover 81
6.1.3.2 Forward Flight 82
6.1.4 Inverse Simulation 83
6.1.4.1 Hurdlehop 84
6.1.4.2 Popup 84
6.1.4.3 Slalom 86
6.2 Validation of Hibrom: Comparison with Flight Test Data 87
6.3 Chapter Summary 89

Chapter 7 Manoeuvring of an Advanced Rotorcraft Configuration: The Compound Helicopter 90
7.1 Trim 91
7.1.1 Effect of Wing 91
7.1.1.1 Wing Parameters 92
7.1.1.2 The Wing Forces and Moments 93
7.1.1.3 Results 94
7.1.2 Effect of Auxiliary Thrust 95
7.1.2.1 Preliminary Results Using Auxiliary Thrust 95
7.1.2.2 Alternative Solutions Using Auxiliary Thrust 97
7.1.3 Individual Blade Tail Rotor and Propeller Models 99
7.1.3.1 Individual Blade Tail Rotor Model 100

7.1.3.2 Individual Blade Propeller Model 103
7.1.3.3 Results 105
7.2 Inverse Simulation - Manoeuvring of the Compound Configuration 105
7.2.1 Hurdlehop and Popup 106
7.2.2 Slalom and Rapid Slalom 107
7.2.3 Acceleration and Deceleration 107
7.2.4 Viability of Inverse Simulation Results 108
7.3 Chapter Summary 108

Chapter 8 Conclusions 110
8.1 Research Conclusions 110
8.1.1 Achievements and Developments 110
8.1.2 Conclusions from Research 111
8.1.3 Suggestions for Future Work 113
8.2 Chapter Summary 114

Appendix 1 The Euler Rigid Body Equations of Motion 115

Appendix 2a HGS. Main and Tail Rotor Models 117
A2a.1 Overview of Model 117
A2a.2 Rotor Model 118
A2a.2.1 Introduction 118
A2a.2.2 Kinematics of a Blade Element 119
A2a.2.3 Rotor Forces and Moments 122
A2a.2.3.1 The Rotor Aerodynamic Forces 123
A2a.2.3.2 The Rotor Inertial Forces 126
A2a.2.3.3 Total Rotor Forces 126
A2a.2.3.4 Rotor Moments 127
A2a.2.4 Blade Flapping and the Multiblade Transformation 128
A2a.3 Tail Rotor Model 130
A2a.4 Glauert Inflow Model 130

Appendix 2b HGS. Fuselage, Fin and Tail Plane Models 133
A2b.1 The Fuselage Forces and Moments 133
A2b.2 Fin and Tail Plane Forces and Moments 134

Appendix 3 Helinv: Differentiation Based Inverse Simulation Method 138
A3.1 Introduction 138
A3.2 Inputs to Helinv 138
A3.2.1 Flight Path 138
A3.2.2 Additional Constraint 139
A3.2.2.1 Heading Constraint 139
A3.2.2.2 Side Slip Constraint 139
A3.3 Helinv Solution Procedure 140
A3.3.1 Evaluation of Euler Angles and Rates 141
A3.3.2 Evaluation of Body Referenced Translational Velocities and Accelerations 142
A3.3.3 Evaluation of Body Referenced Rotational Velocities and Accelerations 143
A3.3.4 Determination of Forces and Moments 143
A3.3.5 Update of Current Estimate of Control and Attitude Angles 144

Appendix 4 Mathematical Definition of Manoeuvres 145
A4.1 A General Flight Path Definition 145
A4.2 Example: Linear Repositioning Manoeuvres 146

Appendix 5 The Peters-HaQuang Dynamic Inflow Model 148

Appendix 6 The McVicar-Bradley Partial Periodic Trimmer 152

Appendix 7 Inflow Model for Tail Rotor and Propeller 155

Appendix 8 Configurational and Aerodynamic Data 157
Table A8.1 Lynx Configurational Data 157
Table A8.2 Compound Lynx Configurational Data 158

Figures
Figure 1.1 159
Figures 3.1-3.7 160-166
Figures 4.1-4.4 167-170
Figures 5.1-5.6 171-176
Figures 6.1-6.29 177-205

Figures 7.1-7.16 206-221

Appendix Figures

Figures A2.1-A2.2 222-223
Figures A4.1-A4.3 224-226
Figures A5.1-A5.2 227-228
Figures A8.1-A8.3 229-231

References 232

Acknowledgements

I would like to express sincere gratitude to Dr. Douglas G. Thomson who has offered tremendous supervison and support, both throughout the research and during the course of writing the dissertation itself.

Financial support was offered by the EPSRC (Engineering and Physical Sciences Research Council) and DRA (Defence Research Agency). The facilities necessary for this research were made available by the Department of Aerospace Engineering, University of Glasgow.

A vote of thanks is offered to everyone within the Department of Aerospace Engineering, at DRA Bedford, and all my family and friends. The brevity of these acknowledgements does not reflect the number of people who are due thanks, but rather the difficulties in thanking everyone I would like. I hope you know who you are.

Thanks are due to Dr. Eric Gillies who proof-read the manuscript.

This dissertation is dedicated to my parents, John and Christine Rutherford, without whom none of the work would have been possible.

Stephen Rutherford

March, 1997

All aspects of the studies described in this dissertation are original in content, except where indicated. The research was conducted between October 1993 and September 1996 at the Department of Aerospace Engineering, University of Glasgow.

Stephen Rutherford

March, 1997

Abstract

Inverse simulation is a technique by which the necessary control actions can be calculated for a vehicle to perform a particular manoeuvre. The manoeuvre definition is thus the input to the problem, and the output is a time history of the control motions. The realism of a result is clearly dependent on the fidelity and sophistication of the vehicle mathematical model. Present inverse simulation algorithms are limited by being model specific and only able to accommodate models of restricted complexity. For helicopters specifically the models used in inverse simulation are, in general, rudimentary in nature. The existing inverse simulation algorithm at Glasgow University, "Helinv" is specific to the helicopter model, "HGS". Though HGS is very advanced by comparison with other inverse simulation helicopter models, it lags far behind the state of the art in conventional simulation. The principal aims of this research were therefore twofold: to develop a robust, generic inverse simulation algorithm, "Genisa"; and to develop a state of the art individual blade helicopter rotor model, "Hibrom". Naturally verification and validation were integral to these aims. These objectives having been achieved the intention was to demonstrate the flexibility of Genisa and the value of Hibrom by performing inverse simulations of various rotorcraft configurations. As well as representing a novel tool in rotorcraft simulation, the development of a flexible inverse simulation algorithm which can accommodate complex models extends the boundaries of inverse problems in general.

Genisa has proven to be both flexible and robust. Hibrom has been verified, validated and - using Genisa - successfully used in inverse simulation. The advantages of an individual blade model in inverse simulation have been demonstrated by comparing results with the disc model, HGS. Inverse simulations have been performed for various rotorcraft configurations identifying the respective benefits of the different vehicles. In all respects the aims identified above have been met in full.

Nomenclature

Acronyms

HGS: "Helicopter Generic Simulation". Existing disc type helicopter model.

Helinv: "Helicopter Inverse". Existing differentiation based inverse simulation method incorporating disc model HGS.

Hibrom: "Helicopter Individual Blade Rotor Model". New individual blade type helicopter rotor model.

Genisa: "Generic Inverse Simulation Algorithm". New integration based inverse simulation method.

General

x	variable
x	constant
$\underline{x}$	vector variable
$\underline{\mathbf{x}}$	vector constant
$[X]$	matrix of variables
[X]	matrix of constants
$\underline{x}_{sub.}^{super.}$	vector where *sub.* refers to a position / location in an axis set, and *super.* is the axis set

Specific

a	local speed of sound in air	(m / s)
A	aspect ratio	
$\underline{a}$	general translational acceleration vector	(m / s^2)
$\underline{a}_{c.g.}^{body}$	translational acceleration vector of helicopter centre of gravity referred to body axes	(m / s^2)
$\underline{a}_{elem.}^{blade}$	translational acceleration vector of blade elemental centre referred to blade axes	(m / s^2)

$\underline{a}_{hinge}^{blade}$	translational acceleration vector of blade hinge referred to blade axes	(m / s^2)
$\underline{a}_{hinge}^{shaft}$	translational acceleration vector of blade hinge referred to shaft axes	(m / s^2)
$\underline{a}_{hub}^{body}$	translational acceleration vector of rotor hub referred to body axes	(m / s^2)
$\underline{a}_{hub}^{disc}$	translational acceleration vector of rotor hub referred to disc axes	(m / s^2)
$\underline{a}_{hub}^{shaft}$	translational acceleration vector of rotor hub referred to shaft axes	(m / s^2)
a_0	lift curve slope	(1/rad)
b_{wing}, c_{wing}	wing span and chord	(m)
c	blade chord	(m)
$c_{elem.}$	elemental chord	(m)
C_l, C_d	lift and drag coefficients	
$\underline{e}$	output error vector	↑
$\underline{e}_{body}$	body period error subvector	
$\underline{e}_{flap}$	flap period error subvector	(units vary)
$\underline{e}_{i.f.}$	inflow period error subvector	
$\underline{e}_{m.f.s.}$	mean flight state error subvector	↓
eR	blade root cut-out	(m)
$\underline{f}_{aero.}^{blade}$	aerodynamic force vector acting on blade element referred to blade axes	(N)
$\underline{F}_{aero.}^{blade}$	aerodynamic force vector acting on blade referred to blade axes	(N)
$\underline{\bar{f}}_{aero.}^{blade}$	aerodynamic force vector per unit blade length referred to blade axes	(N / m)
$\underline{F}_{c.g.}^{body}$	force vector acting at aircraft centre of gravity referred to body axes i.e. external rotor forces	(N)
$\underline{F}_{hinge}^{blade}$	force vector acting at blade hinge referred to blade axes	(N)
$\underline{F}_{hinge}^{disc}$	force vector acting at blade hinge referred to disc axes	(N)
$\underline{F}_{hub}^{disc}$	force vector acting at rotor hub referred to disc axes	(N)
$\underline{f}_{in.}^{blade}$	inertial force vector acting on blade element referred to blade axes	(N)
$\underline{F}_{in.}^{blade}$	inertial force vector acting on blade referred to blade axes	(N)
$\underline{\bar{f}}_{in.}^{blade}$	inertial force vector per unit blade length referred to blade axes	(N / m)

g	acceleration due to gravity	(m / s^2)
h	maximum manoeuvre height / off axis displacement	(m)
I_{xx}, I_{yy}, I_{zz}	aircraft moments of inertia referred to body axes	(kg m^2)
I_{xz}	aircraft product of inertia	(kg m^2)
I_β	blade flapping inertia	(kg m^2)
$\underline{i}$, $\underline{j}$, $\underline{k}$	unit vectors describing an axis set	
$\underline{i}^{body}$, ...	unit vectors describing body axis set	
$\underline{i}^{disc}$, ...	unit vectors describing disc axis set	
$\underline{i}^{shaft}$, ...	unit vectors describing shaft axis set	
$\underline{i}^{blade}$, ...	unit vectors describing blade axis set	
$[J]$	Jacobian	
K_β	blade hinge spring stiffness	(N m / rad)
$[L]$	dynamic gains matrix	
L, M, N	components of external moment on aircraft	(N m)
$\bar{l}_{elem.}$, $\bar{d}_{elem.}$	elemental lift and drag per unit span	(N / m)
l_{fin}, h_{fin}	longitudinal and vertical distances from the fuselage reference point to fin aerodynamic centre	(m)
l_{hub}, h_{hub}	longitudinal and vertical distances from the fuselage reference point to main rotor hub	(m)
$l_{pr.}$, $h_{pr.}$	longitudinal and vertical distances from the fuselage reference point to propeller hub	(m)
$l_{t.p.}$, $h_{t.p.}$	longitudinal and vertical distances from the fuselage reference point to tail plane aerodynamic centre	(m)
$l_{t.r.}$, $h_{t.r.}$	longitudinal and vertical distances from the fuselage reference point to tail rotor hub	(m)
l_{wing}, h_{wing}	longitudinal and vertical distances from the fuselage reference point to mid point of wing aerodynamic centres	(m)
m	aircraft mass	(kg)
M	Mach number	
$[M]$	apparent mass matrix	
m_{blade}	mass of blade	(kg)
$m_{elem.}$	mass of blade element	(kg)
m_{wing}	mass of wing	(kg)
$\bar{m}_{elem.}$	elemental blade mass per unit span	(kg / m)
$\underline{M}_{c.g.}^{body}$	moment vector acting at aircraft centre of gravity referred to body axes i.e. external rotor moments	(N m)

$\underline{M}_{hinge}^{blade}$	moment vector acting at blade hinge referred to blade axes	(N m)
$\underline{M}_{hub}^{disc}$	moment vector acting at rotor hub referred to disc axes	(N m)
M_β	blade mass moment	(kg m)
n_{blades}	number of rotor blades	
n_{clock}	flag indicating rotational direction of main rotor	
$n_{int.}$	number of integration intervals per discretisation interval	
$n_{pts.}$	number of points in inverse simulation / manoeuvre	
n_x	number of elements in state vector	
n_y	number of elements in output vector	
n_u	number of elements in control vector	
n_ζ	number of elements in attitude vector	
P, Q, R	helicopter rotational velocity components at centre of gravity	(rad / s)
r	distance from main rotor hub to point on blade	(m)
$\underline{r}$	general position vector	(m)
R	main rotor radius	(m)
$\underline{r}_{c.g./hub}^{body}$	position vector from helicopter centre of gravity to main rotor hub referred to body axes	(m)
$\underline{r}_{c.g./pr.hub}^{body}$	position vector from helicopter centre of gravity to propeller hub referred to body axes	(m)
$\underline{r}_{c.g./t.r.hub}^{body}$	position vector from helicopter centre of gravity to tail rotor hub referred to body axes	(m)
$r_{elem.}$	distance along blade span from blade hinge to elemental centre	(m)
$\underline{r}_{hinge/elem.}^{blade}$	position vector from blade hinge to elemental centre referred to blade axes	(m)
$\underline{r}_{hub/hinge}^{shaft}$	position vector from main rotor hub to blade hinge referred to shaft axes	(m)
$r_{pr.elem.}$	distance along blade span from propeller hub to propeller blade elemental centre	(m)
$\underline{r}_{pr.hub/pr.elem.}^{pr.blade}$	position vector from propeller hub to blade elemental centre referred to propeller blade axes	(m)
$r_{t.r.elem.}$	distance along blade span from tail rotor hub to tail rotor blade elemental centre	(m)
$\underline{r}_{t.r.hub/t.r.elem.}^{t.r.blade}$	position vector from tail rotor hub to blade elemental centre referred to tail rotor blade axes	(m)
s	manoeuvre groundtrack	(m)
s	main rotor solidity	

S_{wing}	wing surface area	(m^2)
t	time	(sec)
T	main rotor thrust, general thrust	(N)
$[T]$	general axis transformation matrix	
$[T]^{body/disc}$	transformation matrix from body to disc axis sets	
$[T]^{body/pr.disc}$	transformation matrix from body to propeller disc axis sets	
$[T]^{body/t.r.disc}$	transformation matrix from body to tail rotor disc axis sets	
$[T]^{disc/shaft}$	transformation matrix from disc to shaft axis sets	
$[T]^{shaft/blade}$	transformation matrix from shaft to blade axis sets	
$[T]^{pr.disc/pr.blade}$	transformation matrix from propeller disc to propeller blade axis sets	
$[T]^{t.r.disc/t.r.blade}$	transformation matrix from tail rotor disc to tail rotor blade axis sets	
t_k	time point in inverse simulation / manoeuvre definition	
$t_{man.}$	time taken to complete manoeuvre	(sec)
$tol.$	solution tolerance	
$\underline{u}$	control vector	↑
$\underline{u}_{body}$	body state control subvector	
$\underline{u}_{cont.}$	aircraft control subvector	
$\underline{u}_{e.}$	trim control vector	(units vary)
$\underline{u}_{error}$	control error vector	
$\underline{u}_{flap}$	flap state control subvector	
$\underline{u}_{i.f.}$	inflow state control subvector	↓
u, v, w	general translational velocity components	(m / s)
U, V, W	translational velocity components of helicopter centre of gravity	(m / s)
$\underline{v}$	general translational velocity vector	(m / s)
$v_{aero.}$	aerodynamic velocity	(m / s)
$v_{ind.}$	main rotor induced velocity	(m / s)
$\underline{v}_{c.g.}^{body}$	translational velocity vector of helicopter centre of gravity referred to body axes	(m / s)
$V_{f.}$	aircraft flight velocity	(m / s)
$V_{f.\,max.}$	maximum aircraft flight velocity	(m / s)
$\underline{v}_{elem.}^{blade}$	translational velocity vector of blade elemental centre referred to blade axes	(m / s)
$\underline{v}_{hinge}^{blade}$	translational velocity vector of blade hinge referred to blade axes	(m / s)

$\underline{v}_{hinge}^{shaft}$	translational velocity vector of blade hinge referred to shaft axes	(m / s)
$\underline{v}_{hub}^{body}$	translational velocity vector of rotor hub referred to body axes	(m / s)
$\underline{v}_{hub}^{disc}$	translational velocity vector of rotor hub referred to disc axes	(m / s)
$\underline{v}_{hub}^{shaft}$	translational velocity vector of rotor hub referred to shaft axes	(m / s)
$\underline{v}_{pr.hub}^{body}$	translational velocity vector of propeller hub referred to body axes	(m / s)
$\underline{v}_{pr.hub}^{pr.disc}$	translational velocity vector of propeller hub referred to propeller disc axes	(m / s)
$\underline{v}_{pr.hub}^{pr.blade}$	translational velocity vector of propeller hub referred to propeller blade axes	(m / s)
$\underline{v}_{pr.elem}^{pr.blade}$	translational velocity vector of propeller blade element referred to propeller blade axes	(m / s)
$\underline{v}_{t.r.hub}^{body}$	translational velocity vector of tail rotor hub referred to body axes	(m / s)
$\underline{v}_{t.r.hub}^{t.r.disc}$	translational velocity vector of tail rotor hub referred to tail rotor disc axes	(m / s)
$\underline{v}_{t.r.hub}^{t.r.blade}$	translational velocity vector of tail rotor hub referred to tail rotor blade axes	(m / s)
$\underline{v}_{t.r.elem}^{t.r.blade}$	translational velocity vector of tail rotor blade element referred to tail rotor blade axes	(m / s)
v_0, v_{1s}, v_{1c}	uniform and cyclic components of main rotor induced velocity	(m / s)
$v_{perp.}$, $v_{tan.}$	tangential and perpendicular velocity components of air	(m / s)
$\underline{x}$	state vector	(units vary)
X, Y, Z	components of external force on aircraft	(N)
$\underline{x}_{e.}$	trim state vector	(units vary)
$x_{e.}$, $y_{e.}$, $z_{e.}$	displacements relative to an earth fixed inertial frame	(m)
x_{hinge}	blade hinge offset from main rotor hub	(m)
$x_{ref.}$, $z_{ref.}$	longitudinal and vertical distances from centre of gravity to fuselage reference point	(m)
$\underline{y}$	output vector	(units vary)
$\underline{y}_{des.}$	desired output vector	(units vary)
y_{wing}	position of wing aerodynamic centre from wing centre line	(m)
α	aircraft / blade angle of attack	(rad)
$\underline{\alpha}$	general rotational acceleration vector	(rad / s^2)

$\underline{\alpha}^{blade}$	rotational acceleration vector of blade axis set	(rad / s^2)
$\underline{\alpha}^{body}$	rotational acceleration vector of body axis set	(rad / s^2)
$\underline{\alpha}^{disc}$	rotational acceleration vector of disc axis set	(rad / s^2)
$\underline{\alpha}^{shaft}$	rotational acceleration vector of shaft axis set	(rad / s^2)
α_T	general thrust vector angle	(rad)
α_{wing}	wing angle of attack	(rad)
β	aircraft sideslip angle, blade flap angle	(rad)
$\beta_0,\ \beta_{1c},\ \beta_{1s}$	mutiblade (coning, longitudinal, lateral) flapping angles	(rad)
χ	aircraft track angle, rotor wake angle	(rad)
δ	blade profile drag coefficient	
Δt	inverse simulation / manoeuvre discretisation interval	(sec)
δu	control perturbation size	
$\delta r_{elem.}$	blade elemental length	(m)
ϕ	airflow incidence angle	(rad)
ϕ_{wing}	wing incidence angle to airflow	(rad)
$\phi,\ \theta,\ \psi$	aircraft attitude angles	(rad)
γ	aircraft climb angle	(rad)
$\gamma_{sh.}$	shaft tilt angle	(rad)
$[\Lambda]$	mass flow parameter matrix	
$\lambda_0,\ \lambda_{1s},\ \lambda_{1c}$	non-dimensionalised (by rotor tip speed) components of main rotor induced velocity	
λ_β	blade flapping frequency	(1 / s)
$\mu_x,\ \mu_y,\ \mu_z$	general non-dimensionalised (by rotor tip speed) translational velocity components	
θ	blade pitch angle	(rad)
θ_0	main rotor collective pitch angle	(rad)
$\theta_{1s},\ \theta_{1c}$	main rotor longitudinal and lateral cyclic pitch angles	(rad)
$\theta_{0t.r.}$	tail rotor collective pitch angle	(rad)
$\theta_{0pr.}$	propller pitch angle	(rad)
θ_{twist}	blade geometric twist	(rad)
θ_{wing}	fixed wing angle of incidence	(rad)
ρ	local air density	(kg / m^3)
$\underline{\omega}$	general rotational velocity vector	(rad / s)
Ω	main rotor speed	(rad / s)
$\underline{\omega}^{blade}$	rotational velocity vector of blade axis set	(rad / s)
$\underline{\omega}^{body}$	rotational velocity vector of body axis set	(rad / s)

$\underline{\omega}^{disc}$	rotational velocity vector of disc axis set	(rad / s)
$\underline{\omega}^{pr.blade}$	rotational velocity vector of propeller blade axis set	(rad / s)
$\underline{\omega}^{pr.disc}$	rotational velocity vector of propeller disc axis set	(rad / s)
$\underline{\omega}^{shaft}$	rotational velocity vector of shaft axis set	(rad / s)
$\underline{\omega}^{t.r.blade}$	rotational velocity vector of tail rotor blade axis set	(rad / s)
$\underline{\omega}^{t.r.disc}$	rotational velocity vector of tail rotor disc axis set	(rad / s)
$\underline{\xi}$	attitude vector	(units vary)
$\underline{\xi}_{e.}$	trim attitude vector	(units vary)
ψ	aircraft heading angle, blade azimuth angle	(rad)
$\psi_{pr.}$	propeller blade azimuth angle	(rad)
$\psi_{t.r.}$	tail rotor blade azimuth angle	(rad)
ψ_{wind}	wind sideslip angle	(rad)

Superscripts

body	referring to body axis set
blade	referring to blade axis set
disc	referring to disc axis set
s., e.	start and end of period
pr.blade	referring to propeller blade axis set
pr.disc	referring to propeller disc axis set
shaft	referring to shaft axis set
tr.blade	referring to tail rotor blade axis set
tr.disc	referring to tail rotor disc axis set
wind	referring to wind axis set

Subscripts

aux.	referring to auxiliary thrust device
c.g.	referring to aircraft centre of gravity
des.	desired
e.	earth fixed, equilibrium
fin	referring to fin
fus.	referring to fuselage
hub	referring to main rotor hub
k	current time / solution point

m	current estimate
pr.	referring to propeller
ref.	referring to fuselage reference point
rot.	referring to main rotor
t.p.	referring to tail plane
t.r.	referring to tail rotor
wing	referring to wing

Chapter 1 Introduction

Simulation today plays an increasingly important role both in pilot training and in the field of aircraft research and development, particularly because of the widespread and ever increasing availability of powerful, affordable computers. The expanding use of simulation reflects hardware advances as access to more powerful computers has allowed models of ever greater complexity, and hence fidelity, to be developed. Typical examples of research and development include aircraft design (*Busi, Cinquegrana and Parolini, 1993*), studies into handling qualities (*Du Val, 1989*), stability analysis (*Diftler, 1988*) and rotor / fuselage cross-coupling (*Hansford, 1994*): all of which are well served by the type of modelling explored here. The traditional approach is what will henceforth be referred to as *conventional simulation*, where in its most basic form the input to a simulation may be thought of as pilot control, and the output as the vehicle response. Such an approach is sufficient for most problems where the vehicle's open loop response is the prime consideration. There is, however, growing interest in an alternative approach better suited to studies centred on manoeuvring flight where the vehicle response is considered as the input to the problem and the control motions thought of as the output. When using a precisely defined manoeuvre, rather than the vehicle, as the staring point this approach is often a more intuitive, appropriate and rewarding choice. Such an approach is known as *inverse simulation* and is the main focus of the research presented here. Inverse simulation has been used for a variety of applications including flight test augmentation (*Haverdings, 1983*), control design (*Lane and Stengel, 1988; McKillip and Peri, 1989*) and studies into helicopter agility (*Whalley, 1991*).

Limitations associated with current inverse simulation techniques are as a result of both the inverse algorithms themselves and the sophistication of the vehicle mathematical model used. Many present algorithms are model specific (*Whalley, 1991*) and have numerical problems which only allow inclusion of mathematical models of restricted complexity. Clearly this limits the potential range and scope of problems to which inverse simulation can be applied fruitfully. In addition the majority of existing inverse simulation packages incorporate sufficiently rudimentary models that potential numerical problems are not encountered, and therefore the means of avoiding them cannot be identified. If the field of inverse simulation is to progress then solutions must be found for the inevitable numerical problems that will accompany complex models. Finding such solutions requires research using inverse simulation packages with mathematical

models of much greater sophistication than is presently the case.

The two primary aims of this research are to develop a robust inverse algorithm which is applicable to any model; and to develop a state-of-the-art individual blade rotor model facilitating high fidelity simulation of rotorcraft flight dynamics. Successful realisation of these aims is a major advance in the subject of inverse simulation and produces a unique package in rotorcraft simulation. It is also the first example of the next generation of inverse simulation packages and is the first step in discovering the enormous range and scope of problems to which the subject could usefully be applied. The remaining principal research aims are to apply these developments to both a single main and tail rotor helicopter, and an advanced rotorcraft configuration. In doing so it is hoped to demonstrate the flexibility of the inverse simulation algorithm and the value of the individual blade model. Inverse simulation of such complexity and flexibility would be genuinely unique and it is hoped that this groundbreaking research presents a clear indication of the enormous potential offered by the approach. Simulation of an advanced rotorcraft configuration has particular and timely significance given the resurgent interest in finding aircraft capable of offering a high performance alternative to the helicopter, such as Westland's recent plans to investigate a compound derivative of the Lynx.

Implicit in the above advances is verification of the new inverse simulation algorithm and validation of the individual blade model. In addition their performance will be assessed by comparison with existing methods and models. Once the value of the new tools and techniques has been established, conventional and advanced rotorcraft configurations can be compared flying identical manoeuvres, and their respective advantages and disadvantages identified. The limitations of existing inverse simulations - and consequently the motivation for this research - are now discussed in some detail. Specific emphasis will be given to inverse simulation at Glasgow University as the work there to date has laid many of the foundations for this research.

1.1 Existing Inverse Simulation at Glasgow

The inverse approach is particularly useful for helicopters where precise manoeuvres are a major element of their operation. This is especially true of military helicopters for which many tasks - such as manoeuvres in nap-of-the-earth (NOE) flight - are well suited to mathematical definitions and consequently can be readily simulated.

Inverse simulation is especially relevant with respect to the US-Army's ADS-33D guidelines (*Anon., 1994*) defining helicopter handling qualities in terms of specific manoeuvre elements.

Glasgow has been a centre of research in inverse simulation for several years: the first simulation, called "Helinv" (*Thomson and Bradley, 1990a*) was produced by Thomson and was initially used for assessing helicopter agility (*Thomson, 1986*). Subsequently Helinv has found many other applications including solving problems associated with manoeuvring close to obstacles (*Thomson, Talbot et al, 1995*), as a conceptual design tool (*Thomson and Bradley, 1990c*), examining pilot workload (*Padfield, Jones et al, 1994*), studying the dynamic characteristics of constrained flight (*Thomson and Bradley, 1990d*), and, as mentioned earlier, simulating NOE flight (*Thomson and Bradley, 1990b*) and ADS-33D mission task elements (*Thomson and Bradley, 1994*). The widespread use of Helinv has in turn influenced the work of other authors (*Nannoni and Stabellini, 1989; Whalley, 1991; Hess et al, 1991; Lin et al, 1993*). In short the inverse simulation algorithm, Helinv, has proved a valuable tool with many varied applications. Despite its usefulness and computational expediency, however, Helinv has certain limitations.

1.2 Limitations of Existing Inverse Simulation

1.2.1 Limitations of the Inverse Algorithm

As indicated on the opening page the first group of limitations is due to Helinv's inverse simulation algorithm itself, the basis of which will now be summarised.

Helinv uses a process of numerical differentiation, specifically backwards differencing (*Cheney and Kincaid, 1985*), to recast the equations of motion in algebraic rather than differential form. A chosen manoeuvre is modelled by prescribing certain constraints to which the vehicle must adhere, and then changing the continuous manoeuvre into a series of discrete solution points. With these prescribed constraints particular equations can subsequently be reordered and solved in a closed loop fashion, and the remaining algebraic equations solved simultaneously using an iterative scheme. The following trivial example illustrates the manner in which differentiation based inverse simulation algorithms work.

1.2.1.1 Example of Differentiation Based Inverse Simulation Algorithm

As mentioned earlier the starting point of any inverse simulation is to define a manoeuvre as a time history of the vehicle's position in space, and the end point is a time history of its controls. One important assumption is that the initial conditions (normally equivalent to the vehicle's trim state) are known. It will now be shown how numerical differentiation allows the inverse solution for a simple vehicle with one control, and that this solution requires a manoeuvre described in terms of one parameter. Assume a spherical vehicle that cannot rotate (i.e. rotational velocities P, Q, R are all equal to zero), but which has translational freedom. The means of control is a thrust vector of given magnitude, T, the orientation of which can be varied by angle, α_T (the single control), in the vehicle $x-z$ plane. Thus the vehicle has the capacity to accelerate in 2-D space ($\dot{U}$, $\dot{W}$). A diagrammatic representation of such a vehicle is given in Figure 1.1. If the thrust vector acts through the centre of gravity then, as well as having no lateral velocity, V the pitch angle, θ and bank angle, ϕ will also be equal to zero. As the vehicle is unable to rotate, the azimuth angle is constant and can be set to zero for convenience. Thus using these assumptions and referring to the Euler rigid body equations of motion in Appendix 1, the motion of the vehicle can be described by two simple differential equations:

$$\dot{U} = \frac{T\cos\alpha_T}{m}; \tag{1-1}$$

$$\dot{W} = -\frac{T\sin\alpha_T}{m} + g; \tag{1-2}$$

which are augmented by simplified Euler transformation equations.

$$\dot{x}_e = U; \tag{1-3}$$

$$\dot{z}_e = W. \tag{1-4}$$

Using numerical differentiation over successive general solution points t_{k-1} and t_k, and assuming all values at t_{k-1} are known, then equations (1-1) and (1-2) can be recast as:

$$\frac{U_k - U_{k-1}}{t_k - t_{k-1}} - \frac{T\cos\alpha_{T_k}}{m} = 0;$$

$$\frac{W_k - W_{k-1}}{t_k - t_{k-1}} + \frac{T\sin\alpha_{T_k}}{m} - g = 0;$$

i.e. 2 algebraic equations in the 3 unknowns, U_k, W_k and α_{T_k}. Adding equations (1-3) and (1-4):

$$\dot{x}_{e_k} = U_k;$$

$$\dot{z}_{e_k} = W_k.$$

there are now 4 equations in 5 unknowns and so, to find an exact solution, one of the unknowns must be defined. Thus by simply defining the manoeuvre as a time history of $z_e(t)$ (from which $\dot{z}_e(t)$ can be estimated), a time history of the control $\alpha_T(t)$ can be found. Though the above is a trivial example which can easily be solved in a closed loop fashion this will not be true for more complicated cases. The strength of numerical differentiation is that it allows certain closed loop calculations and yields simultaneous algebraic equations which can be solved iteratively.

The most obvious limitation of this method is that the solution procedure depends on the equations of motion themselves. If the vehicle being simulated were a full 6 degree of freedom model (consistent with Appendix 1) rather than the simple example above then the equations and the means of solving them would clearly be completely different, and could not be solved by a trivial closed loop approach. Of course a simulation need not be limited to 6 d.o.f., as modelling enhancement such as including helicopter rotor blade dynamics can be included making the solution procedure more complicated still. A further consideration is that the solution procedure depends upon the number of vehicle controls which, to guarantee an exact solution, must be matched by the number of manoeuvre constraints. This can be seen in the above example by considering the case where the magnitude of thrust, T, can also be varied. The result is that the manoeuvre must be defined in terms of x_e as well as z_e; 2 controls, 2 constraints. Finally the algorithm varies with the choice of constraints. For the four controls of a helicopter the manoeuvre must be defined in terms of all three displacements (x_e, y_e, z_e) plus an attitude angle. While there is little room for variation in the above simple

example, the choice of angle to which a helicopter can be constrained is not unique, and the choice alters the solution procedure. Helinv, and indeed any inverse simulation algorithm based upon numerical differentiation, is thus specific to one mathematical vehicle model of fixed complexity, and one set of constraints.

The second limitation is due to the use of backwards differencing which assumes a linear relationship between successive time points in the solution procedure. If the dynamic system to be modelled is non-linear and possesses high frequencies then such an assumption is inaccurate for too large a time step, while the numerical errors associated with differencing render the use of small time steps impractical. This is true for the wide range of dynamics associated with helicopters, many of which are captured by an individual blade model. The very small time step required to predict blade flapping dynamics (typically around 20Hz) can cause numerical problems, if used for the slower body modes (as low as 0.1Hz), due to the computational errors introduced in differencing similar numbers. Thus the algorithm has the further imposition of being applicable to dynamic systems of confined frequency only, placing an undesirable restriction on the level of modelling enhancements which are possible.

The previous observation considered the actual numerical accuracy of solutions produced by the two methods. A final issue is that of reversibility (i.e. if the control time histories predicted by inverse simulation reproduce the original manoeuvre when used to 'drive' a conventional simulation). To find a solution using the differentiation method involves actually altering the equations of motion from differential to algebraic form. This means that, irrespective of the accuracy of numerical differentiation, the solution is that of a quasi-steady, rather than a dynamic, system. Indeed by recasting the equations of motion the solution is not in fact that of the original system at all, but of the original system redefined, and thus cannot truly be considered reversible. Though tests have firmly established the reversibility of Helinv, what has in fact been confirmed is simply the acceptability of the solution. Whilst this 'acceptability' improves with smaller time steps, the numerical problems associated with a small time step are unavoidable. If increasingly complicated systems with wider ranges of dynamic frequencies were modelled, a redefined problem may not prove to be sufficiently close to the original problem and the conventional and inverse simulations not sufficiently reversible. The integration method, by contrast, uses exactly the same equations of motion as conventional simulation without requiring that they be changed in any way. The integration method of inverse simulation is thus, without doubt, truly reversible.

1.2.2 Limitations of the Helicopter Mathematical Model

The second group of limitations are as a result of the specific model around which a differentiation based inverse simulation algorithm is designed; in Helinv's case the single main and tail rotor helicopter model "HGS" (*Thomson, 1992*). HGS (Helicopter Generic Simulation) uses a *disc* type representation of the main and tail rotors and empirically derived look-up tables for helicopter fuselage, fin and tail plane aerodynamics.

1.2.2.1 Helicopter Mathematical Models

The accuracy and value of results generated by simulation is dependent on the accuracy and sophistication of the mathematical model used. As with inverse simulation the development of vehicle models has grown in line with computing power. Models available today range from low-order, partially-linearised models used for control design to models incorporating individual representations of the forcing and dynamics of each blade. Individual blade models themselves can vary widely in sophistication and application; a particularly advanced example being the use of free wake analysis to investigate the aerodynamic interaction between the main rotor and vehicle fuselage (*Bühler and Newman, 1996*), though for flight mechanics applications the current state-of-the-art is significantly less well evolved typically utilising dynamic inflow models and including elastic modes to observe blade deformation during flight (*Turnour and Celi, 1995*). Inverse simulation - because of its relative immaturity and computational demands - lags still further behind. The HGS model used by Thomson (*1992*) is currently the most sophisticated rotor model used in inverse simulation outwith the research presented here and, although only a disc model, is the most advanced by a considerable distance. The model used by Hess and Gao (*1993*) for example uses linear derivatives for calculating the rotor forces and moments. A convenient categorisation of modelling levels is given in the paper "Validation of Helicopter Mathematical Models" (*Bradley et al, 1990*) describing all helicopter models as Levels 1, 2 or 3. A summary of the modelling levels is given in Table 1.1. While the above model of Bühler and Newman, which uses free wake analysis, is clearly in Level 3, those used in conventional flight mechanics simulations have not extended beyond Level 2. Thomson's HGS model is in fact the only example used in inverse simulation to date which can confidently claim to have even reached Level 1 and then only at entry level.

1.2.2.2 *Limitations of Disc Models*

While a disc representation of the main rotor such as used in HGS, with as many as 9 d.o.f., can produce reasonable estimates of the gross effects acting at the helicopter centre of gravity, it yields very limited information about the rotor itself and its simplifying assumptions are valid only in moderate flight i.e. not suitable for inverse simulation of severe manoeuvres. It is thus entirely unsuitable for simulating flight near the edge of the helicopter's flight envelope, the most obvious restriction being the use of linear aerodynamics which do not recognise the effects of non-linear characteristics such as blade stall. In addition the accuracy of estimates of the total rotor forces and moments is compromised by a scheme which ignores individual blade loadings and calculates averages over the whole disc. For these reasons it was intended to develop a much more sophisticated *individual blade model* approaching Level 2 classification. Such a model, with 14 d.o.f. or more, would be far in advance of anything currently available in inverse simulation and close to state-of the-art for flight mechanics generally.

1.3 Aims of Research and Structure of Dissertation

The research aims were discussed on the first page of this introduction. Subsequent sections detailed the limitations in the current inverse techniques which have motivated this research. The approach adopted in realising the aims is now detailed, including how they are represented in the structure of the dissertation.

1.3.1 Research Aims

i) Robust, Stable, Generic Inverse Simulation Algorithm

The first research aim was to develop a new inverse simulation algorithm, one which is not model specific and is robust and stable. Chapter 2 begins with a historical review of inverse simulation culminating in the current state of the research. A comparison is then made between the two main methods of inverse simulation in use today, based upon numerical differentiation and numerical integration respectively. This comparison takes both the forms of a heuristic inspection and a unique state space development of the two algorithms illustrating precisely how they differ. It then becomes apparent that despite its relative computational efficiency the numerical differentiation

method suffers from being specific to the mathematical model and manoeuvre constraints. Next it is demonstrated that the differentiation method is prone to numerical errors. It is subsequently proposed that the numerical integration based method will demonstrate flexibility in the choice of vehicle, modelling complexity and manoeuvre constraint, and be relatively stable. Consequently the technique of numerical integration is chosen as the basis for the inverse simulation algorithm used here. In Chapter 3 a detailed state space description and flowchart of the "Genisa" (Generic Inverse Simulation Algorithm) is given. Using the HGS disc model inverse simulation results produced by Genisa are presented. These results are verified in three stages: by inspection; by using the resultant control time histories to 'drive' a conventional simulation (i.e. proving that the results are reversible) and by comparison with results from the established Helinv algorithm. Finally examples of numerical instability are demonstrated which, if unresolved, would seriously limit the problems to which Genisa could be applied. Thus in Chapter 4 it is shown how these instabilities can be eliminated and an explanation is offered as to why this is the case. The flexibility of Genisa is also demonstrated by performing additional manoeuvres and by imposing alternative manoeuvre constraints. Finally the algorithm's robustness is investigated by varying its key parameters.

ii) Individual Blade Rotor Model

The second research aim was to develop a new individual blade rotor model, a degree of modelling complexity unprecedented in inverse simulation. The fundamental differences between disc and individual blade models are examined in Chapter 5, and the advantages of the later are highlighted. The modelling theory used in "Hibrom" (Helicopter Individual Blade Rotor Model) is identified and the main simplifying assumptions and modelling features are discussed. Existing theories used in Hibrom's development are included in the Appendices. In Chapter 6 the aim is to verify and validate the individual blade model Hibrom, and to present examples of its advantages over a disc model such as HGS. Verification is achieved in four stages: heuristic analysis of output from Hibrom; comparison of trim controls and attitudes with the established HGS model; inspection and comparison with HGS of open loop responses to control inputs; and finally contrasting the models' control and attitude time histories over identical inverse simulation manoeuvres. This final stage demonstrates the limitations of the disc model compared to the extra information and more accurate predictions possible with the individual blade model. It has never previously been possible to compare two different levels of helicopter model simulating exactly the same manoeuvre and so this is clearly a

significant achievement. Validation involves 'flying' Genisa / Hibrom through a manoeuvre defined by flight test data and comparing the resultant control time histories to those of the actual aircraft.

iii) Inverse Simulation of Individual Blade Rotor Model

As indicated above, the final stage of Hibrom's verification involves inverse simulation. Chapter 6 discusses some of the problems involved in inverse simulation of an individual blade model, and how these can be overcome. Inverse simulation results are presented for an individual blade single main and tail rotor helicopter flying several manoeuvres. This can be considered the central aim of the research; to successfully accommodate an individual blade rotor model in inverse simulation. It has never previously been achieved.

iv) Simulation of Advanced Rotorcraft Configuration

Having used an individual blade model in inverse simulation, the next stage was to demonstrate the adaptability of the inverse algorithm, Genisa, and the possibilities offered by a new level of rotor modelling, Hibrom. Modelling of an advanced rotorcraft configuration is described in Chapter 7, including details of the development of individual blade modelling of the tail rotor and also of the propeller used as an auxiliary thrust device. The practicalities of the configuration are investigated by trimming the vehicle over a range of speeds and also by using the inverse simulation algorithm Genisa to fly a variety of manoeuvres. In this way it is possible to test both the feasibility of different configurations and - by flying identical manoeuvres - to investigate their advantages and disadvantages in comparison with single main and tail rotor helicopters. Chapter 7 includes simulation results for a rotorcraft with individual blade models of the main rotor, tail rotor and propeller. To the best of the author's knowledge no comparable simulation package exists - either in terms of flexibility or modelling sophistication - for evaluating the feasibility and relative benefits of different rotorcraft configurations.

1.3.2 Summary of Research Aims

To summarise then, the four main aims of the research presented in this dissertation are to:

i) develop a generic inverse simulation algorithm;
ii) develop an individual blade rotor model;
iii) incorporate the rotor model in the inverse simulation algorithm;
and iv) apply the model and algorithm to an advanced rotorcraft configuration.

1.3.3 Research Conclusions

The thesis is completed by the conclusions in Chapter 8 which find that the developed integration based inverse simulation algorithm, Genisa does indeed demonstrate considerable advantages over algorithms founded on numerical differentiation. In addition - as anticipated - an individual blade model does offer benefits compared to a disc model, particularly when simulating alternative, advanced rotorcraft configurations.

1.3.4 Appendices

In addition to the main chapters already discussed, this dissertation includes eight Appendices. As each Appendix covers either existing theories or configurational data it was considered superfluous to discuss them here. They are listed in the contents page.

	Level 1	***Level 2***	***Level 3***
Aerodynamics	linear 2D dynamic inflow / local momentum theory analytically integrated loads	non-linear (limited 3D) dynamic inflow / local momentum theory local effects of blade vortex interaction unsteady 2D compressibility numerically integrated loads	non-linear 3D full wake analysis (free or prescribed) unsteady 2D compressibility numerically integrated loads
Dynamics	i) rigid blades quasi-steady 3 d.o.f. flap 6 d.o.f. flap + lag 6 d.o.f. flap + lag + quasi-steady torsion	i) rigid blades with options as in Level 1 ii) limited number of blade elastic modes	i) detailed structural representation as elastic modes or finite elements
Applications	parametric trends for flying qualities and performance studies well within operational flight envelope low bandwidth control	parametric trends for flying qualities and performance studies up to operational flight envelope medium bandwidth appropriate to high gain active flight control	rotor design rotor limits loads prediction vibration analysis rotor stability analysis up to safe flight envelope

Table 1.1 **Levels of Helicopter Rotor Mathematical Modelling**

Chapter 2 Methods of Inverse Simulation

It is the aim of this chapter to give a general description of the two main methods of inverse simulation currently in use. By using a non-specific state space formulation it is made clear how the respective solution procedures are constructed from the vehicle equations of motion and where they differ. The relative advantages / disadvantages and associated numerical problems are also discussed. The first step, however, is to identify the basic inverse problem, and summarise the development of inverse simulation itself.

2.1 Introduction

2.1.1 The Inverse Problem and Inverse Simulation

Assuming a known starting point, the solution to a *conventional* problem can be described as the process by which the answer is found. When the answer is already known, an *inverse* solution (as the name might imply) is the process by which the starting point can be found. An example of an inverse concept is that of design as the end product must realise certain, established goals while something as fundamental as the starting material may be unknown. In addition many practical constraints such as cost and weight must be observed. This analogy becomes more pertinent by using a simple aerospace example. Consider the case where the lateral stability of an aircraft is unsatisfactory. A conventional approach would be to start with the surface area of the vertical fin (input), and calculate, through a series of equations, the resultant sideforce (output). Assuming that the required sideforce is known, then the inverse approach has two possibilities, each based upon the conventional. The first assumes that the equations may be recast to describe the area as a function of the required sideforce. The second involves modelling the change of sideforce with respect to area so that an iterative technique will yield the fin surface area needed to supply the predefined force. An example of a *constraint* or constant would be the limited range of aerofoil sections available. In both inverse cases the original input has become the output and vice versa.

In his book "Dynamics of Flight", Etkin (*1959*) states that "the equations of airplane dynamics may be regarded as a set of relations which connect two groups of variables (the inputs and outputs) and one group of constants (the constants in the

equations)." He goes on to say that "the usual or direct problem is to solve for the output when the input and constants are known." An alternative approach is that "the output and constants may be given, and the input is to be found". The 'equations of airplane dynamics' are now more commonly known as the equations of motion and can be applied to describe the dynamics of a general body. The six familiar Euler equations of motion for a rigid body are given in Appendix 1 (equations A1.1). As these equations are time differential they can be used to describe how the vehicle moves with respect to time as a function of the externally applied forces and moments. This time evolution process will be referred to as *conventional simulation* where the controls, vehicle configurational data and resultant manoeuvre are analogous to the inputs, constants and outputs in Etkin's definition or the area, aerofoil section and sideforce in the above example. An alternative approach, when applied to the equations of motion, is known as *inverse simulation* and is a process by which the controls (input) can be found which will achieve a desired manoeuvre, or output. A typical example of conventional simulation would be the pitch rate response to a step input of elevator (fixed-wing) or longitudinal cyclic (helicopter), with an inverse simulation example being the control inputs required to accelerate between prescribed velocities over a set distance. The technique of conventional simulation has been used for a long time and is well understood; the alternative idea of inverse simulation is not so common.

2.1.2 History of Inverse Simulation

An early inverse problem was demonstrated by Etkin himself (*1951*), where a fixed wing aircraft was rolled continuously from wings-level to a prescribed angle of bank. The rolling equation and bank angle function were reconstructed allowing the aileron input to be described in terms of bank angle output. Though a genuine example of inverse simulation, the problem was limited in that it dealt with a single-degree-of-freedom rolling motion and derivative based transfer functions. An even earlier example was that of Jones (*1936*), who inversely solved the equations of motion to study gust effects. Again by using a linearised, low order model it was possible to recast the equations analytically. One of the first computer based inverse simulations was produced by Wood et al (*1974*) to evaluate the performance of helicopters flying designated tasks. Unfortunately as the tasks were defined in terms of vehicle parameters it was not possible to compare different helicopters flying exactly the same manoeuvre. In addition the helicopter model used was semi-empirically based and the rotor model of a rudimentary nature. Consequently only limited physical information could be gleaned from the

simulations. With the advent of low cost, powerful computers in the 1980's there was a resurgence of interest in inverse simulation. As computing power increased, so did the complexity of model which could be simulated within a realistic time frame. For inverse simulation specifically, the introduction of previously unrealisable numerical techniques offered new ways of manipulating the equations of motion. The possibilities opened up by computers in the 1980's and 1990's are reflected in the different inverse simulations which have been developed. All resultant inverse simulations can be grouped according to a number of different categories:

i) the type of inverse problem (solution of certain equations or full inverse solution of the equations of motion);
ii) the motivation for using the equations of motion in an inverse form;
iii) the complexity of mathematical model used in simulation;
iv) the method used to invert the equations of motion.

i) Equations

The distinction being made here is whether a full set of equations of motion are being solved (as in inverse simulation), or simply a series of equations in an inverse fashion. A number of inverse solutions have not dealt with the full equations of motion, a good example being Houston and Caldwell (*1984*) who investigated the effect of an active tail plane on helicopter agility. The equations were used in their fully linearised form and, to facilitate matrix inversion, reduced from six to the three longitudinal equations plus roll (matching the four controls). McKillip and Perri (*1989*) decoupled the longitudinal and lateral modes of their model to evaluate a number of control laws. Given the aims of the above authors, the simplifications are reasonable but clearly do not produce full degree of freedom inverse simulations.

ii) Motivation

In addition to the aforementioned work of McKillip and Perri, authors such as Smith and Meyer (*1987*) and Lane and Stengell (*1986*) have used inverse techniques for control analysis. The models in question are suitably simple, often linear models and consequently lend limited insight into the vehicle dynamics. Thus a distinction is made between these examples and inverse simulations for flight dynamics studies.

iii) Model Complexity

In helicopter flight dynamics studies the complexity of model used in conventional simulation varies from low order, linearised models to those incorporating high fidelity, elastic, individual blade, rotor models (*Turnour and Celi, 1996*). To date many models used in inverse simulation have been of the more fundamental variety (*McKillip and Perri, 1989*). More sophisticated helicopter inverse simulation models are typified by full non-linear inertial and gravitational terms but linear derivatives for estimating the aerodynamic external forces and moments (*Hess and Gao, 1993*). Consequently the fidelity of most inverse simulations is limited to small amplitude manoeuvres. By far the most sophisticated inverse simulation helicopter model discussed in this introduction is that used by Thomson (*May 1992*) which employs blade element / momentum theory to produce a multiblade representation of the main rotor. As well as yielding flight parameter information, such modelling also permits observation of the rotor's performance.

iv) Inverse Simulation Method

There are two principle methods of inverse simulation; one using numerical differentiation; the other numerical integration. The first main method uses numerical differentiation to convert the equations of motion from differential to algebraic form. By prescribing manoeuvre outputs it is possible to recast certain equations and solve in closed loop fashion. In practice the remaining equations are often, and most easily, solved numerically for the controls and other unknowns. This method was first identified in the paper "An Analytical Method of Quantifying Helicopter Agility" (*Thomson, 1986*) which used prescribed flight path parameters. It has been used successfully in other algorithms (*Nannoni and Stabellini, 1989; Whalley, 1991*) and in a similar fashion by Kato and Siguira but using vehicle attitudes (*1986*). The second main method leaves the equations of motion undisturbed. Using numerical integration the basis of a solution is an iterative scheme which makes successive estimates of the inputs until the equations of motion predict outputs equal in value to those prescribed by the manoeuvre. Though this method had been used previously in a number of inverse applications (*Meyer and Cicolani, 1981; Haverdings, 1983; McKillip and Perri, 1989*), it was first explicitly documented as a flexible, manoeuvre driven, inverse simulation in the paper "Generalized Technique for Inverse Simulation Applied to Aircraft Maneuvers" (*Hess, Gao and Wang, 1991*). The algorithm described therein can thus be considered the basis for all inverse

simulation algorithms that use numerical integration.

The current techniques used in manoeuvre driven inverse simulation thus fall into two distinct categories: one based on solving the equations of motion iteratively in a conventional time response approach using numerical integration, best illustrated by Hess's algorithm (*1991*), whilst the other method involves discretising the problem and using numerical differentiation to calculate time varying parameters explicitly (*Thomson, 1986*). Glasgow has been a centre of research in inverse simulation for several years, the first simulation produced was called "Helinv" (*Thomson and Bradley, 1990a*) which is of the numerical differentiation category mentioned above. As already indicated the helicopter model, HGS (*Thomson , 1992*), used in Helinv is the most sophisticated discussed in this introduction. More recently a new numerical integration based algorithm, "Genisa" (*Rutherford and Thomson, 1996*), has been developed by this author. Both algorithms are manoeuvre driven in that the inverse solution of the vehicle equations of motion requires a discretised time history of manoeuvre parameters as an input. This chapter discusses the general features of both differentiation and integration based algorithms and, by applying Genisa to HGS, compares results directly in Chapter 3. A brief description of the Helinv algorithm is given in the following sections and a complete treatment in Appendix 3, while the specific development of Genisa is detailed in Chapters 3 and 4.

2.2 *A Comparison of Inverse Simulation Techniques*

Prior to highlighting the differences between the inverse simulations and discussing their relative advantages / disadvantages, it is first essential to outline their respective formulations. The responsibility of this work is not to produce a detailed description of the Helinv algorithm as this has been reported elsewhere (*Thomson, 1994*). It is appropriate, however, to present here an overview of its main features and those of differentiation based algorithms in general. In addition Appendix 3 discusses Helinv in more detail, both for reference and for the sake of completeness. Similarly this section will present an outline of the integration based algorithms with the development and implementation of Genisa specifically left until Chapters 3 and 4.

A general state space description of the two methods is now presented.

2.2.1 General State Space Description of Methods of Inverse Simulation

Before considering the actual inverse simulation methods it is worthwhile looking, in state space form, at the equations of motion and how they are used in conventional simulation. It will consequently become clearer how the two methods differ in their approaches to an inverse solution.

2.2.1.1 Instantaneous Description of System

The instantaneous condition of a system at time $t = t_k$ can be described by the following three sets of equations:

$$\dot{\underline{x}}(t_k) = \underline{f}\left\{\underline{x}(t_k), \underline{\xi}(t_k), \underline{u}(t_k)\right\}, \tag{2.1}$$

$$\dot{\underline{\xi}}(t_k) = \underline{g}\left\{\underline{x}(t_k), \underline{\xi}(t_k)\right\}, \tag{2.2}$$

and

$$\underline{y}(t_k) = \underline{h}\left\{\underline{x}(t_k), \underline{\xi}(t_k), \underline{u}(t_k)\right\}; \tag{2.3}$$

where the state vector, $\underline{x}$ has n_x elements, the attitude vector, $\underline{\xi}$ has n_ξ elements, the output vector, $\underline{y}$ has n_y elements and the control vector, $\underline{u}$ has n_u elements.

2.2.1.2 Conventional Simulation

Conventional simulation uses numerical integration to predict the time evolution of the system from $t = t_k$ to $t = t_{k+1}$ where t_k and t_{k+1} are successive time points in the simulation. This process can be represented by:

$$\underline{x}(t_{k+1}) = \int_{t_k}^{t_{k+1}} \dot{\underline{x}}(t_k)dt + \underline{x}(t_k), \tag{2.4}$$

$$\underline{\xi}(t_{k+1}) = \int_{t_k}^{t_{k+1}} \dot{\underline{\xi}}(t_k)dt + \underline{\xi}(t_k), \tag{2.5}$$

and

$$\underline{y}(t_{k+1}) = \underline{h}\left\{\underline{x}(t_{k+1}), \underline{\xi}(t_{k+1}), \underline{u}(t_{k+1})\right\}. \tag{2.6}$$

Thus given values for the state, attitude and control vectors at $t = t_k$, equations (2.4-2.6) yield the state, attitude and output vectors at $t = t_{k+1}$. Repeated integration between a succession of time points allows the vehicle's motion to be simulated over a set period of time.

2.2.1.3 Numerical Integration Based Inverse Simulation

At time $t = t_k$, all values of the state, attitude and output vectors are known by integration from time $t = t_{k-1}$. The aim of the integration based inverse simulation is to try and predict the control vector at $t = t_k$ which will yield a predefined desired response at $t = t_{k+1}$. Given that the control vector, $\underline{u}(t_k)$, has n_u elements, then n_u constraints must be imposed to find a solution. As state, attitude and output vectors can all be predicted at $t = t_{k+1}$ by conventional simulation (using an estimated $\underline{u}(t_k)$) it is evident that the constrained output vector, $\underline{y}(t_{k+1})$ may contain any n_u elements of $\underline{x}$, $\underline{\xi}$ and $\underline{u}$. Thus if the desired output vector, $\underline{y}_{des.}(t_{k+1})$ is known then an error vector, $\underline{e}(t_{k+1})$, can be defined as the difference between the actual and desired output vectors:

$$\underline{e}(t_{k+1}) = \underline{y}(t_{k+1}, \underline{u}(t_k)) - \underline{y}_{des.}(t_{k+1}). \tag{2.7}$$

Setting equation (2.7) to **nul**, a solution can be found for a unique value of $\underline{u}(t_k)$ by the iterative method of Newton-Raphson (*Cheney and Kincaid, 1985*). This process can be repeated over a series of time intervals yielding a control time history, $\underline{u}(t_k)$, for a complete manoeuvre, $\underline{y}_{des.}(t_{k+1})$, where:

$$0 \le t_k < t_{man.},\ 1 \le k < n_{pts.};$$

$t_{man.}$ is the time taken to complete the manoeuvre; and $n_{pts.}$ is the number of discrete points defining the manoeuvre.

2.2.1.4 Numerical Differentiation Based Inverse Simulation

It is also possible to find a unique inverse solution using numerical differentiation. This is now detailed.

Consider equations (2.1) and (2.2), but with the derivatives estimated by backward

differencing (*Cheney and Kincaid, 1985*):

$$\frac{\underline{x}(t_k)-\underline{x}(t_{k-1})}{t_k-t_{k-1}}=\underline{f}\left\{\underline{x}(t_k),\underline{\xi}(t_k),\underline{u}(t_k)\right\}, \tag{2.8}$$

$$\frac{\underline{\xi}(t_k)-\underline{\xi}(t_{k-1})}{t_k-t_{k-1}}=\underline{g}\left\{\underline{x}(t_k),\underline{\xi}(t_k)\right\}. \tag{2.9}$$

The equations are now in algebraic form and should allow a closed loop solution. Though it can be assumed that variables at t_{k-1} are known, with no differential equations the integration process is removed and variables at t_k cannot be predicted by conventional simulation from $t=t_{k-1}$. The result is that an unknown is introduced for each differential equation. Thus it can be seen that (2.8) contains n_x equations in $n_x+n_\xi+n_u$ unknowns. Using (2.9) introduces another n_ξ equations and no new unknowns so the system now has n_x equations and n_x+n_u unknowns. Unfortunately a prescribed desired output vector $\underline{y}_{des.}(t_k)$ from (2.3) introduces as many new unknowns, n_y, as equations and so does not reduce the problem further. Applying the same criterion as with the integration method, however, a constraint can be applied for each control (i.e. n_u constraints). The system now has n_x equations in n_x unknowns and equation (2.10) can be solved for $\underline{u}(t_k)$, as previously, by a Newton-Raphson scheme:

$$\underline{e}(t_k)=\frac{\underline{x}(t_k)-\underline{x}(t_{k-1})}{t_k-t_{k-1}}-\underline{f}\left\{\underline{x}(t_k),\underline{\xi}(t_k),\underline{u}(t_k)\right\}, \tag{2.10}$$

where $\underline{u}(t_k)$ can clearly contain state and attitude as well as explicit system control variables. As with the integration method the algorithm produces a control time history for a predefined manoeuvre, though each solution is instantaneous rather than over a time interval.

Both methods are now discussed in more specific and accessible terms where the vehicle being simulated can be assumed to be a single main and tail rotor helicopter. The differentiation method is Helinv (*Thomson, 1994*), while the description of the integration method concerns the technique laid down by Hess (*1991*). The associated state, $\underline{x}(t_k)$, attitude, $\underline{\xi}(t_k)$, control, $\underline{u}(t_k)$, and output, $\underline{y}(t_k)$, vectors are now:

$$x(t_k)=\left\{U(t_k)\quad V(t_k)\quad W(t_k)\quad P(t_k)\quad Q(t_k)\quad R(t_k)\right\}^{\mathrm{T}},$$

$$\underline{\xi}(t_k) = \left\{\phi(t_k) \quad \theta(t_k) \quad \psi(t_k)\right\}^{\mathrm{T}},$$

$$\underline{u}(t_k) = \left\{\theta_0(t_k) \quad \theta_{1s}(t_k) \quad \theta_{1c}(t_k) \quad \theta_{0t.r.}(t_k)\right\}^{\mathrm{T}},$$

and

$$\underline{y}(t_k) = \left\{x_{e.}(t_k) \quad y_{e.}(t_k) \quad z_{e.}(t_k) \quad \psi(t_k)\right\}^{\mathrm{T}}.$$

2.2.2 Numerical Differentiation Approach

The discussion presented here can be applied specifically to Helinv (*Thomson, 1994*). The basis of this algorithm is the calculation of the rates of change of the attitude angles using numerical differentiation (backward differencing). Six equations of motion (A1.1) are effectively converted from a series of non-linear differential equations, to a series of non-linear algebraic equations, which are then solved directly for six unknowns (the four control inputs, $\theta_0(t_k)$, $\theta_{1s}(t_k)$, $\theta_{1c}(t_k)$ and $\theta_{0t.r.}(t_k)$; and the roll and pitch attitudes, $\phi(t_k)$ and $\theta(t_k)$) using a Newton-Raphson iterative scheme (*Cheney and Kincaid, 1985*). The simulation is initiated by defining a manoeuvre essentially as a series of positional coordinates (relative to an earth fixed frame of reference), equally spaced in time ($x_{e.}(t)$, $y_{e.}(t)$, $z_{e.}(t)$). The helicopter's component velocities ($\dot{x}_{e.}(t)$, $\dot{y}_{e.}(t)$, $\dot{z}_{e.}(t)$) and accelerations ($\ddot{x}_{e.}(t)$, $\ddot{y}_{e.}(t)$, $\ddot{z}_{e.}(t)$) in the earth fixed frame of reference are then obtained by differentiation. This ensures that the vehicle's centre of gravity follows the correct trajectory, however the vehicle is free to adopt an unspecified attitude. It is therefore necessary to specify one of the vehicle attitude angles (the heading or side slip angle being the most convenient) to guarantee a realistic manoeuvre and vehicle response thus defining the output:

$$\underline{y}(t_k) = \left\{x_{e.}(t_k) \quad y_{e.}(t_k) \quad z_{e.}(t_k) \quad \psi(t_k)\right\}^{T}.$$

If we consider a general time point within the simulation, then at any step in the iterative process, the current estimates of both roll and pitch attitudes are differenced with the values calculated at the previous time point giving estimates for the attitude rates at the current point. Through a series of closed loop calculations all the inertial, gravitational and external forces and moments in the equations of motion can be calculated and hence new estimates of the unknown variables obtained. In this way the four control displacements are calculated directly from the three demanded positional displacements, plus the heading, at each time point.

2.2.3 Numerical Integration Approach

In contrast to Helinv, numerical integration based algorithms do not reduce the equations of motion to algebraic form but rather integrate them numerically, thus allowing a prediction of the states and flight path to be made by conventional simulation. In simple terms a guess is made as to what control inputs are required to move the helicopter from its current position (and heading) to that specified at the next time point in the manoeuvre definition. The equations of motion are then integrated in the usual manner and the actual position produced using the estimated control displacements is calculated. The error between actual and desired position is then used as the basis for an iterative scheme to calculate exactly what control displacements are required to achieve the desired positional and heading change. The output error functions are solved over each interval, producing control time histories for the complete manoeuvre.

2.3 Structure of the Algorithms

As discussed earlier, using the differentiation approach it is necessary to calculate certain time varying parameters numerically thus expressing the differential equations of motion in algebraic form. This entails a degree of rearrangement and manipulation of the equations of motion. Any modifications to the mathematical model which add extra states (which will be time varying) will necessitate further manipulation and restructuring of the algorithm. Clearly this could introduce a significant overhead should a substantial modelling enhancement be desired. Further, using the differentiation scheme, the iteration is based on minimising the error in control and attitude values which are implicit in the equations of motion. Again, changes in the mathematical model may require changes in the structure of the algorithm. This coupling between the mathematical model and the simulation algorithm is a major drawback of the differentiation approach. These disadvantages can be demonstrated by considering the state space representation in section 2.2.1.4 above.

i) In applying constraints to reduce the number of unknowns to n_x, the choice will determine which equations and unknowns are removed and in which order this is done. Thus the solution procedure is dependent upon the actual constraints imposed. In addition vehicles with different numbers of controls, n_u, will require different numbers of constraints and resultant solution procedure.

ii) The equations to be solved can be reduced to n_x which is the number of equations of motion. Clearly this means that simulating different vehicles or using a different complexity of model changes the number of equations to be solved.

iii) The method of first order backward differencing assumes a linear relationship between successive times points. If the dynamic system to be solved is non-linear and of a sufficiently high frequency, then this assumption proves to be grossly inaccurate for too large a time step. Using a smaller time step should, in theory capture the system dynamics, though in practice the differencing introduces unacceptable numerical errors and a solution is impossible. This numerical problem is discussed later in more detail.

These disadvantages are not apparent in methods using the integration scheme where the model and algorithm can be expressed independently. This is primarily because the iteration minimises the error in flight path variables (for example x_{e_i}, y_{e_i}, z_{e_i} and heading, ψ) without requiring that the equations of motion be rearranged. The result of this is that modelling enhancements do not necessitate changes in the algorithm structure and in essence the mathematical model may be treated as a 'module' of the inverse simulation. Hence it is possible to simulate completely different vehicles simply by changing the mathematical model. Further, should an alternative set of input motion constraints be desirable then it is a simple case to modify the error functions in the integration scheme as opposed to the major restructuring which is required in the differentiation algorithm. An example of this is the "Rapid Sidestep" Mission Task Element (*Thomson and Bradley, 1994*). Here the aircraft performs a lateral excursion at constant height and heading. While the most natural choice of constraints might be x_{e_i}, y_{e_i}, z_{e_i} and ψ i.e.:

$$\underline{y} = \left\{ x_{e_i}(t_k) \quad y_{e_i}(t_k) \quad z_{e_i}(t_k) \quad \psi(t_k) \right\}^{\mathrm{T}},$$

where $x_{e_i} = z_{e_i} = \psi = 0$ and $y_{e_i} = f(t)$, it is more akin to the pilot's view of the manoeuvre to specify it in terms of x_{e_i}, z_{e_i}, ψ and bank angle, $\phi = g(t)$ i.e.:

$$\underline{y} = \left\{ x_{e_i}(t_k) \quad z_{e_i}(t_k) \quad \phi(t_k) \quad \psi(t_k) \right\}^{\mathrm{T}},$$

where the focus is then on the roll attitude rather than lateral position. Though making

this modification to the integration based algorithm is straightforward, it would require major restructuring of the differentiation based algorithm. Again referring to the state space discussion, it is apparent that equations (2.1-2.6) are not changed and the choice of constraints is flexible, thus the integration method can be used to find an inverse solution to any mathematical model which can be simulated in the conventional way. The one major disadvantage is that the number of numerical integrations mean that the algorithm is computationally intensive and takes much longer to execute than the differentiation method.

2.4 Numerical Stability

Both algorithms suffer from problems associated with numerical stability. This is now discussed.

2.4.1 Numerical Differentiation Approach (Helinv)

The main problem with any algorithm which uses numerical differencing is that it will be prone to rounding errors when subtracting similar numbers. There are two possible situations where this may arise. Firstly in attempting to differentiate a slowly changing variable using a small time increment, which is epitomised by the calculation of pitch rate at time point t_k from the expression for backwards differencing:

$$\dot{\theta}(t_k) = \frac{\theta(t_k) - \theta(t_{k-1})}{t_k - t_{k-1}}.$$

In a turning manoeuvre, for example, where the pitch attitude changes slowly, the values of $\theta(t_k)$ and $\theta(t_{k-1})$ will be similar over a small time interval and hence errors may occur when differencing them. Secondly, in calculating the Jacobian for the Newton-Raphson iteration scheme where the functions to be differentiated may not be sensitive to small increments of the unknown variables. An example is the rate of change of the first equation of motion (A1.1) (longitudinal acceleration) with respect to helicopter tail rotor collective:

$$\frac{\partial e_1}{\partial \theta_{0t.r.}},$$

where $$e_1 = \dot{U} + (WQ - VR) - \frac{X}{m} + g\sin\theta,$$

which may be small as e_1 is insensitive to $\theta_{0t.r.}$. Careful selection of both the time increment used in the discretisation, and the increments used for the Jacobian calculation are therefore essential for a stable numerical solution. A problem also arises when the aircraft's dynamics exhibit a wide range of characteristic frequencies. In the case of the helicopter where blade flapping dynamics have been modelled, the frequency of the motion is typically around 20Hz. In order to capture the effects of blade flapping, a small time increment will therefore be required. The rigid body modes are much slower (possibly with frequencies of around 0.1Hz) and consequently there may be numerical problems associated with the rounding errors caused when differencing body states, which exhibit little change, over such a small time increment.

These instabilities often occur when attempting to simulate severe manoeuvres and typically have the effect of the algorithm being unable to find a converged solution.

2.4.2 Numerical Integration Algorithms

As with the differentiation approach the calculation time step Δt strongly influences both the accuracy and stability of the solution. In common with Helinv, integration based algorithms can suffer from numerical problems if a high frequency model, such as a helicopter with blade flapping dynamics, is employed. As flapping modes are of a much higher frequency than body modes a smaller time step is needed to adequately capture all of the flapping characteristics. If too large a time step is used the results show apparently unstable oscillations of a frequency consistent with the flapping dynamics.

This phenomenon is similar to the 'multiple solutions' observed by Hess et al (*1991, 1993*). Although acknowledging the problem, Hess does not resolve it; rather the oscillations are removed from the final results using a high frequency filter. It is in fact possible to reduce the amplitude of the oscillations by using successively smaller values of Δt and indeed they can almost be eliminated completely. This indicates that the multiple solutions may occur as a result of simulating a quickly changing system with too large an integration step i.e. 'skipping' certain dynamic features.

The implication from above is that using as small a time step as possible is

desirable, however there are also problems associated with too small a time step. As first presented by Lin et al (*1993*) "when there is an uncontrolled state variable, the integration inverse method may be unstable for small time step". As we are considering a conventional helicopter with four controls, and even a rudimentary helicopter model with multiblade flapping has at least nine degrees of freedom, it is clear that there will be uncontrolled states. One of the significant achievements of the current research is the elimination of these instabilities from integration based inverse simulations. The technique used is detailed in Chapter 4 and undoubtedly represents a major advance in simulation theory.

2.5 Chapter Summary

In this chapter the general inverse problem and inverse simulation specifically have been defined. The two main methods of inverse simulation are based upon numerical differentiation and numerical integration respectively. It has been established that of the current manoeuvre driven, helicopter flight dynamics, inverse simulations Helinv employs the most advanced mathematical model. However Helinv, and numerical differentiation methods in general, suffer numerical problems and are limited by being model specific and unable to incorporate dynamic models above a certain complexity. For this reason a new integration based algorithm, Genisa, has been developed which offers much greater flexibility and can incorporate more sophisticated mathematical models.

Chapter 3 details the formulation and verification of the integration inverse simulation algorithm, Genisa. The aforementioned numerical instabilities consistent with both too large and too small a time step are also presented, and it is demonstrated in Chapter 4 how such errors can be eliminated.

Chapter 3 Genisa: Generic Inverse Simulation Algorithm

The two methods of inverse simulation, based upon numerical differentiation and integration, were discussed in Chapter 2. This Chapter will attempt to describe in detail, the Genisa algorithm which uses numerical integration. Results are produced using the HGS helicopter model (*Thomson, 1992*), Appendix 2, and Genisa is then verified by comparison with the established Helinv algorithm. Chapter 2 also alluded to certain numerical problems associated with integration based inverse simulation algorithms. Typical examples are demonstrated here before a technique for eliminating them is discussed in Chapter 4.

3.1 The Genisa Algorithm

3.1.1 Overview

The natural choice of initial conditions for an inverse simulation is the trim state. For the purposes of Genisa we assume that trim is defined by:

i) rectilinear flight;
ii) zero resultant body accelerations;
iii) aircraft heading north;
iv) attitude rates zero.

Using the process of numerical integration, conventional simulation of the equations of motion predicts the actual position reached after a given time, Δt, by a specific set of control inputs. As the desired position after time Δt is known from the flight path definition, the difference between the actual and desired positions then provides the basis for an iterative scheme to establish the control inputs required to achieve the desired manoeuvre output i.e. the error in the flight path can be minimised. Control time histories can then be produced for an entire manoeuvre by repeating this process over a series of solution intervals. The basis for this algorithm is the method described by Hess et al (*1991*), however to ensure clear understanding of the problem the Genisa algorithm is given here in some detail.

3.1.2 State Space Representation of the Genisa Algorithm

Consider that the problem is discretised into a series of time points, t_k, at each of which there is a desired output vector $\underline{y}_{des.}(t_k)$ (as defined by the manoeuvre model) describing the position and heading of the helicopter. At the current time point $t = t_k$, the value of $\underline{x}(t_k)$ and $\underline{\xi}(t_k)$ are known by integration of the state and attitude derivatives, $\dot{\underline{x}}(t_{k-1})$ and $\dot{\underline{\xi}}(t_{k-1})$, from the previous time point $t = t_{k-1}$. The influence of the control vector, $\underline{u}(t_k)$, on $\dot{\underline{x}}(t_k)$ can be found by perturbing the current value. In addition the effect of $\underline{u}(t_k)$ on $\dot{\underline{\xi}}(t)$ (via $\underline{x}(t)$ for $t_k < t \le t_{k+1}$), $\underline{x}(t_{k+1})$, $\underline{\xi}(t_{k+1})$ and $\underline{y}(t_{k+1})$ can be established using integration. The problem is then effectively to find a solution for the control vector, $\underline{u}(t_k)$, which will produce a value of $\underline{y}(t_{k+1})$ equal to $\underline{y}_{des.}(t_{k+1})$. Referring to the flowchart in Figure 3.1, a step by step description of the solution procedure is now given.

Before commencing with the inverse simulation it is necessary to define the manoeuvre model (see Appendix 4). From this we obtain the desired output vector, $\underline{y}_{des.}$, which is expressed as a series of $n_{pts.}$ discrete points, equally spaced in time. A time history describing the desired manoeuvre is thus established:

$$\underline{y}_{des.}(t_k);$$

where $$0 \le t_k < t_{man.}, \quad k = 1, n_{pts.}.$$

The initial solution occurs at $t = 0$. The elements of the state, $\underline{x}$, and attitude, $\underline{\xi}$, vectors are known from their respective trim values, $\underline{x}_{e.}$ and $\underline{\xi}_{e.}$, and the first estimates of the step control inputs, $\underline{u}$, are taken as being equal to the trim controls, $\underline{u}_{e.}$. In the general case (the m^{th} estimate at the k^{th} time point) $\dot{\underline{x}}(t_k)_m$ and $\dot{\underline{\xi}}(t_k)$ can be evaluated as in equations (3.1) and (3.2) using $\underline{x}(t_k)$, $\underline{\xi}(t_k)$ and the current estimate for the controls, $\underline{u}(t_k)_m$:

$$\dot{\underline{x}}(t_k)_m = \underline{f}\left\{\underline{x}(t_k), \underline{\xi}(t_k), \underline{u}(t_k)_m\right\}, \tag{3.1}$$

$$\dot{\underline{\xi}}(t_k) = \underline{g}\left\{\underline{x}(t_k), \underline{\xi}(t_k)\right\}. \tag{3.2}$$

These in turn can be integrated, using for example the method of Runge-Kutta

(*Press et al, 1986*). A fourth order Runge-Kutta integration was chosen as it is relatively easy to implement, and to quote Press et al "succeeds virtually always" and is "adequate for most problems." The integration scheme yields estimates of $\underline{x}(t_{k+1})_m$, $\underline{\xi}(t_{k+1})_m$ and $\underline{y}(t_{k+1})_m$ at the next time point:

$$\underline{x}(t_{k+1})_m = \int_{t_k}^{t_{k+1}} \underline{\dot{x}}(t)_m dt + \underline{x}(t_k), \tag{3.3}$$

$$\underline{\xi}(t_{k+1})_m = \int_{t_k}^{t_{k+1}} \underline{\dot{\xi}}(t)_m dt + \underline{\xi}(t_k), \tag{3.4}$$

$$\underline{y}(t_{k+1})_m = \underline{h}\left\{\underline{x}(t_{k+1})_m, \underline{\xi}(t_{k+1})_m, \underline{u}(t_{k+1})_m\right\}. \tag{3.5}$$

An error function is defined as the difference between the latest estimate of the output vector, $\underline{y}(t_{k+1})_m$, and the desired value $\underline{y}_{des.}(t_{k+1})$:

$$\underline{e}(t_{k+1})_m = \underline{y}(t_{k+1})_m - \underline{y}_{des.}(t_{k+1}). \tag{3.6}$$

The error function is tested against a predefined tolerance. If less than the tolerance then the solution proceeds to the next time point $k+1$ and continues from equation (3.1). However if $\underline{e}(t_{k+1})_m$ is greater than the tolerance then, using a Newton-Raphson (*Cheney and Kincaid, 1985*) iteration, new control estimates are made. The standard form of this iteration as used by Hess et al (*1991*) is given in equation (3.7) below:

$$\underline{u}(t_k)_{m+1} = \underline{u}(t_k)_m - [J]_m^{-1} \underline{e}(t_{k+1})_m, \tag{3.7}$$

where the Jacobian, $[J]$ describes the rate of change of the output vector with respect to the control vector. The details of the Jacobian formulation are given in the next section. Genisa uses a modified form of this iteration:

$$\underline{u}(t_k)_{m+1} = \underline{u}(t_k)_m - \underline{u}_{error}(t_k)_m,$$

which in contrast to equation (3.7) does not involve inverting the Jacobian explicitly. Instead the control error vector, $\underline{u}_{error}(t_k)_m$, is evaluated by solution of the linear system in equation (3.8) using LU Factorisation (*Cheney and Kincaid, 1985*) or, in the case of

an optimal (Least Squares) solution, Singular Value Decomposition (*Press et al, 1986*):

$$[J]_m \underline{u}_{error}(t_k)_m = \underline{e}(t_{k+1})_m. \tag{3.8}$$

This method differs significantly from methods used by other investigators in that it avoids matrix inversion. Consequently it should be more accurate and stable for a wider range of Jacobians, making an important contribution to the improved performance of Genisa over other simulators.

3.1.3 Evaluation of the Jacobian

Assuming that the problem to be solved involves a vehicle with n_u controls flying a manoeuvre defined by n_u parameters (or constraints) then for the m^{th} estimate at the k^{th} time point, the Jacobian is an $n_u \times n_u$ matrix, the entries of which, $j_{ij}(t_k)_m$, are evaluated by differentiating each of the elements of the output error vector, $e_i(t_{k+1})_m$, with respect to each of the elements of the control vector, $u_j(t_k)_m$. The expression for determining a Jacobian element is thus:

$$j_{ij}(t_k)_m = \frac{\partial e_i(t_{k+1})_m}{\partial u_j(t_k)_m}.$$

Within the algorithm, however, there are no analytical expressions for the output vector, $\underline{y}$, and so the Jacobian's elements must be calculated numerically, by central differencing, the general representation of which is given below:

$$\frac{\partial e_i(t_{k+1})_m}{\partial u_j(t_k)_m} = \frac{e_i\left\{t_{k+1}, \left(u_j(t_k) + \delta u_j(t_k)\right)\right\}_m - e_i\left\{t_{k+1}, \left(u_j(t_k) - \delta u_j(t_k)\right)\right\}_m}{2\delta u_j(t_k)_m}.$$

It is clear then that all n_u output elements must be calculated at positive and negative perturbations from their current estimates and hence equations (3.1 - 3.6) must be used a further $2n_u$ times, giving a total of $2n_u+1$. The Jacobian can be written explicitly as:

$$[J]_m = \begin{bmatrix} \vdots & & \vdots \\ \dfrac{\partial e_1(t_{k+1})}{\partial u_1(t_k)} & \cdots & \dfrac{\partial e_1(t_{k+1})}{\partial u_{n_u}(t_k)} \\ \vdots & \ddots & \vdots \\ \dfrac{\partial e_{n_u}(t_{k+1})}{\partial u_1(t_k)} & \cdots & \dfrac{\partial e_{n_u}(t_{k+1})}{\partial u_{n_u}(t_k)} \end{bmatrix}_m .$$

This algorithm has been implemented on a DEC Alpha 3000 workstation in FORTRAN 77, and the verification process is documented in the following section.

3.2 Verification of the Genisa Algorithm

3.2.1 Concept of Verification

The verification process is important for any simulation as without confirmation of the algorithm's correct implementation it is impossible to present results with any degree of confidence. Verification can be said to be in three stages:

i) whether or not the results make qualitative sense;
ii) if the results are reversible;
and iii) how the results compare with established simulation(s).

Having obtained control time histories by inverse simulation, the first stage is to justify the trends in the plots by consideration of how the aircraft should respond to each control input. Obviously this requires appreciation of the physics of the modelled vehicle. The second stage (if the results are reversible) involves using the control time histories as inputs for a time response or conventional simulation of the same mathematical model used in the inverse solution. If the inverse simulation has been implemented correctly then the outputs should match the constraints imposed by the original manoeuvre definition. For the third stage it was decided to make use of the existing inverse simulation, Helinv, and its inherent mathematical model HGS. One can assume that if both Helinv and Genisa share the same mathematical model, HGS, then the control time histories produced by the two algorithm should be the same. If each of these three tests are satisfied then the results can be confidently presented as inverse simulations of the vehicle mathematical model. Section 3.2.3 is concerned with the first two stages of verification, section 3.2.4 with the third. Firstly, however, the vectors and matrices from

the above state space description will be expanded, showing how Genisa applies them to the HGS model.

3.2.2 Genisa Algorithm Applied to HGS Model

As the system in question is the HGS representation of a conventional single main and tail rotor helicopter, then the state vector, $\underline{x}$, is expressed as:

$$\underline{x}(t_k) = \left\{U(t_k) \quad V(t_k) \quad W(t_k) \quad P(t_k) \quad Q(t_k) \quad R(t_k)\right\}^{\mathrm{T}};$$

the attitude vector, $\underline{\xi}$ as:

$$\underline{\xi}(t_k) = \left\{\phi(t_k) \quad \theta(t_k) \quad \psi(t_k)\right\}^{\mathrm{T}};$$

the control vector, $\underline{u}$ as:

$$\underline{u}(t_k) = \left\{\theta_0(t_k) \quad \theta_{1s}(t_k) \quad \theta_{1c}(t_k) \quad \theta_{0t.r.}(t_k)\right\}^{\mathrm{T}};$$

and the output vector, $\underline{y}$ as:

$$\underline{y}(t_k) = \left\{x_{e.}(t_k) \quad y_{e.}(t_k) \quad z_{e.}(t_k) \quad \psi(t_k)\right\}^{\mathrm{T}}.$$

The specific representation of a 4 x 4 Jacobian matrix can be made in terms of the actual output and control elements used within Genisa as applied to the HGS model. If the desired output is defined in terms of earth fixed displacements and heading angle then the Jacobian is:

$$[J] = \begin{bmatrix} \dfrac{\partial(x_{e.} - x_{e.des.})}{\partial\theta_0} & \dfrac{\partial(x_{e.} - x_{e.des.})}{\partial\theta_{1s}} & \dfrac{\partial(x_{e.} - x_{e.des.})}{\partial\theta_{1c}} & \dfrac{\partial(x_{e.} - x_{e.des.})}{\partial\theta_{0t.r.}} \\ \dfrac{\partial(y_{e.} - y_{e.des.})}{\partial\theta_0} & \dfrac{\partial(y_{e.} - y_{e.des.})}{\partial\theta_{1s}} & \dfrac{\partial(y_{e.} - y_{e.des.})}{\partial\theta_{1c}} & \dfrac{\partial(y_{e.} - y_{e.des.})}{\partial\theta_{0t.r.}} \\ \dfrac{\partial(z_{e.} - z_{e.des.})}{\partial\theta_0} & \dfrac{\partial(z_{e.} - z_{e.des.})}{\partial\theta_{1s}} & \dfrac{\partial(z_{e.} - z_{e.des.})}{\partial\theta_{1c}} & \dfrac{\partial(z_{e.} - z_{e.des.})}{\partial\theta_{0t.r.}} \\ \dfrac{\partial(\psi - \psi_{des.})}{\partial\theta_0} & \dfrac{\partial(\psi - \psi_{des.})}{\partial\theta_{1s}} & \dfrac{\partial(\psi - \psi_{des.})}{\partial\theta_{1c}} & \dfrac{\partial(\psi - \psi_{des.})}{\partial\theta_{0t.r.}} \end{bmatrix}.$$

where the variables are as defined earlier i.e. the numerators are the three earth axis positions, and heading angle; and the denominators are the four controls for a conventional single main and tail rotor helicopter. It is worthwhile noting that Genisa's flexibility allows the output vector to be composed of any 4 states, attitudes and even constrained controls. As the results are to be used for comparison with Helinv, however, it is logical that the same constraints of flight path displacements and heading be applied.

3.2.3 Inverse Simulation of a Hurdlehop Manoeuvre

A range of manoeuvres and flight states have been used to verify the Genisa algorithm. Representative sample results from a hurdlehop manoeuvre simulation are presented here.

To define the hurdlehop, Figure 3.2, it is assumed that the pilot's task is to clear an obstacle, height h, and then return to the original altitude over some distance, s. The obstacle is assumed to be located at the mid point of the manoeuvre i.e. $x_{e_0} = s/2$. In order to ensure continuity, initial and final accelerations are assumed equal to zero. Thus applying the following boundary conditions at the entry, exit and mid point of the manoeuvre:

$$\begin{aligned}
&\text{i) } t = 0, && z_{e_0} = 0, && \dot{z}_{e_0} = 0, && \ddot{z}_{e_0} = 0 \\
&\text{ii) } t = \frac{t_{man.}}{2}, && z_{e_0} = -h \\
&\text{iii) } t = t_{man.}, && z_{e_0} = 0, && \dot{z}_{e_0} = 0, && \ddot{z}_{e_0} = 0
\end{aligned}$$

allows the altitude to be represented by a simple polynomial. As there are seven boundary conditions, a 6th order altitude profile given by:

$$z_{e_0}(t) = 64h\left[\left(\frac{t}{t_{man.}}\right)^3 - 3\left(\frac{t}{t_{man.}}\right)^2 + 3\left(\frac{t}{t_{man.}}\right) - 1\right]\left(\frac{t}{t_{man.}}\right)^3, \qquad (3.9)$$

where $t_{man.}$ is the time taken to complete the manoeuvre, has been found to be suitable. To complete the description we assume that the hurdlehop is performed at constant heading (i.e. $\psi = 0$) and velocity, V_{f_0}, and that there are no lateral excursions (i.e. the manoeuvre is longitudinal and performed in the $x_{e_0} - z_{e_0}$ plane, giving $y_{e_0} = 0$). The longitudinal displacement, $x_{e_0}(t)$, can be evaluated numerically from:

$$\dot{x}_{e.}(t) = \sqrt{V_{f.}^2 - \dot{z}_{e.}(t)^2},$$

whilst the manoeuvre time, $t_{man.}$, can be calculated by specifying the total track distance s, then noting that:

$$s = \int_0^{t_{man.}} \dot{x}_{e.}(t)dt.$$

In essence the complete manoeuvre may be defined by specifying values for the parameters s, h and $V_{f.}$. Thus the required input to the inverse simulation of a time history of the desired output vector, $\underline{y}_{des.}(t)$ can be easily constructed using three earth fixed displacements and heading, i.e. $\underline{y}_{des.}(t) = \{x_{e.}(t) \quad y_{e.}(t) \quad z_{e.}(t) \quad \psi(t)\}^{\mathrm{T}}$. This approach may seem simplistic but past experience (*Thomson and Bradley, 1990b*) has shown that profiles such as that given in equation (3.9) provide realistic trajectories.

Inverse simulation results were generated using the manoeuvre input values:

$$h = 30\text{m}, \; s = 500\text{m}, \; V_{f.} = 80\text{kts};$$

the quasi-steady blade flapping version of the HGS model; and configurational data representing a Westland Lynx helicopter. The control time histories shown in Figure 3.3 were generated using Genisa. With reference to the hurdlehop diagram (Figure 3.2), a positive application of collective, θ_0 (which predominantly controls vertical acceleration), is required in the climbing phase. This becomes negative (with respect to trim) just before the manoeuvre half way point in order to attain zero vertical velocity at the peak of the hurdlehop profile. Collective is then negative throughout the descent until the helicopter approaches the manoeuvre exit, when a positive input is applied to level off with zero vertical velocity. Considering the first period corresponding to positive collective the other three results can be explained as follows. The increase in tail rotor collective, $\theta_{0t.r.}$, is used to balance the increased torque from the main rotor due to the collective pitch, and hence greater drag on each blade. Lateral cyclic is used to balance the right sideforce caused by the tail rotor; a positive input being consistent with left stick tilting the thrust vector to the left. Hence θ_0, θ_{1c} and $\theta_{0t.r.}$ have broadly similar shapes. A negative application of longitudinal cyclic, θ_{1s}, is consistent with forward stick and is

used to maintain forward velocity as the helicopter climbs. The relatively low pitch attitude excursions also show that the manoeuvre is principally a translatory motion up and over the hurdle (i.e. a 'hop') as opposed to the nose following the flight path as in a pitch rate dominated manoeuvre. A preliminary conclusion is that the results appear to make sense, certainly in their trends, and hence pass the first stage of verification.

It is also possible to use the control time histories generated by Genisa to 'drive' the mathematical model (HGS) in a time response (conventional simulation) calculation. The outcome of this is that the flight trajectory flown as a result of applying the calculated controls can be established. This of course provides a useful verification of the inverse algorithm as the calculated flight path should match closely the initially defined (polynomial) flight path. This is shown to be the case in Figure 3.4 where the altitude profile of the flight path has been captured to near precision whilst a small error of less than 2.5cm lateral displacement and 0.004° heading have been accumulated over the 500m track. In addition a constant flight velocity has been maintained to an accuracy of ± 0.04%. Thus having passed the second stage of verification, further weight is added to the conclusion that the algorithm is functioning as required. The third and final stage of the verification is by comparison with results produced by the established inverse simulation algorithm, Helinv.

3.2.4 Comparison Between Genisa and Helinv

Results produced using both the Genisa and Helinv inverse simulation algorithms are plotted in Figure 3.5, and as the broken line (Helinv) is almost completely obscured, it is evident that the different methods produce identical results. The question of the validity of the results has been addressed elsewhere, and it is sufficient to say that HGS has been validated over a range of representative manoeuvres and gives good results (*Thomson and Bradley, 1990a*). The one significant difference between the solutions is the time taken to produce such results: Genisa is typically much slower then Helinv, mainly due to the large number of numerical integrations which have to be performed. For example the results presented in Figure 3.5 were solved for the same tolerance and solution interval, requiring approximately 21 and 7 seconds on the DEC Alpha 3000 for Genisa and Helinv respectively. On this basis Helinv, which can provide real time solutions when implemented on a moderately powerful workstation, would appear to be the preferred method. As has already been discussed, however, algorithms based upon numerical differentiation are limited in that they must be model specific. In addition they

suffer from certain numerical instabilities which, as discussed earlier, restrict the complexity of mathematical model to which they can be applied. For these reasons the integration based algorithm is chosen. Integration based algorithms such as Genisa, however, also suffer from the numerical instabilities mentioned in Chapter 2, Section 2.4.2 and these are now presented.

3.3 Examples of Numerical Instability

As discussed in Chapter 2, the calculation time step Δt strongly influences both the accuracy and stability of the solution. This can be demonstrated by considering the results from simulations using the full blade flapping equations in HGS (the previous results used the simplified quasi-steady representation) which need a much smaller time step if the flapping dynamics are to be captured. Whereas a time step of say 0.1 seconds will yield good results when the quasi-steady flapping model is employed, it is found to be impossible to obtain a solution using full blade flapping dynamics if Δt is greater than 0.05 seconds. Figure 3.6 shows controls evaluated by Genisa using a discretisation interval of 0.04 seconds. The plots demonstrate oscillations at the flap frequency which appear to be unstable and consistent with the 'multiple solutions' observed by Gao and Hess (*1993*).

It was suggested in Chapter 2, Section 2.4.2, that these oscillations may be a result of 'skipping' certain dynamic features, and so it would be reasonable to expect the amplitude to reduce with the time step, Δt. This does indeed transpire to be the case, but as the time step is reduced the results start to suffer from other instabilities. Figure 3.7 for example was produced by Genisa using a time step of 0.01 seconds. Although the amplitude of the oscillations at the flapping frequency has been reduced greatly, the small discretisation interval has introduced other unstable oscillations whose period matches the size of Δt. This feature, being due to a small time step, is probably that identified by Lin et al (*1993*) where "if there is any *uncontrolled* state variable in the problem, the integration inverse method may have problems for small time step". The assertion is reinforced by considering the number of uncontrolled states - a single main and tail rotor helicopter has only four controls whilst HGS with multiblade flapping has nine degrees of freedom.

The two features described above are typical of those observed in other inverse

simulations of this type and are without doubt serious drawbacks to the use of such techniques. In the case of systems which have a wide range of characteristic frequencies, such as the helicopter, these problems can be restrictive as small discretisation intervals are unavoidable. Indeed if more sophisticated individual blade, helicopter models are to be utilised for inverse simulation, then a solution to the problem of numerical stability with small time steps is essential. A method for stabilising the Genisa algorithm is described in Chapter 4.

3.4 Chapter Summary

This chapter has detailed a flexible, integration based, inverse simulation algorithm which is independent of the vehicle mathematical model used or the constraints imposed on the vehicle's motion. The robustness of the algorithm has been increased by avoiding inversion of the Jacobian matrix used in the iterative solution scheme. Resultant control time histories produced using the helicopter model HGS have been verified by comparison with the existing differentiation based algorithm, Helinv which has been verified and validated extensively.

Numerical instabilities associated with the integration method have been identified previously in the literature and reproduced here using Genisa. The nature of the instabilities are such that they would compromise the accuracy of results produced with higher frequency dynamic systems. A solution to the problem is therefore essential. Chapter 4 identifies a means of eliminating these instabilities thus greatly increasing the range of models to which Genisa can be applied. This represents a notable advance in the study and use of inverse simulation.

Chapter 4 An Investigation of the Stability, Flexibility and Robustness of the Genisa Algorithm

The numerical instabilities associated with integration based inverse simulation algorithms, such as Genisa, were illustrated in the previous chapter. It was shown that if the model being simulated has sufficiently high characteristic frequencies then the accuracy of results is compromised, irrespective of the solution time step used. This chapter presents a simple way of stabilising solutions which does not require any changes to the structure of the algorithm. An explanation is then offered for the success of this simple method. Results are also presented for a lateral manoeuvre, the slalom, demonstrating that Genisa works well (within the limitations of the vehicle model) for different flight states. Finally the effect of changing algorithm parameters - such as the solution and integration interval size - is investigated.

4.1 Stability of Genisa

As discussed in Chapter 3 (equation 3.6) the iterative solution most often used in integration inverse algorithms is based upon minimising the difference between the actual and desired vehicle position:

$$\underline{y} - \underline{y}_{des.} = \underline{0}, \tag{4.1}$$

where, for the HGS helicopter model, the output vector $\underline{y}$ contains the elements $x_{e.}$, $y_{e.}$, $z_{e.}$ and ψ. The rationale behind making this choice is that it is most convenient and natural to describe a manoeuvre in terms of these parameters. A simple alternative to this is that the error to be minimised should be defined in terms of the aircraft's acceleration i.e. the output vector $\underline{y}$ is composed of the elements $\ddot{x}_{e.}$, $\ddot{y}_{e.}$, $\ddot{z}_{e.}$ and $\ddot{\psi}$. In the manoeuvre definition used to initiate the simulation the desired accelerations are evaluated simply by differentiating the representative polynomials (equation (3.9) describing a hurdlehop for example is readily differentiated to give $\ddot{z}_{e.}$) and thus $\underline{y}_{des.}$ can be established. The body referenced accelerations ($\dot{U}$, $\dot{V}$, $\dot{W}$ and $\dot{R}$) are also easily obtained and are subsequently transformed through the Euler angles (equation A1.3, using current estimates of ϕ, θ, ψ) to give earth axis values, hence establishing the vector, $\underline{y}$. The algorithm as described in Chapter 3 is unchanged; that is, estimates of

control displacements are made and the equations of motion are integrated between time points until equation (4.1) is satisfied.

This simple modification has the effect of eliminating the instabilities observed previously. Figure 4.1 shows controls calculated for the sample hurdlehop described in Chapter 3, Section 3.2.3, again using a time step of 0.01 seconds. Direct comparison can then be made between Figures 3.7 and 4.1 and it is evident that the instabilities associated with a small time increment have been eliminated leaving only low amplitude oscillations consistent with blade flapping. The results can also be verified by performing a time response with the control time histories in Figure 4.1 as inputs, and it has been found that this produces a flight path which is as accurate as that of the quasi-steady model presented in Figure 3.4. A larger time increment, consistent with the unstable control time histories observed in Figure 3.6, yields equally good solutions. It is apparent then that a simple modification has produced a significant improvement in the quality of the results and some explanation of this dramatic improvement is clearly required.

Again it is convenient to describe the inverse simulation in state space form. Hence solution of the vehicle equations of motion (equation A1.1) can be obtained by considering them expressed as the initial value problem:

$$\dot{\underline{x}} = \underline{f}(\underline{x}, \underline{\xi}, \underline{u}); \quad \underline{x}(0) = \underline{x}_{e_0} \tag{4.2}$$

$$\dot{\underline{\xi}} = \underline{g}(\underline{x}, \underline{\xi}); \quad \underline{\xi}(0) = \underline{\xi}_{e_0}$$

and

$$\underline{y} = \underline{h}(\underline{x}, \underline{\xi}), \tag{4.3}$$

where $\underline{x}$ and $\underline{\xi}$ are the system state and attitude vectors respectively, the external forces and moments are functions of the control vector $\underline{u}$, and $\underline{y}$ is the output vector. Differentiating equation (4.3) with respect to time then yields:

$$\begin{aligned} \dot{\underline{y}} &= \frac{d\underline{h}(\underline{x}, \underline{\xi})}{d\underline{x}} \dot{\underline{x}} + \frac{d\underline{h}(\underline{x}, \underline{\xi})}{d\underline{\xi}} \dot{\underline{\xi}} \\ &= \frac{d\underline{h}(\underline{x}, \underline{\xi})}{d\underline{x}} \underline{f}(\underline{x}, \underline{\xi}, \underline{u}) + \frac{d\underline{h}(\underline{x}, \underline{\xi})}{d\underline{\xi}} \underline{g}(\underline{x}, \underline{\xi}), \end{aligned} \tag{4.4}$$

and if equation (4.4) is invertible with respect to $\underline{u}$ it can be rewritten as:

$$\underline{u} = \underline{H}\left(\underline{x}, \underline{\xi}, \underline{\dot{y}}\right). \tag{4.5}$$

Substitution of equation (4.5) into equation (4.2) produces a general expression for the equations of motion, $\underline{\dot{x}}$ as a function of the state vector, $\underline{x}$, attitude vector, $\underline{\xi}$, and rate of change of output vector, $\underline{\dot{y}}$:

$$\begin{aligned} \underline{\dot{x}} &= \underline{f}\left\{\underline{x}, \underline{\xi}, \underline{H}\left(\underline{x}, \underline{\xi}, \underline{\dot{y}}\right)\right\} \\ &= \underline{F}\left(\underline{x}, \underline{\xi}, \underline{\dot{y}}\right). \end{aligned} \tag{4.6}$$

If, as is the case with the HGS model, the function $\underline{h}$ in equation (4.3) is the Euler transformation from body velocities (U, V, W) to inertial velocities then the output vector $\underline{y}$ must contain the elements $\dot{x}_{e_i}$, $\dot{y}_{e_i}$ and $\dot{z}_{e_i}$. Thus given that the vector $\underline{\dot{y}}$ in equation (4.6) contains the elements $\ddot{x}_{e_i}$, $\ddot{y}_{e_i}$ and $\ddot{z}_{e_i}$ it has been shown that the system is forced by the inertial accelerations rather than velocities or displacements. This demonstration was first made by Bradley (*1995*).

Further evidence is given by considering that, for HGS, perturbations in the control, or blade pitch, angles have an instantaneous effect on the blade aerodynamic forces and hence rotor thrust. Thus there is a direct link between the applied pitch displacements and the vehicle's accelerations. By contrast, the resultant changes in velocities and displacements will occur only after a finite period of time. Consequently an error function associated with accelerations will have greater sensitivity to control displacements than will one associated with positional displacements. This has implications when using numerical differentiation to calculate the Jacobian. As explained in Chapter 3, Section 3.1.3, the Jacobian is evaluated by calculating values of the error functions at small positive and negative perturbations from the current estimates of the controls, central differencing being used to obtain the derivatives. When using a very short time interval the positional displacements due to small perturbations in controls may be similar, hence leading to rounding errors in the differencing process. This will not be the case using the more sensitive acceleration error function where even small positive and negative control displacements should produce distinct and differentiable function values. In addition, though any inaccuracies in the integration scheme will inevitably affect all outputs, defining the constraints in terms of accelerations reduces the influence of errors on the actual Genisa solution procedure. By contrast, solving for displacements

places considerable emphasis on an accurate numerical integration process.

4.2 A Demonstration of the Flexibility of Genisa

In Chapter 3, all inverse simulation results were produced using the hurdlehop. Patently the robustness and fidelity of the algorithm cannot be assumed on the basis of this one longitudinal manoeuvre and further evidence is required. During the development of Genisa successful inverse simulations were in fact achieved using many different manoeuvres. Presented here, for example, are results for a lateral manoeuvre: the Rapid Slalom.

The Rapid Slalom is an example of an Aggressive Mission Task Element (MTE) as defined by the U.S. Military Rotorcraft Handling Qualities Requirements (*Anon., 1994*) where the manoeuvre is to be initiated in level flight at a constant speed of 60 knots or above. The aircraft is to be displaced laterally to a distance of 15.2m (50ft) from a centreline marked on the ground, then rolled in the opposite direction to the same distance on the opposite side of the centreline. The manoeuvre is completed by returning to the centreline. It is also stipulated that the maximum bank angle, ϕ should be greater than 50 degrees, and the altitude should be maintained below 15.2m. Before a mathematical description of the manoeuvre can be found it is necessary to determine the shape of the flight path. In this case, as it will be assumed that the altitude is kept constant, the manoeuvre is simply a track in the earth $x_e - y_e$ plane. A likely possible shape is shown in Figure 4.2, where it is assumed that the manoeuvre is symmetrical about the x_e axis. Noting that the flight velocity, V_f, throughout the manoeuvre is constant, the lateral displacement, y_e, can be expressed as a function of time by considering the following boundary conditions:

$$
\begin{aligned}
&\text{i) } t = 0, && y_e = 0, && \dot{y}_e = 0, && \ddot{y}_e = 0 \\
&\text{ii) } t = t_1, && y_e = -h, && \dot{y}_e = 0 \\
&\text{iii) } t = 2t_1, && y_e = h, && \dot{y}_e = 0 \\
&\text{iv) } t = 3t_1, && y_e = 0, && \dot{y}_e = 0, && \ddot{y}_e = 0
\end{aligned}
$$

where h is the lateral displacement of 15.2m. The simplest mathematical function fulfilling these conditions is a 9th order polynomial (the ten coefficients being selected to satisfy the ten boundary conditions). The polynomial is found to be:

$$y_{e_r}(t) = \frac{h}{16}\left[-2\left(\frac{t}{t_1}\right)^9 + 27\left(\frac{t}{t_1}\right)^8 - 144\left(\frac{t}{t_1}\right)^7 + 378\left(\frac{t}{t_1}\right)^6 - 486\left(\frac{t}{t_1}\right)^5 + 243\left(\frac{t}{t_1}\right)^4\right]. \quad (4.7)$$

This expression can be differentiated to give the velocity and acceleration in the y_{e_r} axis direction, and, as altitude is to be kept constant (i.e. $z_{e_r}(t) = const.$):

$$\dot{z}_{e_r}(t) = 0;$$

thus, the velocity in the x_{e_r} axis direction is given by:

$$\dot{x}_{e_r}(t) = \sqrt{V_{f_r}^2 - \dot{y}_{e_r}^2}. \quad (4.8)$$

The position and acceleration of the aircraft along the x_{e_r} axis can be found by integration and differentiation respectively of equation (4.8). To complete the definition of the manoeuvre it is assumed that the helicopter is flown without side slip so that:

$$\beta(t) = 0;$$

where $$\beta(t) = \sin^{-1}\left\{\frac{V}{V_{f_r}}\right\}.$$

At this stage it is worth noting Genisa's flexibility. As already mentioned Helinv, and other differentiation methods, are model and solution specific. This means that when constraining side slip, $\beta(t)$, the associated heading angle, $\psi(t)$, must be calculated before the inverse simulation can commence. Given $V(t) = 0$ this calculation involves a non-trivial solution of the Euler transformation equations; Appendix 3, Section 3.2.2.2. Obviously different constraints would require further augmentations or changes to the solution procedure. By contrast Genisa simply requires that the heading error function in the hurdlehop is replaced by a value of side slip angle; readily available from the vehicle model. Alternative constraints are equally simple to apply. Justification for this choice of definition for the Rapid Slalom is made by Padfield et al (*1994*).

Instabilities associated with constrained displacements were demonstrated in Chapter 3. While these instabilities were only evident for the hurdlehop when the multiblade flapping dynamics were included, the slalom manoeuvre actually posed

problems for both the dynamic and quasi-steady models. It in fact proved impossible to attain stable, displacement or velocity based results using either blade flapping representation. The use of constrained accelerations, however, again eliminated all instabilities yielding successful results for both models. Figure 4.3 shows slalom control time histories produced by both Genisa and Helinv using the quasi-steady HGS model. Again, as with the hurdlehop, the results are almost identical. Considering the extensive testing of Helinv this is further proof that the Genisa algorithm successfully incorporates the HGS model in inverse simulation. Additional verification is given by the time response (conventional) simulation control time histories in Figure 4.4. where the groundtrack shape is closely captured, less than 30cm altitude is gained over the manoeuvre's 300m track and the desired 60kts flight speed is maintained to within 0.1%. Also evident is that the bank angle time history, $\phi(t)$, produced by conventional simulation does exceed the 50° stipulated in the manoeuvre definition, and is identical to that given by the inverse solution.

A point worthwhile noting is that the lateral cyclic control limit, $\theta_{1c_{max.}}$, is exceeded. This is no reflection on either the Helinv or Genisa algorithms as they have simply solved the demanded numerical problem. Rather it is a limitation of the HGS model as the linear aerodynamics are unable to model blade stall and thus cannot predict that the helicopter (in its given configuration) is performing outwith the boundaries of its flight envelope.

As further successful results are presented in later chapters for a different model, and the aim here is not to justify the validity of the HGS model, it is reasoned that these two manoeuvres (one longitudinal, one lateral) are sufficient evidence that the algorithm performs well.

4.3 Alternative Manoeuvre Constraints

Consider that the hurdlehop and slalom inverse simulations are, principally, driven by the z_e and y_e axis translations respectively. Assuming for the moment that the helicopter's responses can be decoupled then the associated controls would be collective, θ_0 and lateral cyclic, θ_{1c}. Whereas there is a relatively direct relationship between applying collective pitch and the resultant vertical acceleration, the influence of lateral cyclic on the lateral translational motion is only secondary; the primary effect being to roll the aircraft. Consequently if perturbations in collective pitch can yield poor predictions of

$\dot{z}_{e_0}$ in the hurdlehop, then any numerical problems will be exacerbated by the less direct relationship between lateral cyclic and $\dot{y}_{e_0}$ in the slalom. Further credence is given to this assertion by using the bank angle time history in Figure 4.4, $\phi(t)$, to drive another inverse simulation where $\underline{y} = \{\dot{x}_{e_0} \quad \phi \quad \dot{z}_{e_0} \quad \beta\}^T$. By the Euler transformation equations (A1-3) constraining attitudes requires precisely the same solution as constraining the earth fixed velocities. As constraining bank attitude is successful, however, and solving for the velocities ($\underline{y} = \{\dot{x}_{e_0} \quad \dot{y}_{e_0} \quad \dot{z}_{e_0} \quad \beta\}^T$) leads to algorithm failure it is clear that the more direct relationship between lateral cyclic and bank attitude angle reduces numerical errors in the central differencing process, thus enabling a more accurate prediction of the Jacobian to be made and a successful inverse simulation. Again this demonstrates the flexibility of an integration based inverse simulation algorithm as a differentiation algorithm would have required substantial restructuring. As defining the manoeuvres in terms of attitudes requires knowledge of the vehicle dynamics, however, this makes the manoeuvre and vehicle to be simulated interdependent. Consequently constraining earth fixed accelerations is, in general, preferable.

4.4 Changing Algorithm Parameters

The influence of certain algorithm parameters was investigated, both to test the robustness of the algorithm and the effect of these changes on the solution accuracy. The change in respective run times was also recorded. To test the algorithm, Genisa was applied to the quasi-steady HGS model flying the hurdlehop from Chapter 3. The default algorithm is as described in Chapter 3, Section 3.1 where the error functions are defined in terms of accelerations and solved to a tolerance of nine decimal places. Thus the main parameters and defaults are as follows:

	solution time step, Δt	0.01sec;
	no. intermediate integrations, $n_{int.}$	0;
	solution tolerance, *tol.*	1×10^{-9};
	control perturbation size, δu	$1\times10^{-7}\times control$;
with	DEC Alpha 3000 cpu time	21.6sec.

A time step of $\Delta t = 0.01$sec was chosen. For consistency, a solution tolerance, *tol.* of 1×10^{-9} was decided upon as Press et al (1986) indicate that the highest accuracy

achievable using a Runge-Kutta fourth order scheme is $O(\Delta t^5)$ i.e. 1×10^{-10}.

i) Solution Time Step, Δt

Firstly the effect of varying the solution time step, Δt, or number of solution points, $n_{pts.}$, was investigated. Below 0.03sec the most significant result of changing Δt is the cpu time required to complete the inverse simulation. Time intervals have little apparent influence on the number of iterations per solution point and so the cpu time is less for larger Δt due to the fewer numerical integrations, e.g. for $\Delta t = 0.02$sec the run time is reduced to 12.1sec. When the resultant control time histories are used to drive time responses (conventional simulations) outputs are very similar in all cases. Above approximately 0.03sec intermediate integration points are required to obtain solutions, taking longer to run due to the number of integrations e.g. 0.2sec needs $n_{int.} = 10$ and takes 17.5sec. As Δt increases in this range the lower resolution results produce decreasingly good flight path correlation.

ii) Intermediate Integrations Per Interval, $n_{ints.}$

Though not required for smaller Δt the effect of intermediate integrations was investigated nonetheless. It was found that as $n_{int.}$ increased there was a run time penalty as a consequence of the increased number of integrations, but no significant improvement in the results. If the above default is used but with $n_{int.} = 10$ the cpu time increases from 21.6sec to 3min, a factor of 9.

iii) Convergence Tolerance, tol.

As would reasonably be expected, decreasing the value of the demanded tolerance, *tol.* increases the number of iterations per solution point and consequently the cpu time required to perform a given inverse simulation. For example using the above default but increasing the tolerance to $tol. = 1\times10^{-3}$, the quality of the results is not greatly compromised but the simulation only takes 11.3sec. By contrast $tol. = 1\times10^{-13}$ takes 32.8sec with no significant improvement in the results, perhaps as the integration accuracy may, at best, be no better than 1×10^{-10}.

iv) Perturbation Size, δu

Next the perturbation size, δu was varied. Genisa was found to be very resistant to changes in δu, no difference being made to solution accuracy or cpu time unless δu was nearly as large as the current value of the control itself. This resulted in algorithm failure. One point noted is that Genisa has difficulty converging to a small tolerance, *tol.* if δu is too large, e.g. solving to $tol. = 1 \times 10^{-13}$ for $\delta u = 0.1 \times control$ proves to be slow. In contrast if solving for displacements or velocities δu must be of sufficient magnitude to ensure differentiable function values. Otherwise δu has little effect on the algorithm robustness, run time, or solution accuracy.

v) The Use of Ramps

Genisa, when solving for controls, assumes step inputs over the solution interval. The alternative of solving for ramp inputs was found to have no influence on the results.

vi) Calculation of Jacobian Elements

Calculation of the Jacobian elements requires central differencing; that is positive and negative perturbations of the controls. It is of course also possible to use forward (only positive perturbations) or backward differencing (only negative perturbations), the obvious advantage being fewer numerical integrations per iteration and quicker run time. In practice the run time is not necessarily quicker, however, as more iterations are generally required. The algorithm also has a tendency to fail more readily as, for example, only positive perturbations may not yield the correct information if a negative displacement is required. Consequently central differencing is maintained as the longer cpu time is justified in maintaining Genisa's robustness.

It would seem then that the governing factor in cpu time is the numerical integration routine; the amount of time required to complete an inverse simulation being roughly proportional to the number of integrations, whether this be due to solution interval, intermediate integrations or the number of iterations per solution point. Though a small solution interval, Δt, large number of intermediate integrations, $n_{int.}$, and small demanded tolerance, *tol.*, do all lead to marginally more accurate results, the overriding effect is to increase the run time. Thus it appears that the solution accuracy is closely governed by the accuracy of the numerical integration routine itself. Certainly Press et al

(*1986*) suggest doubling and redoubling the number of solution points and comparing results, and there is no apparent gain for Δt less than about $0.02\,\text{sec}$ and *tol.* of less than 1×10^{-5}. Investigating other potentially, more accurate integration techniques was discarded as they are more problematic to implement and the results produced by Runge-Kutta fourth order are easily good enough for the purposes of this research.

4.5 Chapter Summary

If manoeuvre constraints are described in terms of displacements or velocities then the resultant integration based, inverse simulation results may be unstable for a high frequency system. In this chapter it has been demonstrated that the inverse simulation is in fact driven directly by the accelerations. Consequently solving for accelerations yields a quicker, more accurate prediction of the system response and the results are stabilised. This widens the spectrum of mathematical models to which Genisa can be applied, and represents an important advance in the theory of inverse simulation, and indeed inverse problems in general.

It has been shown through the Rapid Slalom manoeuvre that inverse simulation of a helicopter model is more readily driven by attitude angles than inertial displacements or velocities. To describe a manoeuvre in terms of vehicle attitudes, however, requires foreknowledge of the vehicle dynamics. As such interdependence may not always be desirable, inertial accelerations are preferred. Using accelerations, successful inverse simulation of the Rapid Slalom demonstrates that Genisa works well for a variety of manoeuvres.

A number of algorithm parameters have been varied, and Genisa has been proven to be robust. The principle factor in inverse simulation run time and accuracy is the numerical integration routine. This is easily the process which consumes the most computing power.

The Rapid Slalom manoeuvre used in this chapter represents one typical of ADS-33 MTE's. As one of the uses of helicopter inverse simulation is the study of workload and handling qualities (*Thomson and Bradley, 1994*), there is clearly a need to be able to simulate vehicle flight close to its limits. In the Rapid Slalom results, the control limits were exceeded thus demonstrating a weakness in the HGS model. This problem is

addressed in Chapter 5 which describes the development of a more sophisticated individual blade rotor model, Hibrom.

Chapter 5 Development of a Helicopter Individual Blade Rotor Model: Hibrom

It was demonstrated in Chapter 4 (Figure 4.3) that a helicopter model incorporating a disc representation of the main rotor has limitations when simulating manoeuvres at the edge of the vehicle's flight envelope. As a major motivation for this research is to study advanced rotorcraft configurations, the edge of the flight envelope and the rotor's aerodynamic limits will be encountered frequently. Thus it was deemed necessary to overcome this inadequacy; the most appropriate action being to replace the disc representation of the rotor with an individual blade model. This has the advantage of being able to model the blade dynamics separately, and to include empirically derived blade aerodynamic data. The latter is particularly useful in high speed flight as compressibility effects can be considered and the angle of attack range can capture features such as blade stall and reversed flow. In addition an individual blade rotor model has never previously been implemented in inverse simulation, indicating once more the novelty of this research and the advance in inverse simulation which it represents.

5.1 Introduction: Disc Model vs. Individual Blade Model

To successfully simulate the dynamics of a given vehicle requires calculation of the forces and moments generated by each of its components. The familiar Euler rigid body equations (Appendix 1) form the basis of simulating the motion of the vehicle's centre of gravity. They are expressed in terms of the body velocities and accelerations (U, V, W, P, Q, R and their derivatives) and the total external forces and moments (X, Y, Z, L, M, N). Typically a helicopter model consists of a main rotor (subscript *rot.*), tail rotor ($t.r.$), fuselage (*fus.*), tail plane ($t.p.$) and fin (*fin*). Therefore the total forces and moments are composed as follows:

$$X = X_{rot.} + X_{t.r.} + X_{fus.} + X_{t.p.} + X_{fin};$$

$$Y = Y_{rot.} + Y_{t.r.} + Y_{fus.} + Y_{t.p.} + Y_{fin};$$

$$Z = Z_{rot.} + Z_{t.r.} + Z_{fus.} + Z_{t.p.} + Z_{fin};$$

$$L = L_{rot.} + L_{t.r.} + L_{fus.} + L_{t.p.} + L_{fin};$$

$$M = M_{rot.} + M_{t.r.} + M_{fus.} + M_{t.p.} + M_{fin};$$

and $$N = N_{rot.} + N_{t.r} + N_{fus.} + N_{t.p.} + N_{fin}.$$

Modelling the main rotor occupies the majority of effort as it is the most complex component and produces both the force to lift the aircraft and to propel it in the commanded direction. In the context of helicopter simulation there are two commonly adopted approaches: the *disc* model and the *individual blade* model.

Traditionally, both model types have used a common starting point to evaluate the forces and moments acting instantaneously on a blade. As both the velocity and acceleration of the airflow vary with radial position, the aerodynamic and inertial forces are determined by integrating the load on a incremental element along the blade span. This approach is known as Blade Element Theory. It is of course additionally the case, however, that the blade velocities and accelerations vary cyclically with time as the blade rotates, and the loads on each element will be a function not only of radial location but also of azimuthal position. Blade forces and moments are hence periodic in nature, but this feature is not always modelled. The disc model utilised in HGS (*Thomson, 1992*) assumes a multiblade representation for the calculation of rotor forces and moments. In this technique the incremental inertial and aerodynamic forces acting on a blade element are integrated, analytically, along the blade span. HGS and other disc models assume that only the steady components of the periodic forces and moments generated by the rotor influence the vehicle dynamics. Although this ignores the rotor periodicity, by using simple blade geometric and aerodynamic representations it does allow the elemental forces and moments to be integrated over the plane of the disc thus allowing estimation of the forces and moments produced by the whole rotor. One approach to capturing the rotor periodicity is to use an individual blade model (*Houston, 1991; Mansur, 1995*) where each blade is represented separately. In this technique, the elemental forces and moments are integrated (often numerically) along the blade span, and the total rotor forces and moments determined instantaneously by summing the contributions from each blade. The forcing is therefore unsteady, even in trim, varying with each blade's current azimuthal position. Hibrom is an example of such a model.

In both cases correct modelling of the rotor additionally requires that blade element

modelling be combined with either Vortex or Momentum Theory. This allows, by determining the nature of the induced flow through the rotor, the thrust to be predicted. In Vortex Theory (*McCormick, 1995*) the flow of the air over a blade is considered in 3-dimensions and the downwash distribution related to the magnitude and distribution of the wake structure. To accurately model a rotating, manoeuvring rotor system in this way, however, is computationally intensive (*Scully, 1975*) and its development outwith the scope of the current work. Consequently the forces and moments produced by the Hibrom rotor are determined by Blade Element / Momentum Theory (*Prouty, 1990*) where the thrust produced by the whole rotor is related to the downwash (or inflow velocity) distribution over the plane of the disc. Hibrom uses the dynamic inflow model of Peters and HaQuang (*1988*).

Individual blade modelling offers a higher fidelity than is possible with a rotor disc representation since the technique readily permits the inclusion of more complex blade geometries and aerodynamic properties, and captures the periodic nature of the forces and blade dynamics. Better prediction of the vehicle's behaviour at the edges of the flight envelope is therefore possible.

Determination of the rotor forces and moments is detailed in section 5.3, but first the main modelling features and simplifying assumptions will be discussed. To simulate a full helicopter, Hibrom is used in tandem with the tail rotor, fuselage, tail plane and fin models from HGS (Appendix 2).

5.2 Main Rotor Modelling Assumptions

As, to the best of the author's knowledge, no previous attempts have been made to incorporate an individual blade model in inverse simulation, it was decided to restrict the number of modelling features to a manageable level. This avoids clouding the issue of implementing the model in an inverse simulation framework with the complexities of advanced modelling features such as vortex modelling or aeroelastic behaviour. Clearly this does not rule out model augmentation at a later date. The modelling assumptions are as follows.

i) Ideal atmospheric conditions.

Calm International Standard Atmosphere conditions are assumed. No attempt has been made to model the influence of either gusts or a steady wind. Although typical manoeuvres, being Nap-of-the-Earth (NOE), will be low altitude, they will generally be performed at sufficiently high speed to neglect Ground Effect. The air density is assumed to be that at sea level.

ii) 2D aerodynamics.

As trailing vortices are not modelled, the spanwise flow over the blade is not considered. Consequently the aerodynamic forces are accepted to consist of components only parallel (drag) and perpendicular (lift) to the aerofoil angle of attack. These forces are assumed to act through the aerodynamic centre, understood to be coincident with the quarter chord point. The aerodynamic pitching moment about this point is ignored, implying torsional rigidity.

iii) Inertial forces.

As the inertial (other than spanwise) forces acting upon the rotor are much smaller than the aerodynamic forces, they are omitted from some models. Derivation of the accelerations and subsequently inertial forces has, however, been included here. By comparison with other forces the weight of the blades has been assumed small enough to neglect.

iv) Wake / Inflow Model.

The behaviour of the flow around a helicopter rotor is, in reality, very complex. While attempts have previously been made to model this flow using Vortex Theory - culminating in either a prescribed (*Beddoes, 1985*) or free wake model (*Scully, 1975*) - simulating the wake for the purposes of inverse simulation was deemed impractical due to its computational intensity and the development time required. It is, however, still necessary to observe the velocity induced on the local airstream by a rotating system of blades as this has an effect on the resultant velocity, the local angle of attack, and consequently the aerodynamic forces generated by the rotor. Having abandoned vortex theory the obvious alternative is Blade Element / Momentum theory where the flow over

the aerofoil and the induced velocity are treated separately using 2D aerodynamics and the inflow model respectively. The nature of vortices and hence blade-vortex interactions in the wake are not examined.

A commonly used, rudimentary model for estimating the inflow velocity, $v_{ind.}$, is based upon momentum theory as developed by Glauert (*1926*) and is in fact the inflow model employed in HGS. In Glauert's model the inflow consists of a velocity component v_0 - uniform over the plane of the rotor disc - which is related to the thrust generated by the rotor, T, using the following expression:

$$v_0 = \frac{T}{2\rho\pi R^2 \sqrt{\left(u^2 + v^2 + \left(w - v_0\right)^2\right)}},$$

where u, v and w are the velocity components of the rotor hub, radius R. Glauert appreciated that the rotor would behave very much like an equivalent finite wing of span equal to the rotor diameter, giving an upwash at the leading edge of the rotor and an increase in induced velocity at the trailing edge. Consequently radially and azimuthally varying components are superimposed to model this effect, the magnitudes of the longitudinal, v_{1c}, and lateral, v_{1s}, constants depending on the current flight speed and direction. Thus the inflow distribution, as a function of radial and azimuthal position (r and ψ) can be calculated for the entire rotor plane by equation (5.1) below:

$$v_{ind.} = v_0 + \frac{r}{R}\left(v_{1s}\sin\psi + v_{1c}\cos\psi\right). \tag{5.1}$$

There are, however, two main problems with this formulation: namely that the air is assumed to accelerate instantaneously as it crosses the plane of the disc; and that the effects of pitching and rolling moments are disregarded. More sophisticated dynamic inflow models attempt to address these limitations. Firstly, as determination of the inflow velocities is governed by a first order differential equation, the lag between the application of pitch changes and thrust changes can be modelled using a mass matrix, $[M]$. This also allows the blade / inflow coupling to be captured as the respective dynamics are of a similar order of magnitude. Secondly, the effects of the aerodynamic pitching, M, and rolling, L, moments are observed; the inflow velocities and rotor forcing being related by a gains matrix, $[L]$. The result is a governing equation for dynamic inflow models of the form:

$$[M]\begin{Bmatrix}\dot{v}_0\\ \dot{v}_{1s}\\ \dot{v}_{1c}\end{Bmatrix}+[L]^{-1}\begin{Bmatrix}v_0\\ v_{1s}\\ v_{1c}\end{Bmatrix}=\begin{Bmatrix}T\\ L\\ M\end{Bmatrix},$$

with an inflow distribution over the rotor disc, as with Glauert's model, described by equation (5.1). The rotor model discussed here uses the particular dynamic model of Peters and HaQuang (Appendix 5) which is a development of the earlier model of Pitt and Peters (*1981*). It is currently the only dynamic inflow model which takes into account the effect of sideward flight and thus the most suitable model for use in inverse simulation. In his review of inflow models Chen (*1989*) states that at the rotor "correlation with several sets of test data indicate that the Pitt / Peters' first harmonic inflow model works well" and indeed "as well (or as poorly) as the state-of-the-art prescribed- and free wake codes". These findings reinforce the model's suitability for use in inverse simulation.

There are, however, two significant weaknesses in using blade element / inflow rather than blade element / wake models. The first is that the assumption of 2D aerodynamics, by ignoring spanwise airflow, cannot acknowledge blade tip losses. Though this modelling deficiency is not a problem when using a disc model, the error in thrust, for a given collective, can be quite considerable for a finite number of blades (*Johnson, 1980*). To account for this, only drag is assumed present for elements outboard of 97% of the rotor radius. Johnson suggests that this crude correction gives good correlation with flight data. Secondly, in ignoring the wake, there is no appreciation of how the induced velocity affects the fuselage forces and moments at low speed and those of the tail plane and tail rotor at high speed. Although consideration of this wake / airframe interaction is beyond the scope of this research it may be included in the future.

v) Constant rotorspeed.

Due to computational problems discussed elsewhere (*Rutherford and Thomson, 1996*) and later in Chapter 6, the discretisation time interval used in inverse simulation has to match one complete period of the rotor (1 / 4 revolution for a 4 bladed rotor in Hibrom). For initial manageability in inverse simulation a constant rotorspeed is assumed, thus allowing the discretisation interval to be predicted early in the computational process. A variable rotorspeed would require a variable discretisation size which in manoeuvring flight would be extremely difficult to ascertain.

vi) Blade Dynamics.

Blade Elasticity. The elastic deformation of the blades due to their loading has been deemed beyond the scope of this research. Turnour and Celi (*1996*) suggest that elastic modelling "has a very small effect on the dynamics of the helicopter" for articulated rotors. This claim is reinforced by Lewis (*1993*). As Hibrom is predominantly to be used for flight dynamics, the assumption of fully rigid rotor blades would therefore appear to be reasonable. It is however anticipated that the off-axis vehicle response will not be as accurate when simulating semi-rigid rotors, (*Sturisky and Schrage, 1993*). Mansur (*1995*), who uses a rigid individual blade model similar to Hibrom to simulate the AH-64A Apache, concurs that on-axis responses do match flight test data much better than off-axis. Hill, DuVal et al (*1990*) also found that elastic models demonstrate improved correlation with flight test data, and as such may be considered for future development.

Lead / lag freedom. The periodicity of the drag force from the blades means that a helicopter rotor requires a lead / lag damper to alleviate fatigue damage. However modelling this feature increases the period of the rotor and consequently is inconvenient for use in inverse simulation. Thus lead / lag dynamics have not been included in Hibrom. The implicit, balancing assumption is that the in-plane stiffness and strength of the hinge are sufficient to prevent motion without structural damage.

Torsional freedom. As already stated elastic effects have been neglected, the result of which is that torsional rigidity is assumed. Torsional freedom would also add undesirable complications due to the effect on the local angle of attack.

Flap freedom. Though torsional and lead / lag dynamics have been neglected, flap displacements are of sufficient magnitude that to ignore them would result in very poor prediction of the rotor forces and moments. The full second order differential equation which governs the flapping dynamics of a blade has therefore been included in the rotor model and their development from first principles is given in section 5.4.

vii) Aerodynamic Data.

The blade aerodynamic data consists of 2-dimensional look-up tables where the coefficients of lift, C_l, and drag, C_d, are functions of angle of attack, α, and Mach

number, M.

Angle of attack range ($C_l(\alpha)$, $C_d(\alpha)$). Chapter 4, Section 4.2, demonstrated that disc models can allow solutions at unrealistically high angles of attack, α. This is due to the assumption of linear aerodynamics, $C_l = a_0\alpha$ which is valid over a restricted angle of attack range and does not acknowledge blade stall or subsequent control failure. As this research will explore the limits of the capabilities of both conventional and advanced rotorcraft, it is desirable to simulate blade stall and control failure at too high a speed or for too severe a manoeuvre. In addition, the high speed flight of compound helicopters may result in a large reversed flow region on the retreating side of the rotor. In such a region the effect is that of air passing over an aerofoil section from trailing edge to leading edge. As the blade sections in question are both reversing and invariably at negative local angles of attack they produce negative lift; relatively high drag; and have rapid, abrupt stall characteristics. Even with individual blade models it is impossible to model such features if aerodynamic data is not available for a wide enough angle of attack range. It was therefore decided to include $C_l(\alpha)$ and $C_d(\alpha)$ data which extends over the full 360 degrees. With such data it is possible to calculate blade loadings into the fully stalled region, and also allows the phenomenon of reversed flow to be modelled. As the fully stalled aerofoil is acting essentially as a bluff body, compressibility adjustments have been neglected for the data at high angles of attack. It is also reasonable to ignore compressibility effects in the reversed flow region as the local air encountered will always be at low speed. All empirically obtained aerodynamic data is for an aerofoil immersed in steady flow, thus the effect of dynamic stall is not included.

Compressibility effects ($C_l(M)$, $C_d(M)$). At low speeds it can be assumed that the air is incompressible. Indeed it is convenient, and usually reasonable, to make this assumption up to a Mach number of approximately $M = 0.3$. In their book "Computational Fluid Dynamics and Heat Transfer" Anderson et al (*1984*) state that "for air flows with $M < 0.3$ the assumption of incompressibility is a good approximation." Only at higher speeds does this assumption introduce unacceptable errors where the compressed air acts, in essence, like a different fluid with very different aerodynamic properties. Clearly, however, $M = 0.3$ is an entirely arbitrary limit as compressibility occurs, to a greater or lesser extent, at all speeds and so ignoring it always introduces an error. For this reason the aerodynamic look-up tables accommodate empirically obtained aerodynamic data which vary with the Mach number, M. Thus, for any given angle of attack, as the Mach number increases, the lift coefficient decreases and drag coefficient

increases.

High angle of attack and reversed flow aerodynamic data is particularly useful for observing the behaviour of retreating blades which, when used in tandem with data for the compressibility effects (significant for the advancing blade) enhances modelling of high speed flight. All aerodynamic data is for a NACA 0012 aerofoil.

viii) Effective flap hinge offset.

From the earlier statement that the blades are fully rigid it can be assumed that all blade flapping occurs as a result of angular displacements about an idealised hinge. The hinge has to be modelled in such a fashion as to give a reasonable estimate of the forces and moments acting at the rotor hub centre. Any semi-rigid or fully-articulated rotor can thus be modelled in one of three ways: by a centrally sprung hinge with a restoring moment related to the flapping angle, β using the equivalent spring stiffness, K_β; by a free pivot with no restoring moment but positioned some distance - the effective hinge offset, x_{hinge} - from the hub centre; or by a combination of spring stiffness and hinge offset (*Johnson, 1980*). The hinge model chosen here is the effective hinge offset with no spring stiffness: where a semi-rigid rotor is represented by a large hinge offset; and a fully-articulated rotor by a relatively small value. The actual value for the effective hinge offset is that which achieves the correct flapping frequency, λ_β, as determined by the following relationship (*Young, 1962*):

$$\lambda_\beta^2 - 1 = \frac{K_\beta}{I_\beta \Omega^2} + \frac{x_{hinge} M_\beta}{I_\beta}, \tag{5.2}$$

where Ω is the rotorspeed, and M_β and I_β are the blade mass moment and flapping inertia respectively. The suitability of equation (5.2) was justified by Padfield (*1981*) where $\lambda_\beta^2 = 1.2$ for a Westland Lynx. It is applicable to any of the three hinge models and obviously simplifies for the model chosen in Hibrom when $K_\beta = 0$.

ix) Blade geometry.

Blade Twist. In a rotating system the tip of each blade has a much higher local velocity than the root i.e. the local velocity is directly related to the radial position. As the aerodynamic forces are proportional to the velocity squared then clearly much more lift

can be generated in the outboard section of the blade. To produce a more uniform lift distribution and reduce the bending moment at the hinge, blades are manufactured with a spanwise geometric twist where the pitch at the tip is reduced relative to that at the root - typically in the region of 6-10°. A simple linear twist variation has been included in the elemental data, though other, more complex, variations can be just as readily incorporated.

Chord variation. Disc type models commonly assume a constant chord in order to simplify algebraic expressions. In practice, however, helicopter blades possess a variable chord due to, for example, the root cut out, swept back tips or - in the case of the EH101 - the BERP tip. To vary the dimensions of the chord in individual blade models is a trivial problem and accordingly chord variation has been incorporated simply by using discrete values for each element. The root cut out is assumed to contribute no lift and only drag.

The individual blade model will now be detailed.

5.3 Individual Blade Model for Helicopter Main Rotor

As the rotor model is an individual blade type and is based upon blade element theory, it follows that its contribution to the external forces and moments requires knowledge of the velocity and accceleration, referred to local axes, of each blade element. In formulating such expressions it is initially assumed that the elements are of unit span, that the velocities and accelerations are uniform over each element and are equal to those at the elemental centres. Thus starting from known velocities and accelerations at the helicopter centre of gravity (referred to the body axis frame), determination of the desired values involves a series of axes transformations, culminating in the velocity and acceleration at a blade element referred to the local blade axis frame. Figure 5.1 shows the axis sets, described below, relating an individual blade element to the helicopter centre of gravity:

where ***body*** refers to the body axis set; centred at c.g., moving with vehicle, $\underline{i}^{body}$ axis along vehicle centreline, $\underline{k}^{body}$ axis pointing down, $\underline{j}^{body}$ axis completing a right handed axis set;

disc refers to the disc axis set, centred at hub, moving with vehicle, orientation obtained by rotation of shaft tilt angle, $\gamma_{sh.}$ about the $\underline{j}^{body}$ axis;

shaft refers to the shaft axis set, centred at hub, moving with shaft, orientation obtained by rotation of angle ψ about the $\underline{k}^{disc}$ axis;

and ***blade*** refers to the blade axis set, centred at hinge, moving with blade, orientation obtained by rotation of angle β about the $\underline{j}^{shaft}$ axis.

The development of the velocity and acceleration of a blade element is now detailed.

5.3.1 Kinematics of a Blade Element

5.3.1.1 Velocity of a Blade Element

The general expression for the absolute velocity of a point, p, referred to an orthogonal axis set q, with origin o, is given as:

$$\underline{v}_p^q = \underline{v}_o^q + \frac{d\underline{r}_{o/p}^q}{dt};$$

$$\Rightarrow \qquad \underline{v}_p^q = \underline{v}_o^q + \frac{\partial \underline{r}_{o/p}^q}{\partial t} + \underline{\omega}^q \times \underline{r}_{o/p}^q.$$

For a rigid system the point p is fixed in relation to origin o, thus:

$$\frac{\partial \underline{r}_{o/p}^q}{\partial t} = \underline{0},$$

and the expression can be simplified as in equation (5.3) below:

$$\underline{v}_p^q = \underline{v}_o^q + \underline{\omega}^q \times \underline{r}_{o/p}^q, \tag{5.3}$$

where $\underline{v}_o^q$ is the translational velocity of the origin, o, of the axis set q;

$\underline{r}^q_{o/p}$ is the vector describing the position of point p relative to origin o, referred to the axis set q;

$\underline{\omega}^q$ is the rotational velocity of the axis set, q, about the origin of the axes, o;

and $\frac{\partial \underline{r}^q_{o/p}}{\partial t}$ is the translational velocity of the point, p, relative to the axis set origin, o.

Now considering the specific case of the modelled rotor system, the first stage is to describe, in *body* axes, the velocity of the hub centre with respect to the helicopter's centre of gravity. Thus from equation (5.3) the hub velocity can be expressed as:

$$\underline{v}^{body}_{hub} = \underline{v}^{body}_{c.g.} + \underline{\omega}^{body} \times \underline{r}^{body}_{c.g./hub};$$

where

$$\underline{v}^{body}_{c.g.} = \{U \quad V \quad W\}^T,$$

$$\underline{\omega}^{body} = \{P \quad Q \quad R\}^T,$$

$$\underline{r}^{body}_{c.g./hub} = \{x_{ref.} + l_{hub} \quad 0 \quad z_{ref.} + h_{hub}\}^T;$$

$x_{ref.}$, $z_{ref.}$ are distances along the $\underline{i}^{body}$ and $\underline{k}^{body}$ axes from the helicopter centre of gravity to the fuselage reference point (the fuselage reference point is both the point at which the fuselage's aerodynamic loadings are referred and the datum from which all other points on the helicopter are measured, thus allowing c.g. variation to be incorporated in the model);

and l_{hub}, h_{hub} are distances along the $\underline{i}^{body}$ and $\underline{k}^{body}$ axes from the fuselage reference point to the hub centre i.e. the hub height above and length fore / aft of the fuselage reference point.

It is assumed that the rotor shaft is inclined with respect to the body axes by the shaft tilt angle, $\gamma_{sh.}$, and hence the hub velocity must be related to an axis set aligned with the shaft. Referring to Figure 5.2, the translational and rotational hub velocities should

be expressed in terms of the *disc* axis set, centred at the hub and fixed in relation to the body axes set. This is achieved by rotation about the $\underline{j}^{body}$ axis through the shaft tilt angle:

$$\begin{aligned} \underline{v}_{hub}^{disc} &= \left[T^{body/disc}\right]\underline{v}_{hub}^{body} \\ &= \left\{u_{hub}^{disc} \quad v_{hub}^{disc} \quad w_{hub}^{disc}\right\}^{T}, \end{aligned} \tag{5.4}$$

$$\underline{\omega}^{disc} = \left[T^{body/disc}\right]\underline{\omega}^{body},$$

where the transformation matrix from body to disc axes is given as:

$$\left[T^{body/disc}\right] = \begin{bmatrix} \cos\gamma_{sh.} & 0 & -\sin\gamma_{sh.} \\ 0 & 1 & 0 \\ \sin\gamma_{sh.} & 0 & \cos\gamma_{sh.} \end{bmatrix}.$$

The next step is to refer the hub velocities to the *shaft* axis set, Figure 5.3. Like the disc axis set, the shaft axes are centred at the hub. Unlike the disc axes the shaft set is a rotating one. For the translational velocity the transformation simply involves rotation about the $\underline{k}^{disc}$ axis through the shaft azimuth angle ψ, however, the rotational velocity must also include the rotorspeed, $\Omega = \dot{\psi}$. Thus:

$$\underline{v}_{hub}^{shaft} = \left[T^{disc/shaft}\right]\underline{v}_{hub}^{disc},$$

$$\begin{aligned} \underline{\omega}^{shaft} &= \left[T^{disc/shaft}\right]\underline{\omega}^{disc} + n_{clock}\left\{0 \quad 0 \quad \Omega\right\}^{T} \\ &= \left\{p^{shaft} \quad q^{shaft} \quad r^{shaft}\right\}^{T} \end{aligned} \tag{5.5}$$

where the integer n_{clock} ensures consistency with a right handed axis set i.e. a clockwise rotating rotor when viewed from above has $n_{clock} = 1$ and an anticlockwise rotating rotor has $n_{clock} = -1$. The disc to shaft transformation matrix is given as:

$$\left[T^{disc/shaft}\right] = \begin{bmatrix} -\cos\psi & -\sin\psi & 0 \\ \sin\psi & -\cos\psi & 0 \\ 0 & 0 & 1 \end{bmatrix}.$$

If the helicopter is modelled with no hinge offset then the translational velocity of the hinge is equal to that of the hub centre; otherwise the contribution due to the effective

hinge offset must be included. Hence:

$$\underline{v}_{hinge}^{shaft} = \underline{v}_{hub}^{shaft} + \underline{\omega}^{shaft} \times \underline{r}_{hub/hinge}^{shaft},$$

where $$\underline{r}_{hub/hinge}^{shaft} = \left\{ x_{hinge} \quad 0 \quad 0 \right\}^{\mathrm{T}}.$$

The translational velocity of the hinge expressed in *blade* axes is now calculated by rotation of blade flap angle, β about the $\underline{j}^{shaft}$ axis. Figure 5.4 illustrates the transformation from the shaft to the rotating blade axes set. The rotational velocity of the blade axes set, of which the hinge is the origin, is similarly transformed and the flapping rate, $\dot{\beta}$, then added to the $\underline{j}^{blade}$ component.

$$\underline{v}_{hinge}^{blade} = \left[T^{shaft/blade} \right] \underline{v}_{hinge}^{shaft},$$

$$\underline{\omega}^{blade} = \left[T^{shaft/blade} \right] \underline{\omega}^{shaft} + \left\{ 0 \quad \dot{\beta} \quad 0 \right\}^{\mathrm{T}}. \tag{5.6}$$

Equation (5.7) describes the transformation from shaft to blade axes:

$$\left[T^{shaft/blade} \right] = \begin{bmatrix} \cos\beta & 0 & -\sin\beta \\ 0 & 1 & 0 \\ \sin\beta & 0 & \cos\beta \end{bmatrix}, \tag{5.7}$$

where the instantaneous values of β and $\dot{\beta}$ are determined by the blade flapping equations in section 5.4. Finally the translational velocity of each element, referred to blade axes, can be calculated by considering the spanwise distance from the hinge offset to the respective elemental centre, $\underline{r}_{hinge/elem.}^{blade}$:

$$\begin{aligned} \underline{v}_{elem.}^{blade} &= \underline{v}_{hinge}^{blade} + \underline{\omega}^{blade} \times \underline{r}_{hinge/elem.}^{blade} \\ &= \left\{ u_{elem.}^{blade} \quad v_{elem.}^{blade} \quad w_{elem.}^{blade} \right\}^{\mathrm{T}}, \end{aligned} \tag{5.8}$$

where $$\underline{r}_{hinge/elem.}^{blade} = \left\{ r_{elem.} \quad 0 \quad 0 \right\}^{\mathrm{T}}.$$

Having calculated the translational velocities it is possible to evaluate the 2D aerodynamic forces acting upon each blade element, but first the local acceleration of each blade element is detailed.

5.3.1.2 Acceleration of a Blade Element

The acceleration of a blade element, referred to local axes, is needed to calculate the inertial forces acting on each blade, which when added to the aerodynamic forces yield the total forces from each blade acting upon the rotor hub. The spanwise inertial (centripetal) force is of particular importance as it is needed to balance the aerodynamic forces in the flap plane (and also in the lag plane if the lag degree of freedom were modelled). By comparison the chordwise and perpendicular inertial forces are small but to ensure consistency are included here nonetheless. The formulation of the accelerations will now be described though, as the procedure is similar, less pedantically than for the velocities. As with the velocities let us first consider the general formulation so that the absolute acceleration of a point, p, referred to an orthogonal axis set, q, with origin o, can be expressed as:

$$\underline{\boldsymbol{a}}_p^q = \underline{\boldsymbol{a}}_o^q + \frac{d^2 \underline{\boldsymbol{r}}_{o/p}^q}{dt};$$

$$\Rightarrow \qquad \underline{\boldsymbol{a}}_p^q = \underline{\boldsymbol{a}}_o^q + \frac{\partial^2 \underline{\boldsymbol{r}}_{o/p}^q}{\partial t^2} + 2\underline{\boldsymbol{\omega}}^q \times \frac{\partial \underline{\boldsymbol{r}}_{o/p}^q}{\partial t} + \underline{\boldsymbol{\omega}}^q \times \left(\underline{\boldsymbol{\omega}}^q \times \underline{\boldsymbol{r}}_{o/p}^q\right) + \underline{\boldsymbol{\alpha}}^q \times \underline{\boldsymbol{r}}_{o/p}^q.$$

Again the system can be considered rigid, so that the point p is fixed in relation to origin o, thus:

$$\frac{\partial \underline{\boldsymbol{r}}_{o/p}^q}{\partial t} = \frac{\partial^2 \underline{\boldsymbol{r}}_{o/p}^q}{\partial t^2} = \underline{\mathbf{0}};$$

and the expression can be simplified as in equation (5.9) below:

$$\underline{\boldsymbol{a}}_p^q = \underline{\boldsymbol{a}}_o^q + \underline{\boldsymbol{\omega}}^q \times \left(\underline{\boldsymbol{\omega}}^q \times \underline{\boldsymbol{r}}_{o/p}^q\right) + \underline{\boldsymbol{\alpha}}^q \times \underline{\boldsymbol{r}}_{o/p}^q; \tag{5.9}$$

where $\underline{\boldsymbol{a}}_o^q$ is the translational acceleration of the origin, o, of the axis set q;

$\underline{\boldsymbol{\alpha}}^q$ is the rotational acceleration of the axis set, q, about the origin of the axes, o;

$\frac{\partial^2 \underline{r}^q_{o/p}}{\partial t^2}$ is the translational acceleration of the point, p relative to the axis set origin, o;

and the other terms are as defined earlier.

It thus follows from equation (5.9) that the acceleration of the hub centre in body axes can be expressed as:

$$\underline{a}^{body}_{hub} = \underline{a}^{body}_{c.g.} + \underline{\omega}^{body} \times \left(\underline{\omega}^{body} \times \underline{r}^{body}_{c.g./hub}\right) + \underline{\alpha}^{body} \times \underline{r}^{body}_{c.g./hub},$$

where the translational and rotational accelerations of the centre of gravity, in body axes, are respectively:

$$\underline{a}^{body}_{c.g.} = \begin{Bmatrix} \dot{U} + WQ - VR \\ \dot{V} + UR - WP \\ \dot{W} + VP - UQ \end{Bmatrix},$$

$$\underline{\alpha}^{body} = \begin{Bmatrix} \dot{P} & \dot{Q} & \dot{R} \end{Bmatrix}^{\mathrm{T}},$$

and $\underline{\omega}^{body}$ and $\underline{r}^{body}_{c.g./hub}$ are as before. The accelerations are next transformed to disc axes, then shaft axes, and the rate of change of the rotorspeed (if variable rotor speed is modelled) added to the $\underline{k}^{shaft}$ term of the rotational acceleration so that:

$$\underline{a}^{disc}_{hub} = \left[T^{body/disc}\right]\underline{a}^{body}_{hub},$$

$$\underline{\alpha}^{disc} = \left[T^{body/disc}\right]\underline{\alpha}^{body},$$

$$\underline{a}^{shaft}_{hub} = \left[T^{disc/shaft}\right]\underline{a}^{disc}_{hub},$$

and $$\underline{\alpha}^{shaft} = \left[T^{disc/shaft}\right]\underline{\alpha}^{disc} + n_{clock}\begin{Bmatrix} 0 & 0 & \dot{\Omega} \end{Bmatrix}^{\mathrm{T}}.$$

Now it is possible to find the translational acceleration of the hinge expressed in shaft, and - via transformation through flap angle, β - blade axes:

$$\underline{a}_{hinge}^{shaft} = \underline{a}_{hub}^{shaft} + \underline{\omega}^{shaft} \times \left(\underline{\omega}^{shaft} \times \underline{r}_{hub/hinge}^{shaft}\right) + \underline{\alpha}^{shaft} \times \underline{r}_{hub/hinge}^{shaft},$$

$$\underline{a}_{hinge}^{blade} = \left[T^{shaft/blade}\right] \underline{a}_{hinge}^{shaft}. \tag{5.10}$$

Finally the translational acceleration of the centre of a blade element can be evaluated:

$$\underline{a}_{elem.}^{blade} = \underline{a}_{hinge}^{blade} + \underline{\omega}^{blade} \times \left(\underline{\omega}^{blade} \times \underline{r}_{hinge/elem.}^{blade}\right) + \underline{\alpha}^{blade} \times \underline{r}_{hinge/elem.}^{blade}, \tag{5.11}$$

where the rotational acceleration of the blade axes, $\underline{\alpha}^{blade}$, is determined by transformation from the shaft axis set and inclusion of the second order flap derivative, $\ddot{\beta}$, as will be derived in section 5.4:

$$\underline{\alpha}^{blade} = \left[T^{shaft/blade}\right] \underline{\alpha}^{shaft} + \left\{0 \quad \ddot{\beta} \quad 0\right\}^{T}, \tag{5.12}$$

allowing calculation of the inertial forces acting on each element.

5.3.2 Rotor Forces and Moments

5.3.2.1 Aerodynamic Forces Acting Upon a Blade Element

The velocity of a blade element derived in section 5.3.1.1 (equation 5.8) can be used to calculate the aerodynamic forces acting upon each element of unit span. Assuming two-dimensional aerodynamics then the lift and drag per unit span are $\bar{l}_{elem.}$ and $\bar{d}_{elem.}$ respectively. To calculate these forces it is first necessary to determine the tangential and perpendicular components of the velocity of the air over the blade i.e. in the opposite sense to the motion of the blade itself. Thus if the chordwise blade motion is in the same direction as the $\underline{j}^{blade}$ axis (as for a clockwise rotating rotor, Figure 5.5) then the tangential component of velocity is given by:

$$v_{tan.} = v_{elem.}^{blade}.$$

For an anticlockwise rotating rotor it is apparent that the chordwise velocity and $\underline{j}^{blade}$ axis are in opposite directions, so the tangential velocity is defined as:

$$v_{tan.} = -v_{elem.}^{blade},$$

and using the integer flag n_{clock} defined earlier it is possible to define a single expression applicable to both clockwise ($n_{clock} = 1$) and anticlockwise ($n_{clock} = -1$) rotating systems:

$$v_{tan.} = n_{clock} v_{elem.}^{blade}.$$

The perpendicular component is not influenced by the direction of rotation and, as seen in Figure 5.6, can be expressed as follows:

$$v_{perp.} = w_{elem.}^{blade} - v_{ind.} \cos\beta,$$

where the induced velocity, $v_{ind.}$ is assumed to be composed of a uniform component over the whole disc, v_0 and harmonic components, v_{1s} and v_{1c}:

$$v_{ind.} = v_0 + \frac{r}{R}\left(v_{1s} \sin\psi + v_{1c} \cos\psi\right), \tag{5.13}$$

where $$r = r_{elem.} + x_{hinge}.$$

The uniform induced velocity and the rotor thrust are interdependent and, as such, v_0 has to be solved iteratively. The inflow model is described in Appendix 5.

Calculation of the elemental lift and drag requires knowledge of the local lift and drag coefficients. These can be found using look-up tables as functions of local Mach number, M and angle of attack, α. The local Mach number is determined by the ratio of the aerodynamic velocity - defined as the resultant of the tangential and perpendicular velocity components - to the local speed of sound of air, a:

$$v_{aero.} = \sqrt{\left(v_{tan.}^2 + v_{perp.}^2\right)},$$

$$M = \frac{v_{aero.}}{a},$$

while the angle of attack (which through the inflow model implicitly considers induced effects) is the sum of the incidence of the elemental centre with respect to the airflow, ϕ,

and the blade pitch angle, θ:

$$\alpha = \theta + \phi,$$

with the incidence defined as that relating the tangential and perpendicular velocities:

$$\phi = tan^{-1}\left(\frac{v_{perp.}}{v_{tan.}}\right).$$

Blade pitch angle, θ is composed of the pitch at the blade root - due to the collective, θ_0, longitudinal cyclic, θ_{1s} and lateral cyclic, θ_{1c} controls inputs - and the spanwise geometric twist, θ_{twist}:

$$\theta = \theta_{root} + \theta_{twist}(r_{elem.}),$$

where $$\theta_{root} = \theta_0 + \theta_{1s}\sin\psi + \theta_{1c}\cos\psi.$$

The geometric twist can be expressed as discrete values for each element or as a continuous (often linear) function. Thus linear interpolation of the aerodynamic look-up tables yields estimates of the lift and drag coefficients for each element and the associated forces per unit span can be calculated using expressions in the traditional aerodynamic form:

$$\bar{l}_{elem.} = \frac{1}{2}\rho v_{aero.}^2 c_{elem.} C_l(\alpha, M),$$

$$\bar{d}_{elem.} = \frac{1}{2}\rho v_{aero.}^2 c_{elem.} C_d(\alpha, M),$$

where ρ and $c_{elem.}$ are the air density and the blade element chord respectively.

The lift and drag - which are respectively perpendicular to and parallel with the local velocity - are subsequently transformed using the angle of incidence, ϕ, to find the aerodynamic forces per unit span referred to the blade axis set:

$$\underline{\bar{f}}_{aero.}^{blade} = \begin{Bmatrix} 0 \\ -n_{clock}\bar{d}_{elem.}\cos\phi + n_{clock}\bar{l}_{elem.}\sin\phi \\ -\bar{l}_{elem.}\cos\phi - \bar{d}_{elem.}\sin\phi \end{Bmatrix},$$

In the limit (as unity $\rightarrow dr_{elem.} \rightarrow 0$) spanwise integration of these forces would allow evaluation of the aerodynamic forces acting over the entire blade, $\underline{F}_{aero.}^{blade}$. Due to the difficulty in expanding the above expressions algebraically with respect to $r_{elem.}$, however, the total blade forces are in practice estimated numerically. Numerical integration simply involves summing the aerodynamic forces acting on a finite number, $n_{elem.}$, of blade elements, length $\delta r_{elem.}$. Hence:

$$\underline{F}_{aero.}^{blade} = \int_{x_{hinge}}^{R} \underline{f}_{aero.}^{blade} dr_{elem.}$$

can be approximated by:

$$\underline{F}_{aero.}^{blade} = \sum_{k=1}^{n_{elem.}} \underline{f}_{aero._k}^{blade} \delta r_{elem._k},$$

In order to find the total forces acting on each blade it is also necessary, of course, to include the inertial contribution to the forces which requires knowledge of the elemental accelerations derived in the previous section. Formulation of the inertial forces is described in the following section.

5.3.2.2 *Inertial Force Acting Upon a Blade Element*

Having calculated the acceleration of the centre point of the blade element then by Newton's 2nd Law the product of this and the elemental mass will yield the inertial force acting upon the element. Thus if $\overline{m}_{elem.}$ is the mass per unit span then the inertial force per unit span is given by the following expression:

$$\underline{\bar{f}}_{in.}^{blade} = \overline{m}_{elem.} \begin{Bmatrix} a_{x\,elem.}^{blade} \\ a_{y\,elem.}^{blade} \\ a_{z\,elem.}^{blade} \end{Bmatrix},$$

which, in common with the aerodynamic forces, is integrated numerically to estimate the inertial forces acting over the length of the blade:

$$\underline{F}_{in.}^{blade} = \sum_{k=1}^{n_{elem.}} \underline{f}_{in._k}^{blade} \delta r_{elem._k}.$$

The next stage is to calculate the forces and moments acting about the hub centre due to all of the blades.

5.3.2.3 Forces and Moments at Hub due to Blade Forces

What we first want to calculate is the force transmitted to the hinge by each blade, $\underline{F}_{hinge}^{blade}$ i.e. the equal and opposite force to that supplied by the hub. Thus applying Newton III to the m^{th} blade, force equilibrium demands that the following is observed:

$$-\underline{F}_{hinge_m}^{blade} + \int_{x_{hinge}}^{R} \underline{f}_{aero.}^{blade} dr_{elem.} = \int_{x_{hinge}}^{R} \underline{f}_{in.}^{blade} dr_{elem.} \tag{5.14}$$

represented numerically by:

$$-\underline{F}_{hinge_m}^{blade} + \sum_{k=1}^{n_{elem.}} \underline{f}_{aero._k}^{blade} \delta r_{elem._k} = \sum_{k=1}^{n_{elem.}} \underline{f}_{in._k}^{blade} \delta r_{elem._k},$$

which when rearranged yields an expression for the forces from each of m blades acting at their respective hinges:

$$\begin{aligned} \underline{F}_{hinge_m}^{blade} &= \sum_{k=1}^{n_{elem.}} \underline{f}_{aero._k}^{blade} \delta r_{elem._k} - \sum_{k=1}^{n_{elem.}} \underline{f}_{in._k}^{blade} \delta r_{elem._k} \\ &= \sum_{k=1}^{n_{elem.}} \underline{f}_{elem._k}^{blade} \delta r_{elem._k} \end{aligned}$$

The moment reactions are calculated by taking the cross product of the distance between each elemental force and the hinge:

$$\underline{M}_{hinge_m}^{blade} = \sum_{k=1}^{n_{elem.}} \left(\underline{r}_{hinge/elem._k}^{blade} \times \underline{f}_{elem._k}^{blade} \delta r_{elem._k} \right),$$

though in Hibrom only the moment in the $x-y$ plane, $N_{hinge\,z_m}^{blade}$, need be considered due to the rotor assumptions stated earlier. To reiterate: the absence of lag freedom necessitates a restoring moment in the $x-y$ plane, the result of using an effective hinge

offset however is that there is complete flap freedom (i.e. no restraining spring) and consequently no moment in the $x-z$ plane for either a fully-articulated or semi-rigid rotor model. Additionally there is no torsional moment as the aerodynamic centre is assumed coincident with the centre line of the blade and the position vector, $\underline{r}^{blade}_{hinge/elem._k}$, has only an $\underline{i}^{blade}$ component. Having calculated the forces and moments produced by the blades they can now be resolved to establish the main rotor's contribution to the external forces and moments in the Euler equations of motion.

5.3.2.4 *Main Rotor's Contribution to External Forces and Moment*

The forces and moments acting on the main rotor's hinges can be manipulated to find their cumulative effect upon the rotor hub. Each blade's contribution is firstly transformed, via the shaft axis set, to the non-rotating disc axes of which the hub is the centre - a process involving the transposes of the *shaft / blade* and *disc / shaft* transformation matrices from section 5.3.1.1. As the hinge is not coincident with the hub the moments must be augmented with components due to the influence of the effective hinge offset. The constituents from each blade are then summed to find the total forces and moments, referred to disc axes, at the hub:

$$\underline{F}^{disc}_{hub} = \sum_{m=1}^{n_{blades}} \underline{F}^{disc}_{hinge_m}$$

$$= \sum_{m=1}^{n_{blades}} \left[T^{disc/shaft}\right]^{\mathrm{T}} \left[T^{shaft/blade}\right]^{\mathrm{T}} \underline{F}^{blade}_{hinge_m},$$

$$\underline{M}^{disc}_{hub} = \sum_{m=1}^{n_{blades}} \left(\left[T^{disc/shaft}\right]^{\mathrm{T}} \left[T^{shaft/blade}\right]^{\mathrm{T}} \underline{M}^{blade}_{hinge_m} + \underline{r}^{disc}_{hub/hinge_m} \times \underline{F}^{disc}_{hinge_m} \right).$$

These hub forces are then transformed from disc to body axes yielding the external forces acting at the helicopter centre of gravity due to the main rotor:

$$\underline{F}^{body}_{c.g.} = \left[T^{body/disc}\right]^{\mathrm{T}} \underline{F}^{disc}_{hub} = \begin{Bmatrix} X_{rot.} \\ Y_{rot.} \\ Z_{rot.} \end{Bmatrix}.$$

The moments are similarly transformed and the component due to the distance between the centre of gravity and the hub included. This supplies the main rotor's contribution to the external moments acting about the helicopter centre of gravity:

$$\underline{M}_{c.g.}^{body} = \left[T^{body/disc}\right]^{\mathrm{T}} \underline{M}_{hub}^{disc} + \underline{r}_{c.g./hub}^{body} \times \underline{F}_{c.g.}^{body} = \begin{Bmatrix} L_{rot.} \\ M_{rot.} \\ N_{rot.} \end{Bmatrix}.$$

5.4 *Equations Governing the Blade Flapping Dynamics*

Each blade is assumed to flap about its hinge as a result of the aerodynamic moment, $M_{aero.}$, due to the offset aerodynamic forces acting upon each element. Equilibrium is maintained by the similarly offset inertial elemental forces and, if modelled, a restoring hinge spring producing a moment proportional to the instantaneous flapping angle, β. Assuming the hinge model described in section 5.2, however, there is no restoring moment (i.e. $\underline{M}_{hinge}^{blade} = \underline{0}$) and so the aerodynamic and inertial moments acting about the hinge must be equal:

$$\int_{x_{hinge}}^{R} \underline{r}_{hinge/elem.}^{blade} \times m_{elem.} \underline{a}_{elem.}^{blade} dr_{elem.} = \int_{x_{hinge}}^{R} \underline{r}_{hinge/elem.}^{blade} \times \underline{f}_{aero.}^{blade} dr_{elem.}. \qquad (5.15)$$

The right hand side of equation (5.15) is the forcing term and can be evaluated numerically in the same fashion as the moments transmitted to the main rotor:

$$\underline{M}_{hinge\ aero.}^{blade} = \sum_{k=1}^{n_{elem.}} \left(\underline{r}_{hinge/elem._k}^{blade} \times \underline{f}_{aero._k}^{blade} \delta r_{elem._k} \right) = \begin{Bmatrix} L_{aero.} \\ M_{aero.} \\ N_{aero.} \end{Bmatrix}.$$

The left hand side of equation (5.15) can be expanded to describe the flapping dynamics. Firstly consider the acceleration vector, $\underline{a}_{hinge}^{blade}$, which using small angle approximations - the cosine of an angle is equal to unity, the sine equal to the angle - can be expressed in terms of the shaft axes set including terms in β, $\dot{\beta}$ and $\ddot{\beta}$. Equation (5.16):

$$\underline{a}_{elem.}^{blade} = \underline{a}_{hinge}^{blade} + \underline{\omega}^{blade} \times \left(\underline{\omega}^{blade} \times \underline{r}_{hinge/elem.}^{blade} \right) + \underline{\alpha}^{blade} \times \underline{r}_{hinge/elem.}^{blade}, \qquad (5.16)$$

and from equations (5.6), (5.10) and (5.12):

$$\underline{a}_{elem.}^{blade} = \left[T^{shaft/blade}\right]\underline{a}_{hinge}^{shaft} + \left(\left[T^{shaft/blade}\right]\underline{\omega}^{shaft} + \begin{Bmatrix}0 & \dot{\beta} & 0\end{Bmatrix}^{T}\right) \times \left(\left(\left[T^{shaft/blade}\right]\underline{\omega}^{shaft} + \begin{Bmatrix}0 & \dot{\beta} & 0\end{Bmatrix}^{T}\right) \times \underline{r}_{hinge/elem.}^{blade}\right) + \left(\left(\left[T^{shaft/blade}\right]\underline{\alpha}^{shaft} + \begin{Bmatrix}0 & \ddot{\beta} & 0\end{Bmatrix}^{T}\right) \times \underline{r}_{hinge/elem.}^{blade}\right),$$

which upon further expansion, using equations (5.5) and (5.7), can be expressed as follows:

$$\underline{a}_{elem.}^{blade} = \begin{Bmatrix} a_{hinge\,x}^{shaft} - \beta a_{hinge\,z}^{shaft} \\ a_{hinge\,y}^{shaft} \\ \beta a_{hinge\,x}^{shaft} + a_{hinge\,z}^{shaft} \end{Bmatrix} + \begin{Bmatrix} -r_{elem.}\left(\left(q^{shaft} + \dot{\beta}\right)^2 + \left(\beta p^{shaft} + r^{shaft}\right)^2\right) \\ r_{elem.}\left(q^{shaft} + \dot{\beta}\right)\left(p^{shaft} - \beta r^{shaft}\right) \\ r_{elem.}\left(\beta p^{shaft} + r^{shaft}\right)\left(p^{shaft} - \beta r^{shaft}\right) \end{Bmatrix} + \begin{Bmatrix} 0 \\ r_{elem.}\left(\beta \alpha_x^{shaft} + \alpha_z^{shaft}\right) \\ -r_{elem.}\left(\alpha_y^{shaft} + \ddot{\beta}\right) \end{Bmatrix}. \tag{5.17}$$

In the interests of clarity it is, perhaps, better to simplify the notation used in equation (5.17) yielding the following, more friendly expression:

$$\underline{a}_{element}^{blade} = \begin{Bmatrix} a_x - \beta a_z \\ a_y \\ \beta a_x + a_z \end{Bmatrix} + \begin{Bmatrix} -r_{elem.}\left(\left(q + \dot{\beta}\right)^2 + \left(\beta p + r\right)^2\right) \\ r_{elem.}\left(q + \dot{\beta}\right)\left(p - \beta r\right) \\ r_{elem.}\left(\beta p + r\right)\left(p - \beta r\right) \end{Bmatrix} + \begin{Bmatrix} 0 \\ r_{elem.}\left(\beta \alpha_x + \alpha_z\right) \\ -r_{elem.}\left(\alpha_y + \ddot{\beta}\right) \end{Bmatrix}. \tag{5.18}$$

For blade flapping only the $\underline{j}^{blade}$ component resulting from the cross product on the left hand side of (5.15) need be considered. Thus substituting (5.18) and integrating equation (5.15) yields the following expression:

$$-M_\beta\left(\beta a_x + a_z\right) - I_\beta\left(\left(\beta p + r\right)\left(p - \beta r\right) - \left(\alpha_y + \ddot{\beta}\right)\right)\underline{j}^{blade} = M_{aero}\,\underline{j}^{blade} \tag{5.19}$$

where $$M_\beta = \int_{x_{hinge}}^{R} m_{elem.} r_{elem.} dr_{elem.},$$

and $$I_\beta = \int_{x_{hinge}}^{R} m_{elem.} r_{elem.}^2 dr_{elem.}.$$

Finally equation (5.19) can be expanded and recast to produce the second order differential equation presented in (5.20) describing the dynamics of rotor blade flapping about a hinge. The term in K_β is included to take account of a hinge which is modelled with a restoring spring stiffness. Using the simpler notation:

$$\ddot{\beta} = -pr\beta^2 + \left(p^2 - r^2 + \frac{M_\beta}{I_\beta} a_x + \frac{K_\beta}{I_\beta} \right)\beta + \left(pr - \alpha_y + \frac{M_\beta}{I_\beta} a_z \right) + \frac{M_{aero.}}{I_\beta}, \tag{5.20}$$

and with the full notation:

$$\ddot{\beta} = -p^{shaft} r^{shaft} \beta^2 + \left(p^{shaft 2} - r^{shaft 2} + \frac{M_\beta}{I_\beta} a_{x\,hinge}^{shaft} + \frac{K_\beta}{I_\beta} \right)\beta + \left(p^{shaft} r^{shaft} - \alpha_y^{shaft} + \frac{M_\beta}{I_\beta} a_{z\,hinge}^{shaft} \right) + \frac{M_{aero.}}{I_\beta}.$$

5.5 Chapter Summary

This chapter described the development of the individual blade rotor model, Hibrom. When implemented in inverse simulation Hibrom should provide a higher fidelity of results than is possible with disc models such as HGS, particularly near the edges of the rotorcraft's flight envelope. In addition Hibrom will be used for simulating advanced rotorcraft configuration where control limits are unknown, necessitating modelling of blade stall and reversed flow. The aerodynamic data encompasses these phenomena. The Hibrom computer code has also been written in such a fashion as to readily accommodate changes in the aerodynamic or configurational data.

It is intended that future enhancements will include features such as variable rotorspeed, lead / lag freedom, elastic blades and a more physically realistic wake model. The later is currently under investigation at the University of Glasgow (*Ewing, 1997*) and will be the subject of further research.

Finally it is worth noting the high value of this research simply on the grounds that an individual blade model has never previously been used in inverse simulation. Chapter 6 will detail the verification and validation of the Hibrom model.

Chapter 6 Verification and Validation of the Helicopter Individual Blade Rotor Model: Hibrom

Chapter 5 detailed the development of the helicopter individual blade rotor model, Hibrom. Before using the model in simulation it is necessary to ensure its accuracy, otherwise results cannot be interpreted with any degree of confidence. Consequently this chapter addresses the issues of verification and validation, using configurational data for a Westland Lynx. The verification is a process encompassing four stages. The first stage of verification is by inspection of representative results from Hibrom. Results are examined and it is then hypothesised whether or not the model is performing as expected. The second stage of verification entails collating the trim controls and attitudes over a range of forward flight speeds with the existing disc model, HGS. In the third stage Hibrom's open loop responses to control perturbations from trim are compared to those of HGS. Finally Genisa is used to 'fly' the two models - Hibrom and HGS - through identical inverse simulation manoeuvres and the resultant control time histories are contrasted. Though comparison with existing models can confirm if the computer programme is implemented as intended, it does not guarantee the fidelity of the theory used in simulating the helicopter. Therefore this chapter also considers the validity of Hibrom by likening inverse simulation control time histories to data recorded during flight tests. In order to simulate a complete helicopter, the Hibrom main rotor is combined with the tail rotor, fuselage, tail plane and fin component models from HGS. Two notable accomplishments made during this chapter are the application of the McVicar / Bradley periodic trimmer (*McVicar and Bradley, 1992*) to Hibrom, and its implementation in inverse simulation; a first for an individual blade rotor model. The verification process is now detailed.

6.1 Verification of Hibrom

As mentioned above the verification of the Hibrom individual blade model comprises four stages. The first stage involves heuristic analysis of the results; the others comparisons with an existing simulation, HGS. Each of the four stages is now described.

i) Inspection. Typical output is analysed e.g. how individual blade information such

as angle of attack, α, or lift coefficient, C_l, varies with blade azimuthal position, ψ, at different trim speeds. Thus, by inspection, it can be verified if the model is accurately simulating the behaviour of a rotor. Analogous with the description in Chapter 3, Section 3.1.1 we assume that trim is defined by:

i) rectilinear flight;
ii) average inertial accelerations over a rotor turn equal to zero;
iii) average heading or side slip over a rotor turn is constant;
and that iv) periodicity is conserved.

Clearly this differs from the earlier description of trim regarding HGS, both by stipulating conservation of periodicity, and by demanding zero average rather than zero instantaneous accelerations. The considerable task of trimming an individual blade rotor model is discussed in section 6.1.1 and in greater detail in Appendix 6.

ii) Trim Controls and Attitudes. Hibrom's trim controls and attitudes are compared with those of HGS over a range of forward flight speeds. As HGS has been extensively verified in the past (*Thomson and Bradley, 1990a*) it can be established with some certainty whether the Hibrom model performs appropriately in trim.

iii) Open Loop Responses. The Hibrom model is trimmed at certain flight speeds and each control perturbed from its trim value. By running the model in conventional simulation the open loop response can be compared to HGS. Again it can be judged whether or not Hibrom responds satisfactorily.

iv) Closed Loop Responses (Inverse Simulation). Using the Genisa algorithm, both Hibrom and HGS are used in inverse simulation of identical manoeuvres and the verity of Hibrom determined by comparison with the established HGS disc model. Implementing an individual blade model in inverse simulation requires careful consideration of the discretisation interval, a problem addressed in section 6.1.4.

6.1.1 Inspection of Results

6.1.1.1 Hover

The first basic test of Hibrom involves trimming the full helicopter model in hover

(actual values for trim controls and attitudes over a range of flight speeds are presented in the next section). In this regime the components of vertical thrust from the main (and tail rotor) should match the weight of the helicopter. Referring to the upper plot in Figure 6.1, it is evident that the total rotor thrust is slightly less that the vehicle's weight. However, if the tail rotor is included the predicted vertical thrust over a rotor turn matches the helicopter weight to within 0.002% which, given the complexity of the full model, can easily be attributed to numerical errors. The small vertical thrust component from the tail rotor also helps balance the positive pitching moment caused by the longitudinal c.g. / hub offset. Closer inspection of the rotor thrust indicates that it is not constant but is in fact periodic, shown in the lower plot of Figure 6.1. Examining the vertical scale of Figure 6.1 it becomes apparent that the magnitude of the thrust periodicity is very small, but present nonetheless, and of a frequency of 4 per revolution consistent with the 4 bladed Lynx. Though the left and right hand sides of the rotor both experience the same velocity in hover, low amplitude oscillations still occur due to the small cyclic control inputs which are required. An input of longitudinal cyclic, θ_{1s}, is needed to help counteract the pitching moment due to the centre of gravity offset from the shaft axis and some lateral cyclic, θ_{1c}, is required to balance the sideforce from the tail rotor and the off-axis rolling moment resulting from longitudinal input.

Each individual blade should also exhibit low amplitude, periodic behaviour but at a frequency of one per revolution. This is seen in Figure 6.2 which illustrates the variation of local Mach number, M with respect to blade azimuth. The curves for the two blades (blade 1 aft at $\psi = 0°$, blade 3 fore at $\psi = 0°$) are clearly 180° out of phase with the upper and lower plots referring to elements at approximate radial positions, r/R of 0.38 and 0.88 respectively. As can be seen there is negligible variation with azimuthal position ($M = \text{const.} \pm < 0.01$) but the outer element is moving very much more quickly as a result of its greater distance from the rotating hub. Similarly the inflow, ϕ, and pitch, θ, angles demonstrate little cyclic variation. The former - by $\phi = \tan^{-1}\left(v_{perp.}/v_{tan.}\right)$ - is more negative at the slower moving inboard element and the later is significantly less at the outboard element because of the geometric twist. This inbuilt twist contrives to give a higher angle of attack, α (Figure 6.3) and lift coefficient, C_l (Figure 6.4) at the lower velocity sections, and so a more even spanwise lift distribution than would result from untwisted blades. Such a distribution helps reduce blade bending, requires less power from the engine, and delays local blade sections from reaching their aerodynamic limits. It is worth noting the direct relationship between angle of attack and lift coefficient in hover as the aerofoil data never exceeds the limits approximate to a linear lift curve slope

i.e. $C_l \approx a_0 \alpha$. Also observe that the drag coefficient is small and nearly constant.

From the above results and discussion it can be deduced that the individual blade model is behaving as expected in hover, and so the next stage is to examine its performance at a high forward speed, 160 knots.

6.1.1.2 Forward Flight

Figure 6.5 shows the thrust produced over the period of a rotor turn at 160 knots which, referring back to Figure 6.1, is very different to the thrust produced in hover. This is because at high speed the rotor thrust must have a significant forward component to overcome the fuselage and hub drag and is hence much larger than the weight. The reason why the vertical thrust component (including that of the tail rotor) is still significantly greater than the weight is to help balance the negative pitching moment introduced in forward flight by the tail plane. Also evident from the graph is that the thrust periodicity is of a much greater amplitude than in hover as at any given moment two blades are 'advancing' with the vehicle and two are 'retreating'. This asymmetry is clearly seen in the Mach number variation, Figure 6.6, where the blades observe a large change in velocity with azimuthal position. The amplitude of variation is approximately equal to $\pm V_f$, the flight speed. When combined with the speed due to rotation the result is a maximum 'advancing' speed of 287m/s at $\psi = 90°$ for the outer element of blade 1 ($r/R = 0.88$) and a minimum 'retreating' speed of only 125m/s at $\psi = 270°$. At the inner element ($r/R = 0.3$) the speed due to rotation is less than the flight speed resulting in negative velocity over a region of the retreating side; a phenomenon known as 'reversed flow'.

Consider, for the moment, only the outer element, which makes a much higher contribution than the inner element to the blade forces and moments as a result of its relatively high speed. Due to the tangential speed variation the inflow angle, ϕ, is most negative at the retreating side and least negative at the advancing which would result in a large negative rolling moment and backward tilt of the rotor disc if not compensated for by the controls. In rectilinear forward trimmed flight such a rolling moment is clearly undesirable and a forward disc tilt is required. Consequently a large negative input of longitudinal cyclic is used causing high blade pitch, θ, on the retreating side (blade 3 at $\psi = 90°$) and low blade pitch on the advancing side (blade 1 at $\psi = 90°$) as seen in the lower plot of Figure 6.7. The result is a high retreating angle of attack and low advancing angle of attack, Figure 6.8 (lower plot), and thus more even lift distribution with respect

to azimuth. Figure 6.9 illustrates the height variation of the centre of the outer element with respect to the rotor plane; greater at the rear (blade 1 at $\psi = 0°$) than at the front (blade 3 at $\psi = 0°$) indicating a forward tilting disc as desired.

Chapter 5, Section 5.2 highlighted that the aerodynamic data used in Hibrom is non-linear and covers the full angle of attack range. Thus information is revealed about the blades that cannot be captured by a disc model such as HGS or an individual blade model with a limited angle of attack range. For instance, inner blade sections (e.g. $r/R = 0.3$) experience negative inflow angles which are far too large for the controls to overcome. Consequently the angle of attack, Figure 6.8, of a retreating blade is fully stalled over a significant proportion of the span, with the innermost sections even reversing (Figure 6.6), incurring large negative lift and very high drag coefficients (Figures 6.10, 6.11). Because of the relatively low speed the associated forces are not prohibitively large but blades moving in and out of stall do contribute to vibration, and more significantly for this research the information allows prediction of the onset of control failure.

In conclusion then, the individual blade model does appear to have accurately modelled the expected features of helicopter forward flight. Thus in combination with the good hover results, it can be stated with confidence that the model has successfully passed the first stage of verification. In addition the comprehensive aerodynamic data available for each blade allows the features of stall and reversed flow to be captured, an invaluable tool for simulating high speed flight and severe manoeuvres.

6.1.2 Trim Controls and Attitudes

The next stage of verification is to compare Hibrom's trim controls and attitudes with those of HGS. Before comparing results, however, the strategy for trimming an individual blade model will be explained with further details given in Appendix 6. The simplest way to fully trim a disc model is to demand that the six body accelerations ($\dot{U}$, $\dot{V}$, $\dot{W}$, $\dot{P}$, $\dot{Q}$, $\dot{R}$) are equal to zero. This is conveniently done using the Genisa algorithm by solving for six unknowns; the four controls (θ_0, θ_{1s}, θ_{1c}, θ_{0T_R}) and the pitch and roll attitudes (θ, ϕ). Though the same criteria can be applied to an individual blade model it does not result in a complete solution. An accurate solution which observes both the individual blade dynamics and periodic forcing is a much more complicated process. First the issue of the periodic forcing will be addressed. Figure

6.12 - the variation of the six body accelerations over a rotor turn at 160 knots - illustrates the differences in trim between the steady disc model and the periodic individual blade model. Clearly from this graph trimming Hibrom requires that the average rather than instantaneous forces must be zero. Secondly the effect of the periodicity on the trim state values must be considered. The associated body velocities are presented in Figure 6.13 and it is apparent the velocities are not constant; for example the roll rate, P, at the start of a revolution ($\psi = 0°$) differs greatly from its value after an eighth of a turn ($\psi = 45°$). Thus while for HGS every state has a unique value for a given trim condition, Hibrom's trim demands that each and every state must have the same initial and final value with respect to a rotor turn. Consequently a full periodic trim solution for the Hibrom main rotor described in Chapter 5 requires that Genisa imposes 23 constraints in 23 unknowns. Details of the McVicar / Bradley periodic trimmer (*McVicar and Bradley, 1992*) used for Hibrom are given in Appendix 6.

Figure 6.14 presents the four controls and pitch and roll attitudes for trim speeds of 0 to 180 knots forward flight. The results from Hibrom and HGS correlate very well throughout the speed range, the largest differences being in lateral cyclic, θ_{1c}, and bank angle, ϕ. Hibrom's calculation of a larger lateral cyclic input and bank angle is consistent with previous observations that individual blade models predict higher incidences of cross-coupling than disc models. As both helicopter models share a common tail rotor, any discrepancies in collective can be attributed to different predictions of torque by the main rotor. Figure 6.15 compares the torque and power requirements calculated by the Hibrom and HGS main rotor models. Again the two models agree very well, the divergence at higher speeds being due to Hibrom's more accurate aerodynamic look-up tables which take account of the greater drag and lower lift associated with high angles of attack and compressibility effects.

Qualitatively all results are reasonable; the reduction in collective, torque and power until about 60 knots before increasing is typical of helicopters. Longitudinal cyclic and pitch attitude are also as expected, the helicopter having to tilt forward with flight speed to produce a propulsive component of thrust. Indeed the trends in Figures 6.14 and 6.15 demonstrate excellent correlation with typical plots in the established literature such as Bramwell's "Helicopter Dynamics" (*1976*) and Padfield's "Helicopter Flight Dynamics" (*1996*). In Padfield's book flight data showing the variation of lateral cyclic with respect to forward flight speed is closer to Hibrom than the author's own Helistab disc model upon which HGS was based, reinforcing the verity of Hibrom. By comparison with

HGS and consideration of the expected trends, Hibrom therefore appears to be performing acceptably in trim.

6.1.3 Open Loop Responses

This, the third stage of verification, compares the open loop responses of Hibrom with those of HGS. Starting from a desired trim speed, each of the four controls are perturbed and the helicopter model's time responses are observed. The objective in this section is not to quantify the changes in body rates but rather to test that the responses demonstrate the anticipated trends. As in section 6.1.1 the first test case will be hover.

6.1.3.1 Hover

From an initial condition of hover a doublet of each of the four controls is applied and the velocity time response of the helicopter recorded and compared to HGS. As Hibrom and HGS are found to be acceptably stable in unperturbed free response, perturbed flight results can subsequently be interpreted with confidence. A typical control input time history is illustrated in Figure 6.16. Before the doublet is applied the model is allowed to run in free response for 1 second. For each of the four controls the doublet takes the form of a 10% step input in one direction followed by a 20% step input in the other direction. After 3 seconds the controls are returned to trim and the simulation continued for a further 2 seconds. No results from doublets in the other sense are presented here. Tests have confirmed that they do produce responses in the opposite direction which are similar in both shape and magnitude, though not identical as the helicopter is not symmetrical. In all cases (doublet in main rotor collective, longitudinal cyclic, lateral cyclic and tail rotor collective) Hibrom shows greater responses, particularly off axis. Figure 6.17, for example, shows the response of the body rotational velocities (P, Q, R) to a lateral cyclic doublet, θ_{1c}. The responses of both Hibrom and HGS demonstrate very similar trends but Hibrom's peak response is much greater. This disparity is consistent with previous observations (*Padfield and Duval, 1991; Kaletka, 1991*) which find that different models of the same helicopter can produce "widely differing (>50%) derivative estimates" (*Padfield, 1991*). Changes in the translational velocities are comparatively small.

By inspection it can be seen that the direction of the pitch and roll responses are correct for the anticlockwise rotating Lynx main rotor. Consider the first step input

corresponding to a 10% increase in the trim lateral cyclic. The result is increased pitch on the rear blade ($\psi = 0^{\circ}$) and reduced pitch on the front blade ($\psi = 180^{\circ}$) which, assuming a 15° phase lag, culminates in maximum flap at 75° and minimum flap at 255°. This is analogous to the rotor disc tilting to the left and forwards producing negative roll, P, and pitch, Q, rates. The opposite effect - positive rates - occurs with a 10% reduction in lateral cyclic. Both predictions are consistent with the pitch and roll rate time histories in Figure 6.17. Yaw rate, R, being in the same direction as P is consistent with the Lynx's positive product of inertia, I_{xz}.

6.1.3.2 Forward Flight

As in hover, a doublet is applied to the helicopter using each of the four controls. This time however, the helicopter has been trimmed in forward flight. A trim velocity of 80 knots was chosen as it is representative of a typical 'Nap-of-the-Earth' (NOE) flight speed. Again unperturbed flight demonstrates satisfactorily stability for both Hibrom and HGS allowing confidence in analysis of perturbed results.

Figures 6.18 to 6.21 illustrate velocity responses of Hibrom and HGS for collective, θ_0; longitudinal cyclic, θ_{1s}; lateral cyclic, θ_{1c}; and tail rotor collective, $\theta_{0t.r.}$, doublets respectively. The first observation to be made is the similarity in the responses of Hibrom and HGS for most of the results, the general differences being as in hover i.e. Hibrom predicting greater peak amplitude responses, particularly off-axis. This statement is particularly true for the longitudinal and lateral doublets, Figures 6.19 and 6.20 where the shape of the rotational rates correlate excellently. In both cases the amplitude of the yaw rates, R match very closely. The on-axis peak responses also compare very well; particularly the pitch rate, Q, for the longitudinal doublet.

The response to collective doublet, Figure 6.18, can be explained as follows. A positive step input ($1 \rightarrow 2$sec) produces more lift on the advancing than retreating side and maximum flap in the second azimuthal quadrant, rolling the aircraft to the left and pitching it backwards i.e. negative roll rate, P, and positive pitch rate, Q. Clockwise yaw rate - positive R - will result from the increased torque. Changes in the translational velocities are due to the rotor thrust vector having been tilted: to the left tilt causes negative lateral velocity, V; a backwards tilt retards the forward velocity, U. Though the initial influence of collective is to increase lift and hence climb ($-W$) this is soon offset by a lower forward velocity which reduces the lift from all of the blades and the aircraft

drops ($+W$). A negative step input ($2 \rightarrow 3$sec) will yield responses in the opposite direction, though only reducing rather than reversing the retardation of forward velocity. With the exception of roll rate, P, Hibrom and HGS agree excellently in trend and reasonably in amplitude. The discrepancy in roll rate cannot be explained, though the above analysis indicates that Hibrom's response is the more realistic. For the tail rotor (Figure 6.21) the primary responses - roll rate, R and lateral velocity, V - are alike in both shape and magnitude. Changes in translational velocity in the other axes are minimal.

From the open loop responses presented in this section it has been established that Hibrom behaves as expected and is similar in trend to the established HGS model, particularly the on-axis responses. Though the peak amplitude of responses varies considerably, similar disparities have been found in previous comparisons between disc and individual blade models (*Mansur et al, 1990*) without establishing which is the more accurate for predicting gross effects on the helicopter dynamics. Overall the response trends in this section have confirmed that Hibrom has been implemented correctly.

6.1.4 Inverse Simulation

The fourth and final test of verification involves a comparison between inverse simulation results from the disc and individual blade models. As the principal aim in Hibrom's development is its use in inverse simulation this is undoubtedly the most important test of the model's verity. One of the first issues to be decided upon is the choice of discretisation interval, Δt. In using a disc model such as HGS in inverse simulation - as discussed in Chapter 3, Section 3.3 - the choice of discretisation interval is determined primarily by numerical stability. For inverse simulation using an individual blade rotor model further consideration of the solution interval is required. This is due to the influence of the rotor dynamics. Too short a solution interval will result in poor prediction of the influence of control perturbations on the longer term dynamics of the aircraft due to transient effects. This can subsequently lead to failure of the Genisa algorithm. Consequently an interval must be chosen which is sufficiently long to allow the transient dynamics to settle. Typically this requires a time consistent with at least half a turn of the main rotor. The oscillatory nature of the rotor forcing also means that the solution interval must coincide with an integer number of main rotor periods (a quarter turn for the 4 bladed helicopter model used here). Note that this effect imposes the constraint of assuming constant rotorspeed on the model. For consistency the same

interval ($\pi/\Omega \approx 0.086$s for the Lynx configuration) is used in both simulations.

6.1.4.1 Hurdlehop

Using Genisa, Hibrom and HGS were 'flown' through the same hurdlehop manoeuvre as used in Chapters 3 and 4. Both models predict very similar control displacements. Though this may seem like a disappointing result, it should be borne in mind that this is only a moderately severe manoeuvre and the linear assumptions made in the disc model will be valid. The similarity of the HGS results to the supposedly more realistic individual blade model suggests that disc models are valid for inverse simulation of moderately severe manoeuvres. It is also worth noting that over a typical inverse simulation discretisation interval the open loop responses of Hibrom and HGS are very much closer in magnitude than the reactions to doublets in section 6.1.3, and so similar inverse simulation control time histories are not unexpected. With increasing manoeuvre severity, however, the solutions predicted by the disc and individual blade models diverge, exemplified by the following results for the popup manoeuvre.

6.1.4.2 Popup

The 'popup' manoeuvre is illustrated in Figure 6.22, where it is assumed that the pilot's task is to clear an obstacle, height h, over some distance, s. The obstacle is assumed to be located at the end of the manoeuvre. A series of boundary conditions are applied to the altitude of the helicopter at the entry and exit of the manoeuvre. The simplest analytical function which satisfies these conditions is a fifth order polynomial:

$$z_e(t) = -h\left[6\left(\frac{t}{t_{man.}}\right)^5 - 15\left(\frac{t}{t_{man.}}\right)^4 + 10\left(\frac{t}{t_{man.}}\right)^3\right] \tag{6.1}$$

where $t_{man.}$ is the time taken to complete the manoeuvre. As with the hurdlehop the description is completed by assuming that the popup is performed at constant heading and that there are no lateral excursions. The popup considered here demands that the height to be cleared, h, is 25m and the distance, s, is 200m. Control time histories produced by Genisa / HGS and Genisa / Hibrom for a popup flown at 80kts are shown in Figure 6.23 and, like the hurdlehop, are very similar. Increasing the severity of the popup manoeuvre, however, has a significant effect on the results. Figure 6.24 shows a comparison of results for a popup flown at 85 knots. Whilst HGS predicts control

displacements which are very similar to those in Figure 6.23, Hibrom's results are quite different. This is most evident in the discontinuous section of the lateral cyclic time history and can be explained by consideration of the fuselage pitch angle during the manoeuvre, Figure 6.25. It can be seen that during the exit phase of the manoeuvre where the aircraft performs a 'push-over' (in fact the minimum load factor drops below $0.5g$) to clear the obstacle, the fuselage pitch attitude drops to around -20°. At this attitude and flight speed the perpendicular velocity component, $v_{perp.}$, (see Figure 5.6) becomes negative over a significant portion of the disc. The consequence of this is that on the retreating side of the disc where the tangential velocity, $v_{tan.}$, is small we find large negative angles of attack, α. Figure 6.25 illustrates the variation of angle of attack of an in-board blade element ($r / R = 0.25$) during the popup manoeuvre as predicted by Hibrom. In both simulations the modelled aerofoil section is the NACA 0012 profile, however only the tabulated data used in Hibrom captures the stall characteristics of this section ($\alpha_{C_{l\,max.}} = \pm 15°$). It is clear from Figure 6.25 that the stall is encountered on the retreating side of the disc throughout the push-over phase of the manoeuvre. The result of this is that a net rolling moment is generated, and the remedial action predicted by Hibrom is a rapid input of lateral cyclic stick to counteract this moment. This effect is entirely missed by the HGS disc model as the stalling characteristics are not predicted by the linear representation of lift coefficient.

It could be argued of course that such large and rapid inputs are unlikely to be applied by a real pilot. In this case a real pilot would be likely to feel the onset of the stall through vibration, and 'ease-off' slightly during the push-over. From the results shown here it is clear that the manoeuvre can be flown well within the control limits of the helicopter, but the low load factor in the push-over phase causes severe blade stalling, an important feature simply not captured by the disc model. In fact as the speed of the helicopter through the manoeuvre is gradually increased (thereby increasing the severity of the manoeuvre) the individual blade model, Hibrom, predicts a limiting case of around 90 knots before severe blade stall causes failure of the Genisa algorithm (suggesting that this manoeuvre cannot be flown). On the other hand the disc model, HGS, continues to predict solutions well beyond this velocity before control limits are breached. It can be concluded that the linear approximations made in the disc model are insufficient to accurately predict the aerodynamic loading of the rotor in severe flight states. It follows that if accurate results are required for manoeuvres close to the extremities of the flight envelope, then an individual blade rotor model must be used.

6.1.4.3 Slalom

When verifying the Genisa algorithm in Chapter 4 it was deemed appropriate to test its robustness in lateral as well as longitudinal flight (Section 4.2). Similarly any conclusions made about the performance of Hibrom would be inconclusive if a lateral manoeuvre were not investigated. In Chapter 4, Section 4.2 inverse simulation of the Rapid Slalom MTE, Figure 4.2, was successfully performed using Genisa / HGS despite that fact that the lateral cyclic control was pushed beyond its limit. This of course is due to the linear aerodynamics used in HGS which do not recognise blade stall or prohibitively high drag. On this basis the more sophisticated look-up tables used in Hibrom should better predict the aerodynamic limits of the blades. This does indeed transpire to be the case as attempting the same manoeuvre with Genisa / Hibrom leads to the usually disappointing result of algorithm failure. The result in this case is not discouraging as the helicopter in its given configuration should not be able to fly a Rapid Slalom and hence in failure Genisa has predicted the correct result. Less severe slalom manoeuvres, however, are possible using the Hibrom model. Figure 6.26 compares the controls and attitudes calculated by Genisa / Hibrom to those of Genisa / HGS for a slalom defined by $V_f = 60kts$, $s = 500\text{m}$ and $h = 10\text{m}$ i.e. a Rapid Slalom ($h = 15.2\text{m}$) in all but lateral displacement. The controls are, in general, similar; the most obvious disparity being the large amplitude, low frequency ($\approx 0.73\text{Hz}$) longitudinal cyclic inputs, θ_{1s}, predicted by Hibrom which are also obvious on the pitch attitude, θ, time history. Thomson and Bradley (*1990d*) in their paper "Prediction of the Dynamic Characteristics of Helicopters in Constrained Flight" found similar oscillations both in inverse simulation and also in data from highly constrained flight tests, asserting that "the pilot effectively becomes a high gain controller hence affecting the system dynamics." As an inverse simulation algorithm acts as an infinite gain controller it is not unreasonable to expect that such oscillations are present in the state and control time histories. It is significant that the feature is most apparent in Hibrom's longitudinal cyclic, θ_{1s}, and pitch attitude, θ, for the lateral, slalom manoeuvre. This is consistent with the findings of Thomson and Bradley who suggest the effect is most pronounced in "those states which are secondary to (the) task and are therefore weakly controlled." Results in their paper demonstrate that these oscillations are also very prominent in the 'secondary' controls as well as states. It is hypothesised that Hibrom is more prone to this phenomenon than HGS as a result of its higher cross coupling, and that this is accentuated by the transient dynamics which may not allow the off-axis responses to die down before further control displacements are applied. Evidence to support this theory can be found by increasing the manoeuvre

discretisation interval, Δt, thus imposing less stringent constraints on the helicopter and reducing the need for the controls to 'fight' the transient dynamics. The result is a significant reduction in the amplitude of the 'constrained oscillations', Figure 6.27; the opposite effect being observed if the interval is cut to a quarter revolution.

Results presented in this final stage of verification indicate that Hibrom acts largely like the extensively verified HGS model. By the four stages of verification in this section it can be stated that Hibrom is performing satisfactorily. The main differences occur as a result of Hibrom's more accurate blade aerodynamics, allowing better prediction of control limits. The higher frequency dynamics, periodic forcing and increased cross coupling in the individual blade model have been successfully accommodated in inverse simulation thus demonstrating the flexibility of Genisa. It is anticipated that future modelling augmentations should pose no insurmountable problems in inverse simulation while improving the fidelity of the Hibrom model.

6.2 *Validation of Hibrom: Comparison with Flight Test Data*

The most common way of validating a mathematical model is to compare flight test results with those from the simulation. In simple terms a standard control input may be applied to both vehicle and simulation, and the open loop responses of both compared. In the context of an inverse simulation it is possible to fly the vehicle and simulation through identical manoeuvres, then compare both state and control time histories (*Bradley et al, 1990*). Such a validation method is unique to inverse simulation.

For the current study, data from flight trials undertaken by the Defence Research Agency (DRA), Bedford, U.K., have been used. These trials were performed using a Westland Lynx helicopter, and the manoeuvre flown was the 'quickhop'. This manoeuvre is initiated from the hover, the pilot being instructed to translate forward to a new location some fixed distance away. Constant altitude and heading are to be maintained, and the aircraft is to be returned to the hover at the final position. On-board rate and attitude gyros and accelerometers permit the vehicle's states to be established throughout the manoeuvre. The pilot's control inputs are also measured allowing blade pitch angles to be obtained. The aircraft's position during the manoeuvre is recorded from ground based measurements.

The flexibility of the integration inverse simulation technique, Genisa is of particular value when validating mathematical models. It is possible to use the data measured during the trials as the error function for the simulation, in this case we have:

$$\underline{y}_{des.} = \begin{bmatrix} Q & P & R & \dot{W} \end{bmatrix}^T;$$

and with appropriate configurational data in the model ($m \approx 3600$kg) it is possible to simulate the Lynx flying precisely that manoeuvre flown by the real aircraft. Using a differentiation based inverse simulation algorithm such as Helinv the constraints must be defined in earth axis displacements. This requires remote recording of the vehicle's position and does not have the accuracy of on-board measurements.

A comparison between the measured data from a quickhop manoeuvre of distance 300ft (91m) and that produced by Genisa / Hibrom is shown in Figure 6.28 confirming that the inverse simulation algorithm has converged and so any discrepancies in the controls are due to the helicopter model. The flight test and inverse simulation control time histories are presented in Figure 6.29. From these plots it is apparent that the overall trends in each case have been captured by the simulation although the amplitude of some inputs do appear to be inaccurate (the initial pulse in longitudinal cyclic, for example). When considering where the modelling deficiencies lie one must consider again the initial assumptions made in constructing the main rotor model. For example, the assumption that the blades are rigid may have a significant effect on the results, particularly the off-axis responses. The torsional flexibility of the blades will superimpose pitch inputs in addition to those applied by the pilot, an effect which is not present in the mathematical model. Likewise the modelled flapping dynamics and inflow may not completely replicate those of the real aircraft. A disc model is used for the tail rotor, and under-prediction of the collective, $\theta_{0_{T.R.}}$, is consistent with the observations of other authors (*Padfield and DuVal, 1991*).

The simulation results shown in Figure 6.29 are sufficiently close to those from the flight tests to give confidence in the model's use in many flight mechanics applications. The type of modelling enhancements required to improve the predictions will require little or no change to the inverse algorithm itself.

6.3 Chapter Summary

The four stages of Hibrom's verification have predominantly involved comparison with the well established HGS disc model. In the overwhelming majority of cases it has been demonstrated that the two models predict identical trends, confirming the correct implementation of Hibrom. Where the models differ, however, is in the magnitude of their open loop responses to control inputs. Validation of Hibrom against flight test data in inverse simulation portrays a similar theme; that the qualitative performance of the model is exemplary, but questions remain over its quantitative accuracy. This however is a wider question concerning the fidelity of helicopter models in general, requiring a scope and intensity of research not possible here.

The primary aim of this chapter has been resoundingly met and is illustrated in inverse simulation comparisons between Genisa / Hibrom (individual blade) and Genisa / HGS (disc). For moderate manoeuvres the simplifying assumptions used in a disc model are valid and result in Hibrom and HGS predicting closely matching control time histories. For more severe manoeuvres near the edge of the flight envelope Hibrom's more sophisticated dynamic and aerodynamic modelling allows the onset of control failure to be anticipated, predicting the limits of a given helicopter configuration. This is of enormous advantage in high speed, severe manoeuvring flight.

Chapter 7 Manoeuvring of an Advanced Rotorcraft Configuration: The Compound Helicopter

Previous chapters illustrated the verification and validation of the inverse simulation algorithm, Genisa and of the individual blade model, Hibrom, and their value was established through application to a single main and tail rotor helicopter. This chapter gives further evidence of Genisa's capabilities by applying it to alternative, advanced rotorcraft configurations. It will be shown that Genisa is able to trim and perform inverse simulation manoeuvres for rotorcraft with controls in addition to those of a conventional helicopter. The flexibility of the algorithm is demonstrated by the fact that it allows exact solutions where the number of controls are matched by the number of constraints, and also optimal solutions where one or more controls are redundant. In addition the high fidelity individual blade model developed during this research, Hibrom applied to a propeller, will be used to investigate the benefits offered by the specific case of a compound helicopter i.e. a single main and tail rotor helicopter augmented with a lift device (wing) and auxiliary thrust device. The perceived use of a wing added to a conventional helicopter is that it will produce lift in forward flight. With increasing forward velocity the wing will increasingly relieve the main rotor of its lifting responsibilities. The advantages of this are several: some of the rotor's thrust will be freed for the purposes of manoeuvring; the helicopter should be able to attain a higher forward speed as the high speed limitations of the rotor will not be such a handicap; and power consumption will be less resulting in lower fuel consumption or availing power for other purposes such as auxiliary thrust. The idea behind an auxiliary thrust device is to relieve the main rotor of its propulsive responsibilities at high speed and also to carry the main burden of acceleration; thus avoiding the large pitch attitude excursions experienced by a conventional helicopter when accelerating or decelerating.

The advanced rotorcraft configuration will be built in a piecewise fashion allowing demonstration of how Genisa incorporates these developments, both in trimming the aircraft and in inverse simulation manoeuvres. The first development will be the wing, the defining parameters of which have been based on the chapter "Winged Helicopters" in Stepniewski's and Key's book "Rotary-Wing Aerodynamics" (*1984*). A description of the forces and moments generated by such a wing is detailed in this chapter, section 7.1.1.2, and configurational data is given in Appendix 8, Table A8.2. Using Genisa, and Hibrom, the advantages of a winged, and a compound, helicopter over a

conventional single main and tail rotor helicopter will now be investigated, where the baseline configurational data is that of a Westland Lynx (Appendix 8, Table A8.1). The first investigations will concern trim solutions.

7.1 Trim

7.1.1 Effect of Wing

The maximum forward speed (never-exceed-speed) of a Westland Lynx is documented as less than 140kts (*Jane's Aircraft, 1994*). Modelling the Lynx using the individual blade model, Hibrom, for the main rotor and the HGS models for the tail rotor, fuselage, tail plane and fin, Genisa predicts that the main rotor collective and power limit are exceeded beyond 180kts trim forward flight, indicating an absolute maximum. Genisa fails to find a converged solution at 190kts and above. The initial question to be answered is whether or not a wing, by off-loading the main rotor, can increase this top speed, and so a wing model, positioned at the helicopter centre of gravity, is added to the simulation. To trim with the wing involves no modifications to Genisa, simply an additional component in the rotorcraft model yielding the following expressions for the total external forces and moments:

$$X = X_{rot.} + X_{t.r.} + X_{fus.} + X_{t.p.} + X_{fin} + X_{wing};$$

$$Y = Y_{rot.} + Y_{t.r.} + Y_{fus.} + Y_{t.p.} + Y_{fin} + Y_{wing};$$

$$Z = Z_{rot.} + Z_{t.r.} + Z_{fus.} + Z_{t.p.} + Z_{fin} + Z_{wing};$$

$$L = L_{rot.} + L_{t.r.} + L_{fus.} + L_{t.p.} + L_{fin} + L_{wing};$$

$$M = M_{rot.} + M_{t.r.} + M_{fus.} + M_{t.p.} + M_{fin} + M_{wing};$$

and $$N = N_{rot.} + N_{t.r.} + N_{fus.} + N_{t.p.} + N_{fin} + N_{wing}.$$

Before the results are discussed, the parameters describing the wing evaluation of the forces and moments it generates (subscript *wing*) are described.

7.1.1.1 Wing Parameters

Parameters for the wing are based on details given in the chapter "Winged Helicopters" from "Rotary-Wing Aerodynamics" (*Stepniewski and Keys, 1984*). The defining parameters with a short explanation of their chosen values are as follows.

Area, S_{wing}. A value for wing surface area was chosen based upon the winged helicopter configurational data given by Stepniewski and Keys. The vehicle in question had a mass and surface area of 6800kg and 9.4m². Proportioning for a Lynx of approximately 4500kg suggests that a wing surface area of 6.2m² is reasonable.

Mass, m_{wing}. Again proportioning according to dimensions given by Stepniewski and Keys it is assumed that the wing and the required structural modifications to the fuselage add 159kg to that of the basic Lynx. The effect of the wing on the vehicle centre of gravity or vehicle inertia is not considered.

Aspect Ratio, A. An aspect ratio of 6 is chosen as a compromise between the higher induced drag of a low aspect ratio, and the greater vertical drag of a high aspect ratio wing in hover.

Wing Span, b_{wing} and Chord, c_{wing}. Given an area and aspect ratio of 6.2m² and 6, the wing span (including the fuselage width) and chord are 6.09m and 1.02m respectively. A rectangular wing is assumed.

Location, l_{wing} and h_{wing}. As already indicated, wing location is effectively positioned coincident with the centre of gravity. Given the rudimentary nature of the vertical drag model, vertical position has little effect beyond physical interference with other vehicle components. The longitudinal position can be moved if investigating different wing / auxiliary thrust combinations.

Airfoil Section. The extensive aerodynamic data available for the NACA 0012 profile (discussed in Chapter 5, given in Appendix 8 Tables A8.1-A8.3) used for modelling the rotor blades make it an expedient choice.

7.1.1.2 The Wing Forces and Moments

Two dimensional incompressible aerodynamics are assumed for the wing. Assuming incompressibility is reasonable given that the compound is not expected to fly above 250kts ($M = 0.38$). The wing is composed of two aerodynamic centres to account for different lifting surfaces on either side of the fuselage. The lift and drag coefficients, $C_{l\,wing}$ and $C_{d\,wing}$, are obtained from look-up tables which are functions of each aerodynamic centre's angle of attack with respect to the airflow, α_{wing}, which in turn can be calculated from:

$$\alpha_{wing} = \theta_{wing} + \phi_{wing},$$

where θ_{wing} denotes the fixed angle of incidence of the wing relative to the fuselage centreline. The incidence due to the relative airflow passing over the airfoil, ϕ_{wing}, can be evaluated from:

$$\phi_{wing} = \tan^{-1}\left\{\frac{w_{wing}}{u_{wing}}\right\};$$

where
$$\begin{Bmatrix} u_{wing} \\ v_{wing} \\ w_{wing} \end{Bmatrix} = \underline{v}_{c.g.}^{body} + \underline{\omega}^{body} \times \underline{r}_{c.g./wing}^{body} - \begin{Bmatrix} 0 \\ 0 \\ k_{wet} v_0 \end{Bmatrix}.$$

The position vector of the wing with respect to the centre of gravity, $\underline{r}_{c.g./wing}^{body}$ is shown in Figure 7.1 and defined as:

$$\underline{r}_{c.g./wing}^{body} = \left\{ l_{wing} + x_{ref.} \quad n_{wing} y_{wing} \quad h_{wing} + z_{ref.} \right\}^{\mathrm{T}};$$

where l_{wing} is the distance along the $\underline{i}^{body}$ axis from the fuselage reference point to the wing aerodynamic centre;

y_{wing} is the distance along the $\underline{j}^{body}$ axis from the fuselage reference point to the wing aerodynamic centre;

and h_{wing} is the distance along the $\underline{k}^{body}$ axis from the fuselage reference point to the wing aerodynamic centre.

The integer flag n_{wing} acknowledges the different velocities due to rotation on each

side of the wing and is equal to 1 for the right hand side and -1 for the left. To take approximate account of the vertical drag due to the main rotor downwash the uniform inflow component, v_0 is assumed to act on the wing. The parameter $k_{wet} = 1.5 c_{wet}/c_{wing}$ reflects the approximation that the downwash has accelerated halfway to its freestream value $2v_0$ and the wetted chord, c_{wet} is governed by the geometry of the wing and a simple cylindrical streamtube inclined at the rotor wake angle, χ. Thus in hover and at low speeds the wing is entirely or partially immersed in the rotor downwash whilst clear at high speeds. Having estimated the lift and drag coefficients, the lift and drag forces acting on each side of the wing can be calculated using the following traditional aerodynamic relationships:

$$L = \frac{1}{2}\rho V_{f.wing}^2 S_{wing} C_{l\,wing}, \qquad D = \frac{1}{2}\rho V_{f.wing}^2 S_{wing} C_{d\,wing};$$

where the wing area is the area on either side of the fuselage, and the total velocity, $V_{f,\,wing}$ is given by:

$$V_{f.wing} = \sqrt{u_{wing}^2 + v_{wing}^2 + w_{wing}^2}.$$

Thus the contribution of each side of the wing to the external forces and moments can be written as:

$$\begin{Bmatrix} X_{wing} \\ Y_{wing} \\ Z_{wing} \end{Bmatrix} = \begin{Bmatrix} -D\cos\phi_{wing} + L\sin\phi_{wing} \\ 0 \\ -L\cos\phi_{wing} - D\sin\phi_{wing} \end{Bmatrix},$$

and

$$\begin{Bmatrix} L_{wing} \\ M_{wing} \\ N_{wing} \end{Bmatrix} = \underline{r}_{c.g./wing}^{body} \times \begin{Bmatrix} X_{wing} \\ 0 \\ Z_{wing} \end{Bmatrix}.$$

7.1.1.3 Results

Figure 7.2 compares the trim control and attitude plots with respect to forward speed for the conventional helicopter with those of the winged helicopter, the wing initially having a fixed incidence of 10°. Figure 7.3 shows the power curves. What is patently clear is that there are no obvious benefits offered by this wing, the control limits

having been kept within limits only fractionally longer. In fact the two sets of plots are almost identical, the principal differences being an increase in collective pitch and power in hover due to the vertical drag on the wing, and the increased negative pitch on the fuselage at high speeds to overcome the added longitudinal drag. Inspection of the fuselage pitch attitude indicates that the negative pitch required in forward flight is sufficient to neutralise the wing geometric incidence, thus resulting in a small angle of attack and consequently little lift contribution from the wing. This increased pitch-down attitude is consistent with the observations of Bühler and Newman (*1996*) who have developed a free-wake model to investigate the aerodynamics of the winged and compound helicopters. A rudimentary appreciation of the vertical drag in hover has been included as described in the previous section and, in tandem with the greater mass, explains the increased power consumption in hover by comparison with the standard Lynx.

Wing incidence was then increased to 20° with the control and attitude plots also shown in Figure 7.2. This time the increased drag of the wing has caused Genisa to pitch the fuselage further forward, completely neutralising the positive wing pitch. The increased drag has in fact meant that the control limits are breached sooner.

A fixed wing then offers very limited benefits due to its dependence on a suitable fuselage pitch attitude. Pitch attitude is impossible to govern with single main and tail rotor controls, however, and an additional control is therefore required. Previous winged helicopters have required additional controls surfaces to control pitch attitude, such as adjustable wing tips on a derivative of the SA.341 Gazelle (*Torres, 1976*) or a stabilator on the Sikorsky S-67 (*Dumond and Simon, 1972*). One possible solution would appear to be relieving the rotor of its propulsive duties, which by removing the need for 'nose-down' forward flight can ensure that the wing is always at a productive angle of attack. Such a solution leads to the concept of the compound helicopter.

7.1.2 Effect of Auxiliary Thrust

7.1.2.1 Preliminary Results Using Auxiliary Thrust

As an idealised examination of the effect of auxiliary thrust, the first test concerns a thrust vector acting along the helicopter's longitudinal axis through the centre of gravity. This introduces an additional control, the value of auxiliary thrust, which demands an

additional constraint if Genisa is to find an exact solution. Given the previous observations that pitch attitude excursions are detrimental to the wing's influence a constraint of zero pitch attitude was chosen. To trim with the auxiliary thruster now involves solving for five controls, the fifth variable being auxiliary longitudinal thrust, $X_{aux.}$ and the fifth constraint the pitch attitude rate averaged over a rotor turn, $\overline{\dot{\theta}}$. This auxiliary thrust is of course now an additional component in the rotorcraft model yielding the following expressions for the total longitudinal force:

$$X = X_{rot.} + X_{t.r.} + X_{fus.} + X_{t.p.} + X_{fin} + X_{wing} + X_{aux.}.$$

With the main rotor now relieved of its propulsive duties there should be no requirement for a negative pitch attitude as the main rotor cyclic pitch inputs will be able to balance any moments that are present, allowing the wing to effectively unload the rotor of its lift requirements. Having decided on the extra constraint and control the Genisa algorithm has no trouble finding a trim solution. Figure 7.4 shows control and attitude trim plots produced by Genisa for a Westland Lynx with a thrust vector, and a wing inclined at 10° giving a high C_l at zero pitch attitude but with several degrees leeway to avoid wing stall if the pitch attitude increases. Now that the fuselage pitch attitude is controlled the wing manages to unload the rotor to an ever greater extent as the flight velocity increases. Coupled with the auxiliary thruster supplying the propulsive force Genisa finds a trim solution up to and beyond 250kts with the small rotor control inputs suggesting that the rotor has been almost completely relieved of its lifting and propulsive duties. From the attitude plots it is evident that this occurs without the 'nose-down' attitude required by the helicopter. The power curves, Figure 7.5, illustrate that the main rotor has been nearly unloaded. These results do not of course address the power required by the auxiliary thruster itself but do clearly indicate the advantages of a helicopter augmented with a wing and thrusting device so far as offloading the main rotor and potentially increasing the maximum possible speed are concerned, and the more favourable attitude angles which are possible. One major disadvantage of this exact solution is that zero pitch attitude offers no great benefits in hover and low speed, but does require a thrust input to balance the pitching moments.

The practicalities of an auxiliary thrust device and the power required are discussed in section 7.1.3. Before the power requirements are addressed, however, it is worthwhile considering the realism of the thrust inputs in the above case. For example the Lockheed Cheyenne compound helicopter was reputedly able to achieve 220kts

forward flight (*Forman, 1996*) using a thrust approximate to 10% of the aircraft's weight (*Prouty, 1996*). Such performance is consistent with the objective maximum speed of 210kts based upon research by Eurocopter, France (*Rieugnié and François, 1995*). Considering these statistics and contrasting the 14kN required at 210kts with 10% of the Lynx's weight (≈4.3kN), suggests that an alternative trim strategy must be found. That the Cheyenne's main rotor was still supplying 30% of the weight at high speeds suggests a controlled but non-zero pitch attitude is preferable i.e. given that the main rotor cannot be 'switched-off' at high speed it is inadvisable to completely ignore its large propulsive capacity in favour of the smaller capacity of a propeller. This assertion is supported by flight test data from the Sikorsky RSRA (Rotor Systems Research Aircraft) (*Arcidiacono, deSimone and Occhiato, 1982*) which, in its compound incarnation, is flown with fixed main rotor collective input. Though the turbofans used for auxiliary propulsion in the RSRA can produce as much as 68% of the aircraft's weight, none of the results shown exceed 22% weight. The next question is naturally how to achieve a desirable pitch attitude, but before considering the different solutions it is worthwhile trying to determine what an achievable value of generated thrust would be.

Dimensioning according to parameters given by Eurocopter, a realistic propeller would appear to be one of similar size and speed as the Lynx's tail rotor, though a linear twist of -30° rather than 0° has been found to produce more favourable results. The model for this propeller is detailed in section 7.1.3.2 and the configurational data given in Appendix 8. It suffices to say for the present that by solving for zero pitch attitude the propeller fails at 180kts, whilst the solution at 170kts requires 7.8kN, or 18% of the weight of the Lynx indicating that thrust exceeding more than 10 or 15 percent of the aircraft's weight can not be expected. Using Genisa, different approaches for achieving the desired flight speed of 210-220kts without exceeding reasonable thrust levels will now be considered. The focus will primarily be on the thrust vector with the propeller reintroduced later to test the practicalities of the solutions.

7.1.2.2 Alternative Solutions Using Auxiliary Thrust

Three alternatives to the above solution for five controls with zero pitch attitude, all of which leave the pitch attitude unconstrained, have been used to investigate the compound helicopter and these are listed as follows:

i) exact solution for 4 controls (θ_0, θ_{1s}, θ_{1c} and $\theta_{0t,r}$), auxiliary

thrust, $X_{aux.}$, defined as a function of forward speed;

ii) exact solution for 4 controls ($X_{aux.}$, θ_{1s}, θ_{1c} and $\theta_{0t.r.}$), main rotor collective pitch, θ_0, set to a constant value;

and iii) minimal solution for all 5 controls.

i) *Auxiliary Thrust Defined as Function of Forward Speed*

In this first alternative Genisa finds an exact solution for the four helicopter controls given a simple linear relationship, established through repeated tests, between auxiliary thrust and forward speed, leaving pitch attitude unconstrained. As already indicated, to maintain zero pitch attitude at low speed and hover is of no advantage but does require auxiliary thrust. With reference to the pitch of the 10° winged helicopter in Figure 7.2, zero pitch occurs at approximately 100kts. Consequently auxiliary thrust is set to zero until this speed. Given that 7.8kN appears possible with the propeller, maximum thrusts of 4.3kN (10% weight) and 6.45kN (15%) were attempted. If zero pitch attitude is desired then a maximum of 10% of the aircraft's weight (4.3kN) is exceeded at 140kts, and a limit of 15% of the aircraft's weight (6.45kN) is exceeded at 160kts. Therefore auxiliary thrust is increased linearly from 100kts until the maximum values are reached. Above the given speeds, when auxiliary thrust is at its limit, zero pitch attitude is no longer possible and Genisa must adjust the other controls so that the rotor supplies some of the forward propulsion. In this way a solution can be found which does not require unachievable magnitudes of thrust input. As can be seen in Figure 7.6 the compound can now fly to 200kts without exceeding control limits using 4.3kN, and 220kts if a thrust of 6.45kN is used. The latter meets the maximum speed objectives.

ii) *Main Rotor Collective Pitch Set to Constant Value*

The second alternative allows qualitative validation by comparison with flight test data for the Sikorsky RSRA (*Arcidiacono, deSimone and Occhiato, 1982*) where the main rotor collective pitch is set to 40% (10°) and 50% (11.5°) of the maximum. Genisa can easily accommodate such a solution simply by solving for the auxiliary thrust rather than the collective pitch. Setting the compound Lynx collective pitch to 10° Genisa finds the auxiliary thrust input and fuselage pitch attitude shown in Figure 7.7, where the trim velocity is increased from 90 to 170kts. As with the RSRA, fuselage pitch attitude, θ, decreases with forward flight and auxiliary thrust increases, qualitatively validating

Genisa's solution and further demonstrating the algorithm's applicability to different constraints.

iii) *Minimal (Least Squares) Solution*

A further alternative solves for both pitch attitude and auxiliary thrust which, being a redundant problem requires an optimal solution. Genisa flexibility is clearly illustrated using this approach as it requires only a different solution to the linear relationship:

$$[J]\underline{u}_{error} = \underline{e} \tag{7.1}$$

first given in equation (3.8) without any additional changes to the algorithm. The method chosen is to find a least squares solution to the problem using Singular Value Decomposition (*Press et al, 1986*). This method, in common with thrust definition, also requires a degree of experimentation, however, as there is no one unique solution to equation (7.1) and rather the answer found is one which minimises the length of the vector $\underline{u}_{error}$. Given the simple thrust vector it is possible to find different solutions by adjusting the weight on the auxiliary thrust control variable and hence the length of the vector. For example an input of 4300N will produce the same output as one of 4.3kN, but will result in a much longer vector. The method will thus tend to ignore auxiliary thrust in favour of the main rotor if it demands too large an input, but will use the thruster more freely if it contributes to a shorter vector than rotor control inputs. Consequently the weighting for the auxiliary thrust input has an important influence on the solution. Weights of 500, 750 and 1000N have been added to the auxiliary thrust input producing the solutions shown in Figure 7.8. As the weighting increases the vehicle behaves progressively less like a winged helicopter, and more like the earlier compound solution where the pitch attitude was constrained to zero. The advantage all the solutions have in common over the exact solution, however, is that the thrust input is close to zero in hover and small at low speeds. A weighting of 750N looks particularly promising as it finds a solution at approximately 210kts which requires 6.45kN, matching the imposed 15% limit of the aircraft's weight. Using an individual blade propeller model, the feasibility of this solution will now be tested.

7.1.3 Individual Blade Tail Rotor and Propeller Models

As already indicated, to test the practicalities of the auxiliary thrust solutions, a

propeller was modelled allowing estimation of the auxiliary power required and observation of control failure. As the propeller will predominantly encounter axial flow, a disc model - similar to that used for the HGS main and tail rotors - was precluded. This is because the small angle assumptions used to develop the analytical relationships in the rotor models become invalid when large excursions from edgewise flight are involved. The propeller modelling thus had to be of the individual blade type, allowing exact rather than approximate inflow angles to be used. To ensure consistency individual blade modelling was also extended to the tail rotor.

7.1.3.1 Individual Blade Tail Rotor Model

In essence the individual blade tail rotor model is a simplified version of the main rotor model, Hibrom, though of course with different parameters. Simplifying assumptions made by comparison with the main rotor model are that blade flapping is neglected and the inflow model is a much reduced version of the Peters - HaQuang dynamic inflow model, described in Appendix 7. In addition the inertial forces acting upon the tail rotor are neglected. Modelling is further simplified by the fact that there are no cyclic inputs and the blades are untwisted. Thus knowledge of the local velocity will yield the aerodynamic forces acting on a blade element leading in turn to the tail rotor's contribution to the external forces and moments.

i) Velocity of a Tail Rotor Blade Element

The axes systems describing the transformation from *body* to *t.r.blade* axis are shown in Figure 7.9. As with the main rotor, once the velocity of the vehicle's centre of gravity is known, the first step is to calculate the velocity of the hub:

$$\underline{v}_{t.r.hub}^{body} = \underline{v}_{c.g.}^{body} + \underline{\omega}^{body} \times \underline{r}_{c.g./t.r.hub}^{body} \tag{7.2}$$

$$\underline{r}_{c.g./t.r.hub}^{body} = \left\{ x_{ref.} + l_{t.r.} \quad 0 \quad z_{ref.} + h_{t.r.} \right\}^{\mathrm{T}};$$

where $l_{t.r.}$ is the distance along the $\underline{i}^{body}$ axis from the fuselage reference point to the tail rotor hub;

and $h_{t.r.}$ is the distance along the $\underline{k}^{body}$ axis from the fuselage reference point to the tail rotor hub.

Next the tail rotor hub velocity is transformed to the $t.r.disc$ axis set:

$$\underline{v}_{t.r.hub}^{t.r.disc} = \left[T^{body/t.r.disc}\right]\underline{v}_{t.r.hub}^{body},$$

$$\underline{\omega}^{t.r.disc} = \left[T^{body/t.r.disc}\right]\underline{\omega}^{body};$$

where
$$\left[T^{body/t.r.disc}\right] = \begin{bmatrix} 1 & 0 & 0 \\ 0 & 0 & 1 \\ 0 & -1 & 0 \end{bmatrix}; \tag{7.3}$$

and then to the $t.r.blade$ axis set which, as the tail rotor hub and its hinges are assumed coincident and there is no flapping, rotates about the $\underline{k}^{t.r.blade}$ at the tail rotor speed, $\Omega_{t.r.}$:

$$\underline{v}_{t.r.hub}^{t.r.blade} = \left[T^{t.r.disc/t.r.blade}\right]\underline{v}_{t.r.hub}^{t.r.disc},$$

$$\underline{\omega}^{t.r.blade} = \left[T^{t.r.disc/t.r.blade}\right]\underline{\omega}^{t.r.disc} + \left\{0 \quad 0 \quad \Omega_{t.r.}\right\}^{\mathrm{T}};$$

where
$$\left[T^{t.r.disc/t.r.blade}\right] = \begin{bmatrix} -\cos\psi_{t.r.} & -\sin\psi_{t.r.} & 0 \\ \sin\psi_{t.r.} & -\cos\psi_{t.r.} & 0 \\ 0 & 0 & 1 \end{bmatrix};$$

and $\psi_{t.r.}$ is the tail rotor shaft azimuth angle. Finally, considering the distance from the hub to a blade element, it is possible to calculate the velocity of the centre of a tail rotor blade element referred to local $t.r.blade$ axes:

$$\begin{aligned} \underline{v}_{t.r.elem.}^{t.r.blade} &= \underline{v}_{t.r.hub}^{t.r.blade} + \underline{\omega}^{t.r.blade} \times \underline{r}_{t.r.hub/t.r.elem}^{t.r.blade} \\ &= \left\{u_{t.r.elem.}^{t.r.blade} \quad v_{t.r.elem.}^{t.r.blade} \quad w_{t.r.elem.}^{t.r.blade}\right\}^{\mathrm{T}}, \end{aligned} \tag{7.4}$$

where
$$\underline{r}_{t.r.hub/t.r.elem.}^{t.r.blade} = \left\{r_{t.r.elem.} \quad 0 \quad 0\right\}^{\mathrm{T}}.$$

It is now possible to calculate the aerodynamic forces acting upon an element.

ii) Tail Rotor Forces and Moments

Having calculated the velocity components of a blade element, equation (7.4), the aerodynamic forces can be evaluated, the first stage being to calculate the tangential and

perpendicular components of the velocity of the air over the blade:

$$v_{tan.} = n_{clock_{t.r.}} v_{t.r.elem.}^{t.r.blade}, \qquad v_{perp.} = w_{t.r.elem.}^{t.r.blade} - v_{ind.};$$

where $n_{clock_{t.r.}} = 1$ for an clockwise rotating tail rotor and -1 for one which rotates in an anticlockwise direction. The means of determining the inflow distribution, equation (7.5), are the same as for the main rotor though the uniform component, v_0, and radial and harmonic variations, v_{1s} and v_{1c}, are calculated in a somewhat simpler fashion as described in Appendix 7.

$$v_{ind.} = v_0 + \frac{r_{t.r.elem.}}{R_{t.r.}}\left(v_{1s}\sin\psi_{t.r.} + v_{1c}\cos\psi_{t.r.}\right) \tag{7.5}$$

To calculate the elemental lift and drag naturally requires that the lift and drag coefficients - C_l and C_d - are known. As with the main rotor these are obtained from aerodynamic look-up tables as functions of angle of attack, α and Mach number, M, where the Mach number is the ratio of the total aerodynamic velocity, $v_{aero.}$, to the local speed of sound, a:

$$M = \frac{v_{aero.}}{a}, \qquad v_{aero.} = \sqrt{v_{tan.}^2 + v_{perp.}^2};$$

and the angle of attack is the sum of the blade pitch angle, θ and the inflow angle, ϕ:

$$\alpha = \theta + \phi;$$

where $\theta = \theta_{0t.r.}$, $\qquad \phi = \tan^{-1}\left\{\frac{v_{perp.}}{v_{tan.}}\right\}$. (7.6)

The lift and drag per unit blade span can now be calculated:

$$\bar{l}_{t.r.elem.} = \frac{1}{2}\rho v_{aero.}^2 c_{t.r.elem.} C_l(\alpha, M), \qquad \bar{d}_{t.r.elem.} = \frac{1}{2}\rho v_{aero.}^2 c_{t.r.elem.} C_d(\alpha, M);$$

allowing the force vector per unit span to be referred to *t.r.blade* axes:

$$\underline{\bar{f}}^{t.r.blade}_{t.r.elem.} = \begin{Bmatrix} 0 \\ -n_{clock_{t.r.}} \bar{d}_{t.r.elem.} \cos\phi + n_{clock_{t.r.}} \bar{l}_{t.r.elem.} \sin\phi \\ -\bar{l}_{t.r.elem.} \cos\phi - \bar{d}_{t.r.elem.} \sin\phi \end{Bmatrix}.$$

Assuming that the velocity at an elemental centre is uniform over a finite element of spanwise length, $\delta r_{t.r.elem.}$ then the tail rotor's contribution to the external forces and moments can be calculated by summing the elemental terms and transforming back to the body axis set. Hence:

$$\begin{Bmatrix} X_{t.r.} \\ Y_{t.r.} \\ Z_{t.r.} \end{Bmatrix} = \left[\boldsymbol{T}^{body/t.r.disc}\right]^{\mathrm{T}} \sum_{m=1}^{n_{t.r.blades}} \left[\boldsymbol{T}^{t.r.disc/t.r.blade}\right]^{\mathrm{T}} \sum_{k=1}^{n_{t.r.elem.}} \underline{f}^{t.r.blade}_{t.r.elem._k} \delta r_{t.r.elem._k}; \qquad \text{and}$$

$$\begin{Bmatrix} L_{t.r.} \\ M_{t.r.} \\ N_{t.r.} \end{Bmatrix} = \left[\boldsymbol{T}^{body/t.r.disc}\right]^{\mathrm{T}} \sum_{m=1}^{n_{t.r.blades}} \left[\boldsymbol{T}^{t.r.disc/t.r.blade}\right]^{\mathrm{T}} \sum_{k=1}^{n_{t.r.elem.}} \left(\underline{r}^{t.r.blade}_{t.r.hub/t.r.elem._k} \times \underline{f}^{t.r.blade}_{t.r.elem._k} \delta r_{t.r.elem._k} \right)$$

$$+ \underline{r}^{body}_{c.g./t.r.hub} \times \begin{Bmatrix} X_{t.r.} \\ Y_{t.r.} \\ Z_{t.r.} \end{Bmatrix}.$$

7.1.3.2 Individual Blade Propeller Model

With the exception of the orientation, blade twist, and configurational data, the propeller model is identical to that of the individual blade tail rotor model. The propeller hub is assumed located on the vehicle $\underline{i}^{body}$ axis, one tail rotor radius aft of the tail rotor hub. Its contribution to the vehicle mass or inertia is not considered. The axis systems describing the transformation from *body* to *pr.blade* axis are shown in Figure 7.10. Thus starting from equation (7.2), where all *t.r.* subscripts and superscripts are replaced with *pr.*, the calculation of the velocity of a propeller element is as for the tail rotor, the one difference being the transformation matrix in equation (7.3) which is now:

$$\left[\boldsymbol{T}^{body/pr.disc}\right] = \begin{bmatrix} 0 & 0 & 1 \\ 0 & 1 & 0 \\ -1 & 0 & 0 \end{bmatrix}.$$

Calculation of the propeller forces and moments are again as for the tail rotor save

the calculation of blade pitch angle, θ, which incorporates geometric twist and so equation (7.6) becomes:

$$\theta = \theta_{0pr.} - r_{pr.elem.}\theta_{pr.twist}\left(r_{pr.elem.}\right).$$

Now, having calculated the aerodynamic forces, the propeller's contribution to the external forces and moments can be written as:

$$\begin{Bmatrix} X_{pr.} \\ Y_{pr.} \\ Z_{pr.} \end{Bmatrix} = \left[T^{body/pr.disc}\right]^{\mathrm{T}} \sum_{m=1}^{n_{pr.blades}} \left[T^{pr.disc/pr.blade}\right]^{\mathrm{T}} \sum_{k=1}^{n_{pr.elem.}} \underline{f}_{pr.elem._k}^{pr.blade} \delta r_{pr.elem._k}; \quad \text{and}$$

$$\begin{Bmatrix} L_{pr.} \\ M_{pr.} \\ N_{pr.} \end{Bmatrix} = \left[T^{body/pr.disc}\right]^{\mathrm{T}} \sum_{m=1}^{n_{pr.blades}} \left[T^{pr.disc/pr.blade}\right]^{\mathrm{T}} \sum_{k=1}^{n_{pr.elem.}} \left(\underline{r}_{pr.hub/t.r.elem._k}^{pr.blade} \times \underline{f}_{pr.elem._k}^{pr.blade} \delta r_{pr.elem._k}\right)$$
$$+ \underline{r}_{c.g./pr.hub}^{body} \times \begin{Bmatrix} X_{pr.} \\ Y_{pr.} \\ Z_{pr.} \end{Bmatrix}.$$

To find the total external forces and moments, the contributions from the propeller must of course be added to those of the other components:

$$X = X_{rot.} + X_{t.r.} + X_{fus.} + X_{t.p} + X_{fin} + X_{wing} + X_{pr.};$$

$$Y = Y_{rot.} + Y_{t.r.} + Y_{fus.} + Y_{t.p} + Y_{fin} + Y_{wing} + Y_{pr.};$$

$$Z = Z_{rot.} + Z_{t.r.} + Z_{fus.} + Z_{t.p} + Z_{fin} + Z_{wing} + Z_{pr.};$$

$$L = L_{rot.} + L_{t.r.} + L_{fus.} + L_{t.p} + L_{fin} + L_{wing} + L_{pr.};$$

$$M = M_{rot.} + M_{t.r.} + M_{fus.} + M_{t.p} + M_{fin} + M_{wing} + M_{pr.};$$

and $$N = N_{rot.} + N_{t.r.} + N_{fus.} + N_{t.p} + N_{fin} + N_{wing} + N_{pr.}.$$

7.1.3.3 Results

As already indicated in section 7.1.2.1, an exact solution demanding zero pitch attitude is unrealistic given that the maximum speed the propeller can achieve is 170kts. Using the promising results produced by the optimal solutions, however, constraints consistent with a thrust weighting of 750N were applied to the compound with propeller.

i) Minimal (Least Squares) Solution

Finding a beneficial redundant solution for different propeller rather than thrust vector weightings proves difficult given the complex relationship between propeller pitch and longitudinal force. In fact introducing too large a weighting pushes the model into stall. If the weightings are not too severe Genisa does manage to find a converged solution but the results offer no visible advantages over the exact, zero-pitch-attitude solutions. It is, however, still possible to test the feasibility of the redundant auxiliary thrust solutions in section 7.1.2.2 as the different weightings in Figure 7.8 produce different linear variations of fuselage pitch angle with respect to flight speed i.e. $\theta(V_{f.}) = \text{const.} V_{f.}$ Consequently the compound helicopter was constrained to match the pitch attitude consistent with the 750N weighting and an exact solution found for the five controls. The successful result, as illustrated in Figures 7.11 and 7.12 was a solution up to 210 knots, for a propeller thrust of 5.33kN or 12.4% of the weight and 2199kW total power. Being within the stipulated 15% of the weight, the thrust looks attainable. In addition the predicted value for power compares favourably with the maximum power of the Westland Lynx, 1670kW, which is met at 180kts. As expected, imposing constraints consistent with the different weightings produce different rotor : propeller power ratios. Thus the flexibility of Genisa has been demonstrated by finding both exact and optimal trim solutions for a thrust compounded helicopter, and the realism of the later established by applying the results to a compound helicopter with individual main rotor, tail rotor and propeller models.

7.2 Inverse Simulation - Manoeuvring of the Compound Configuration

Having investigated trim solutions generated by Genisa for a winged and compound helicopter the next stage is to look at the inverse simulations produced for a variety of different manoeuvres. The manoeuvres attempted will be the same as those

flown by the conventional single main and tail rotor helicopter in Chapter 6 - hurdlehop, popup and slalom - and also longitudinal accelerations and decelerations. It is not anticipated that the wing will make a beneficial contribution to these manoeuvres but, having been necessary for the higher speed trim solutions, is included for consistency. As with trim the initial propulsive device will be an idealised thrust vector which, by supplying the longitudinal thrust, should allow Nap-of-the-Earth manoeuvring without the large attitude excursions experienced by a traditional helicopter.

7.2.1 Hurdlehop and Popup

If Genisa is to find an exact solution for the four helicopter controls (main rotor collective, θ_0, longitudinal cyclic, θ_{1s}, lateral cyclic, θ_{1c}, and tail rotor collective, $\theta_{0t.r.}$) plus the auxiliary thrust, $X_{aux.}$, then five manoeuvre constraints must be imposed. For the hurdlehop and popup, the first four constraints are as for the helicopter - inertial accelerations; $\ddot{x}_{e.}$, $\ddot{y}_{e.}$, $\ddot{z}_{e.}$ and heading attitude rate, $\dot{\psi}$ - while the fifth constraint is one of zero pitch attitude. Thus, having trimmed the vehicle, the desired output vector is:

$$\underline{y}_{des.} = \left\{ \ddot{x}_{e.} \quad \ddot{y}_{e.} \quad \ddot{z}_{e.} \quad \dot{\psi} \quad \dot{\theta} \right\}^{\mathrm{T}};$$

where $\dot{\theta}$ is the pitch attitude rate. Genisa successfully manages solutions for the hurdlehop and popup manoeuvres first defined in Chapter 3, Section 3.2.3 ($s = 500$m, $h = 30$m, $V_{f.} = 80$kts) and Chapter 6, Section 6.1.4.2 ($s = 200$m, $h = 25$m, $V_{f.} = 80$kts) respectively. The resultant control and attitude time histories for the popup can be seen in Figure 7.13 (tail rotor collective is not displayed) where they are compared with those of the conventional helicopter. What is first evident is that Genisa has indeed found a solution where the manoeuvre can be flown with zero fuselage pitch attitude rather than the forward pitch of 13° required by the helicopter. Bank attitude is also reduced. It can be seen that the manoeuvre requires first reverse then forward auxiliary thrust in order to balance the changing pitching moments caused by the main rotor as the vehicle 'hops'. An increased collective input is required, but the cyclic inputs are reduced and all control time histories are smoother. The compound helicopter, by avoiding large negative pitch attitudes, can in fact be flown over slightly quicker popup manoeuvres than the helicopter without experiencing main rotor blade stall e.g. an 85kts popup for which the helicopter failed in Chapter 6, Section 6.1.4.2. Similar results are produced with the hurdlehop.

7.2.2 Slalom and Rapid Slalom

In Chapter 6, Section 6.1.4.3, Genisa was used to find an inverse solution for a Westland Lynx flying a slalom manoeuvre ($s = 300\text{m}$, $h = -10\text{m}$, $V_{f_e} = 60\text{kts}$). The compound configuration was flown through the same manoeuvre where the heading rate in the above popup manoeuvre was replaced by sideslip rate, $\dot{\beta}$. Figure 7.14 compares the resultant control and fuselage attitude time histories with those of the helicopter. As with the popup manoeuvre, it has proved possible to fly the slalom without changing the vehicle's pitch attitude. This is particularly useful in a slalom as pitch attitude variation is an off-axis response, and its elimination allows the compound to negotiate the manoeuvre simply by rolling in one direction, and then rolling in the other direction, while maintaining constant speed and altitude. The control plots indicate that by using the auxiliary thrust to balance variations in pitching moment rather than a combination of longitudinal and lateral cyclic reduces both the frequency and amplitude of these inputs, though again the collective inputs have increased. Also worth noting is that the compound managed to perform the Rapid Slalom ($h = 15.2\text{m}$) - described in Chapter 4, Section 4.2 - without the main rotor failure experienced by the helicopter as predicted by the individual blade model Hibrom.

7.2.3 Acceleration and Deceleration

One of the perceived advantages of a compound configured helicopter is its ability to accelerate and decelerate without having to pitch the vehicle nose down or up respectively. This is of particular value in Nap-of-the-Earth flight where, for example, a pilot may want to perform a low altitude quickhop between trees without being seen. While there is the risk with a helicopter of exposing the tail in an acceleration, and hitting the tail off the ground or reducing visibility in deceleration, with a compound such problems can be eliminated. Such a concept is also beneficial in commercial transport aircraft where the ability to change speed without pitching the aircraft would undoubtedly be appreciated by the passengers. Figure 7.15 shows the control and attitude time histories for both a Westland Lynx and its compound derivative flying a longitudinal acceleration where the aircraft is asked to accelerate from 0 to 50kts over a distance of 150m while maintaining constant altitude and heading. The compound, as with earlier manoeuvres, is additionally required to fly at zero pitch attitude. Genisa successfully finds a solution where, as desired, the compound flies at constant pitch attitude whereas the Lynx must adopt a nose down attitude of as much as 15°. In addition it can be seen

that the main rotor inputs are reduced indicating that the concept of a compound configured helicopter in accelerating flight does indeed offer the advantages perceived over the single main and tail rotor helicopter. Evident on the graphs for the Westland Lynx are the constraint oscillations described and discussed in Chapter 6, Section 6.1.4.3. A deceleration from 50 to 0kts over the same distance was also performed with similar, even more dramatic, improvement in the results (Figure 7.16).

7.2.4 Viability of Inverse Simulation Results

Though the above inverse simulation results are encouraging, what has not yet been discussed is the magnitude and hence realism of the required auxiliary thrust estimated by Genisa. In each and every manoeuvre shown or discussed here, the majority of which could be successfully negotiated by the Westland Lynx, the auxiliary thrust has exceeded the 15% weight ceiling imposed in section 7.1.2.1, suggesting that these manoeuvres could not be flown in practice by a propeller compound helicopter. Incorporating the individual blade propeller, detailed in section 7.1.3.2, reinforces this assertion as Genisa predicts propeller blade stall in all manoeuvres and the algorithm ultimately fails. Additional experiments where the position of the thrust vector and / or wing were moved offered no obvious benefits. A strategy employing zero pitch attitude with a propeller is therefore unrealistic, suggesting that an alternative must be found to either the manoeuvre constraints or the means of propulsion.

7.3 Chapter Summary

Using the example of the compound helicopter, it is clear from the results presented in this chapter that Genisa offers great flexibility and scope for simulating different rotorcraft (or indeed any vehicle) both in trim and manoeuvring. In addition it is possible to impose different combinations of constraints yielding different exact solutions, or even finding optimal solutions where the vehicle is not fully constrained and one (or more) controls are redundant. Further demonstration has been given to Genisa's ability to accommodate sophisticated modelling and a wide range of characteristic frequencies by solving for a compound helicopter with individual blade main rotor, tail rotor and propeller. Genisa thus offers tremendous potential for exploring the manoeuvring of different vehicles and experimenting with various trim and manoeuvring strategies. The individual blade modelling used here is of additional benefit as it allows the practicalities

of different rotorcraft configuration to be investigated.

Though the primary aim of this chapter was to demonstrate the flexibility of Genisa and not to undertake a feasibility study on the compound helicopter, the observations made here are worth summarising. Clearly the concept of a compound configured helicopter offers many potential advantages, given how the main rotor can be offloaded and retreating blade stall delayed by using an auxiliary lifting device (wing) and auxiliary thrust device. It has been seen, however, that for the maximum speed of a compound helicopter to be significantly greater than that of a single main and tail rotor the wing must supply a large amount of the lift. This requires strict control of the fuselage pitch attitude, requiring levels of thrust which a propeller struggles to achieve. Similarly governing of the fuselage pitch attitude is required for a compound helicopter to offer advantages during the manoeuvres investigated; a task apparently beyond the abilities of the propeller.

Chapter 8 Conclusions

This chapter summarises the achievements and observations detailed during the course of the dissertation, particularly in relation to the aims outlined in Chapter 1. To reiterate, the main motivating factors for the research aims are both as a result of the weaknesses identified in differentiation based inverse simulation methods, and of the limitations of the helicopter rotor models which are currently in use. Consequently the objectives were to develop a robust, generic inverse simulation method which is applicable to sophisticated mathematical models, and also to develop a sophisticated individual blade helicopter rotor model. In realising these objectives the intention was to produce more powerful tools for use in rotorcraft simulation. More generally, and more importantly, successful implementation of a generic inverse simulation algorithm incorporating a model of unprecedented complexity represents the next generation of inverse simulation packages. It is hoped that the breakthroughs achieved during the course of this research will aid future developments in the field of inverse simulation. The conclusions are as follows.

8.1 Research Conclusions

What follows is a summary of the research detailed in this dissertation. The statements are broken into three groups: the achievements and developments made during the course of the research; conclusions which can be drawn from the research; and suggestions for further work and for the future direction of the research.

8.1.1 Achievements and Developments

1. A generic, integration based, inverse simulation algorithm, "Genisa", has been developed which is independent of the vehicle mathematical model used or the constraints imposed on the vehicle's motion. The robustness of this algorithm has been increased by avoiding inversion of the Jacobian matrix used in the iterative solution scheme. The development of such an algorithm opens up new possibilities in inverse simulation.

2. Control time histories produced by Genisa using the helicopter disc rotor model, "HGS" have been verified by comparison with the existing differentiation based

algorithm, "Helinv". Helinv, which employs HGS, has itself been extensively verified and validated. This confirms Genisa to be a valid inverse simulation tool.

3. Genisa's flexibility has been illustrated by demonstrating that it works well for a variety of manoeuvres. By varying a number of algorithm parameters, Genisa has been proven to be robust. This lends greater confidence to the use of Genisa for a range of problems.

4. As a result of the limitations of disc models, an individual blade rotor model, "Hibrom" has been developed for use in inverse simulation. An individual blade model, or indeed a model of comparable complexity, has never previously been used in inverse simulation. Hibrom has been verified by comparison with the well established HGS disc model. For moderate manoeuvres the simplifying assumptions used in a disc model are valid and result in Hibrom and HGS predicting closely matching control time histories. For more severe manoeuvres near the edge of the flight envelope Hibrom's more sophisticated dynamic and aerodynamic modelling allows the onset of control failure to be anticipated, thus predicting the limits of a given helicopter configuration. This is of enormous advantage in high speed, severe manoeuvring flight. The successful inverse simulation of a mathematical model of Hibrom's complexity is a genuine breakthrough. In addition to extending the boundaries of rotorcraft simulation it is the first step in extending the subject of inverse simulation to include complex mathematical models applicable to a wide range of problems.

8.1.2 Conclusions from Research

5. Methods of inverse simulation which are based upon numerical differentiation suffer from numerical problems. They are also limited by being model specific and unable to incorporate dynamic models above a certain complexity or frequency. Using a state space formulation it has been shown that inverse simulation methods using numerical differentiation have to solve as many unknown as there are equations of motion in the simulation model. By contrast methods which use numerical integration only have to solve a number of unknowns equal to the number of vehicle controls. The state space demonstration of how the two methods of inverse simulation differ in approach and structure is unique and lends valuable insight into the workings of the algorithms.

6. Numerical instabilities associated with the integration method have been identified previously in the literature and are reproduced here using Genisa. The nature of the instabilities are such that, if a solution were not found, they would compromise the accuracy of results produced with higher frequency dynamic systems. Such instabilities are present if the inverse simulation algorithm solves for constrained displacements. It has been shown that the integration based inverse simulation method is in fact driven by the accelerations. Consequently solving for accelerations yields a quicker, more accurate prediction of the system response and the results are stabilised. This widens the spectrum of mathematical models to which the method can be applied, particularly models covering a wide range of dynamic frequencies, and represents an important advance in the theory of inverse simulation.

8. Using the example of the compound helicopter, it has been found that Genisa offers great flexibility and scope for simulating different rotorcraft (or indeed any vehicle) both in trim and manoeuvring. In addition it is possible to impose different combinations of constraints yielding different exact solutions, or even finding optimal solutions where the vehicle is not fully constrained and one (or more) controls are redundant. Further credibility has been given to Genisa's capacity to accommodate sophisticated modelling and a wide range of characteristic frequencies by solving for a compound helicopter with an individual blade main rotor, tail rotor and propeller. Genisa thus offers tremendous potential for exploring the manoeuvring of different vehicles and experimenting with various trim and manoeuvring strategies. The individual blade model, Hibrom is of particular benefit as it allows the practicalities of different rotorcraft configurations to be investigated. Inverse simulation of a model of such complexity is a great advance and suggests that the inverse approach could be applied to a wide range of sophisticated models.

9. It is worthwhile reiterating the observations made concerning the compound helicopter. For the wing to offload the main rotor requires strict control of the fuselage pitch attitude, requiring levels of thrust which a propeller struggles to achieve. Similarly governing of the fuselage pitch attitude is required for a compound helicopter to offer advantages during the manoeuvres investigated; a task apparently beyond the abilities of the propeller. This research suggests that propeller driven compound helicopters are not viable. Given the resurgent interest in compound helicopters, these results are of great value and suggest that much more research is required.

8.1.3 Suggestions for Future Work

10. Rotor Models. Prior to this research, the most sophisticated rotor model in inverse simulation was the disc model, HGS. Incorporation of the individual blade model Hibrom has been an enormous advance, and there has been no indication that Genisa could not be applied to more sophisticated models still. Structural dynamics could be included as is currently the case in conventional simulation. Given the rate of growth in computing power, it will hopefully not be too long before inverse simulation of rotorcraft includes the present state-of-the-art free wake models.

11. Advanced Rotorcraft Configurations. Given the tools that have been developed, it is evident that many different configurations could be explored. If a rotorcraft is to be found that will satisfy the current demand for a high performance rotorcraft derivative then much more work could be done. In short many of the ideas that have never been tested or not explored in sufficient depth could be investigated using this work as a basis. In addition the possibilities offered by non-unique (optimal solutions) have only been touched upon in this research and merit much closer attention.

12. General Inverse Simulation. Though the results presented in this dissertation have been for various rotorcraft configurations it is hoped the groundwork has been laid here which will allow the inverse simulation of many different vehicles of increasing modelling complexity.

13. Pilot Models. While the simple mathematical manoeuvre definitions used during this research have yielded valuable results, they are inflexible and do not reflect the choices open to a pilot in different situations e.g. whether or not to withdraw from a manoeuvre if control limits are approached. Further research into pilot models are therefore required for inverse simulation of sophisticated vehicle models to realise its full potential.

14. Inverse Problems. Inverse problems in their most general sense are those where a desired solution is known. The flexibility of the Genisa algorithm and complexity and dynamic range of model that it has managed to accommodate suggests an enormous number of potential applications. It is hoped that this work has extended the areas in which inverse problems can be applied, particularly by resolving technical issues which may be encountered.

8.2 Chapter Summary

In summary the research presented in this dissertation has shown the considerable advantages of integration based inverse simulation methods over differentiation based methods. A significant finding has been that inverse simulations are driven by the vehicle accelerations, and consequently defining manoeuvres in terms of accelerations rather than displacements produces stable results. An individual blade model, Hibrom, has been incorporated successfully into the inverse simulation algorithm, Genisa, and the benefits it offers compared to less sophisticated models such as disc type are made clear. The combination of Genisa and Hibrom have been used to simulate advanced rotorcraft configurations, with the interesting prediction that propeller compound helicopters require more auxiliary thrust than would appear to be practical. This final observation clearly merits further investigation.

The flexibility of the Genisa algorithm coupled with the sophisticated models which it can clearly accommodate has taken inverse simulation into a new area of applicability. Inverse simulation of an individual blade rotor model is unique within the field of rotorcraft simulation.

Appendix 1 The Euler Rigid Body Equations of Motion

To simulate the motion of a vehicle's centre of gravity, the familiar Euler rigid body equations of motion are used:

$$\begin{aligned}
\dot{U} &= -(WQ - VR) + \frac{X}{m} - g\sin\theta, \\
\dot{V} &= -(UR - WP) + \frac{Y}{m} + g\cos\theta\sin\phi, \\
\dot{W} &= -(VP - UQ) + \frac{Z}{m} + g\cos\theta\cos\phi, \\
I_{xx}\dot{P} &= (I_{yy} - I_{zz})QR + I_{xz}(\dot{R} + PQ) + L, \\
I_{yy}\dot{Q} &= (I_{zz} - I_{xx})RP + I_{xz}(R^2 - P^2) + M, \\
I_{zz}\dot{R} &= (I_{xx} - I_{yy})PQ + I_{xz}(\dot{P} - QR) + N.
\end{aligned} \tag{A1.1}$$

where U, V, W are the components of translational velocity relative to the body fixed reference frame in the directions of the unit vectors $\underline{i}^{body}$, $\underline{j}^{body}$, $\underline{k}^{body}$ respectively;

P, Q, R are rotational velocities about the body axes, positive directions consistent with a right handed axis set;

ϕ, θ, ψ are the fuselage roll, pitch and yaw attitudes;

m is the total mass of the vehicle;

I_{xx}, I_{yy}, I_{zz} are the moments of inertia of the vehicle about the body axes;

I_{xz} is the product of inertia of the vehicle;

X, Y, Z are the external forces acting through the vehicle's centre of gravity in the $\underline{i}^{body}$, $\underline{j}^{body}$, $\underline{k}^{body}$ directions respectively;

and L, M, N are the external moments acting about the centre of gravity.

The rates of change of the attitude angles ϕ, θ, and ψ are related to the body axes rotational velocities P, Q and R by the kinematic expressions:

$$\dot{\phi} = P + Q\sin\phi\tan\theta + R\cos\phi\tan\theta,$$

$$\dot{\theta} = Q\cos\phi - R\sin\phi, \tag{A1.2}$$

and $$\dot{\psi} = Q\sin\phi\sec\theta + R\cos\phi\sec\theta.$$

The earth fixed velocities $\dot{x}_{e.}$, $\dot{y}_{e.}$ and $\dot{z}_{e.}$ can be calculated from the translational body fixed velocities U, V and W and the attitude angles θ, ϕ, and ψ by the Euler transformation equations:

$$\begin{Bmatrix} \dot{x}_{e.} \\ \dot{y}_{e.} \\ \dot{z}_{e.} \end{Bmatrix} = \begin{bmatrix} l_1 & m_1 & n_1 \\ l_2 & m_2 & n_2 \\ l_3 & m_3 & n_3 \end{bmatrix} \begin{Bmatrix} U \\ V \\ W \end{Bmatrix}, \tag{A1.3}$$

where
$$l_1 = \cos\theta\cos\psi,$$
$$l_2 = \cos\theta\sin\psi,$$
$$l_3 = -\sin\theta,$$
$$m_1 = \sin\phi\sin\theta\cos\psi - \cos\phi\sin\psi,$$
$$m_2 = \sin\phi\sin\theta\sin\psi + \cos\phi\cos\psi,$$
$$m_3 = \sin\phi\cos\theta,$$
$$n_1 = \cos\phi\sin\theta\cos\psi + \sin\phi\sin\psi,$$
$$n_2 = \cos\phi\sin\theta\sin\psi - \sin\phi\cos\psi,$$
and
$$n_3 = \cos\phi\cos\theta.$$

Appendix 2a HGS: Helicopter Generic Simulation. Main and Tail Rotor Models, and Glauert Inflow

This appendix gives an overview of the disc type helicopter mathematical model, HGS, employed in the inverse simulation packages, Helinv and Genisa.

A2a.1 Overview of Model

The helicopter mathematical model used in the Helinv inverse algorithm is known as Helicopter Generic Simulation (HGS) and was formulated by Thomson (*1992*). The model adopts the commonly used Euler rigid body equations of motion, Appendix 1, equations (A1.1). The fuselage attitude rates can be related to the vehicle rotational velocities via the kinematic equations (A1.2) and the translational velocities are transformed from body to earth axes via the Euler transformation equations (A1.3).

The expressions given by these equations are not unique to helicopter mathematical models and are in fact common to many rigid body simulations. With respect to helicopters, however, a large proportion of the modelling effort is devoted to the formulation of expressions for the external forces and moments denoted by X, Y, Z, L, M and N respectively. In HGS, the total forces and moments are decomposed into their component parts for convenience, with the relevant components being the main rotor (subscript *rot.*), tail rotor ($t.r.$), fuselage (*fus.*), tail plane ($t.p.$) and fin (*fin*).

Thus the total forces and moments can be obtained from:

$$X = X_{rot.} + X_{t.r.} + X_{fus.} + X_{t.p.} + X_{fin},$$

$$Y = Y_{rot.} + Y_{t.r.} + Y_{fus.} + Y_{t.p.} + Y_{fin},$$

$$Z = Z_{rot.} + Z_{t.r.} + Z_{fus.} + Z_{t.p.} + Z_{fin},$$

$$L = L_{rot.} + L_{t.r.} + L_{fus.} + L_{t.p.} + L_{fin},$$

$$M = M_{rot.} + M_{t.r.} + M_{fus.} + M_{t.p.} + M_{fin},$$

$$N = N_{rot.} + N_{t.r.} + N_{fus.} + N_{t.p.} + N_{fin}.$$

The derivation of the expressions which define the rotor and tail rotor forces and moments will now be detailed. Those for the fuselage, fin and tail plane - which are also used by the Hibrom model - are given in Appendix 2b.

A2a.2 Rotor Model

A2a.2.1 Introduction

The majority of mathematical models of a helicopter rotor have traditionally used a common starting point to evaluate the forces and moments acting on a blade. The common origin is that as the elemental velocities and accelerations change with radial position, both the aerodynamic and inertial forces are determined by integrating the load on a incremental element along the blade span. It is additionally the case, however, that the blade velocities and accelerations vary cyclically as the blade rotates, and the loads on each element will be a function not only of radial location but also of azimuthal position. Blade forces and moments are hence periodic in nature, but this feature is not always modelled.

One approach to modelling the periodicity is to determine the blade behaviour individually. In this technique, the elemental forces and moments are integrated (often numerically) along the blade span, and the total rotor forces and moments determined instantaneously by summing the contributions from each blade. The forcing is therefore unsteady, even in vehicle trim, varying with the each blade's current azimuthal position. Hibrom is an example of such a model.

The rotor model utilised in HGS assumes a multiblade or disc representation for the calculation of rotor forces and moments. In this technique the incremental inertial and aerodynamic forces acting on a blade element are also integrated, analytically, along the blade span. HGS and other disc models differ from individual blade models, however, by assuming that only the steady components of the periodic forces and moments generated by the rotor influence the vehicle dynamics. Though this ignores the rotor periodicity, by using simple blade geometric and aerodynamic representations it does allow the elemental forces and moments to be integrated over the whole disc.

Individual blade modelling offers a higher fidelity than is possible with a disc representation since the technique readily permits the inclusion of more complex blade geometries and aerodynamic properties, and captures the periodic nature of the forces and blade dynamics. Disc modelling such as HGS, however, is not nearly so computationally intensive and, though being less valid, still gives good predictions for a wide enough range of flight states to be used in many flight dynamics applications. The HGS main rotor model is now detailed.

To enable closed loop expressions for the rotor forces and moments to be derived, HGS assumes that the main rotor blade geometry and configuration are simplified as follows:

i) the blades are assumed to be rigid with constant chord and aerofoil profile;
ii) the blades are centrally hinged;
iii) the blades have a linear variation in twist incorporated via the twist slope, θ_{twist};
iv) a root cut out extends from the blade centre of rotation to some distance, eR, along the span, R.

Likewise, HGS makes the following assumptions about the blade aerodynamic properties:

i) Mach number and unsteady aerodynamic effects are neglected;
ii) blade stall effects are not modelled;
iii) a constant lift slope curve, a_0 along the whole span is assumed so that (linear) 2D aerodynamic theory can be applied;
iv) the rotor induced velocity satisfies momentum considerations at the rotor centre, with azimuthal and radial variations superimposed.

A2a.2.2 Kinematics of a Blade Element

One fundamental difference between individual blade (Hibrom) and disc (HGS) rotor models is that the rotor exhibits periodic forcing in the former, whereas simplifying assumptions remove this feature from the latter. As these assumptions are made at the stage of calculating the forces and moments, however, given the kinematics of the helicopter centre of gravity the formulation of the velocity and acceleration of a general blade element is essentially the same. For this reason in the following analysis the reader

is referred to certain equations and diagrams in the Hibrom model, Chapter 5, though any differences will be made clear.

Before the rotor forces and moments can be calculated, the velocity and acceleration of a general blade element must be determined. A series of transformations relating the body axes translational and angular velocities to those of a blade element are required, Figure A2.1. As the blades in HGS are assumed to be centrally sprung it is worthwhile noting that the Hub and Hinge in Figure 5.1 (Hibrom) are effectively coincident i.e. $x_{hinge} = 0$. It should also be noted that the signs of certain variables differ; while Hibrom assumes that a clockwise rotation is positive in all cases, HGS adheres to traditional conventions. A good example is the shaft tilt angle, $\gamma_{sh.}$. A forward inclination of the shaft, positive in HGS, involves an anticlockwise rotation with respect to the $\underline{j}^{body}$ axis and is thus defined as negative in Hibrom. With particular emphasis given to the transformation from body to blade axes in Chapter 5, the formulation for HGS will be suitably brief. The velocity of the hub in body axes, assuming a fully rigid system, can be expressed as:

$$\underline{v}_{hub}^{body} = \underline{v}_{c.g.}^{body} + \underline{\omega}^{body} \times \underline{r}_{c.g./hub}^{body},$$

where $\underline{v}_{c.g.}^{body}$ is the translational velocity of the helicopter centre of gravity referred to body axes;

$\underline{\omega}^{body}$ is the rotational velocity of the body axis set;

and $\underline{r}_{c.g./hub}^{body}$ is the position vector from the helicopter centre of gravity to the rotor hub centre.

This is then transformed from the body to disc axes set:

$$\underline{v}_{hub}^{disc} = \left[T^{body/disc}\right]\underline{v}_{hub}^{body},$$

$$\underline{\omega}^{disc} = \left[T^{body/disc}\right]\underline{\omega}^{body},$$

where $$\left[T^{body/disc}\right] = \begin{bmatrix} \cos\gamma_{sh.} & 0 & \sin\gamma_{sh.} \\ 0 & 1 & 0 \\ -\sin\gamma_{sh.} & 0 & \cos\gamma_{sh.} \end{bmatrix},$$

and $\gamma_{sh.}$ is the shaft tilt angle. Now, the hub velocities are referred to the rotating shaft axis set. As with the shaft tilt angle, the angle of positive rotation and integer flag, n_{clock} (positive anticlockwise) are in the opposite direction to Hibrom. Thus:

$$\underline{v}_{hub}^{shaft} = \left[T^{disc/shaft}\right]\underline{v}_{hub}^{disc},$$

$$\underline{\omega}^{shaft} = \left[T^{disc/shaft}\right]\underline{\omega}^{disc} + n_{clock}\{0 \quad 0 \quad \Omega\}^{\mathrm{T}},$$

and

$$\left[T^{disc/shaft}\right] = \begin{bmatrix} -\cos\psi & \sin\psi & 0 \\ -\sin\psi & -\cos\psi & 0 \\ 0 & 0 & 1 \end{bmatrix}.$$

The next stage is to determine the velocity of the hub, and of a blade element referred to blade axes. As the blades are centrally hinged the hinge offset can be ignored. Though the flap angle, β is defined similarly positive in both cases, HGS differs from Hibrom in that it simplifies matters by using the small angle approximation ($\sin\beta \approx \beta$, $\cos\beta \approx 1$). In addition as the disc is assumed steady for any given flight state the terms in $\dot{\beta}$ are harmonic superpositions governed by the multiblade flapping equation (A2.10) in section A2a.2.4, and β is defined in the following fashion by the multiblade transformation:

$$\beta = \beta_0 + \beta_{1s}\sin\psi + \beta_{1c}\cos\psi. \tag{A2.1}$$

Thus hub in blade axes:

$$\underline{v}_{hub}^{blade} = \left[T^{shaft/blade}\right]\underline{v}_{hub}^{shaft},$$

$$\underline{\omega}^{blade} = \left[T^{shaft/blade}\right]\underline{\omega}^{shaft},$$

where

$$\left[T^{shaft/blade}\right] = \begin{bmatrix} 1 & 0 & -\beta \\ 0 & 1 & 0 \\ \beta & 0 & 1 \end{bmatrix};$$

and blade element in blade axes:

$$\begin{aligned} \underline{v}_{elem.}^{blade} &= \underline{v}_{hub}^{blade} + \underline{\omega}^{blade} \times \underline{r}_{hub/elem.}^{blade} \\ &= \left\{u_{elem.}^{blade} \quad v_{elem.}^{blade} \quad w_{elem.}^{blade}\right\}^{\mathrm{T}}; \end{aligned} \tag{A2.2}$$

where $\underline{r}^{blade}_{hub/elem.}$ is the position vector of a blade element with respect to the hub centre, referred to blade axes.

The accelerations are derived similarly. Acceleration of the hub centre in body axes in given by:

$$\underline{a}^{body}_{hub} = \underline{a}^{body}_{c.g.} + \underline{\omega}^{body} \times \left(\underline{\omega}^{body} \times \underline{r}^{body}_{c.g./hub}\right) + \underline{\alpha}^{body} \times \underline{r}^{body}_{c.g./hub},$$

where $\underline{a}^{body}_{c.g.}$ is the translational acceleration of the helicopter centre of gravity referred to body axes;

$\underline{\alpha}^{body}$ is the rotational acceleration of the body axis set;

and the others terms are as defined earlier. The accelerations are next transformed to disc axes, shaft axes, the rate of change of the rotorspeed added to the rotational acceleration, and finally transformed to blade axes so that:

$$\underline{a}^{blade}_{hub} = \left[T^{shaft/blade}\right]\left[T^{disc/shaft}\right]\left[T^{body/disc}\right]\underline{a}^{body}_{hub},$$

and $$\underline{\alpha}^{blade} = \left[T^{shaft/blade}\right]\left(\left[T^{disc/shaft}\right]\left[T^{body/disc}\right]\underline{\alpha}^{body} + \left\{0 \quad 0 \quad \dot{\Omega}\right\}^{T}\right).$$

Finally the linear acceleration of the centre of a blade element can be evaluated:

$$\underline{a}^{blade}_{elem.} = \underline{a}^{blade}_{hub} + \underline{\omega}^{blade} \times \left(\underline{\omega}^{blade} \times \underline{r}^{blade}_{hub/elem.}\right) + \underline{\alpha}^{blade} \times \underline{r}^{blade}_{hub/elem.},$$
$$= \left\{a^{blade}_{x\,elem.} \quad a^{blade}_{y\,elem.} \quad a^{blade}_{z\,elem.}\right\}^{T}. \qquad \text{(A2.3)}$$

The velocity and acceleration of a blade element now having been established it is possible to find the forces and moments due to the rotor system.

A2a.2.3 Rotor Forces and Moments

The HGS model assumes that the forces acting on a blade element can be attributed to aerodynamic and inertial components. The derivation of the rotor forces will now be outlined. It is worthwhile noting that the description of the development of the following

HGS equations is not identical to existing documentation (*Thomson, 1992*). Rather it has been rewritten to be analogous with the Hibrom model, thus making as clear as possible where the models are similar and where they diverge.

A2a.2.3.1 The Rotor Aerodynamic Forces

Taking the blade elemental velocities as given by equation (A2.2), the tangential and perpendicular velocities of the air over an element are expressed as:

$$v_{tan.} = -n_{clock} v_{elem.}^{blade},$$

and

$$v_{perp.} = w_{elem.}^{blade} - v_{ind.},$$

where, in HGS, $n_{clock} = 1$ for an anticlockwise rotating rotor, $n_{clock} = -1$ for a clockwise rotating rotor, and $\cos\beta \approx 1$ (small angle assumption). The induced velocity, $v_{ind.}$ is determined by momentum theory and expressed as:

$$v_{ind.} = v_0 + \frac{r_{elem.}}{R}\left(v_{1s}\sin\psi + v_{1c}\cos\psi\right), \qquad \text{(A2.4)}$$

where, for any given flight state, v_0 is the uniform component over the plane of the disc and v_{1s} and v_{1c} are constants determining the radial and azimuthal variation. In order to find the associated aerodynamic forces requires knowledge of the local angle of attack, α, which is the sum of the blade pitch angle, θ, and incidence with respect to the airflow, ϕ:

$$\alpha = \theta + \phi,$$

where the blade pitch, θ, is a function of the control inputs and linear twist:

$$\theta = \theta_0 + \theta_{1s}\sin\psi + \theta_{1c}\cos\psi + \theta_{twist}\frac{r_{elem.}}{R}, \qquad \text{(A2.5)}$$

and the incidence, ϕ, defines the relationship between the tangential and perpendicular velocities. Assuming small angles, ϕ, can thus be expressed as:

$$\phi = \frac{v_{perp.}}{v_{tan.}}.$$

Now knowing the angle of attack, the assumptions of constant chord and aerofoil profile, and constant lift curve slope allow calculation of the lift and drag per unit span:

$$\bar{l} = \frac{1}{2}\rho v_{aero.}^2 c a_0 \alpha, \qquad \text{(A2.6)}$$

and

$$\bar{d} = \frac{1}{2}\rho v_{aero.}^2 c \delta,$$

where

$$v_{aero.} = \sqrt{\left(v_{tan.}^2 + v_{perp.}^2\right)};$$

a_0 is the blade lift curve slope; c is the blade chord; δ is the blade profile drag coefficient; and ρ is the local air density.

Again remembering that anticlockwise is defined positive and applying the small angle assumption, the aerodynamic force vector per unit span can be referred to blade axes as:

$$\underline{\bar{f}}_{aero.}^{blade} = \begin{Bmatrix} 0 \\ n_{clock}\bar{d}\cos\phi - n_{clock}\bar{l}\sin\phi \\ -\bar{l}\cos\phi - \bar{d}\sin\phi \end{Bmatrix} \approx \begin{Bmatrix} 0 \\ \bar{d} - \bar{l}\phi \\ -\bar{l} \end{Bmatrix},$$

which, using equation (A2.6) can be expanded, and calculated for an elemental length:

$$\underline{f}_{aero.}^{blade} = \frac{1}{2}\rho c a_0 \begin{Bmatrix} 0 \\ \frac{\delta}{a_0} v_{tan.}^2 - v_{perp.} v_{tan.}\theta - v_{perp.}^2 \\ v_{tan.}^2\theta + v_{perp.} v_{tan.} \end{Bmatrix} dr_{elem.}.$$

As HGS uses non-dimensionalised terms the above equation is put into coefficient form, and integrated over the whole blade span from the root cut out, $r_{elem.} = eR$, to the blade tip, $r_{elem.} = R$. Thus:

$$\begin{Bmatrix} C^{blade}_{x\,aero.} \\ C^{blade}_{y\,aero.} \\ C^{blade}_{z\,aero.} \end{Bmatrix} = \frac{1}{2} s a_0 \begin{Bmatrix} 0 \\ \int_0^{1-e} \left(\frac{\delta}{a_0} \bar{v}^2_{tan.} - \bar{v}_{perp.} \bar{v}_{tan.} \theta - \bar{v}^2_{perp.} \right) d\bar{r}_{elem.} \\ -\int_0^{1-e} \left(\bar{v}^2_{tan.} \theta + \bar{v}_{perp.} \bar{v}_{tan.} \right) d\bar{r}_{elem.} \end{Bmatrix};$$

where $$s = \frac{n_{blades} c}{\pi R},$$

$$\bar{r}_{elem.} = \frac{r_{elem.} - eR}{R},$$

and $$\bar{v}_{tan.} = \frac{v_{tan.}}{\Omega R}.$$

The terms $\bar{v}_{tan.}$ and $\bar{v}_{perp.}$ can be expanded according to the kinematic developments in section 2a.2.2 where all translational velocities are non-dimensionalised by ΩR, rotational velocities by Ω and distances by R. Using the flap (A2.1), inflow (A2.4) and pitch (A2.5) first harmonic relationships it is clear that the fully expanded expressions will be functions of $\bar{r}_{elem.}$ and ψ. Integrating the equations with respect to $\bar{r}_{elem.}$ is straightforward enough as they are polynomial functions. The harmonic relationships raise problems, however, as they introduce powers of $\cos\psi$ and $\sin\psi$. The analytical integration is thus dealt with using the symbolic manipulation package, Mathematica (*Wolfram, 1991*). Furthermore, the powers of $\cos\psi$ and $\sin\psi$ are expressed in terms of multiple angles so that the expressions for the total aerodynamic rotor coefficients as a function of azimuthal travel can be given as:

$$\begin{Bmatrix} C^{blade}_{X\,AERO.} \\ C^{blade}_{Y\,AERO.} \\ C^{blade}_{Z\,AERO.} \end{Bmatrix} = -\frac{1}{2} s a_0 \frac{1}{n_{blades}} \times$$

$$\begin{Bmatrix} 0 \\ C^{blade}_{Y_0\,AERO.} + C^{blade}_{Y_{1s}\,AERO.} \sin\psi + C^{blade}_{Y_{1c}\,AERO.} \cos\psi + C^{blade}_{Y_{2s}\,AERO.} \sin 2\psi + \ldots \\ C^{blade}_{Z_0\,AERO.} + C^{blade}_{Z_{1s}\,AERO.} \sin\psi + C^{blade}_{Z_{1c}\,AERO.} \cos\psi + C^{blade}_{Z_{2s}\,AERO.} \sin 2\psi + \ldots \end{Bmatrix}.$$

In order to be consistent with the pitch and flap equations, only zeroth and first harmonic terms are retained. These zeroth and first harmonic rotor coefficients are not

given here as they are lengthy and complicated, and the reader is referred to the report of Thomson (*1992*).

A2a.2.3.2 The Rotor Inertial Forces

Knowing the elemental accelerations (A2.3), the inertial force vector for an element can be written as follows:

$$\underline{f}_{in.}^{blade} = \overline{m}\begin{Bmatrix} a_{x\,elem.}^{blade} \\ a_{y\,elem.}^{blade} \\ a_{z\,elem.}^{blade} \end{Bmatrix} dr_{elem.},$$

where $\overline{m}$ is the mass per unit span, uniform over the whole of the blade. Expanding the acceleration terms, the above inertial equations can be integrated over the blade span. The resultant expressions (not shown) are made clearer by considering the following relationships:

$$m_{blade} = \int_{eR}^{R} \overline{m} dr_{elem.},$$

$$M_{\beta} = \int_{eR}^{R} \overline{m} r_{elem.} dr_{elem.},$$

where m_{blade} is the total blade mass and M_{β} is the blade mass moment. The formulation is completed by expanding terms - such as flap angle - to include azimuthal position. The expanded equations are integrated using Mathematica, the forces non-dimensionalised (by $\rho\left(\left(\Omega R^2\right)\pi R^2\right)$) and, as with the aerodynamic forces, expressed up to the first harmonic in multiple angle form. The blade inertial force coefficients can thus be written as:

$$\begin{Bmatrix} C_{X\,IN.}^{blade} \\ C_{Y\,IN.}^{blade} \\ C_{Z\,IN.}^{blade} \end{Bmatrix} = \begin{Bmatrix} C_{X_0\,IN.}^{blade} + C_{X_{1s}\,IN.}^{blade} \sin\psi + C_{X_{1c}\,IN.}^{blade} \cos\psi \\ C_{Y_0\,IN.}^{blade} + C_{Y_{1s}\,IN.}^{blade} \sin\psi + C_{Y_{1c}\,IN.}^{blade} \cos\psi \\ C_{Z_0\,IN.}^{blade} + C_{Z_{1s}\,IN.}^{blade} \sin\psi + C_{Z_{1c}\,IN.}^{blade} \cos\psi \end{Bmatrix},$$

A2a.2.3.3 Total Rotor Forces

The total forces acting on the hub due to the rotor system are obtained by

subtracting the inertial from the aerodynamic forces, for example $C^{blade}_{Y\,rot.} = C^{blade}_{Y\,AERO.} - C^{blade}_{Y\,IN.}$, giving the vector of coefficients as:

$$\begin{Bmatrix} C^{blade}_{X\,rot.} \\ C^{blade}_{Y\,rot.} \\ C^{blade}_{Z\,rot.} \end{Bmatrix} = \begin{Bmatrix} C^{blade}_{X_0} + C^{blade}_{X_{1s}} \sin\psi + C^{blade}_{X_{1c}} \cos\psi \\ C^{blade}_{Y_0} + C^{blade}_{Y_{1s}} \sin\psi + C^{blade}_{Y_{1c}} \cos\psi \\ C^{blade}_{Z_0} + C^{blade}_{Z_{1s}} \sin\psi + C^{blade}_{Z_{1c}} \cos\psi \end{Bmatrix} = \underline{C}^{blade}_{rot.},$$

where $C^{blade}_{X_0} = C^{blade}_{X_0\,IN.}$, $C^{blade}_{Y_0} = \dfrac{sa_0}{2n_{blades}} C^{blade}_{Y_0\,AERO.} - C^{blade}_{Y_0\,IN.}$

When these coefficients are transformed back into disc, via shaft, axes more powers of $\cos\psi$ and $\sin\psi$ are introduced. Changing to expressions of multiple angles and again neglecting anything above first harmonic however, the result is terms of first harmonic coefficients which are no longer dependent upon azimuthal position ψ. Thus, as stated in the introduction, the aerodynamic forces produced by the main rotor are not periodic. The final stage is to transform the rotor forces from disc to body axes through the shaft tilt angle, $\gamma_{sh.}$. The contribution to the external forces of the helicopter due to the main rotor can therefore be given by:

$$\begin{Bmatrix} X_{rot.} \\ Y_{rot.} \\ Z_{rot.} \end{Bmatrix} = \rho\left(\Omega R^2\right)\pi R^2 \left[T^{body/disc}\right]^{\mathrm{T}} \left[T^{disc/shaft}\right]^{\mathrm{T}} \left[T^{shaft/blade}\right]^{\mathrm{T}} \underline{C}^{blade}_{rot.}.$$

A2a.2.3.4 Rotor Moments

Flapping has been included in the HGS model by assuming that the rotor consists of rigid blades which are hinged at the hub centre and have stiffness in flap. The restoring stiffness is modelled by a torsional spring of strength, K_β. This approach is a simplification of the hinge offset and spring model which can be used to model fully-articulated or semi-rigid rotor types. The validity of the centre spring equivalent rotor is a topic explored by Padfield (*1981*).

The total flapping moment acting on a single rotor blade is determined by summing the elemental inertial and aerodynamic moments over the span, and equating them to the restoring moment attributable to the moment at the rotor hub due to blade flap. The rotor torque is obtained by integrating the elemental torques over the rotor blade span. Thus

the moments from each blade acting on the rotor hub can be expressed as follows:

$$\int_{eR}^{R}\left(\underline{r}_{hub/elem.}^{blade}\times\left(\underline{f}_{aero.}^{blade}-\underline{f}_{in.}^{blade}\right)\right)dr_{elem.}=\begin{Bmatrix}0\\K_\beta\beta\\C_Q^{blade}\rho\left(\Omega R^2\right)\pi R^3\end{Bmatrix}. \qquad \text{(A2.7)}$$

The moment term in $\underline{j}^{blade}$ is most easily dealt with by considering that equilibrium is governed by the blade flapping equation and simply setting it to $K_\beta\beta$. The $\underline{k}^{blade}$ term is more complicated as it requires that C_Q^{blade} is known. Integration of the $\underline{k}^{blade}$ term in the left side of equation (A2.7) is undertaken in a manner similar to the integration of the rotor force expressions, that is the aerodynamic and inertial contributions are evaluated separately. Mathematica was again used to perform the algebraic manipulations to retain the harmonic torque coefficients during the integration. The resultant rotor torque coefficients of a single blade due to aerodynamic and inertial moments can be written as:

$$C_{Q\,AERO.}^{blade}=C_{Q_0\,AERO.}^{blade}+C_{Q_{1s}\,AERO.}^{blade}\sin\psi+C_{Q_{1c}\,AERO.}^{blade}\cos\psi,$$

$$C_{Q\,IN.}^{blade}=C_{Q_0\,IN.}^{blade}+C_{Q_{1s}\,IN.}^{blade}\sin\psi+C_{Q_{1c}\,IN.}^{blade}\cos\psi,$$

and the total rotor blade torque coefficients can be obtained from:

$$C_{Q\,rot.}^{blade}=C_{Q_0.}^{blade}+C_{Q_{1s}.}^{blade}\sin\psi+C_{Q_{1c}.}^{blade}\cos\psi,$$

where $$C_{Q_0}^{blade}=\frac{sa_0}{2n_{blades}}C_{Q_0\,AERO.}^{blade}-C_{Q_0\,IN.}^{blade},\ \text{etc.}$$

As with the forces, the total rotor moments, $\underline{M}_{rot.}^{blade}=\left\{L_{rot.}^{blade}\quad M_{rot.}^{blade}\quad N_{rot.}^{blade}\right\}^{\mathrm{T}}$ must be transformed from blade to body axes for use in the vehicle equations of motion. Thus:

$$\begin{Bmatrix}L_{rot.}\\M_{rot.}\\N_{rot.}\end{Bmatrix}=\left[T^{body/disc}\right]^{\mathrm{T}}\left[T^{disc/shaft}\right]^{\mathrm{T}}\left[T^{shaft/blade}\right]^{\mathrm{T}}\underline{M}_{rot.}^{blade}+\underline{r}_{c.g./hub}^{body}\times\begin{Bmatrix}X_{rot.}\\Y_{rot.}\\Z_{rot.}\end{Bmatrix}.$$

A2a.2.4 Blade Flapping Equation and the Multiblade Transformation

The flapping motion of blade i can be determined from the $\underline{j}^{blade}$ component of

equation (A2.7):

$$\int_{eR}^{R}\left(f_{z\,aero.}^{blade}-\overline{m}a_{z\,elem.}^{blade}\right)r_{elem.}dr_{elem.}=K_{\beta}\beta_i, \tag{A2.8}$$

which when fully expanded, yields an equation of the following form:

$$\ddot{\beta}_i+a\dot{\beta}_i+b\beta_i=f.$$

This is subsequently non-dimensionalised by Ω^2:

$$\beta_i''+c\beta_i'+d\beta_i=h, \tag{A2.9}$$

where $$\beta_i''=\frac{d^2\beta_i}{d\psi^2},$$

and $$\beta_i'=\frac{d\beta_i}{d\psi}.$$

When fully expanded equation (A2.9) can be used to describe flapping motion of an individual blade, however, the flapping model implemented in HGS requires that the flapping motion be described in multiblade coordinates.

In HGS, equation (A2.9) is solved by applying the multiblade transformation which effectively transforms the individual blade angles, β_i $\left(i=1,\ n_{blades}\right)$, into the multiblade co-ordinates given as the coning angle, β_0, the longitudinal and lateral flapping angle, β_{1c} and β_{1s}, and the differential coning angle, β_d. By applying the multiblade transformation for a four blade rotor, the individual blade angles, $\underline{\beta}_I=\left\{\beta_1 \quad \beta_2 \quad \beta_3 \quad \beta_4\right\}^{\mathrm{T}}$, can be determined as follows:

$$\underline{\beta}_I=\left[\boldsymbol{L}_{\beta}\right]\underline{\beta}_M;$$

where:

$$\left[\boldsymbol{L}_{\beta}\right]=\begin{bmatrix}1 & -1 & \cos\psi & \sin\psi\\ 1 & 1 & \sin\psi & -\cos\psi\\ 1 & -1 & -\cos\psi & -\sin\psi\\ 1 & 1 & \sin\psi & \cos\psi\end{bmatrix},$$

and $$\underline{\beta}_M = \{\beta_0 \quad \beta_d \quad \beta_{1s} \quad \beta_{1c}\}^T.$$

Incorporating the multiblade transformation into the flapping equation and expressing the resulting periodic equation in non periodic form, allows the flapping equation to be written as:

$$\underline{\beta''}_M + \left[\boldsymbol{C}_{M_0}\right]\underline{\beta'}_M + \left[\boldsymbol{D}_{M_0}\right]\underline{\beta}_M = \underline{\boldsymbol{h}}_{M_0}. \tag{A2.10}$$

The expressions found in $\left[\boldsymbol{C}_{M_0}\right]$, $\left[\boldsymbol{D}_{M_0}\right]$ and $\underline{\boldsymbol{h}}_{M_0}$ are lengthy in nature and the reader is referred to Thomson (*1992*) for a complete formulation. Equation (A2.10) can be solved for the multiblade angles, however the solution is usually simplified by assuming quasi-steady blade flapping. This assumption implies that the blade flapping dynamics are decoupled from the fuselage dynamics and therefore have little effect on the forces and moments applied by the rotor to the fuselage. The quasi-steady blade flapping motion becomes:

$$\underline{\beta}_M = \left[\boldsymbol{D}_{M_0}\right]^{-1}\underline{\boldsymbol{h}}_{M_0},$$

which can be readily solved for the vector $\underline{\beta}_M$ due to its algebraic nature.

A2a.3 ***Tail Rotor Model***

The modelling of the tail rotor is essentially the same as the HGS main rotor disc model, the exception being the assumption that the blades remain in the tail rotor disc plane i.e. no flapping occurs. The rotor blades are assumed to have constant chord, root cut out and linearly varying blade twist. The rotor inflow representation is of the same form, though the inertial forces and moments of the rotor are assumed small and therefore ignored. For the tail rotor axes systems the reader is referred to Hibrom's individual blade tail rotor model, Chapter 7, Section 7.1.3.1.

A2a.4 ***Glauert Inflow Model***

The rotor inflow model used in HGS employs the established method of representing the induced rotor inflow as the sum of a uniform and first order inflow

harmonics with radial variation. The resulting model has the form presented in equation (A2.4):

$$v_{ind.} = v_0 + \frac{r_{elem.}}{R}\left(v_{1s}\sin\psi + v_{1c}\cos\psi\right), \qquad \text{(A2.11)}$$

where $v_{ind.}$ is the induced velocity at the rotor, v_0 is the uniform inflow component, and v_{1s} and v_{1c} are the harmonic components of rotor inflow. The terms $r_{elem.}$ and R denote the radial position from the centre of the rotor and the blade span respectively. The rotor azimuthal position is given by, ψ. Glauert appreciated that the rotor would behave very much like an equivalent finite wing of span equal to the rotor diameter, giving an upwash at the leading edge of the rotor and an increase in induced velocity at the trailing edge and consequently the term v_{1c} was included to model this effect (*Bramwell, 1976*). Equation (A2.11) can be non-dimensionalised by division by (ΩR) to give:

$$\lambda_{ind.} = \lambda_0 + \frac{r_{elem.}}{R}\left(\lambda_{1s}\sin\psi + \lambda_{1c}\cos\psi\right),$$

where: $\lambda_0 = \frac{v_0}{\Omega R}$, $\lambda_{1s} = \frac{v_{1s}}{\Omega R}$, $\lambda_{1c} = \frac{v_{1c}}{\Omega R}$.

The non-dimensionalised uniform inflow component, λ_0, can be determined from momentum considerations and can be calculated from:

$$\lambda_0 = \frac{C_T}{2\sqrt{\mu^2 + (\mu_z - \lambda_0)^2}};$$

where C_T is the rotor thrust coefficient; μ is the in-plane velocity vector of the rotor hub; and μ_z is the velocity of the rotor hub perpendicular to the rotor hub plane.

The evaluation of the longitudinal inflow component λ_{1c} is aided by the inclusion of an additional rotor wind axes set. This axes set is aligned so that its $\underline{i}^{wind}$ axis is collinear with the resultant in-plane velocity of vector of the rotor hub. The orientation of this axes set is obtained by a rotation about the $\underline{k}^{disc}$ through the rotor sideslip angle, ψ_{wind}. Therefore, the harmonic induced flow components can be obtained from:

$$\begin{Bmatrix} \lambda_{1c} \\ \lambda_{1s} \end{Bmatrix} = \begin{bmatrix} \cos\psi_{wind} & -\sin\psi_{wind} \\ \sin\psi_{wind} & \cos\psi_{wind} \end{bmatrix} \begin{Bmatrix} \lambda_{1c}^{wind} \\ \lambda_{1s}^{wind} \end{Bmatrix},$$

where:

$$\psi_{wind} = \tan^{-1}\left\{\frac{\mu_y}{\mu_x}\right\},$$

and μ_y and μ_x are the non-dimensionalised components of rotor hub velocity. A theoretical value of the longitudinal induced velocity, λ_{1c}^{wind}, is stated by Bramwell (*1976*). It was obtained by considering that when the rotor moves forward through the air, it leaves behind a vortex wake in the form of an elliptical cylinder generated by a series of vortex rings parallel to rotor disc. From this analysis the slope of the ratio $\lambda_{ind.} / \lambda_0$ at the rotor centre was found to be $\tan(\chi/2)$, where χ is the wake angle. Thus the longitudinal inflow components in the wind axes can be obtained from:

$$\lambda_{1c}^{wind} = \lambda_0 \tan\left\{\frac{\chi}{2}\right\} \quad \text{if} \quad \chi < \frac{\pi}{2},$$

$$\lambda_{1c}^{wind} = \lambda_0 \cot\left\{\frac{\chi}{2}\right\} \quad \text{if} \quad \chi > \frac{\pi}{2}.$$

By making the transformation from hub to wind axes, the lateral component of induced velocity is zero:

$$\lambda_{1s}^{wind} = 0.$$

A description of the use of the uniform and harmonic inflow components in the HGS model is outlined section 2a.2.3 of this Appendix.

Appendix 2b HGS: Helicopter Generic Simulation. Fuselage, Fin and Tail Plane Models

The models used to calculate the forces and moments from the fuselage, tail plane and fin are common to the disc model, HGS and the individual blade model, Hibrom. Although the models were developed for use in HGS, the sign convention used here is consistent with the Hibrom axis sets detailed in Chapter 5. Whereas, for example, the fin is defined positive aft and above the fuselage reference point in HGS (*Thomson, 1992*), both directions are in the negative sense when used in Hibrom and the signs differ accordingly. Figure A2.2 shows the positions of the fuselage, tail plane and fin of a Westland Lynx relative to its centre of gravity.

A2b.1 The Fuselage Forces and Moments

Derived from wind tunnel tests, the fuselage force and moment coefficients are denoted by $C_{X\,fus.}$, $C_{Y\,fus.}$, $C_{Z\,fus.}$, $C_{l.fus.}$, $C_{M\,fus.}$ and $C_{N\,fus.}$. These coefficients were determined as functions of the fuselage angle of incidence, $\alpha_{fus.}$, and side slip, $\beta_{fus.}$. The fuselage angle of incidence and side slip can be given by:

$$\alpha_{fus.} = \tan^{-1}\left\{\frac{w_{fus.}}{u_{fus.}}\right\},$$

$$\beta_{fus.} = \sin^{-1}\left\{\frac{v_{fus.}}{V_{f.fus.}}\right\},$$

where the total fuselage velocity and its components are given by:

$$V_{f.fus.} = \sqrt{u_{fus.}^2 + v_{fus.}^2 + w_{fus.}^2};$$

with

$$u_{fus.} = U + Qz_{ref.},$$

$$v_{fus.} = V + Rx_{ref.} - Pz_{ref.},$$

and

$$w_{fus.} = W - Qx_{ref.}.$$

The force and moment coefficient information was included in the mathematical model of the helicopter via a series of look-up tables for convenience. As the forces and moments were measured from a reference point directly below the rotor hub, a distance $x_{ref.}\underline{i}^{body}$ and $z_{ref.}\underline{j}^{body}$ from the centre of gravity, the force and moments can be given by,

$$X_{fus.} = \rho(\Omega R^2)\pi R^2 C_{X\,fus.},$$

$$Y_{fus.} = \rho(\Omega R^2)\pi R^2 C_{Y\,fus.},$$

$$Z_{fus.} = \rho(\Omega R^2)\pi R^2 C_{Z\,fus.},$$

$$L_{fus.} = -z_{ref.} Y_{fus.},$$

$$M_{fus.} = \rho(\Omega R^2)\pi R^3 C_{M\,fus.} + x_{ref.} Z_{fus.},$$

$$N_{fus.} = \rho(\Omega R^2)\pi R^3 C_{N\,fus.} - x_{ref.} Y_{fus.};$$

or using notation consistent with Appendix 2a:

$$\begin{Bmatrix} X_{fus.} \\ Y_{fus.} \\ Z_{fus.} \end{Bmatrix} = \rho(\Omega R)^2 \pi R^2 \begin{Bmatrix} C_{X\,fus.} \\ C_{Y\,fus.} \\ C_{Z\,fus.} \end{Bmatrix},$$

and:

$$\begin{Bmatrix} L_{fus.} \\ M_{fus.} \\ N_{fus.} \end{Bmatrix} = \rho(\Omega R)^2 \pi R^3 \begin{Bmatrix} 0 \\ C_{M\,fus.} \\ C_{M\,fus.} \end{Bmatrix} + \underline{r}^{body}_{c.g./fus.} \times \begin{Bmatrix} X_{fus.} \\ Y_{fus.} \\ Z_{fus.} \end{Bmatrix};$$

where:

$$\underline{r}^{body}_{c.g./fus.} = \begin{Bmatrix} x_{ref.} & 0 & z_{ref.} \end{Bmatrix}^T.$$

A2b.2 ***Fin and Tail Plane Forces and Moments***

The fin and tail plane force coefficients, $C_{Y\,fin}$ and $C_{Y\,t.p.}$, are also obtained from look-up tables which are functions of the fin side slip angle, β_{fin}, and tail plane angle of incidence, $\alpha_{t.p.}$. The fin local angle of side slip can be calculated from:

$$\beta_{fin} = \beta_{fin_0} + \beta_{fin_{local}},$$

where β_{fin_0} denotes the fixed angle of incidence of the fin relative to the fuselage centreline. The incidence due to the relative airflow passing over the airfoil, $\beta_{fin_{local}}$, can be evaluated from:

$$\beta_{fin_{local}} = \sin^{-1}\left\{\frac{v_{fin}}{V_{f.fin}}\right\};$$

where $$v_{fin} = V - P\left(z_{ref.} + h_{fin}\right) + R\left(x_{ref.} + l_{fin}\right),$$ and

$$V_{f.fin} = \sqrt{\left(U + Q\left(z_{ref.} + h_{fin}\right)\right)^2 + \left(V - P\left(z_{ref.} + h_{fin}\right) + R\left(x_{ref.} + l_{fin}\right)\right)^2 + \left(W - Q\left(x_{ref.} + l_{fin}\right)\right)^2}.$$

The tail plane angle of incidence is given by:

$$\alpha_{t.p.} = \alpha_{t.p._0} + \alpha_{t.p._{local}},$$

where $\alpha_{t.p._0}$ denotes the fixed angle of incidence of the tail plane and $\alpha_{t.p._{local}}$ represent the angle of attack of the tail plane due to the relative airflow and can be calculated from:

$$\alpha_{t.p._{local}} = \tan^{-1}\left\{\frac{w_{t.p.}}{u_{t.p.}}\right\};$$

where $$u_{t.p.} = U + Q\left(z_{ref.} + h_{t.p.}\right),$$

and $$w_{t.p.} = W - Q\left(x_{ref.} + l_{t.p.}\right).$$

Hence, the contribution of the fin of area S_{fin}, and tail plane of surface area $S_{t.p.}$, to the external forces and moments can be obtained from:

$$X_{fin} = 0, \qquad X_{t.p.} = 0,$$

$$Y_{fin} = \rho(\Omega R)^2 S_{fin} C_{Y\,fin}, \qquad Y_{t.p.} = 0,$$

$$Z_{fin} = 0, \qquad Z_{t.p.} = \rho(\Omega R)^2 S_{t.p.} C_{Zt.p.},$$

$$L_{fin} = -Y_{fin}\left(h_{fin} + z_{ref.}\right), \qquad L_{t.p.} = 0,$$

$$M_{fin} = 0, \qquad M_{t.p.} = -Z_{t.p.}\left(x_{ref.} + l_{t.p.}\right),$$

$$N_{fin} = Y_{fin}\left(l_{fin} + x_{ref.}\right), \qquad N_{t.p.} = 0.$$

where l_{fin} is the distance along the $\underline{i}^{body}$ axis from the fuselage datum point to the centre of pressure of the fin;

h_{fin} is the distance along the $\underline{j}^{body}$ axis from the fuselage reference point to the fin centre of pressure;

$l_{t.p.}$ is the distance along the $\underline{i}^{body}$ axis from the fuselage datum point to the centre of pressure of the tail plane;

and $h_{t.p.}$ is the distance along the $\underline{j}^{body}$ axis from the fuselage reference point to the tail plane centre of pressure.

Again the following alternative notation can be used:

$$\begin{Bmatrix} X_{fin} \\ Y_{fin} \\ Z_{fin} \end{Bmatrix} = \rho(\Omega R)^2 S_{fin} \begin{Bmatrix} 0 \\ C_{Yfin} \\ 0 \end{Bmatrix},$$

$$\begin{Bmatrix} L_{fin} \\ M_{fin} \\ N_{fin} \end{Bmatrix} = \underline{r}^{body}_{c.g./fin} \times \begin{Bmatrix} 0 \\ Y_{fin} \\ 0 \end{Bmatrix};$$

and:

$$\begin{Bmatrix} X_{t.p.} \\ Y_{t.p.} \\ Z_{t.p.} \end{Bmatrix} = \rho(\Omega R)^2 S_{t.p.} \begin{Bmatrix} 0 \\ 0 \\ C_{Zt.p.} \end{Bmatrix},$$

$$\begin{Bmatrix} L_{t.p.} \\ M_{t.p.} \\ N_{t.p.} \end{Bmatrix} = \underline{r}^{body}_{c.g./t.p.} \times \begin{Bmatrix} 0 \\ 0 \\ Z_{t.p.} \end{Bmatrix};$$

where:

$$\underline{\mathbf{r}}^{body}_{c.g./fin} = \left\{ l_{fin} \quad 0 \quad h_{fin} \right\}^{\mathrm{T}},$$

$$\underline{\mathbf{r}}^{body}_{c.g./t.p.} = \left\{ l_{t.p.} \quad 0 \quad h_{t.p.} \right\}^{\mathrm{T}}.$$

Appendix 3 Helinv: Numerical Differentiation Based Inverse Simulation Method

A3.1 Introduction

A statement of the general inverse problem is given in Chapter 2, Section 2.1. As discussed in Chapters 1 and 2, the methods of inverse simulation can be divided into two groups: those which use numerical differentiation and those which use numerical integration. In the former, the process of numerical differentiation enables the equations of motion to be expressed in algebraic form, allowing a closed loop solution to be found. As has been established in Chapter 2, Section 2.2 the problem involves n_x equations of motion in n_x unknowns and a solution is found iteratively by the method of Newton-Raphson (*Cheney and Kincaid, 1985*). As numerical differentiation introduces a new unknown variable with every additional equation of motion each such inverse simulation algorithm is particular to the model being used.

The Helinv algorithm is a differentiation based method specific to the HGS model (Appendix 2) which, neglecting rotorspeed and blade flapping dynamics, has six equations of motion (A1.1). This Appendix aims to present a lucid discussion of the solution procedure.

A3.2 Inputs to Helinv

A3.2.1 Flight Path

As with Genisa, Helinv incorporates several sets of pre-programmed manoeuvre descriptions which are required as system outputs from a conventional simulation and are essentially the inputs for inverse simulation. Helinv's output vector contains the three earth fixed coordinates. The output vector is then:

$$\underline{y} = \{x_e \quad y_e \quad z_e\}^T.$$

If we consider the case of a manoeuvre taking a time $t_{man.}$, which is divided into a time series of $n_{pts.}$ intervals then a general time point in the solution, t_k, may be defined

as:

$$0 < t_k < t_{man.} \text{ where } 1 < k \leq \left(n_{pts.} + 1\right).$$

The input at this time point is:

$$x_{e.}(t_k),\ y_{e.}(t_k),\ z_{e.}(t_k);$$

which may be differentiated to give:

$$\dot{x}_{e.}(t_k),\ \dot{y}_{e.}(t_k),\ \dot{z}_{e.}(t_k) \text{ and } \ddot{x}_{e.}(t_k),\ \ddot{y}_{e.}(t_k),\ \ddot{z}_{e.}(t_k).$$

The manoeuvre is usually defined by a polynomial and hence algebraic differentiation is a simple process.

A3.2.2 Additional Constraint

Neglecting the rotorspeed equation, the inverse solution algorithm can be described as the solution of the six rigid body equations of motion for seven unknowns (or control vector, $\underline{u}$) (θ_0, θ_{1s}, θ_{1c}, $\theta_{0t.r.}$) and (ϕ, θ, ψ). If a unique solution is to be found then clearly an additional constraint must be specified. This can be achieved by either specifying a heading or side slip constraint.

A3.2.2.1 Heading Constraint

If a heading constraint is applied, then the heading angle is specified directly as a function of time, $\psi(t_k)$, from which the yaw rate and acceleration can be easily determined by differentiating the function. Thus Helinv's output vector becomes:

$$\underline{y} = \left\{x_{e.} \quad y_{e.} \quad z_{e.} \quad \psi\right\}^{\mathrm{T}}.$$

A3.2.2.2 Side Slip Constraint

When it is more convenient to constrain side slip, e.g. in turning flight where heading is constantly changing, the side slip angle is expressed as $\beta(t_k)$. The side slip velocity and acceleration can then be determined from:

$$V = V_{f_e} \sin\beta(t_k),$$

$$\dot{V} = \dot{V}_{f_e} \sin\beta(t_k) + \dot{\beta}(t_k) V_{f_e} \cos\beta(t_k) \ ,$$

where V_{f_e} denotes the flight path velocity and $\dot{\beta}(t_k)$ the rate of change of side slip angle. It is also possible to determine the side slip velocity from the transformation of the earth based velocity components ($\dot{x}_{e_e}$, $\dot{y}_{e_e}$, $\dot{z}_{e_e}$) to the aircraft body axes:

$$V = m_1 \dot{x}_{e_e} + m_2 \dot{y}_{e_e} + m_3 \dot{z}_{e_e}, \tag{A3.1}$$

where m_1, m_2 and m_3 are given by equation (A1.3). Equation (A3.1) can then be rearranged to give:

$$a\cos\psi + b\sin\psi + c = 0, \tag{A3.2}$$

where

$$a = \dot{x}_{e_e} \sin\phi \sin\theta + \dot{y}_{e_e} \cos\phi,$$
$$b = -\dot{x}_{e_e} \cos\phi + \dot{y}_{e_e} \sin\phi \sin\theta,$$
$$c = \dot{z}_{e_e} \sin\phi \cos\theta - V.$$

If values of ϕ and θ are available, then equation (A3.2) can be solved numerically for ψ using a Newton-Raphson method.

A3.3 ***Helinv Solution Procedure***

As already established the problem involves the six equations of motion (Appendix 1, equation (A1.1)) and for which the Helinv inverse algorithm solves the six unknowns, $\underline{u} = \{\phi \quad \theta \quad \theta_0 \quad \theta_{1s} \quad \theta_{1c} \quad \theta_{0t.r.}\}$ (though the problem is actually seven equations in seven unknowns if rotorspeed, Ω is considered). The six equations of motions are first rearranged to give:

$$e_1(\phi, \theta, \Omega, \theta_0, \theta_{1s}, \theta_{1c}, \theta_{0t.r.}) = -m(\dot{U} + WQ - VR) + X - mg\sin\theta = 0$$
$$\vdots$$
$$e_6(\phi, \theta, \Omega, \theta_0, \theta_{1s}, \theta_{1c}, \theta_{0t.r.}) = -\dot{R}I_{zz} + (I_{xx} - I_{yy})PQ + I_{xz}(\dot{P} - QR) + N = 0.$$

The inverse algorithm solves these equations of motion by providing an initial guess of the vector of unknowns, $\underline{u}$. The basis of the algorithm is the calculation of the rates of the unknown attitudes $\dot{\phi}$ and $\dot{\theta}$ by numerical differentiation. This allows the unsteady terms in the equations of motion to be calculated thereby converting the helicopter equations of motion to a set of nonlinear algebraic expressions. The Newton-Raphson scheme can then be used to provide a better estimate of the unknown vector, $\underline{u}$. As the output vector, $\underline{y}$, expresses the flight path in the form of a time history, the inverse algorithm is cast in a 'time marching' form and solves the vehicle equations of motion at each point in the trajectory.

The complex nature of the expressions that form the body velocities, vehicle forces and moments etc., means that the calculation sequence of the inverse algorithm must be undertaken in a specific order. This solution procedure can be summarised as follows:

i) the three earth fixed velocities ($\dot{x}_e$, $\dot{y}_e$, $\dot{z}_e$) and heading attitude, ψ are known from the manoeuvre definition;

ii) estimates are made of the unknown roll, ϕ and pitch, θ attitudes;

ii) the Euler transformations allow determination of the body referenced velocities (U , V , W) and by differentiation the accelerations ($\dot{U}$, $\dot{V}$, $\dot{W}$);

iii) differentiation of the attitudes gives the angular velocities (P, Q, R) and accelerations ($\dot{P}$, $\dot{Q}$, $\dot{R}$);

iv) knowledge of the body velocities will allow the aerodynamic forces and moments on the fuselage to be obtained, whilst the estimated control angles (and all the other state information) ensures that the rotor forces may be found, hence the external forces and moments (X, Y, Z, L, M and N) are available;

v) all the necessary information is now in place to evaluate $\underline{e}$ and obtain - using the Newton-Raphson iteration - new estimates of $\underline{u}$.

The following sections aim to highlight the above sequence whilst providing a detailed discussion of the inverse algorithm itself.

A3.3.1 Evaluation of Euler Angles and Rates

An initial guess at the roll and pitch Euler attitude angles are made at the start of each iteration, m, of the Newton-Raphson method. Considering the pitch attitude at time point t_k, $\theta(t_k)$, the initial estimate is given by:

$$\theta(t_k)_m = \begin{cases} \theta(0) & \text{for } m = 1,\ k = 1 \\ \theta(t_{k-1}) & \text{for } m = 1 \\ \theta(t_k)_{m-1} & \text{for } m > 1 \end{cases}.$$

Thus for the first iteration at each time point, k, in the trajectory, it is evident that the value from the previous point, $k-1$, is used as an initial estimate. Furthermore, for the first iteration at time $t = 0$, the estimate of pitch attitude assumes a predetermined trim value, $\theta(0)$, available at the start of the simulation. The roll attitude, ϕ, is treated in a similar manner.

Using numerical differentiation it is possible to evaluate the first, $\dot{\theta}(t_k)_m$ and second, $\ddot{\theta}(t_k)_m$ derivatives, with respect to time, of the pitch attitude angle:

$$\dot{\theta}(t_k)_m = \frac{\theta(t_k)_m - \theta(t_{k-1})}{t_k - t_{k-1}},$$

$$\ddot{\theta}(t_k)_m = \frac{\dot{\theta}(t_k)_m - 2\dot{\theta}(t_{k-1}) - \dot{\theta}(t_{k-2})}{(t_k - t_{k-1})^2}.$$

The roll attitude is evaluated similarly.

A3.3.2 Evaluation of Body Referenced Translational Velocities and Accelerations

The vehicle body axes translational velocities are evaluated by a series of transformations of the earth fixed velocities ($\dot{x}_e$, $\dot{y}_e$, $\dot{z}_e$) via the Euler attitude angles (ϕ, θ, ψ). This transformation is the transpose of that implied by equation (A1.3) where the output, $\underline{y}$, is related to the system state, $\underline{x}$, and attitude vector, $\underline{\xi}$, through the function $\underline{\boldsymbol{h}}$ (equation (2.3)). Therefore the vehicle translational velocities for the m^{th} iteration of time point k can then be found from:

$$\begin{Bmatrix} U \\ V \\ W \end{Bmatrix}_{(t_k)_m} = \begin{bmatrix} l_1 & l_2 & l_3 \\ m_1 & m_2 & m_3 \\ n_1 & n_2 & n_3 \end{bmatrix} \begin{Bmatrix} \dot{x}_e \\ \dot{y}_e \\ \dot{z}_e \end{Bmatrix}_{(t_k)} , \qquad \text{(A3.3)}$$

where (l_1, l_2, ... , n_3) are the direction cosines given in Appendix 1.

The rotorcraft body axes accelerations can be found by differentiating equation (A3.3) to give:

$$\begin{Bmatrix} \dot{U} \\ \dot{V} \\ \dot{W} \end{Bmatrix}_{(t_k)_m} = \begin{bmatrix} l_1 & l_2 & l_3 \\ m_1 & m_2 & m_3 \\ n_1 & n_2 & n_3 \end{bmatrix} \begin{Bmatrix} \ddot{x}_{e.} \\ \ddot{y}_{e.} \\ \ddot{z}_{e.} \end{Bmatrix}_{(t_k)} + \begin{bmatrix} \dot{l}_1 & \dot{l}_2 & \dot{l}_3 \\ \dot{m}_1 & \dot{m}_2 & \dot{m}_3 \\ \dot{n}_1 & \dot{n}_2 & \dot{n}_3 \end{bmatrix} \begin{Bmatrix} \dot{x}_{e.} \\ \dot{y}_{e.} \\ \dot{z}_{e.} \end{Bmatrix}_{(t_k)},$$

where ($\dot{l}_1$, $\dot{l}_2$, ... , $\dot{n}_3$) are the derivatives with respect to time of the direction cosines and:

$$\dot{l}_1 = -\dot{\theta}(t_k)_m \sin\theta(t_k)_m \cos\psi(t_k) - \dot{\psi}(t_k)\cos\theta(t_k)_m \sin\psi(t_k) \quad \text{etc.}$$

A3.3.3 Evaluation of Body Referenced Rotational Velocities and Accelerations

The vehicle rotational velocities for the k^{th} time point and m^{th} iteration of the Newton-Raphson scheme can be determined by rearranging the Euler angle rates (equation A1.2) so that, for example, the roll rate, P may be found from:

$$P(t_k)_m = \dot{\phi}(t_k)_m - \dot{\psi}(t_k)\sin\theta(t_k)_m,$$

which can be differentiated to give:

$$\dot{P}(t_k)_m = \ddot{\phi}(t_k)_m - \ddot{\psi}(t_k)\sin\theta(t_k)_m - \dot{\psi}(t_k)\dot{\theta}(t_k)_m \cos\theta(t_k)_m.$$

Expressions for $Q(t_k)_m$, $\dot{Q}(t_k)_m$, $R(t_k)_m$ and $\dot{R}(t_k)_m$ may be found in a similar fashion.

A3.3.4 Determination of Forces and Moments

With estimates of all the states now available it is possible to evaluate the external forces and moments as detailed in Appendix 2. Once the net contribution of individual forces and moments generated by the constituent parts of the helicopter is determined, all the information is present with which the error vector, $\underline{e}$, can be calculated.

A3.3.5 Update of Current Estimate of Controls, Attitude Angles

The Newton-Raphson scheme employed in this inverse algorithm has the structure:

$$\begin{bmatrix} \theta \\ \vdots \\ \vdots \\ \theta_{0t.r.} \end{bmatrix}_{(t_k)_{m+1}} = \begin{bmatrix} \theta \\ \vdots \\ \vdots \\ \theta_{0t.r.} \end{bmatrix}_{(t_k)_m} - \begin{bmatrix} \left(\frac{\partial e_1}{\partial \theta}\right) & \cdots & \cdots & \left(\frac{\partial e_1}{\partial \theta_{0t.r.}}\right) \\ \vdots & & & \vdots \\ \vdots & & & \vdots \\ \left(\frac{\partial e_6}{\partial \theta}\right) & \cdots & \cdots & \left(\frac{\partial e_6}{\partial \theta_{0t.r.}}\right) \end{bmatrix}^{-1}_{(t_k)_m} \begin{bmatrix} e_1 \\ \vdots \\ \vdots \\ e_6 \end{bmatrix}_{(t_k)_m} . \qquad \ldots(A3.4)$$

In a fashion similar to Genisa this allows new estimates of the unknown variables to be made. The Helinv algorithm iterates until the error functions are within the prescribed tolerance.

Appendix 4 Mathematical Definition of Manoeuvres

When considering the mathematical definition of a manoeuvre two main requirements must be adhered to; that it is able to accurately compute the vehicle displacements and velocities throughout the manoeuvre, and that it displays a physically realisable degree of continuity. For the first, bearing in mind that an inverse simulation calculates a time history of control inputs which will accurately reproduce a desired, predefined manoeuvre, then the displacements, velocities and accelerations must be expressed as functions of time. Secondly if the resultant profile is insufficiently smooth, then rapid changes or discontinuities in the time derivatives of the profile may lead to numerical problems in the inverse algorithm. For simplicity, polynomial representations have been adopted. As both their order and constants are determined by boundary conditions, the combination of prescribed displacements, velocities and accelerations must be considered carefully. For the example of an aircraft undergoing rectilinear acceleration, a choice of initial and final displacements would be less representative than velocities. Additionally the aircraft may require to be in trim at the initial and final points and thus zero acceleration (or even jerk) must be stipulated, otherwise discontinuities would result at the boundaries.

A4.1 A General Flight Path Definition

For the purposes of inverse simulation, any manoeuvre is a time history of the output vector $\underline{y}$, which contains, for example, the earth fixed translational velocities $\dot{x}_{e_.}$, $\dot{y}_{e_.}$ and $\dot{z}_{e_.}$; and the azimuth or heading angle, ψ. For some manoeuvres, referring to Figures (A4.1 to A4.3), it is easier and indeed sometimes desirable to express the earth fixed velocities in terms of functions of the flight velocity, $V_{f_.}$, track angle, χ and climb angle γ. The equations for velocities below can subsequently be manipulated to calculate displacements or accelerations:

$$\dot{x}_{e_.}(t) = V_{f_.}(t)\cos\gamma(t)\cos\chi(t); \tag{A4.1}$$

$$\dot{y}_{e_.}(t) = V_{f_.}(t)\cos\gamma(t)\sin\chi(t); \tag{A4.2}$$

$$\dot{z}_{e_.}(t) = -V_{f_.}(t)\sin\gamma(t). \tag{A4.3}$$

When the manoeuvre can be expressed in terms of $\dot{x}_{e.}$, $\dot{y}_{e.}$ and $\dot{z}_{e.}$ explicitly, however, equations (A4.1 to A4.3) are obviously unnecessary. For instance consider the Linear Repositioning Manoeuvres, an example of which is the quickhop used in Chapter 6, Section 6.2. It should be noted though that the quickhop in Chapter 6 was driven by flight test data rather than a polynomial representation.

A4.2 ***Example: Linear Repositioning Manoeuvres***

There are three linear repositioning manoeuvres commonly used in helicopter nap-of-the-earth (NOE) flight: the quickhop, the sidestep and the bobup. In each of the three cases the aircraft starts in a trimmed hover state, translates a specified distance, then returns to the original flight state of trimmed hover. Assuming that the earth $x_{e.}$-axis and aircraft x-*body* axis are coincident then the quickhop, sidestep and bobup are flown along the $x_{e.}$, $y_{e.}$ and $z_{e.}$ axes i.e. the manoeuvres are longitudinal, lateral and vertical repositions respectively. Thus considering the relevant axes, the same definition may be used for each type of manoeuvre. It is assumed that the aircraft is flown at a constant heading, ψ, usually equal to zero. The three manoeuvres can therefore be defined by a velocity time history as follows:

quickhop,	$\dot{x}_e(t) = V_{f.}(t);$
sidestep,	$\dot{y}_e(t) = V_{f.}(t);$
bobup,	$\dot{z}_e(t) = V_{f.}(t).$

Defining the form of the velocity polynomial involves imposing boundary conditions. As the manoeuvre is to begin and end in a trimmed hover state it is natural that zero velocity and acceleration at the entry and exit be applied. During the course of the manoeuvre the aircraft accelerates to some maximum velocity, $V_{f.\,max.}$ and then decelerates back to the hover, the maximum velocity assuming to have occurred at the manoeuvre mid point. Having defined four entry and exit, and a mid point boundary condition it is then possible to represent the manoeuvre by a fourth order polynomial:

$$V_{f.}(t) = \left[16\left(\frac{t}{t_{man.}}\right)^4 - 32\left(\frac{t}{t_{man.}}\right)^3 + 16\left(\frac{t}{t_{man.}}\right)^2\right]V_{f.\,max.}, \qquad \text{(A4.4)}$$

where $t_{man.}$ is the time taken to complete the manoeuvre. It is worth noting that when

using the individual blade model, Hibrom, specifying the total time, $t_{man.}$ ensures that the manoeuvre is completed in an integer number of main rotor periods, an issue addressed in Chapter 6, Section 6.1.4. When using the disc model HGS, however, it is more convenient to specify the manoeuvre groundtrack, s rather than the time taken to complete it. Integrating the velocity over the duration of the manoeuvre gives:

$$t_{man.} = \frac{15s}{8V_{f.\,max}}.$$

Hence the manoeuvre may be completely defined by the translational distance, s and the maximum velocity, $V_{f.\,max.}$ where integration and differentiation of equation (A4.4) yield the flight path and acceleration respectively.

Appendix 5 The Peters - HaQuang Dynamic Inflow Model

The expression for the induced velocity, $v_{ind.}$ referred to the rotor *disc* axis set is assumed to be of the form previously defined by equation (5.10):

$$v_{ind.}\left(r_{elem.},\psi\right) = v_0^{disc} + \frac{r}{R}\left(v_{1s}^{disc}\sin\psi + v_{1c}^{disc}\cos\psi\right),$$

where v_0^{disc}, v_{1s}^{disc} and v_{1c}^{disc} are the uniform, lateral and longitudinal variations respectively. This relationship, once the velocity components are known, is used in tandem with the motion of the blade relative to the disc plane to determine the instantaneous angle of attack, α of the centre of each blade element, see Chapter 5.3.2.1.

For the purposes of the inflow calculations it is convenient to first consider all terms related to the *wind* axis set, i.e. velocities v_0^{wind}, $v_{1_s}^{wind}$ and $v_{1_c}^{wind}$, Figure A5.1. These values are non-dimensionalised using the rotor radius, R and the rotor speed, Ω; the associated terms being λ_0^{wind}, $\lambda_{1_s}^{wind}$ and $\lambda_{1_c}^{wind}$. The velocity time histories are governed by the following first order differential equation:

$$[\boldsymbol{M}]\begin{Bmatrix}\dot{\lambda}_0^{wind}\\ \dot{\lambda}_{1_s}^{wind}\\ \dot{\lambda}_{1_c}^{wind}\end{Bmatrix} + [\boldsymbol{L}]_{nl}^{-1}\begin{Bmatrix}\lambda_0^{wind}\\ \lambda_{1_s}^{wind}\\ \lambda_{1_c}^{wind}\end{Bmatrix} = \begin{Bmatrix}C_T^{wind}\\ -C_L^{wind}\\ -C_M^{wind}\end{Bmatrix}_{aero.}, \qquad \text{(A5.1)}$$

where $[\boldsymbol{M}]$ is the apparent mass matrix and is defined as:

$$[\boldsymbol{M}] = \begin{bmatrix}\frac{8}{3\pi} & 0 & 0\\ 0 & -\frac{16}{45\pi} & 0\\ 0 & 0 & -\frac{16}{45\pi}\end{bmatrix},$$

and $[\boldsymbol{L}]_{nl}$ in the wind oriented, nonlinear, inflow gains matrix which relates the inflow components to the aerodynamic thrust, rolling and pitching moments coefficients. The matrix is non-diagonal representing the cross coupling that occurs between the inflow states. The inflow gains matrix is defined as:

$$[L]_{ml} = [L][\Lambda]^{-1};$$

where
$$[L] = \begin{bmatrix} \frac{1}{2} & 0 & \frac{15\pi}{64}\sqrt{\frac{1-\sin\chi}{1+\sin\chi}} \\ 0 & \frac{-4}{1+\sin\chi} & 0 \\ \frac{15\pi}{64}\sqrt{\frac{1-\sin\chi}{1+\sin\chi}} & 0 & \frac{-4\sin\chi}{1+\sin\chi} \end{bmatrix};$$

and
$$[\Lambda] = \begin{bmatrix} \lambda_{tot.} & 0 & 0 \\ 0 & \lambda_{cyc.} & 0 \\ 0 & 0 & \lambda_{cyc.} \end{bmatrix}.$$

The mass flow parameter matrix, $[\Lambda]$ contains the total resultant flow through the rotor disc, $\lambda_{tot.}$ and the mass flow parameter due to cyclic disturbances, $\lambda_{cyc.}$,

where
$$\lambda_{tot.} = \sqrt{\left(\mu^2 + \left(\mu_z - \lambda_{mom.}\right)^2\right)},$$

and
$$\lambda_{cyc.} = \frac{\mu^2 + \left(\mu_z - 2\lambda_{mom.}\right)\left(\mu_z - \lambda_{mom.}\right)}{\lambda_{tot.}}.$$

The above unidentified terms are the non-dimensionalised momentum theory induced velocity due to the rotor thrust, $\lambda_{mom.}$ and the non-dimensionalised in-plane, μ and perpendicular, μ_z component disc velocities, Figure A5.2:

where
$$\mu = \sqrt{\left(\mu_x^2 + \mu_y^2\right)};$$

$$\mu_x = \frac{u_{hub}^{disc}}{\Omega R};$$

$$\mu_y = \frac{v_{hub}^{disc}}{\Omega R};$$

and
$$\mu_z = \frac{w_{hub}^{disc}}{\Omega R}.$$

The wake angle, χ and the wind side slip angle, ψ_{wind} are defined respectively as:

$$\chi = \tan^{-1}\left(\frac{|\mu_z - \lambda_{mom.}|}{\mu}\right),$$

and

$$\psi_{wind} = \tan^{-1}\left\{\frac{\mu_y}{\mu_x}\right\}.$$

Using the ensuing relationships:

$$\begin{Bmatrix} C_T^{wind} \\ -C_L^{wind} \\ -C_M^{wind} \end{Bmatrix}_{aero.} = \left[T^{wind/disc}\right] \begin{Bmatrix} C_T^{disc} \\ -C_L^{disc} \\ -C_M^{disc} \end{Bmatrix}_{aero.};$$

$$\begin{Bmatrix} \lambda_0^{wind} \\ \lambda_{1_s}^{wind} \\ \lambda_{1_c}^{wind} \end{Bmatrix} = \left[T^{wind/disc}\right] \begin{Bmatrix} \lambda_0^{disc} \\ \lambda_{1_s}^{disc} \\ \lambda_{1_c}^{disc} \end{Bmatrix};$$

and

$$\left[T^{wind/disc}\right] = \begin{bmatrix} 1 & 0 & 0 \\ 0 & \cos\psi_{wind} & \sin\psi_{wind} \\ 0 & -\sin\psi_{wind} & \cos\psi_{wind} \end{bmatrix};$$

the theory can be transformed from the wind axes set to one aligned with the rotor disc. Upon expansion equation (A5.1) becomes:

$$[M]\left[T^{wind/disc}\right] \begin{Bmatrix} \dot{\lambda}_0^{disc} \\ \dot{\lambda}_{1_s}^{disc} \\ \dot{\lambda}_{1_c}^{disc} \end{Bmatrix} + [\Lambda][L]^{-1}\left[T^{wind/disc}\right] \begin{Bmatrix} \lambda_0^{disc} \\ \lambda_{1_s}^{disc} \\ \lambda_{1_c}^{disc} \end{Bmatrix} = \left[T^{wind/disc}\right] \begin{Bmatrix} C_T^{disc} \\ -C_L^{disc} \\ -C_M^{disc} \end{Bmatrix}_{aero.} . \quad (A5.2)$$

In order to remove the transformation matrix $\left[T^{wind/disc}\right]$ from the first term of Equation (A5.2), the equation is multiplied by the transpose of the transformation matrix as follows:

$$\left[T^{wind/disc}\right]^{\mathrm{T}}[M]\left[T^{wind/disc}\right]\begin{Bmatrix}\dot{\lambda}_0^{disc}\\ \dot{\lambda}_{1_s}^{disc}\\ \dot{\lambda}_{1_c}^{disc}\end{Bmatrix}+\left[T^{wind/disc}\right]^{\mathrm{T}}[\Lambda][L]^{-1}\left[T^{wind/disc}\right]\begin{Bmatrix}\lambda_0^{disc}\\ \lambda_{1_s}^{disc}\\ \lambda_{1_c}^{disc}\end{Bmatrix}=\begin{Bmatrix}C_T^{disc}\\ -C_L^{disc}\\ -C_M^{disc}\end{Bmatrix}_{aero.}.$$

Because the first element of $\left[T^{wind/disc}\right]$ is unity, and both $[M]$ and $[\Lambda]$ are diagonal matrices, the order of multiplication can be reversed. The result of this is the first order differential equation representing the nonlinear theory of dynamic inflow with respect to the rotor disc plane, equation (A5.3):

$$[M]\begin{Bmatrix}\dot{\lambda}_0^{disc}\\ \dot{\lambda}_{1_s}^{disc}\\ \dot{\lambda}_{1_c}^{disc}\end{Bmatrix}+\left[\hat{L}\right]^{-1}\begin{Bmatrix}\lambda_0^{disc}\\ \lambda_{1_s}^{disc}\\ \lambda_{1_c}^{disc}\end{Bmatrix}=\begin{Bmatrix}C_T^{disc}\\ -C_L^{disc}\\ -C_M^{disc}\end{Bmatrix}_{aero.}, \qquad \text{(A5.3)}$$

where $\left[\hat{L}\right]^{-1}=[\Lambda]\left[T^{wind/disc}\right]^{\mathrm{T}}[L]^{-1}\left[T^{wind/disc}\right].$

Appendix 6 The McVicar-Bradley Partial Periodic Trimmer

While a specific trim state may be described by the vehicle's inertial velocity ($\dot{x}_{e.}$, $\dot{y}_{e.}$, $\dot{z}_{e.}$) and, for example, the heading angle, ψ side slip angle, β or turn rate, $\dot{\chi}$; the periodic forcing of an individual blade model renders the problem of calculating an accurate trim a much more complex one as the solution must take place over a period. Over this period (main rotor turn for Hibrom) the flight parameter values must be averages and each of the vehicle's states must have the same value at the beginning as at the end. The problem then becomes both a question of calculating the vehicle controls which will produce the specific trim state, and finding the periodic value of each of the states. Such a 'periodic trimmer' was first successfully realised by McVicar and Bradley (*1992*). Genisa can readily accommodate this trim algorithm by considering each of the unknowns (vehicle controls, current state values) as elements in a 'pseudo' control vector, $\underline{u}$ and using the flight parameters and periodic state values as functions in an error vector, $\underline{e}$. Thus as with inverse simulation, a Newton-Raphson scheme is used to solve the error vector for the unknown control vector:

$$\underline{u}_{m+1} = \underline{u}_m - \underline{u}_{error\,m};$$

$$[J]_m \underline{u}_{error\,m} = \underline{e}_m \qquad \text{(A6.1)}$$

where $\underline{u}_{error}$ is the estimated error in the control vector, $[J]$ is the Jacobian matrix and m and $m+1$ are successive estimates of the unknown control values.

In the case of a single main and tail rotor helicopter such as a Westland Lynx the control vector, $\underline{u}$ can be written as:

$$\underline{u} = \begin{Bmatrix} \underline{u}_{cont.} \\ \underline{u}_{body} \\ \underline{u}_{i.f.} \\ \underline{u}_{flap} \end{Bmatrix};$$

where the subscripts *cont.*, *body*, *i.f.* and *flap* refer to the vehicle controls; and body, inflow, and flap states respectively. The elements of these vectors are given below and are as defined in the nomenclature:

$$\underline{u}_{cont.} = \begin{Bmatrix} \theta_0 \\ \theta_{1s} \\ \theta_{1c} \\ \theta_{0t.r.} \end{Bmatrix}, \quad \underline{u}_{body} = \begin{Bmatrix} U \\ V \\ W \\ P \\ Q \\ R \\ \phi \\ \theta \end{Bmatrix}, \quad \underline{u}_{i.f.} = \begin{Bmatrix} v_0 \\ v_{1s} \\ v_{1c} \end{Bmatrix}, \quad \underline{u}_{flap} = \begin{Bmatrix} \beta_1 \\ \beta_2 \\ \beta_3 \\ \beta_4 \\ \dot{\beta}_1 \\ \dot{\beta}_2 \\ \dot{\beta}_3 \\ \dot{\beta}_4 \end{Bmatrix}.$$

The error vector, $\underline{e}$ is also subdivided into other vectors where the subscript $m.f.s.$ refers to mean flight state, and the superscripts $e.$ and $s.$ to the end and the start of a period respectively:

$$\underline{e} = \begin{Bmatrix} \underline{e}_{m.f.s.} \\ \underline{e}_{body} \\ \underline{e}_{i.f.} \\ \underline{e}_{flap} \end{Bmatrix};$$

$$\underline{e}_{m.f.s.} = \begin{Bmatrix} \bar{\dot{x}}_e \\ \bar{\dot{y}}_e \\ \bar{\dot{z}}_e \\ \bar{\dot{\psi}} \end{Bmatrix}, \quad \underline{e}_{body} = \begin{Bmatrix} U^{e.} - U^{s.} \\ V^{e.} - V^{s.} \\ W^{e.} - W^{s.} \\ P^{e.} - P^{s.} \\ Q^{e.} - Q^{s.} \\ R^{e.} - R^{s.} \\ \phi^{e.} - \phi^{s.} \\ \theta^{e.} - \theta^{s.} \end{Bmatrix}, \quad \underline{e}_{i.f.} = \begin{Bmatrix} v_0^{e.} - v_0^{s.} \\ v_{1s}^{e.} - v_{1s}^{s.} \\ v_{1c}^{e.} - v_{1c}^{s.} \end{Bmatrix}, \quad \underline{e}_{flap} = \begin{Bmatrix} \beta_1^{e.} - \beta_1^{s.} \\ \beta_2^{e.} - \beta_2^{s.} \\ \beta_3^{e.} - \beta_3^{s.} \\ \beta_4^{e.} - \beta_4^{s.} \\ \dot{\beta}_1^{e.} - \dot{\beta}_1^{s.} \\ \dot{\beta}_2^{e.} - \dot{\beta}_2^{s.} \\ \dot{\beta}_3^{e.} - \dot{\beta}_3^{s.} \\ \dot{\beta}_4^{e.} - \dot{\beta}_4^{s.} \end{Bmatrix}.$$

Thus from above the mean flight state error vector, $\underline{e}_{m.f.s}$ has been matched with the helicopter control vector, $\underline{u}_{cont.}$; the body period error vector, $\underline{e}_{body}$ has been matched with the body control vector, $\underline{u}_{body}$; the inflow period error vector, $\underline{e}_{i.f.}$ with the inflow control vector, $\underline{u}_{i.f.}$; and the blade period error vector, $\underline{e}_{blade}$ with the blade control vector, $\underline{u}_{blade}$. As mentioned in Chapter 6, Section 6.1.2 trimming Hibrom involves Genisa solving 23 constraints in 23 unknowns. Other than the scale of the problem, however, once the control and error vectors have been defined, the solution procedure is exactly as with inverse simulation, Chapter 3, Section 3.1.2.

Modifying the trimmer to accommodate, for example, a propeller is straightforward enough as it only requires adding propeller pitch to the control vector, $\underline{u}_{cont.}$ and, if vehicle pitch attitude is constrained, adding pitch rate, $\dot{\theta}$ to the mean flight state vector, $\underline{e}_{m,f,s}$. Redundant solutions (more controls than error functions) similarly do not any require changes to the algorithm structure, simply an optimal technique for solving equation (A6.1).

Appendix 7 Inflow Model for Individual Blade Tail Rotor and Propeller

The inflow model used for the individual blade tail rotor and propeller is a simplified version of the dynamic inflow model described in Appendix 5 (*Peters and HaQuang, 1988*). Rather than having the full model's three states only the uniform component of induced velocity is expressed by a differential equation, while the longitudinal and lateral variations - steady for a given flight state - are estimated in the same fashion as Glauert's model (*Bramwell, 1976*). The motivation for such a model was one of compromise: between overcoming the difficulties encountered in finding a unique solution for a momentum model in axial flow (as is the case for a tail rotor in sidewards flight, and is invariably the case with a propeller); and yet wanting to avoid the complexity of a full dynamic inflow model. In contrast with the basic momentum model this hybrid proves to have no problems solving for the propeller, while compared to the full dynamic inflow model the number of and complexity of calculations has been greatly reduced. Additionally, though the model ignores the influence of aerodynamic pitching and rolling moments, it does retain an appreciation of the lag between changes in blade pitch angle and the thrust generated by the rotor (for rotor read tail rotor or propeller). In short it has advantages over the Glauert model, yet is much less complicated than the full dynamic inflow model. The equations describing this hybrid inflow model will now be described.

Consider the differential equation (A5.3) from the dynamic inflow model representing inflow with respect to the rotor disc plane:

$$[\boldsymbol{M}]\begin{Bmatrix}\dot{\lambda}_0^{disc}\\ \dot{\lambda}_{1_s}^{disc}\\ \dot{\lambda}_{1_c}^{disc}\end{Bmatrix}+\left[\hat{\boldsymbol{L}}\right]^{-1}\begin{Bmatrix}\lambda_0^{disc}\\ \lambda_{1_s}^{disc}\\ \lambda_{1_c}^{disc}\end{Bmatrix}=\begin{Bmatrix}C_T^{disc}\\ -C_L^{disc}\\ -C_M^{disc}\end{Bmatrix}_{aero.} \quad ; \qquad \text{(A7.1)}$$

where all terms are as defined in Appendix 5. Assuming that the cyclic inflow components are static (i.e. $\dot{\lambda}_{1s}^{disc}$ and $\dot{\lambda}_{1c}^{disc}$ are equal to zero) and there is no contribution from the aerodynamic pitching and rolling moments (i.e. $C_{L_{aero.}}^{disc}$ and $C_{M_{aero}}^{disc}$ are equal to zero) then equation (A7.1) reduces to a single differential equation:

$$\frac{8}{3\pi}\lambda_0^{disc} + 2\lambda_{tot_r}\lambda_0^{disc} = C_T;$$

which can be added to the equations of motion, and λ_{tot_r} is defined and determined as before. The cyclic components - λ_{1s}^{disc} and λ_{1c}^{disc} - are then calculated as in Glauert's method (Appendix 2a, Section A2a.4):

$$\begin{Bmatrix} \lambda_{1c} \\ \lambda_{1s} \end{Bmatrix} = \begin{bmatrix} \cos\psi_{wind} & -\sin\psi_{wind} \\ \sin\psi_{wind} & \cos\psi_{wind} \end{bmatrix} \begin{Bmatrix} \lambda_{1c}^{wind} \\ \lambda_{1s}^{wind} \end{Bmatrix};$$

where:

$$\lambda_{1c}^{wind} = \lambda_0 \tan\left\{\frac{\chi}{2}\right\} \quad \text{if} \quad \chi < \frac{\pi}{2};$$

$$\lambda_{1c}^{wind} = \lambda_0 \cot\left\{\frac{\chi}{2}\right\} \quad \text{if} \quad \chi > \frac{\pi}{2};$$

and

$$\lambda_{1s}^{wind} = 0.$$

Appendix 8 Configurational and Aerodynamic Data

Westland Lynx

Aircraft Data	
mass, m	4313.74 kg
inertia, I_{xx}	2767.09 kg m^2
I_{yy}	13904.5 kg m^2
I_{zz}	12208.83 kg m^2
I_{xz}	2034.8 kg m^2
centre of gravity, $x_{ref.}$	0.127 m

Rotor Parameters	
no. of blades, n_{blades}	4
rotor radius, R	6.4 m
blade chord, c	0.391 m
blade mass, m_{blade}	40.44 kg
mass moment, M_β	114.19 kg m
flapping inertia, I_β	428.74 kg m^2
spring stiffness, K_β	0 N m rad^{-1}
rotor speed, Ω	36.6 rad s^{-1}
tip twist, θ_{twist}	-8 deg
shaft tilt angle, γ_{shaft}	-4 deg
hub height, $h_{rot.}$	-1.3 m
hinge offset, x_{hinge}	0.7525 m

Tail Plane Parameters	
clean area, $S_{t.p.}$	1.2 m^2
setting angle, $\theta_{t.p.}$	-1 deg
height, $h_{t.p.}$	-1.14 m
distance, $l_{t.p.}$	-7.66 m

Fin Parameters	
clean area, S_{fin}	1.11 m^2
setting angle, θ_{fin}	-5 deg
height, h_{fin}	-0.54 m
distance, l_{fin}	-7.68 m

Tail Rotor Parameters	
no. blades, $n_{t.r.blades}$	4
rotor radius, $R_{t.r.}$	1.1 m
blade chord, $c_{t.r.}$	0.18 m
gearing ratio, $G_{t.r.}$	6
hub height, $h_{t.r.}$	-1.14 m
hub distance, $l_{t.r.}$	-7.66 m

Table A8.1 Lynx Configurational Data

Compound Lynx

Aircraft Data	
mass, m	4472.74 kg
inertia, I_{xx}	2767.09 kg m^2
I_{xy}	13904.5 kg m^2
I_{yy}	12208.83 kg m^2
I_{zz}	2034.8 kg m^2
centre of gravity, $x_{ref.}$	0.127 m

Rotor Parameters	
no. of blades, n_{blades}	4
rotor radius, R	6.4 m
blade chord, c	0.391 m
blade mass, m_{blade}	40.44 kg
mass moment, M_β	114.19 kg m
flapping inertia, I_β	428.74 kg m^2
spring stiffness, K_β	0 N m rad^{-1}
rotor speed, Ω	36.6 rad s^{-1}
tip twist, θ_{twist}	-8 deg
shaft tilt angle, γ_{shaft}	-4 deg
hub height, $h_{rel.}$	-1.3 m
hinge offset, x_{hinge}	0.7525 m

Wing Parameters	
clean area, S_{wing}	2.16 m^2
aspect ratio, A	6
setting angle, θ_{wing}	10 deg
height, h_{wing}	0 m
distance, l_{wing}	0 m

Tail Plane Parameters	
clean area, $S_{t.p.}$	1.2 m^2
setting angle, $\theta_{t.p.}$	-1 deg
height, $h_{t.p.}$	-1.14 m
distance, $l_{t.p.}$	-7.66 m

Fin Parameters	
clean area, S_{fin}	1.11 m^2
setting angle, θ_{fin}	-5 deg
height, h_{fin}	-0.54 m
distance, l_{fin}	-7.68 m

Tail Rotor Parameters	
no. blades, $n_{t.r.blades}$	4
rotor radius, $R_{t.r.}$	1.1 m
blade chord, $c_{t.r.}$	0.18 m
gearing ratio, $G_{t.r.}$	6
hub height, $h_{t.r.}$	-1.14 m
hub distance, $l_{t.r.}$	-7.66 m

Propeller Parameters	
no. blades, $n_{pr.blades}$	4
propeller radius, $R_{pr.}$	1.1 m
blade chord, $c_{pr.}$	0.18 m
gearing ratio, $G_{pr.}$	6
hub height, $h_{pr.}$	0 m
hub distance, $l_{pr.}$	-8.76 m
tip twist, θ_{twist}	-30 deg

Table A8.2 **Compound Lynx Configurational Data**

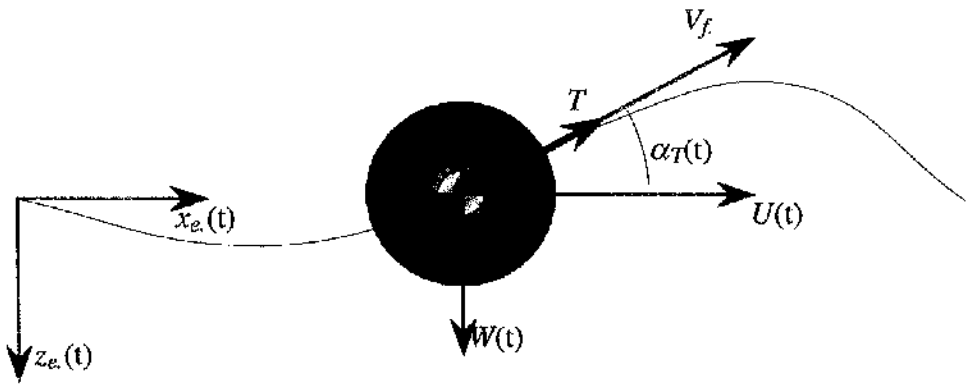

Figure 1.1 **Simple Spherical Vehicle with One Control**

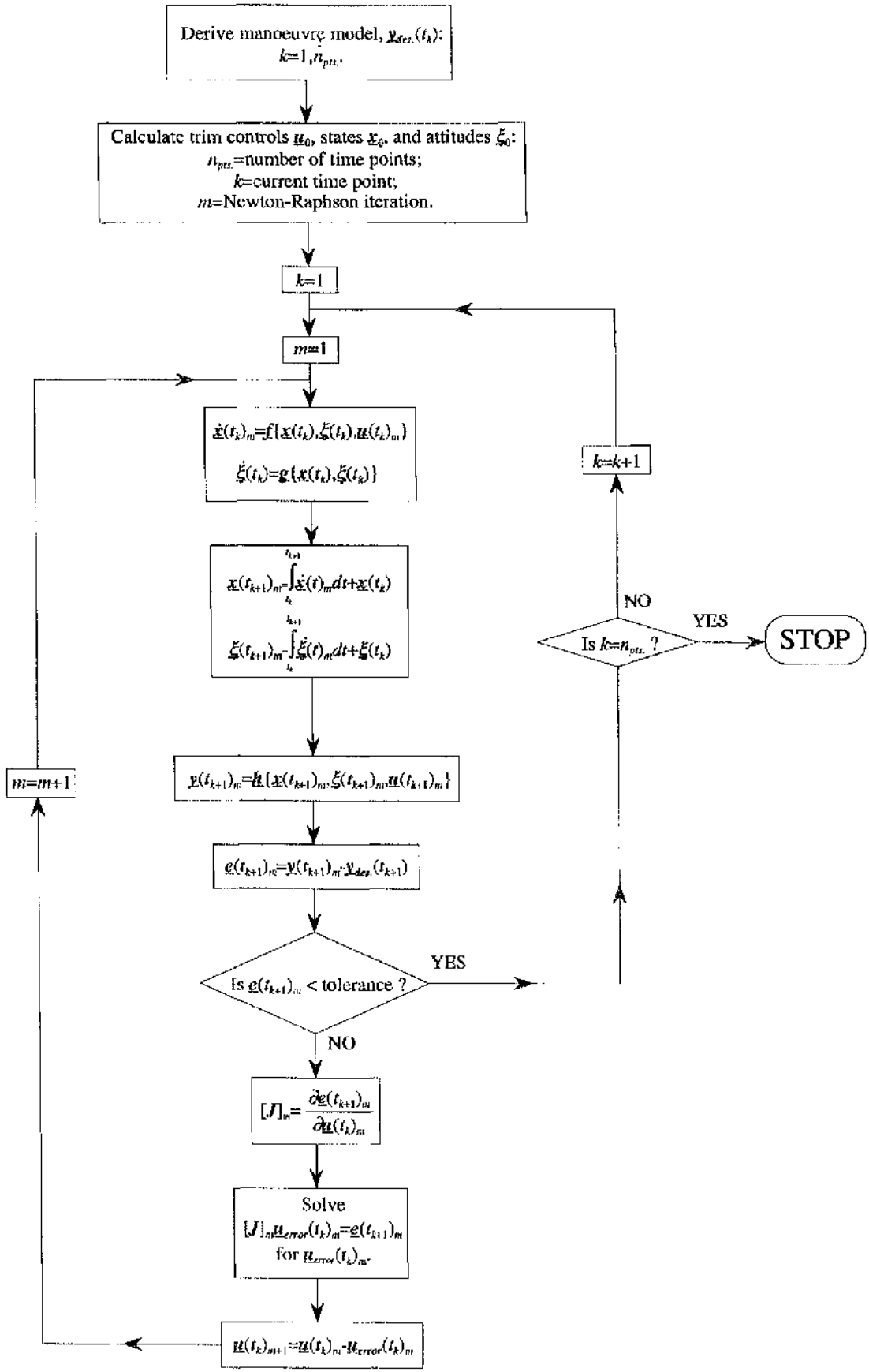

Figure 3.1 Flowchart Describing Genisa Algorithm

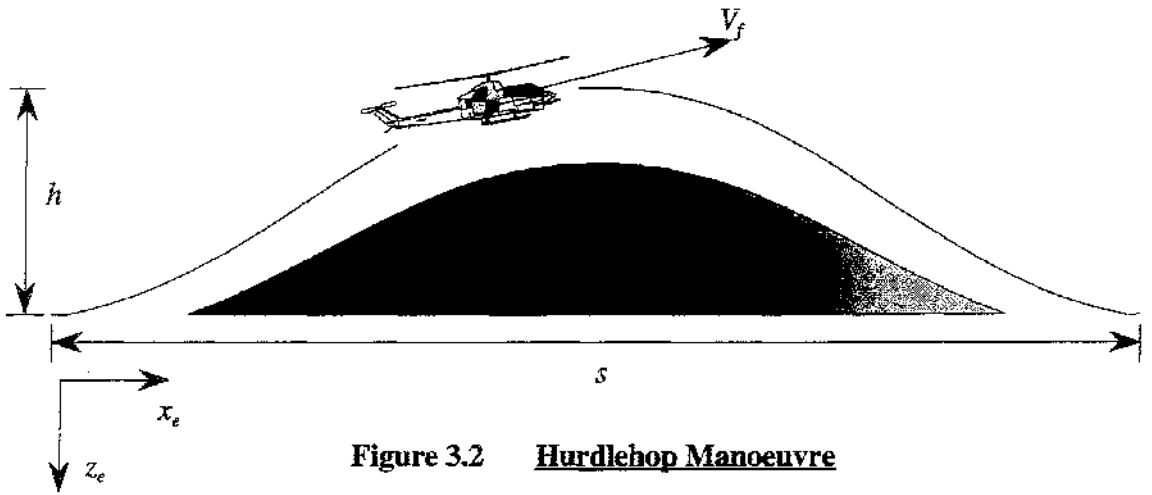

Figure 3.2 **Hurdlehop Manoeuvre**

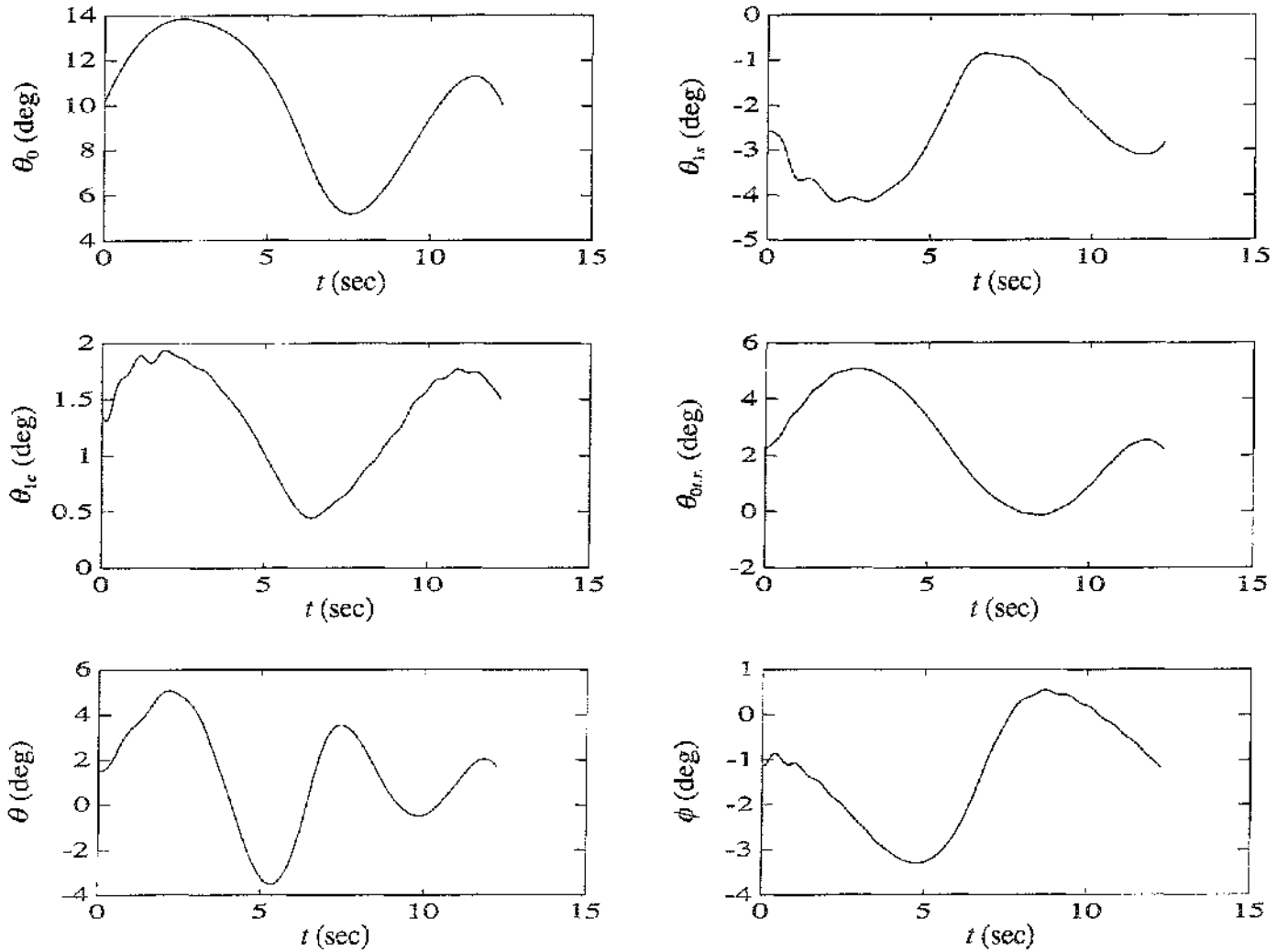

Figure 3.3 **Inverse Simulation Results generated by Genisa for a Hurdlehop Manoeuvre (s=500m, h=30m, V_f=80kts) with Data for a Westland Lynx Helicopter**

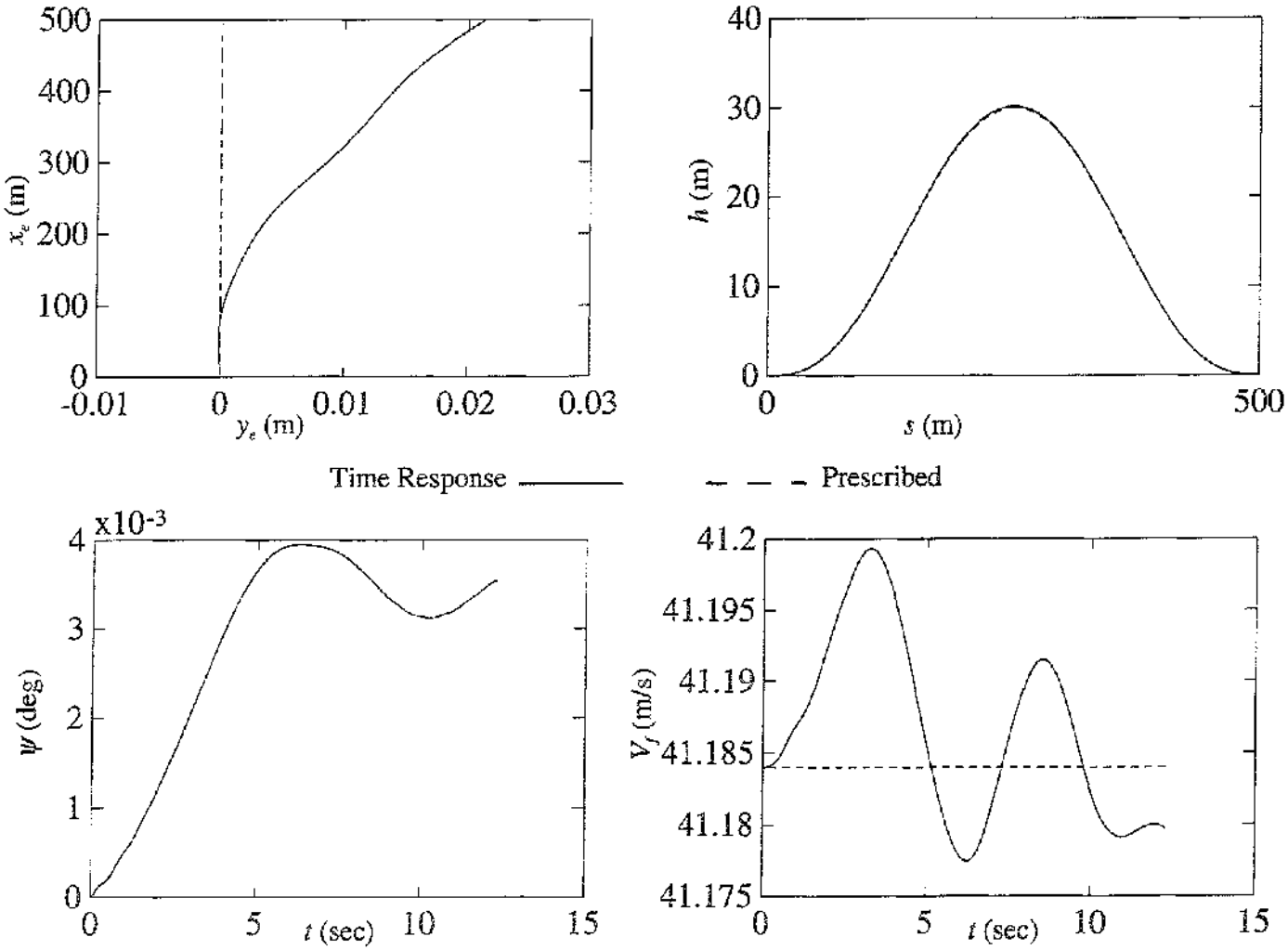

Figure 3.4 **Comparison between Prescribed Flight Path Parameters and those generated by Time Response Solution using Inverse Simulation Control Time Histories**

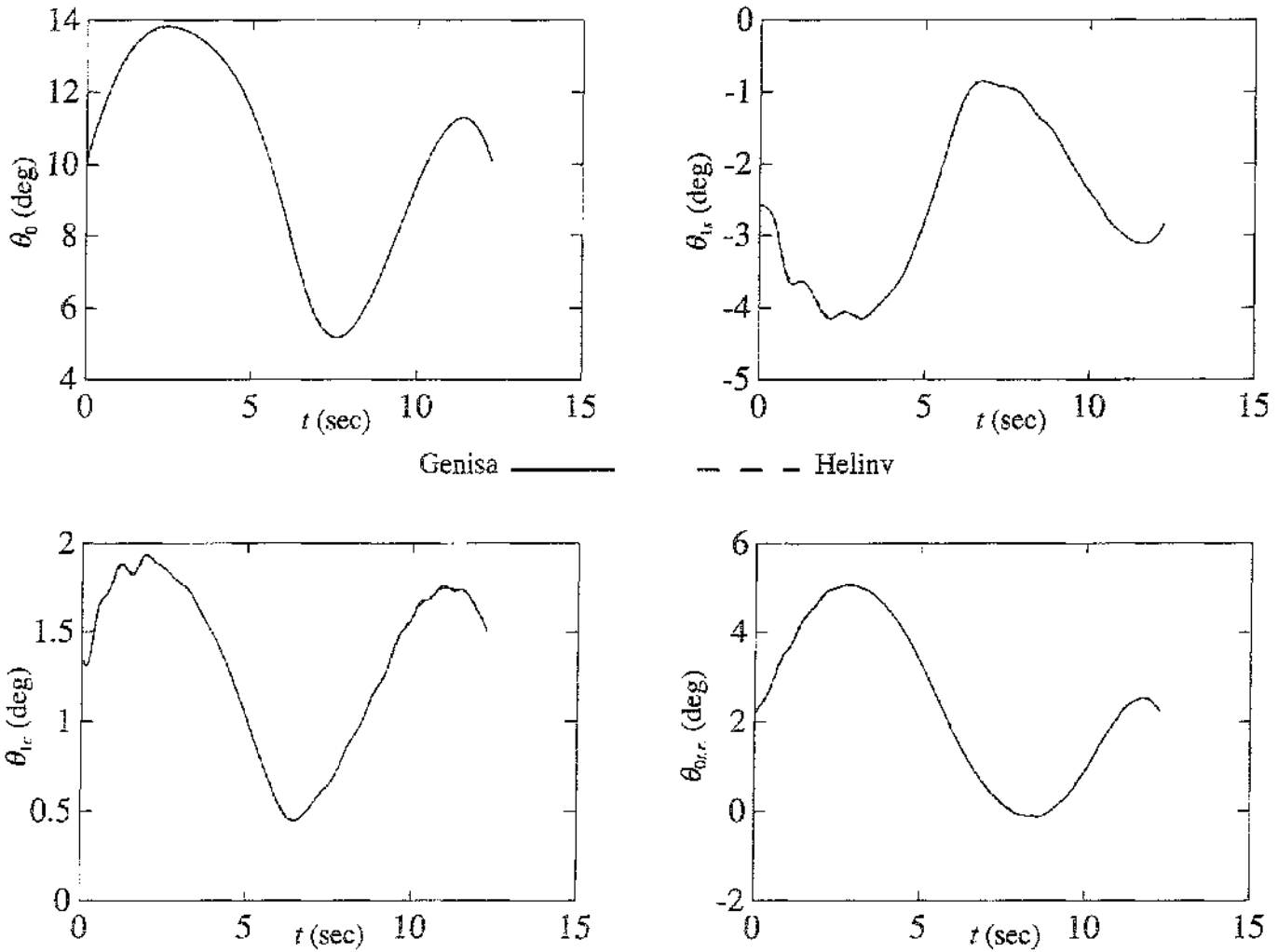

Figure 3.5 **Comparison between Inverse Simulation Results generated by Genisa and Helinv (Hurdlehop; s=500m, h=30m, V_x=80kts)**

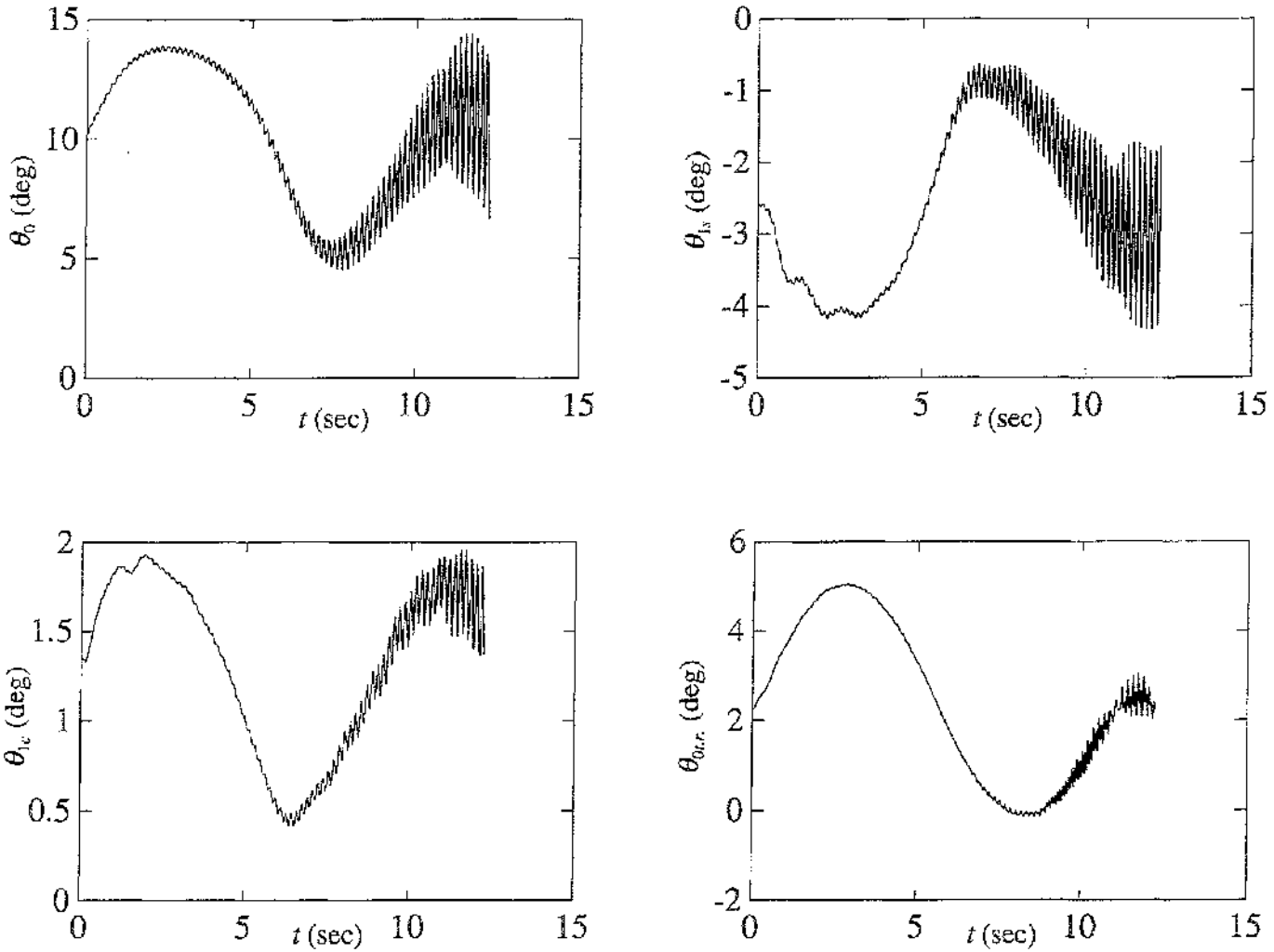

Figure 3.6 **Unstable Inverse Simulation Results generated by Genisa using Output Vector defined by Displacements (Δt=0.04sec)**

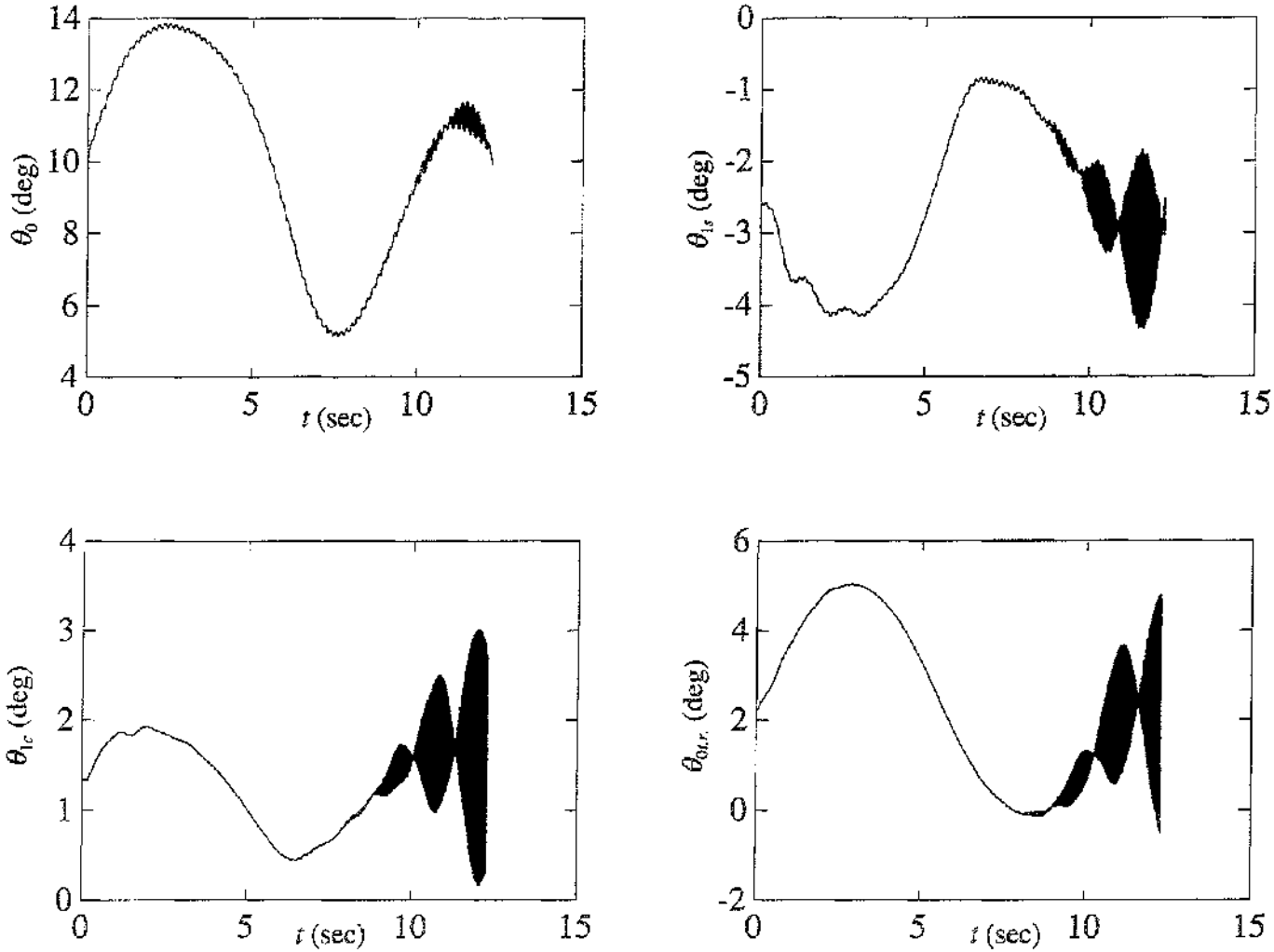

Figure 3.7 **Unstable Inverse Simulation Results generated by Genisa using Output Vector defined by Displacements (Δt=0.01sec)**

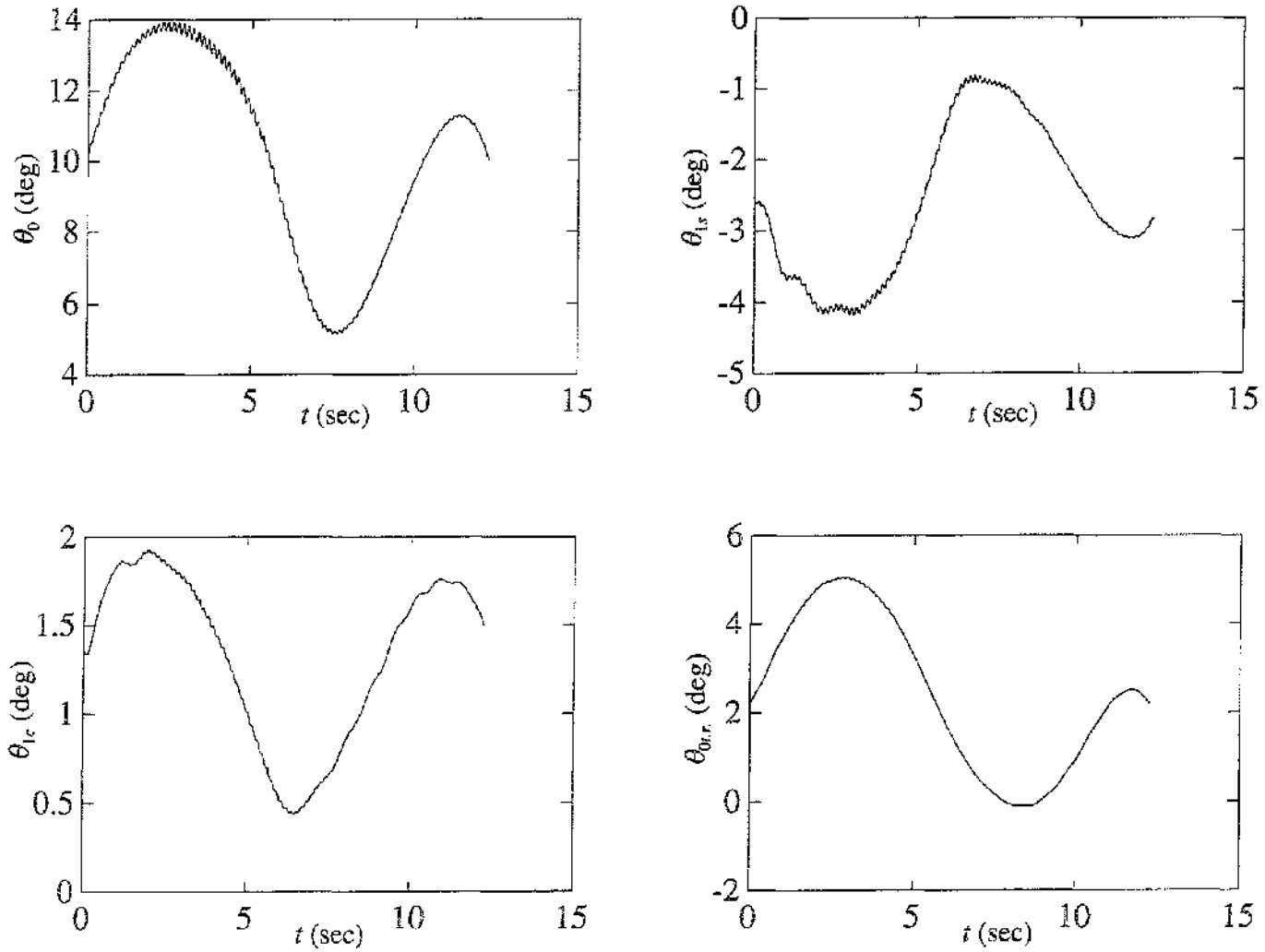

Figure 4.1 **Stable Inverse Simulation Results (Hurdlehop; s=500m, h=30m, V_f=60kts) generated by Genisa using Output Vector defined by Accelerations**

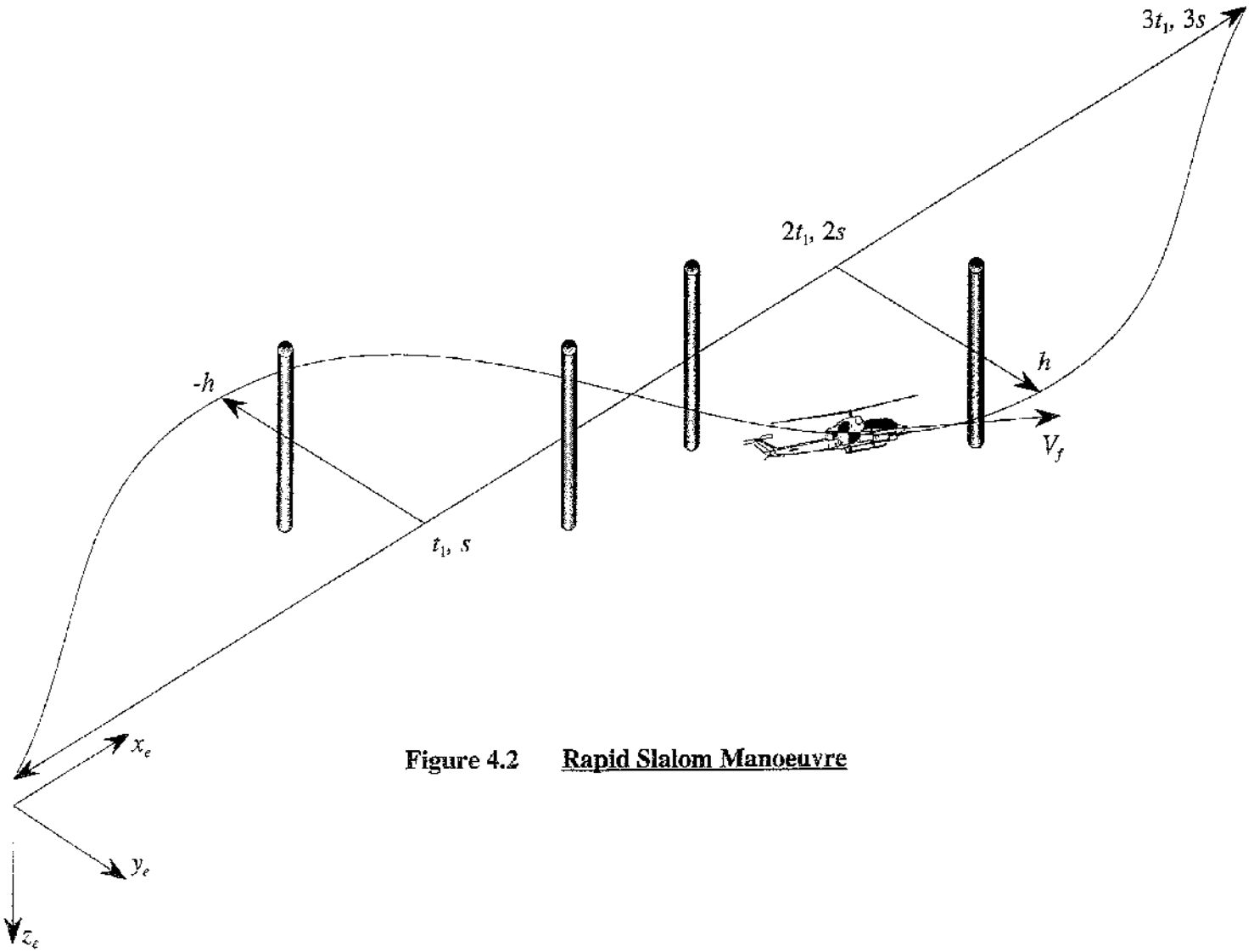

Figure 4.2 **Rapid Slalom Manoeuvre**

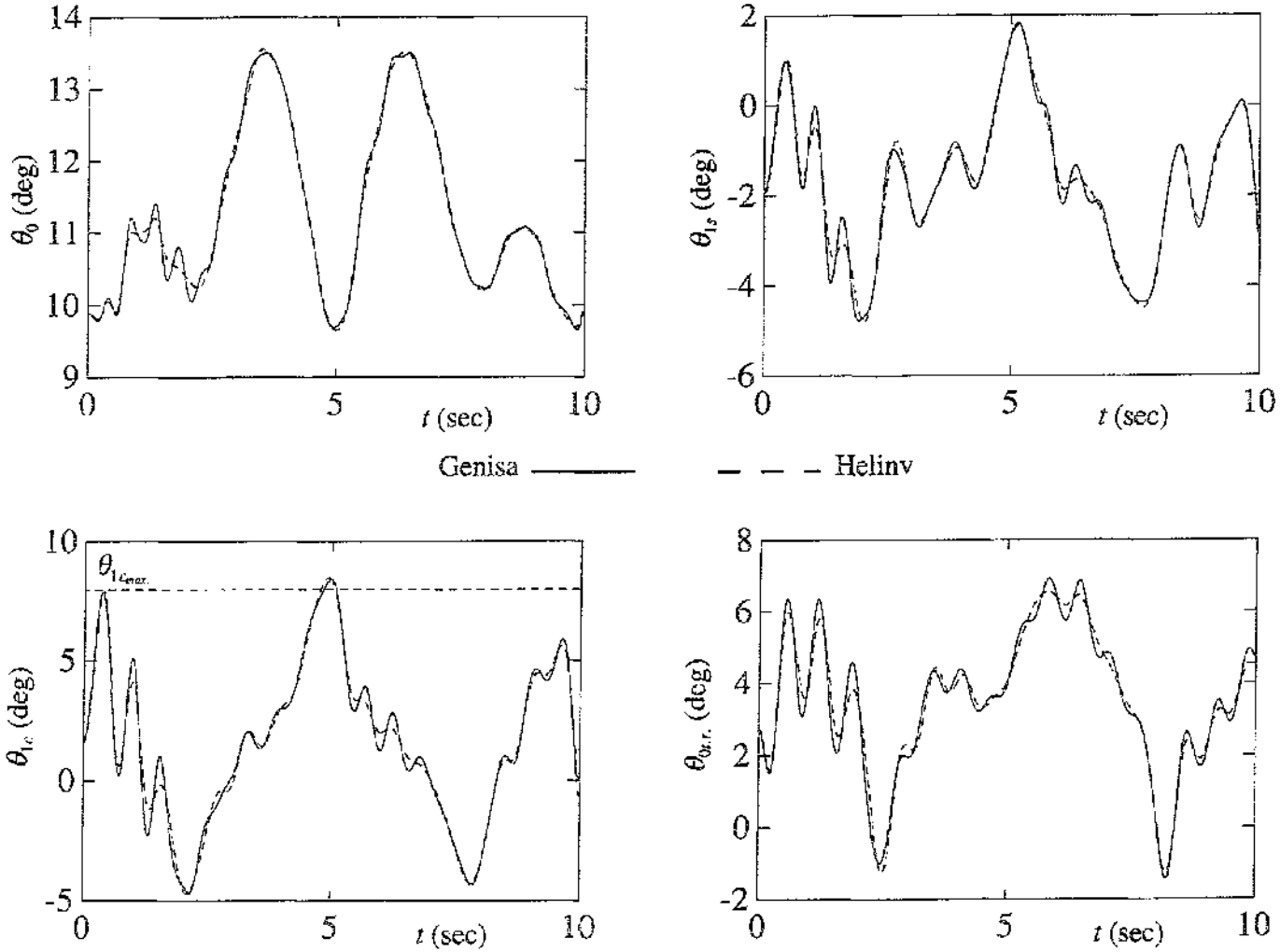

Figure 4.3 **Comparison between Inverse Simulation Results generated by Genisa and Helinv (Rapid Slalom: s=300m, h=-15.2m, V_f=60kts)**

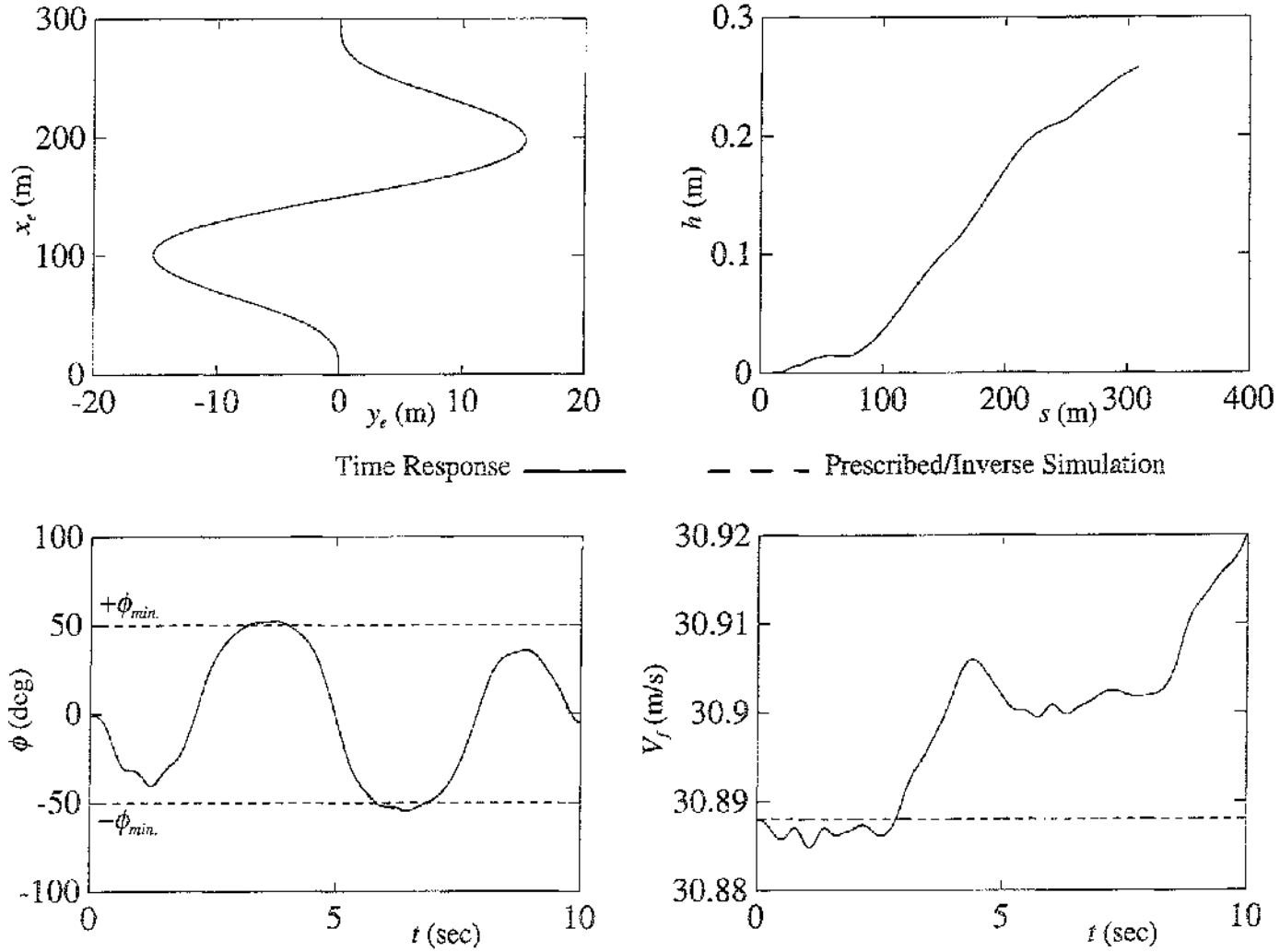

Figure 4.4 **Comparison between Prescribed Flight Path Parameters (Inverse Simulation for ϕ) and those generated by Time Response using Inverse Simulation Control Time Histories**

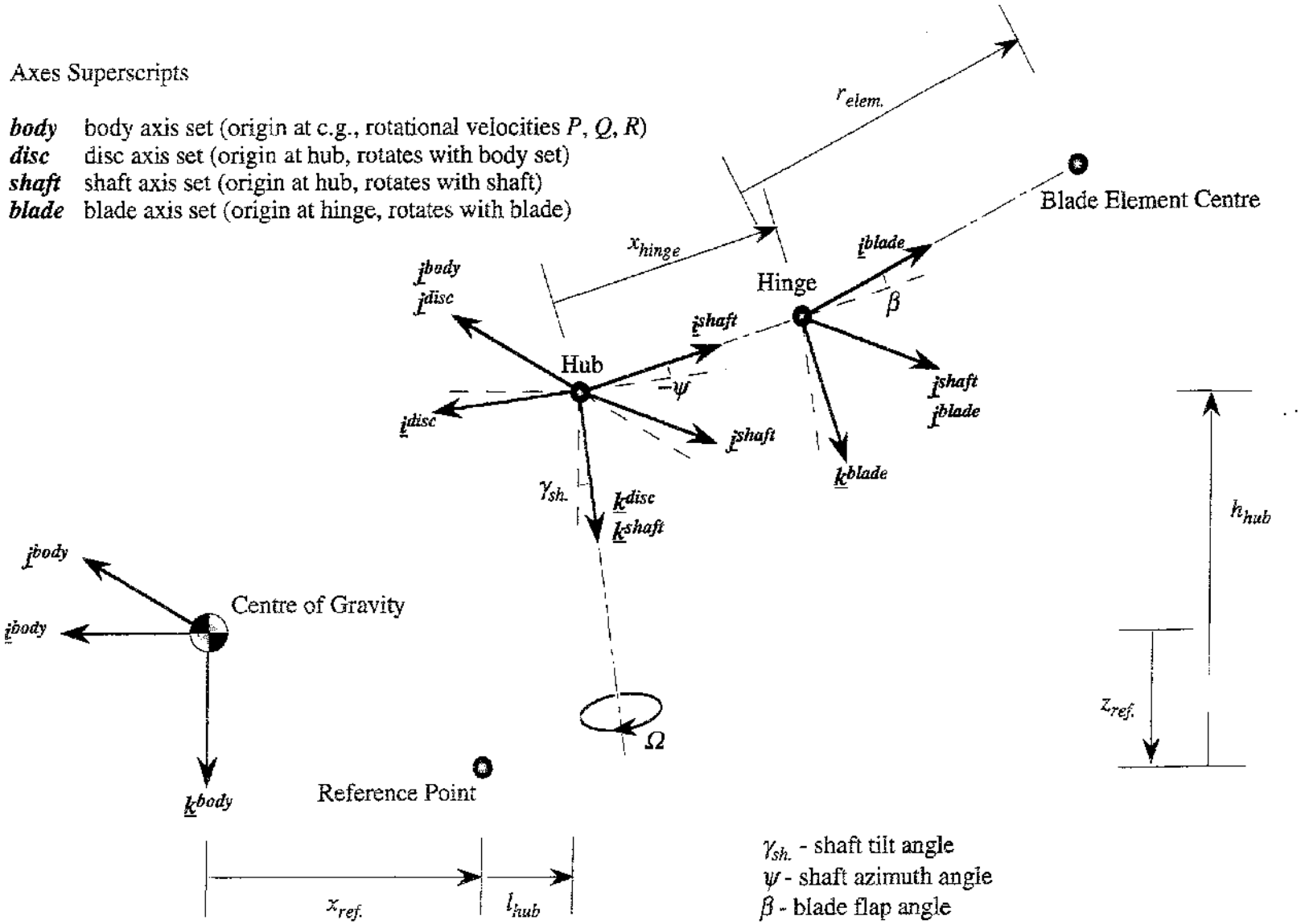

Figure 5.1 Body to Blade Axis Set Transformations

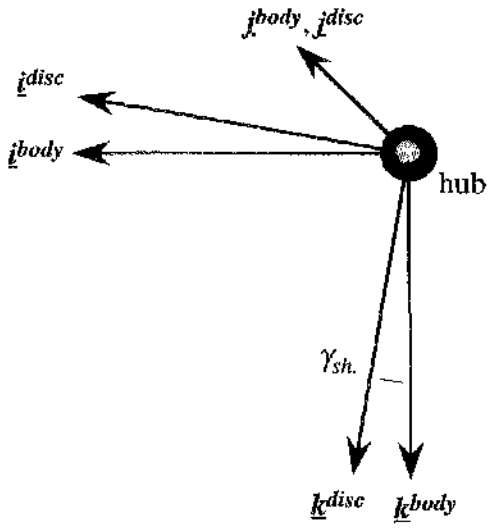

Figure 5.2 **Body to Disc Axes Transformation**

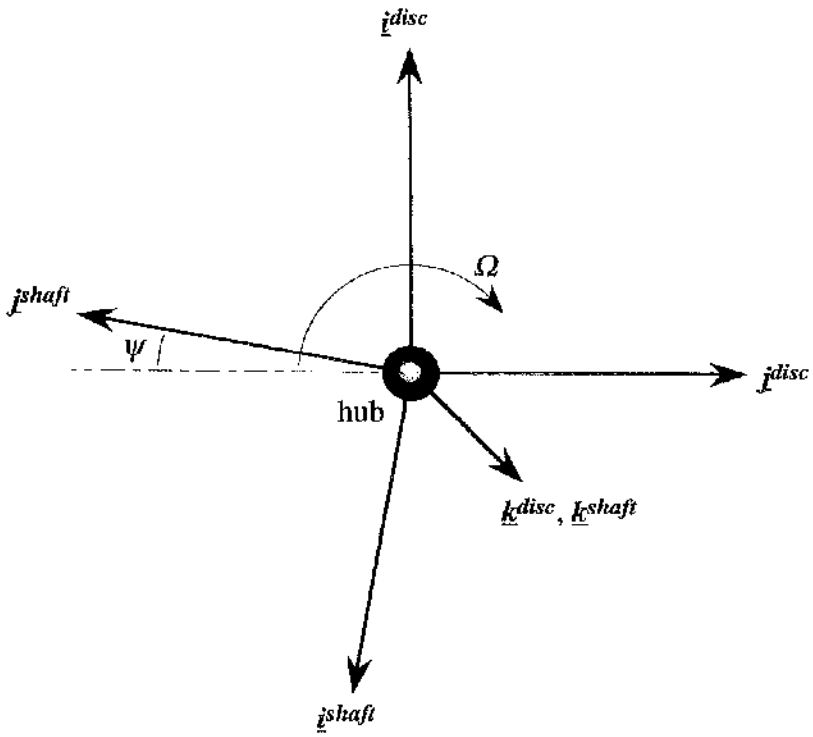

Figure 5.3 **Disc to Shaft Axes Transformation**

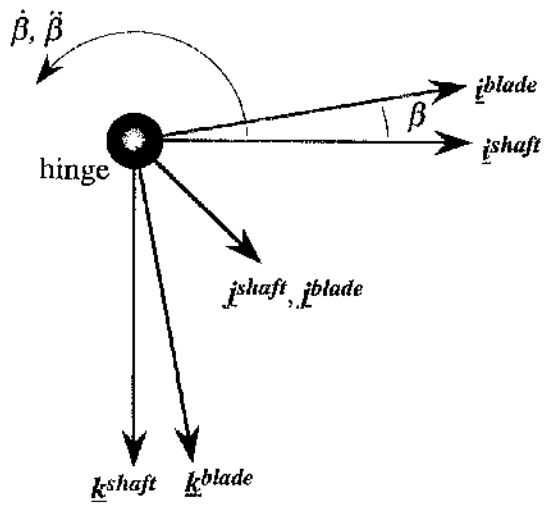

Figure 5.4 **Shaft to Blade Axes Transformation**

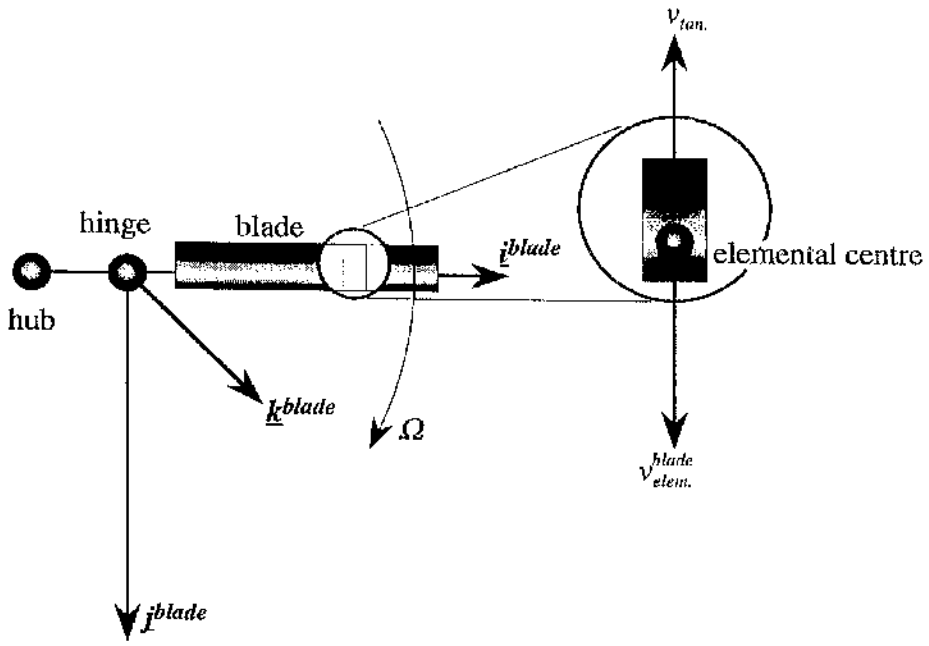

Figure 5.5 **Tangential Component of Velocity of Air With Respect to Blade**

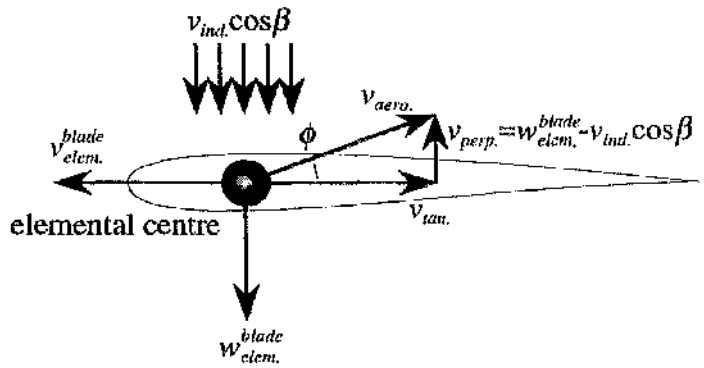

Figure 5.6 **Perpendicular Component of Velocity of Air With Respect to Blade**

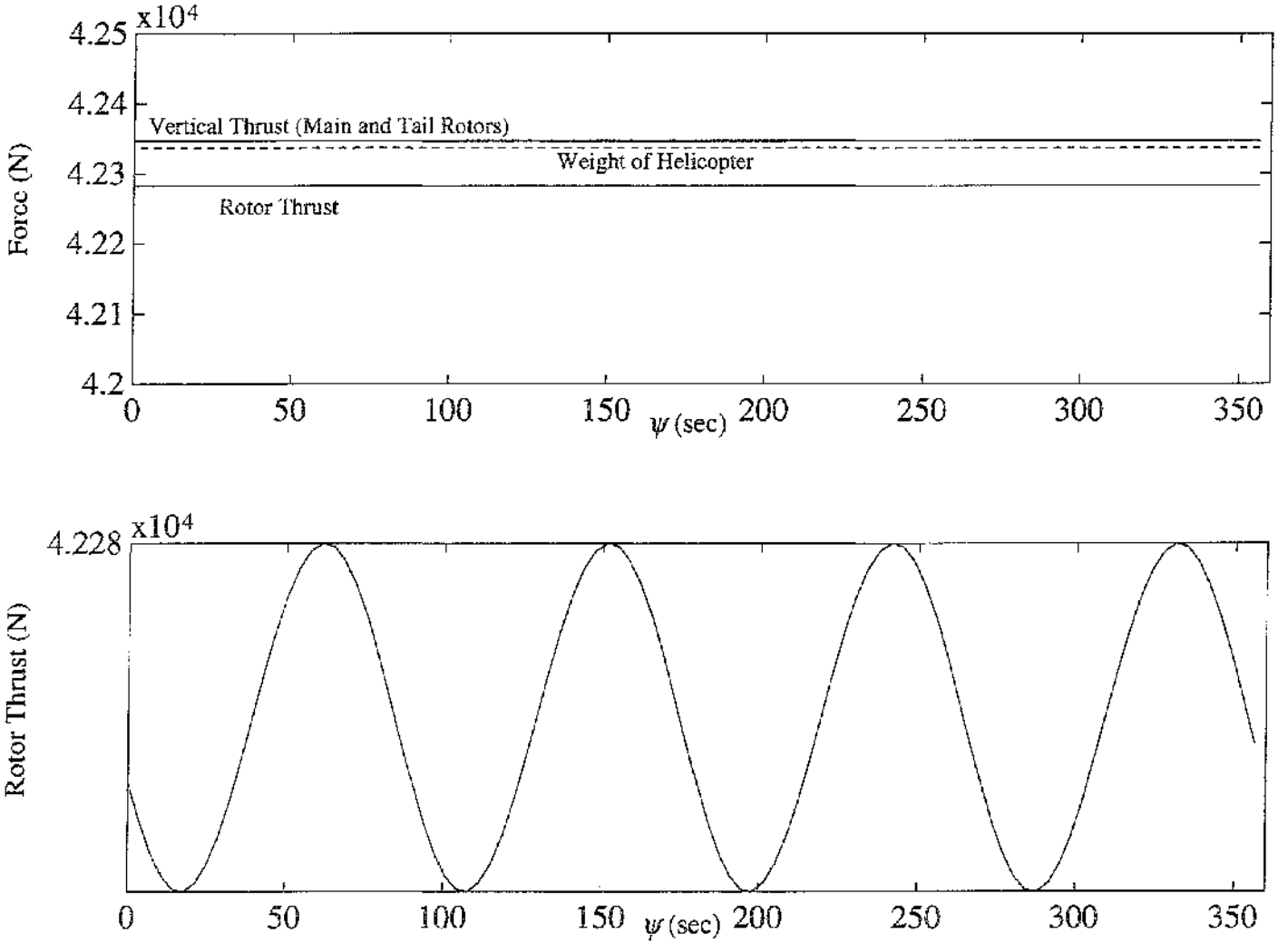

Figure 6.1 **Comparison Between Total Rotor Thrust and Total Vertical Thrust Predicted by Hibrom in Hover, and the Helicopter Weight**

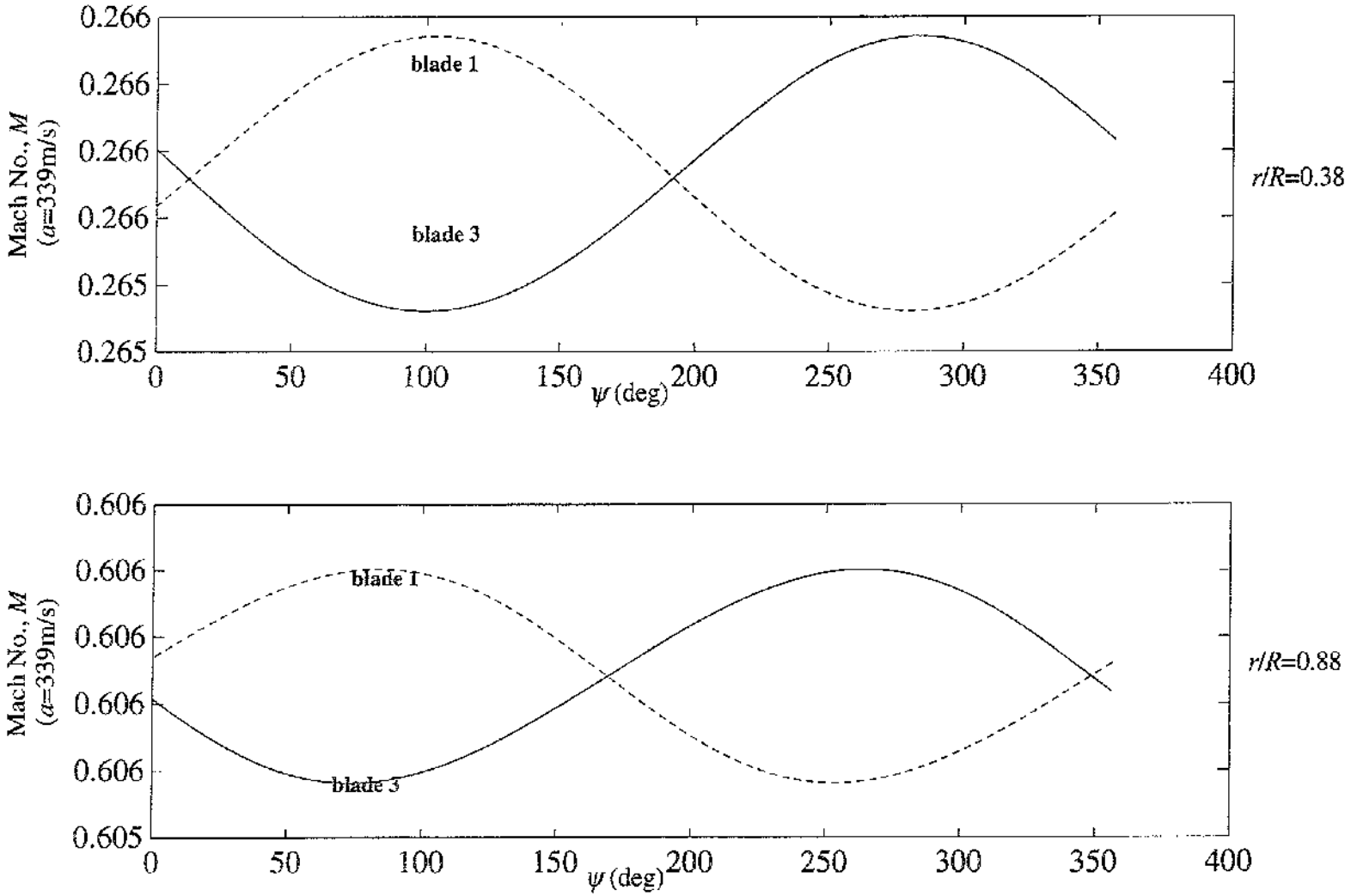

Figure 6.2 **Mach Number Variation with Respect to Blade Azimuthal Position in Hover**

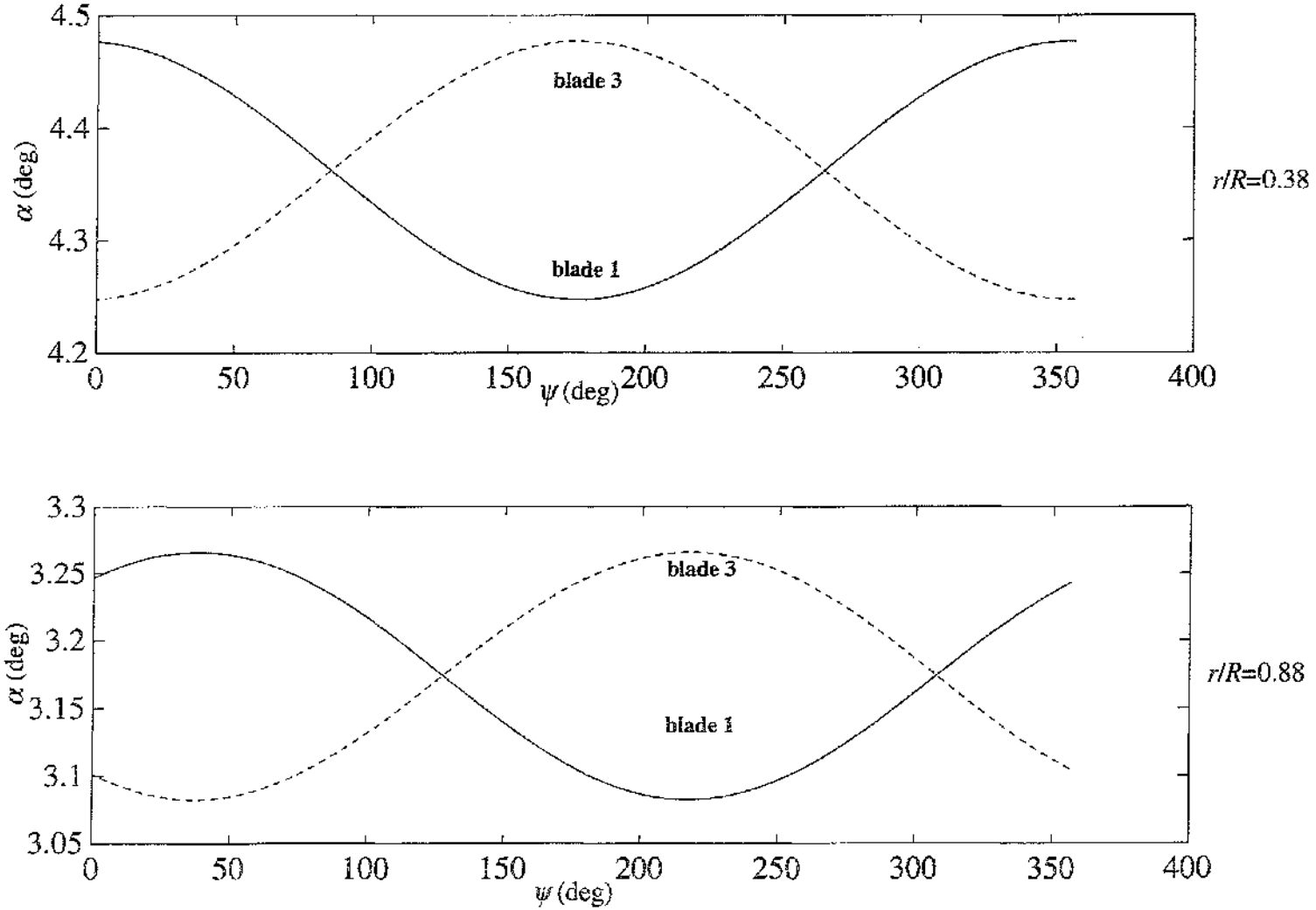

Figure 6.3 **Angle of Attack Variation with Respect to Blade Azimuthal Position in Hover**

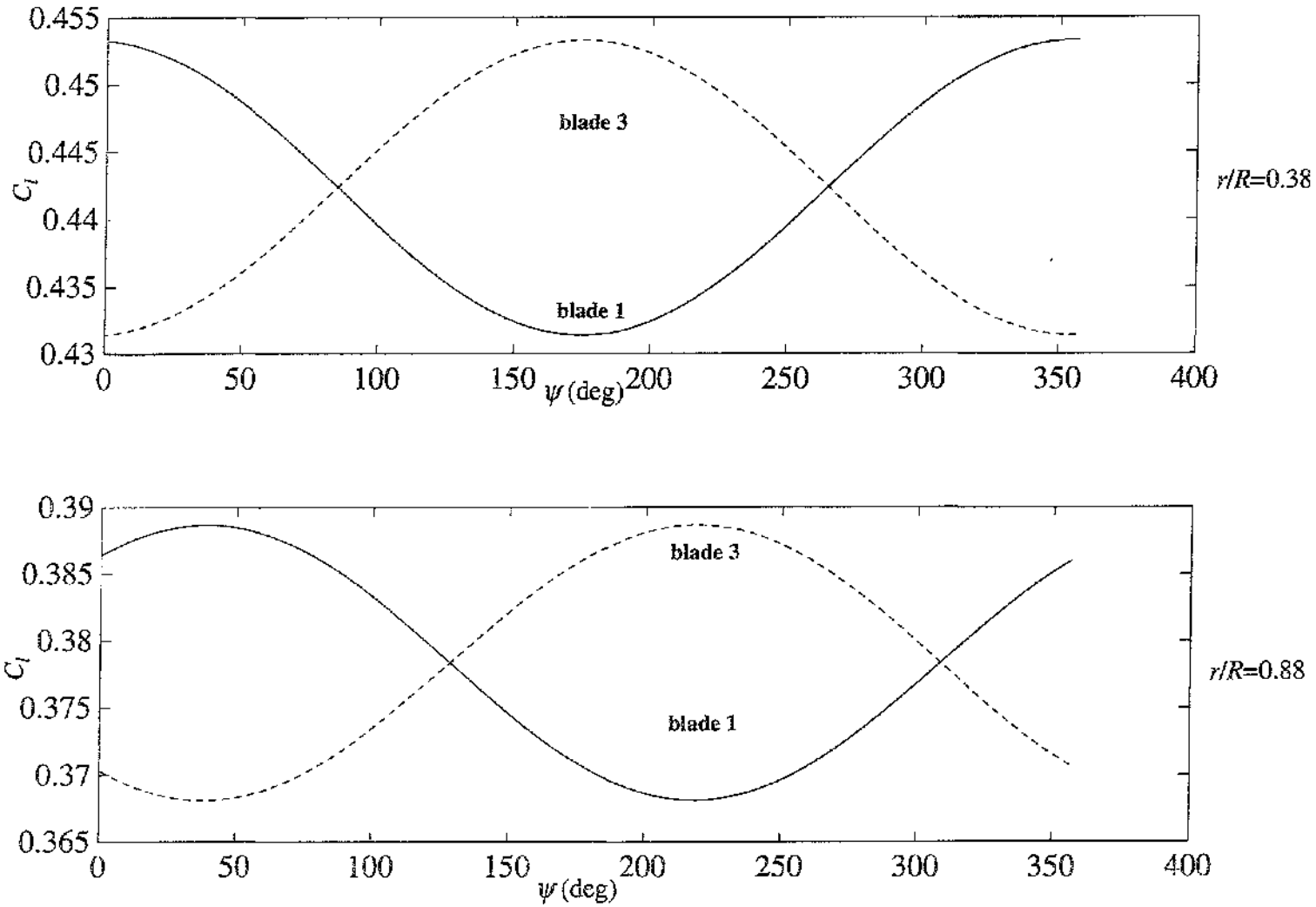

Figure 6.4 **Lift Coefficient Variation with Respect to Blade Azimuthal Position in Hover**

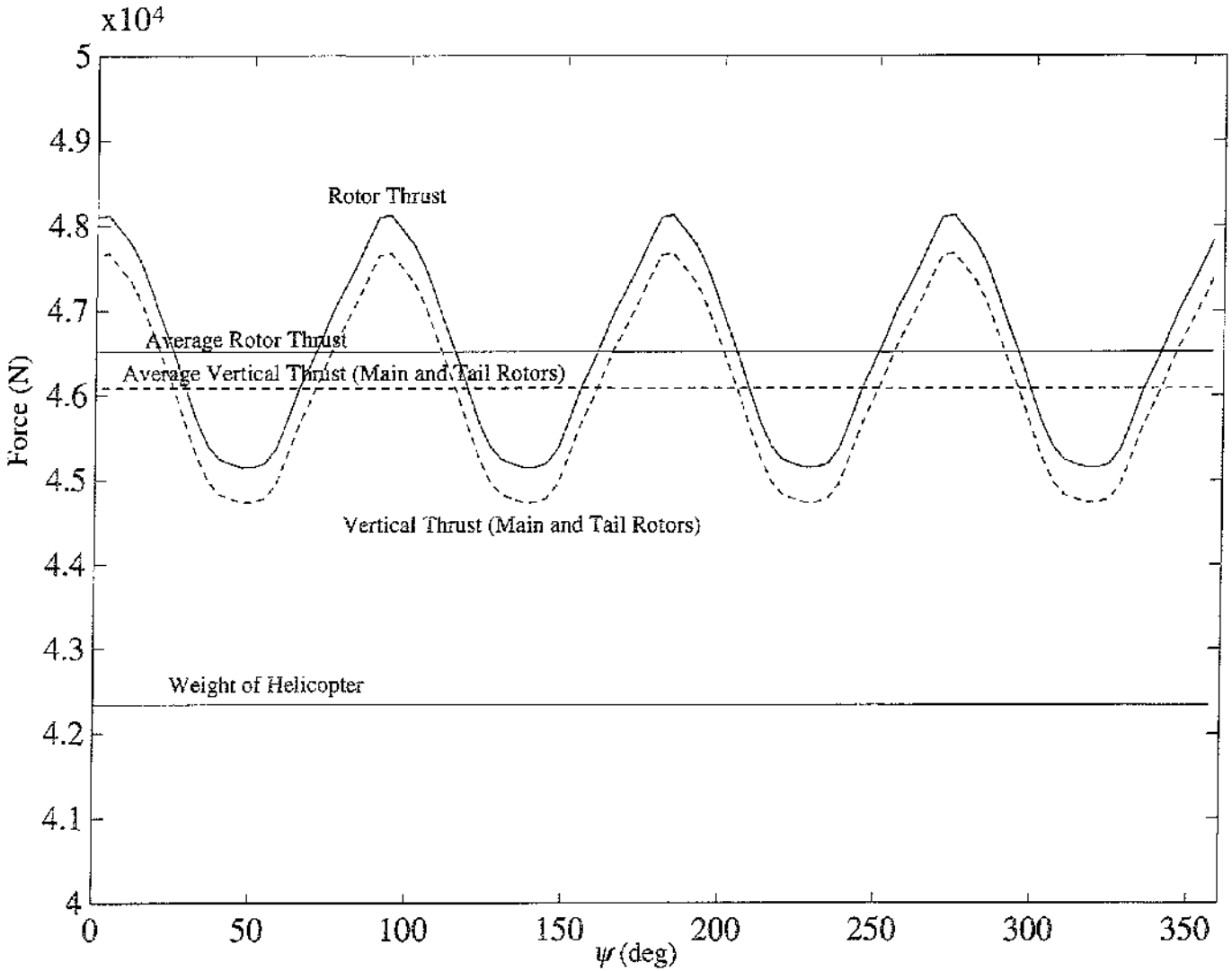

Figure 6.5 **Comparison Between Total Rotor Thrust and Total Vertical Thrust Predicted by Hibrom at 160 knots, and the Helicopter Weight**

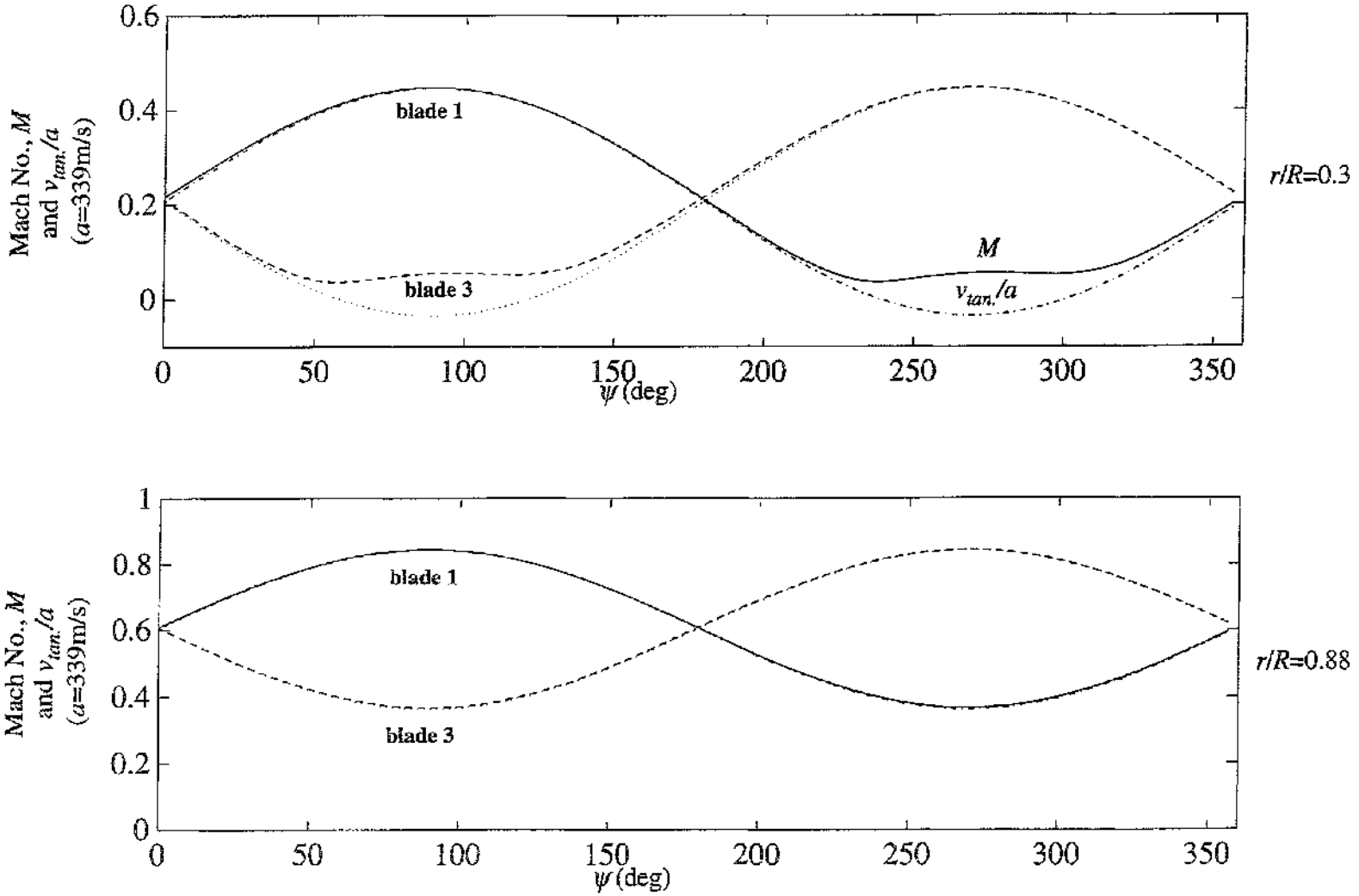

Figure 6.6 **Mach Number and Non-Dimensionialised Tangential Velocity Variation with Respect to Blade Azimuthal Position at 160 knots**

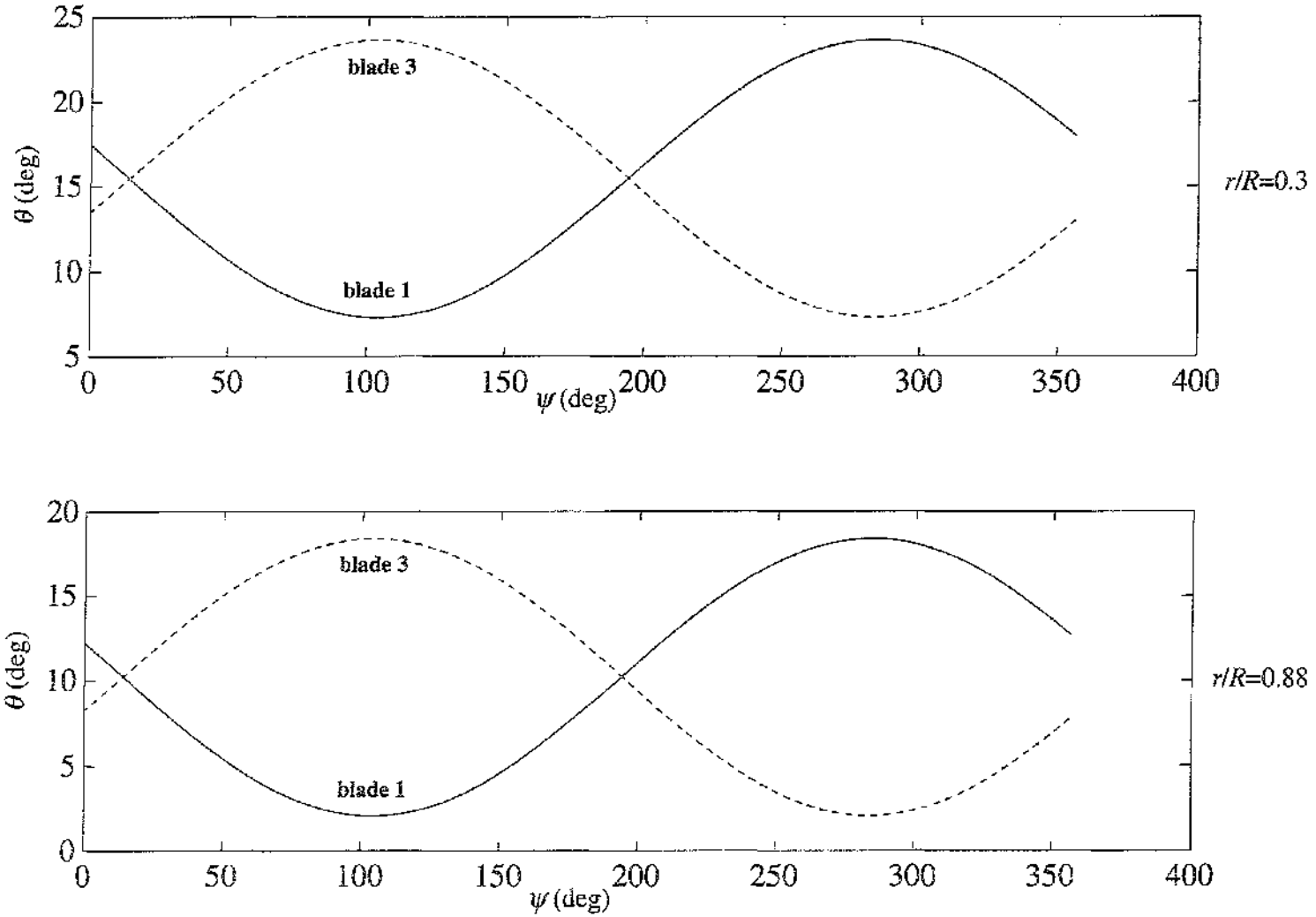

Figure 6.7 **Angle of Pitch Variation with Respect to Blade Azimuthal Position at 160 knots**

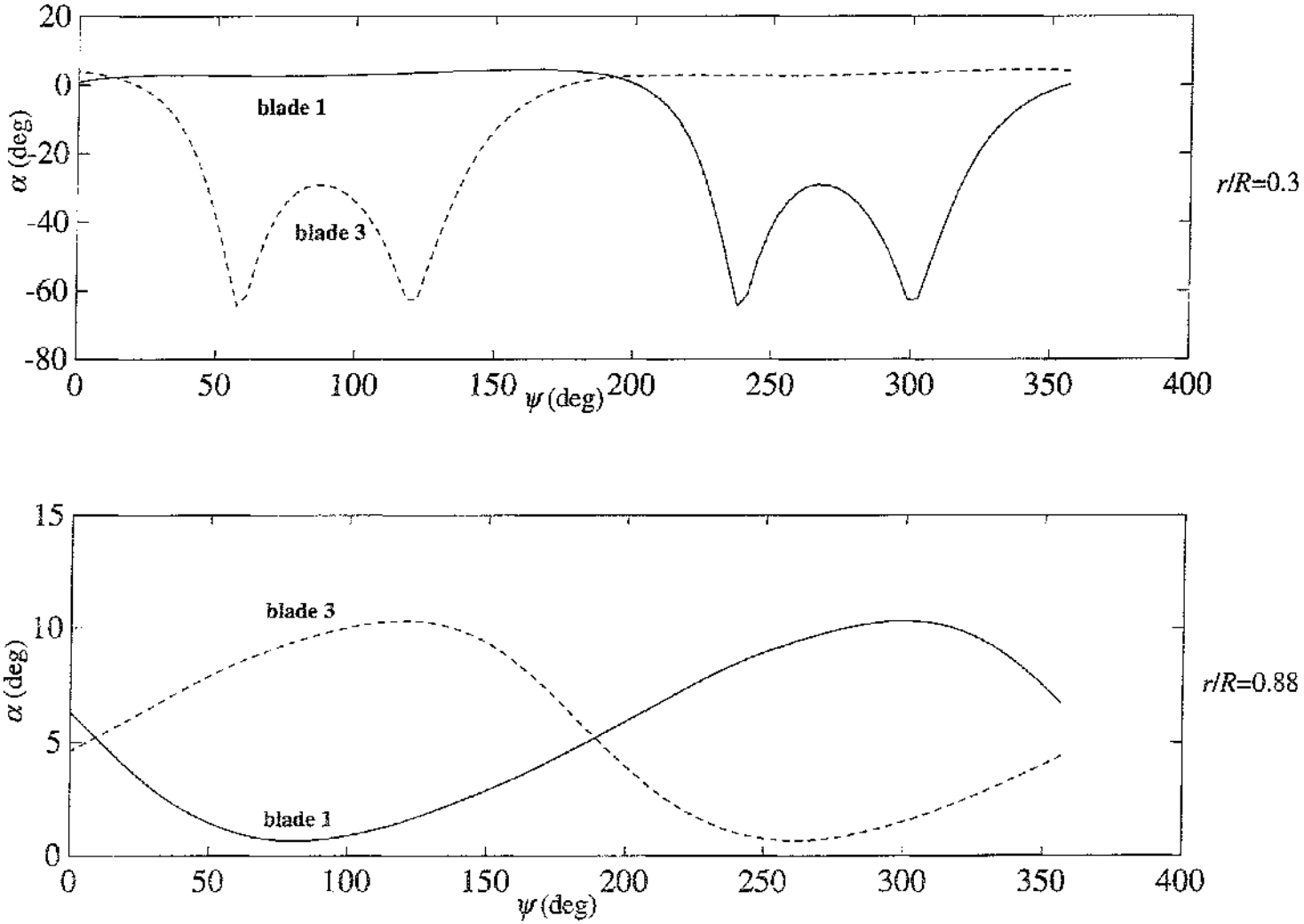

Figure 6.8 **Angle of Attack Variation with Respect to Blade Azimuthal Position at 160 knots**

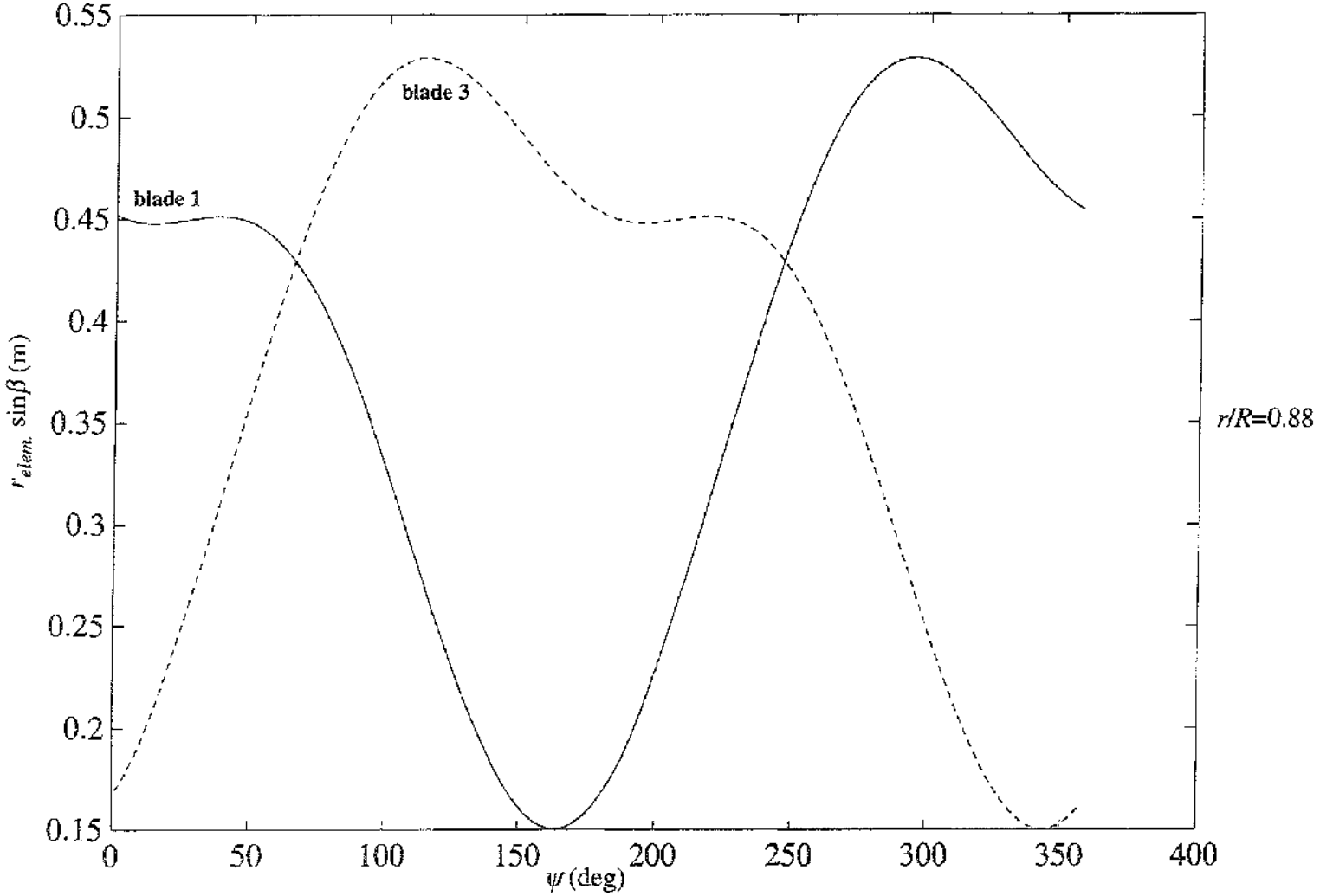

Figure 6.9 **Height Variation with Respect to Blade Azimuthal Position at 160 knots**

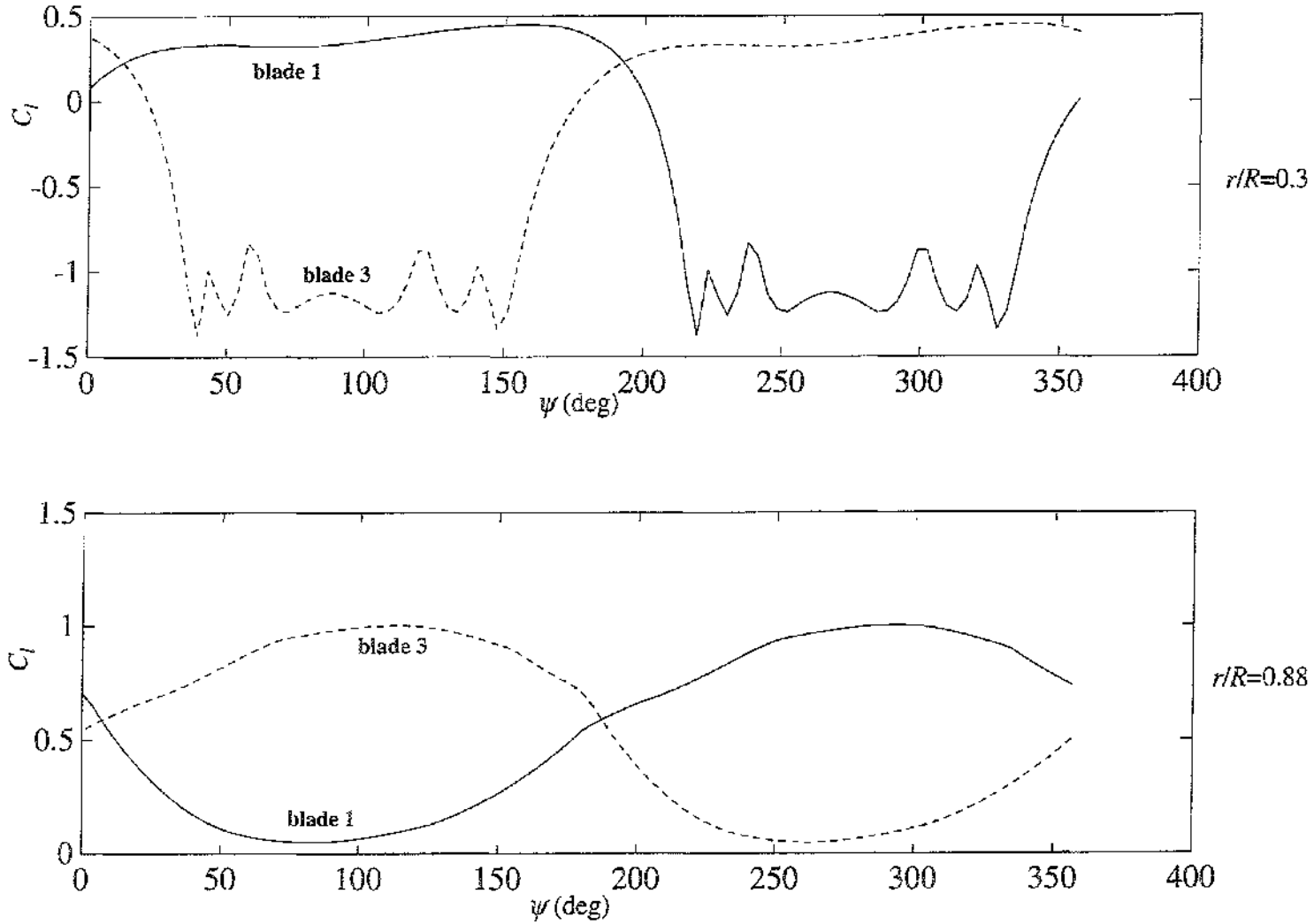

Figure 6.10 **Lift Coefficient Variation with Respect to Blade Azimuthal Position at 160 knots**

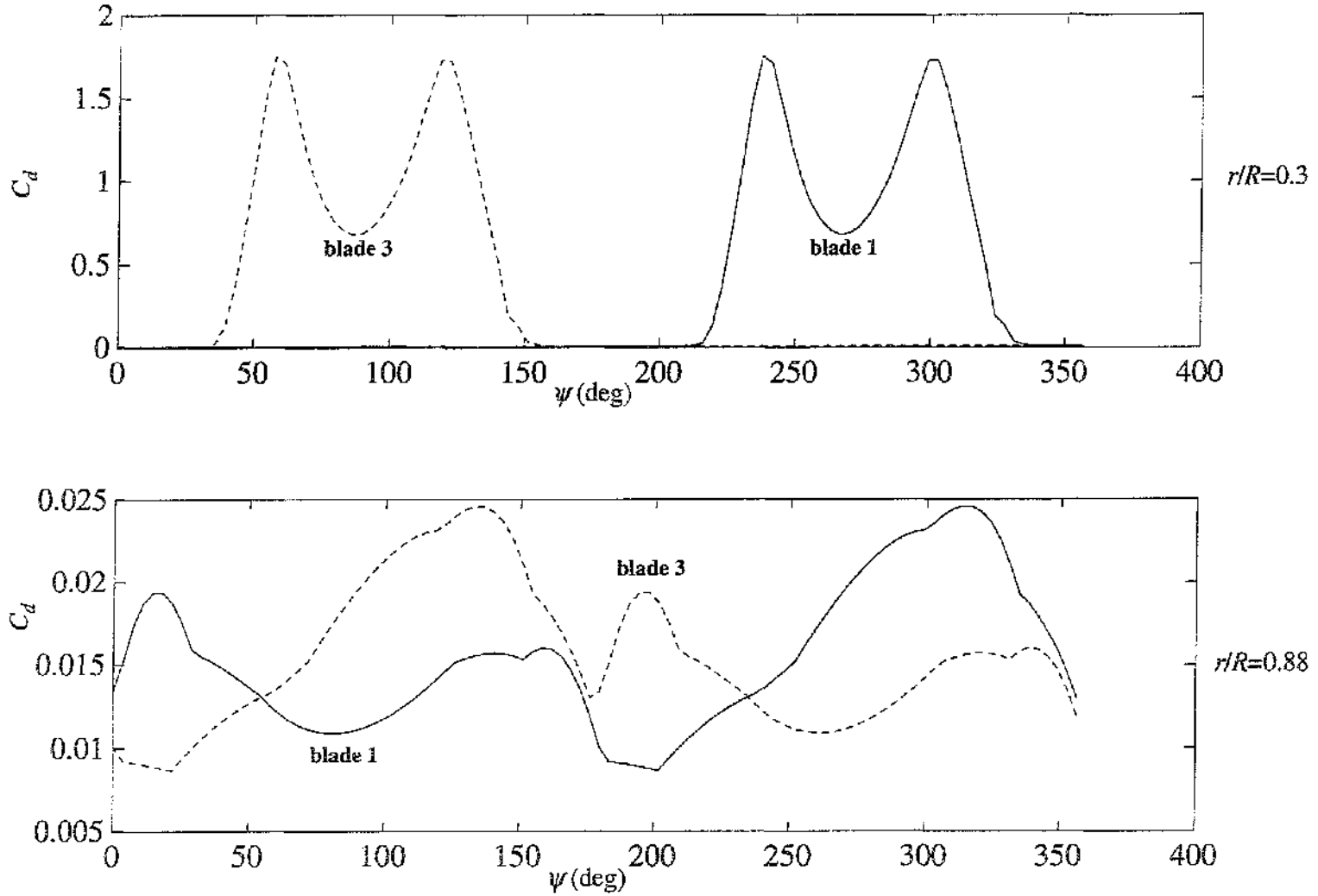

Figure 6.11 **Drag Coefficient Variation with Respect to Blade Azimuthal Position at 160 knots**

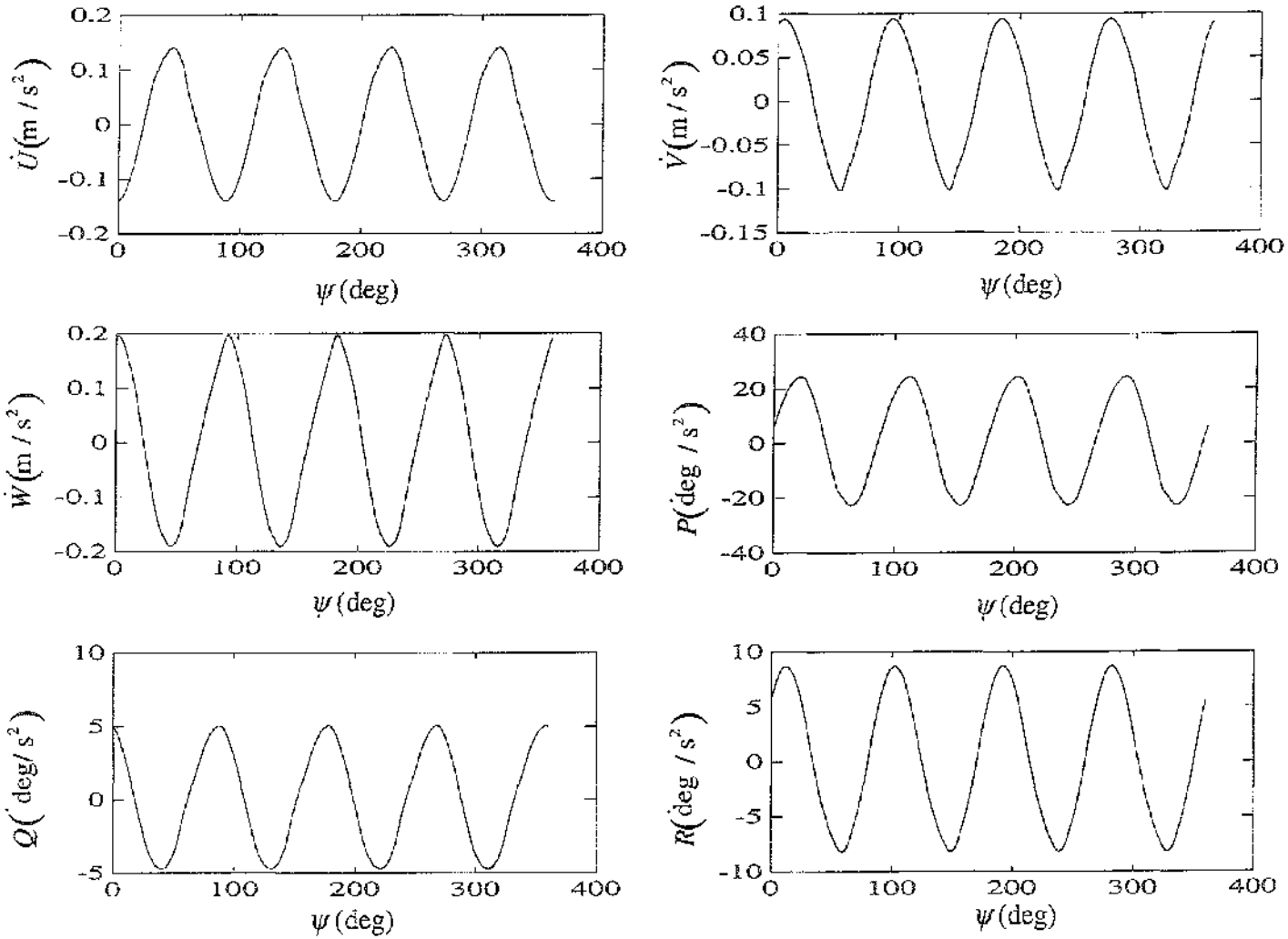

Figure 6.12 **Variation of Body Translational and Rotational Accelerations with Respect to Blade Azimuthal Position at 160 knots**

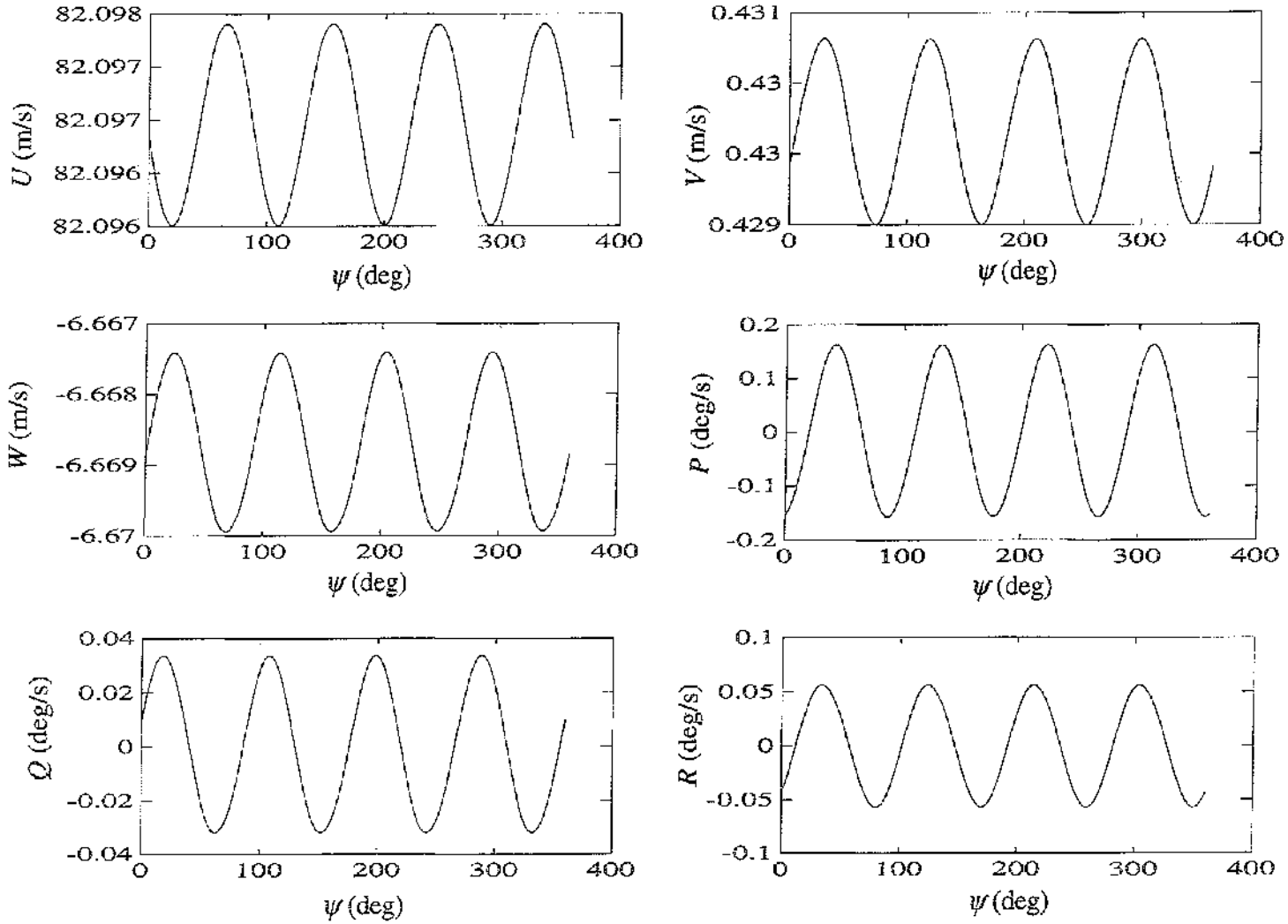

Figure 6.13 **Variation of Body Translational and Rotational Velocities with Respect to Blade Azimuthal Position at 160 knots**

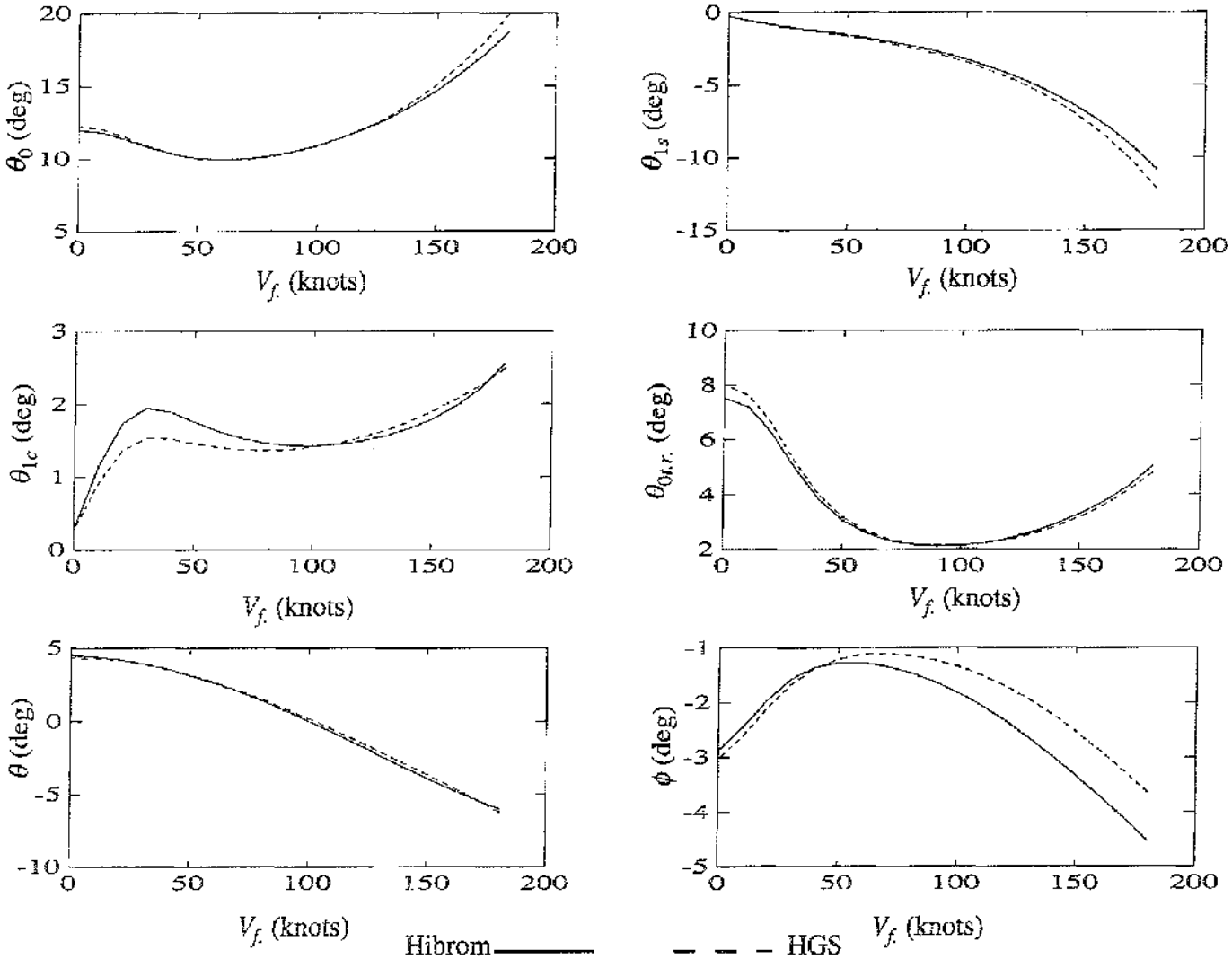

Figure 6.14 **Westland Lynx Trim Controls and Attitudes for 0 to 180 knots Forward Flight**

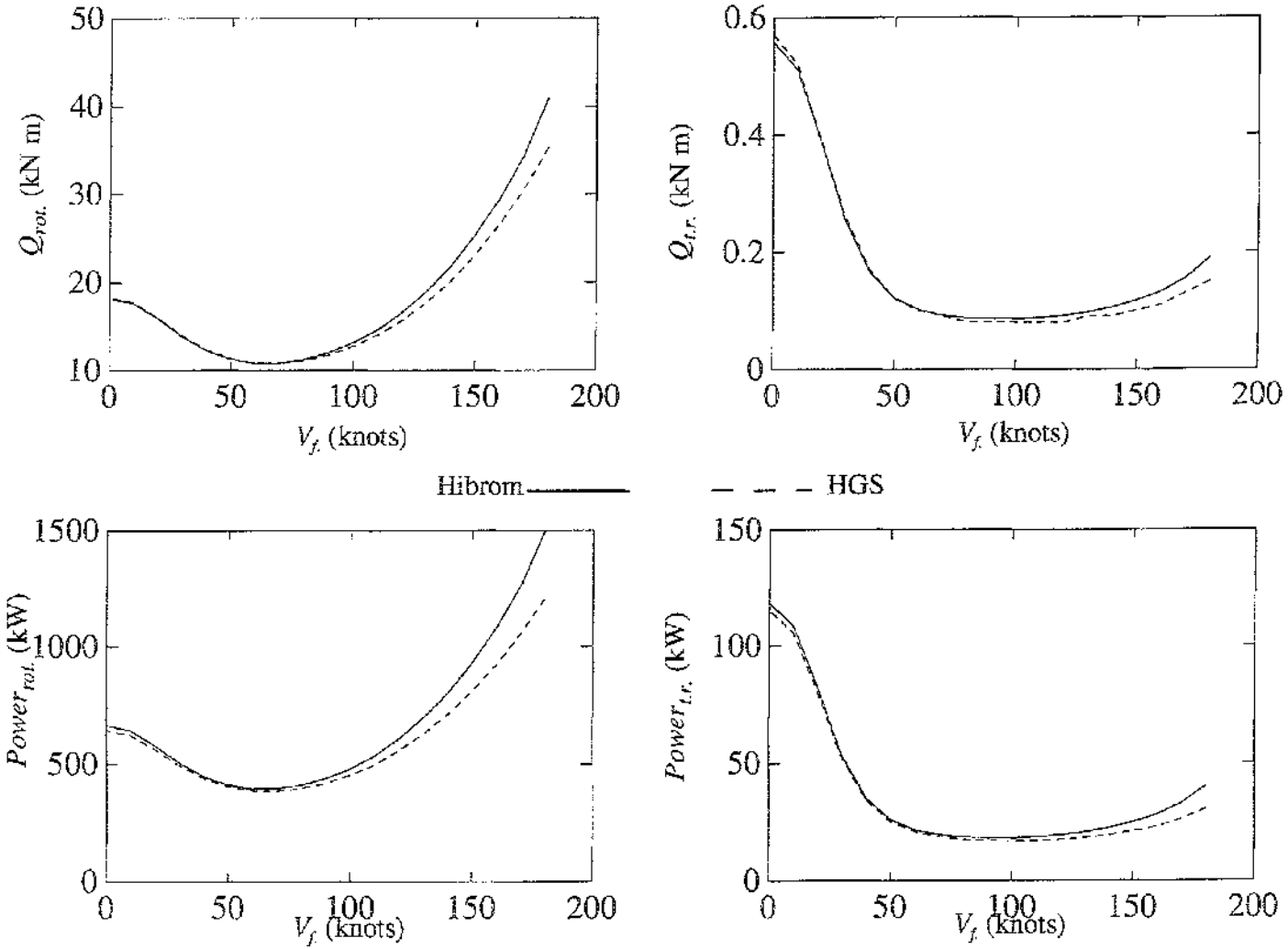

Figure 6.15 **Westland Lynx Trim Main and Tailrotor Torque and Power from 0 to 180 knots Forward Flight**

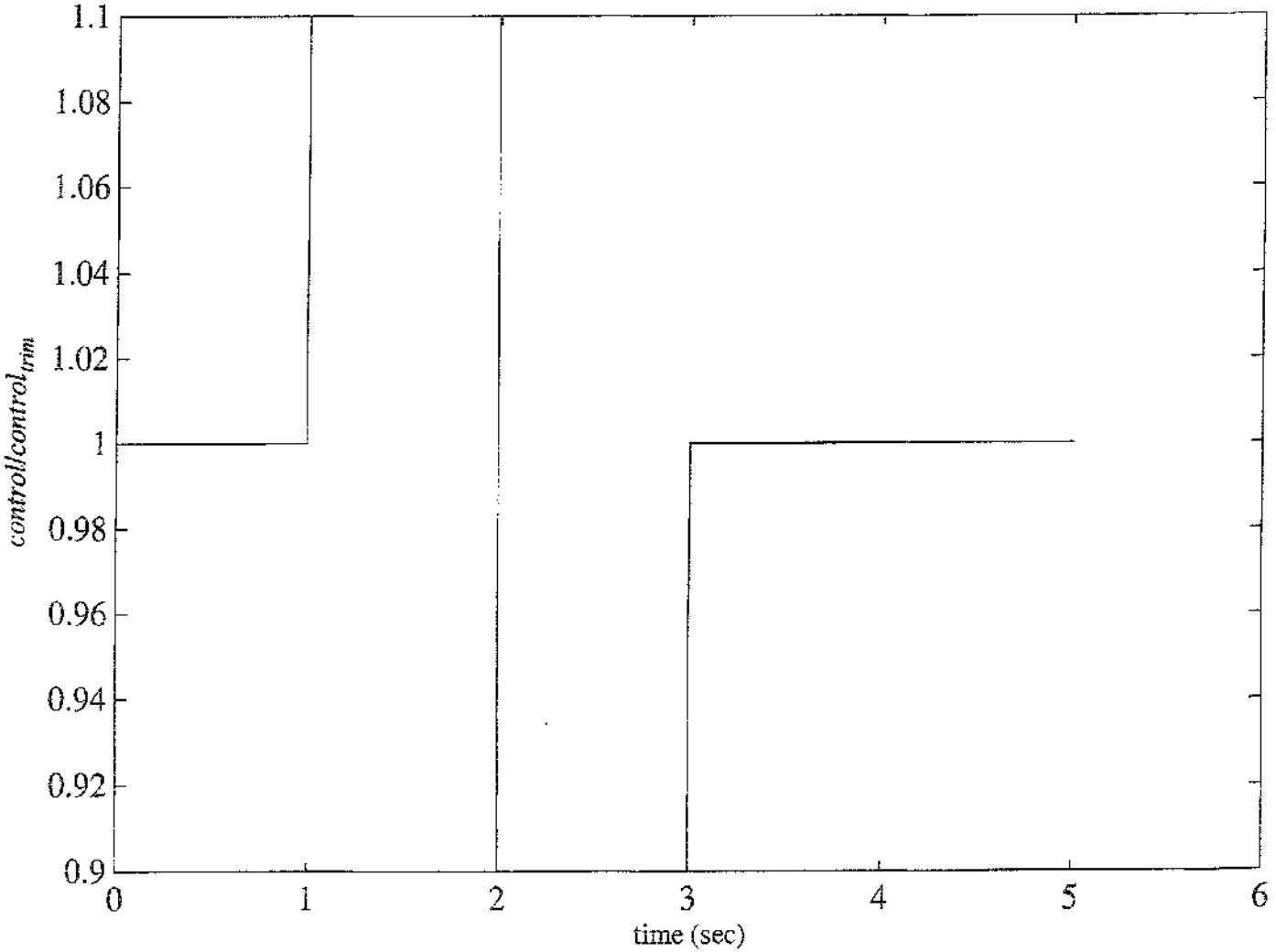

Figure 6.16 **Doublet Control Input (+/-10%)**

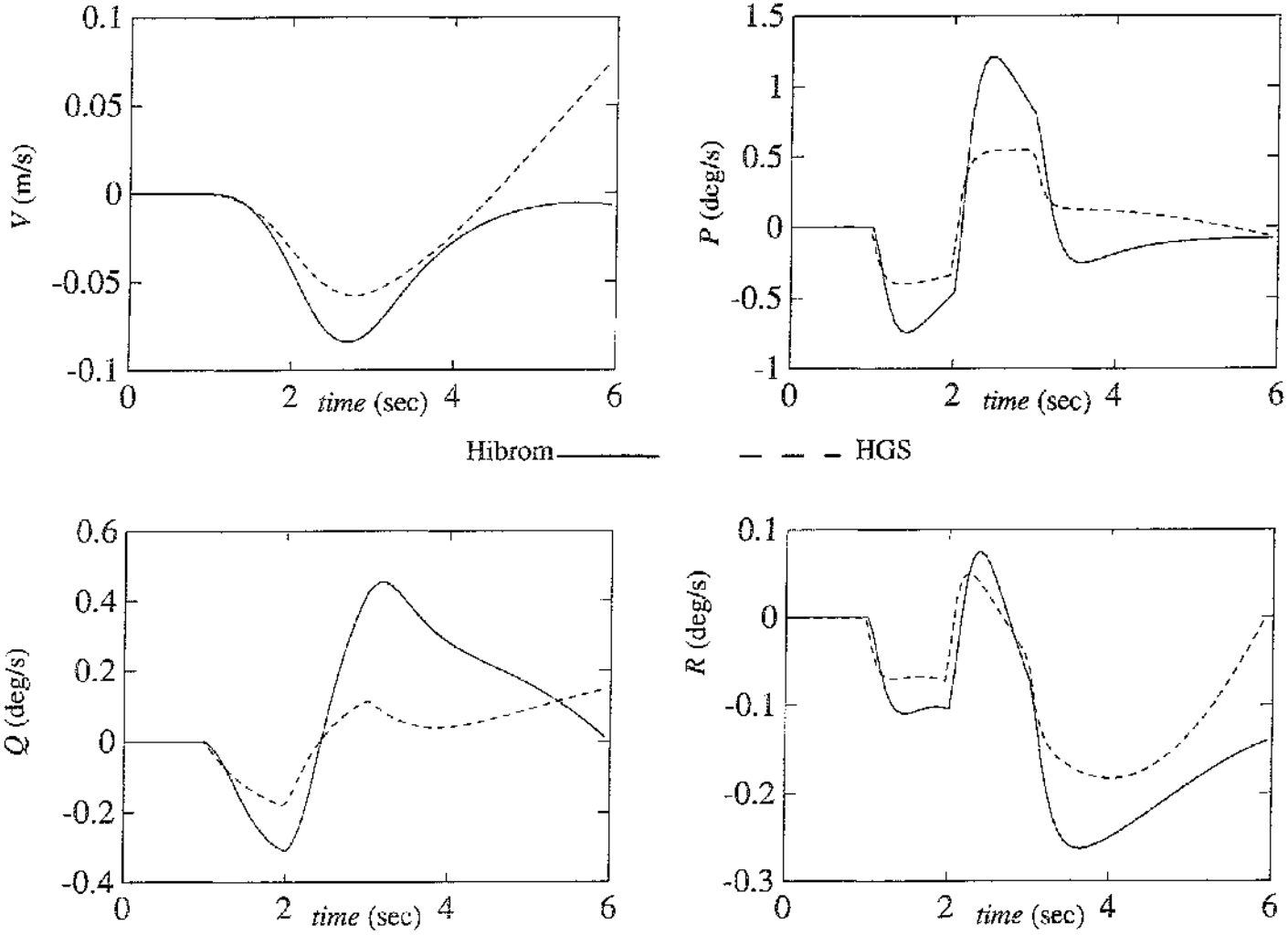

Figure 6.17 **Open Loop Response of Westland Lynx to Doublet in Lateral Cyclic from Hover**

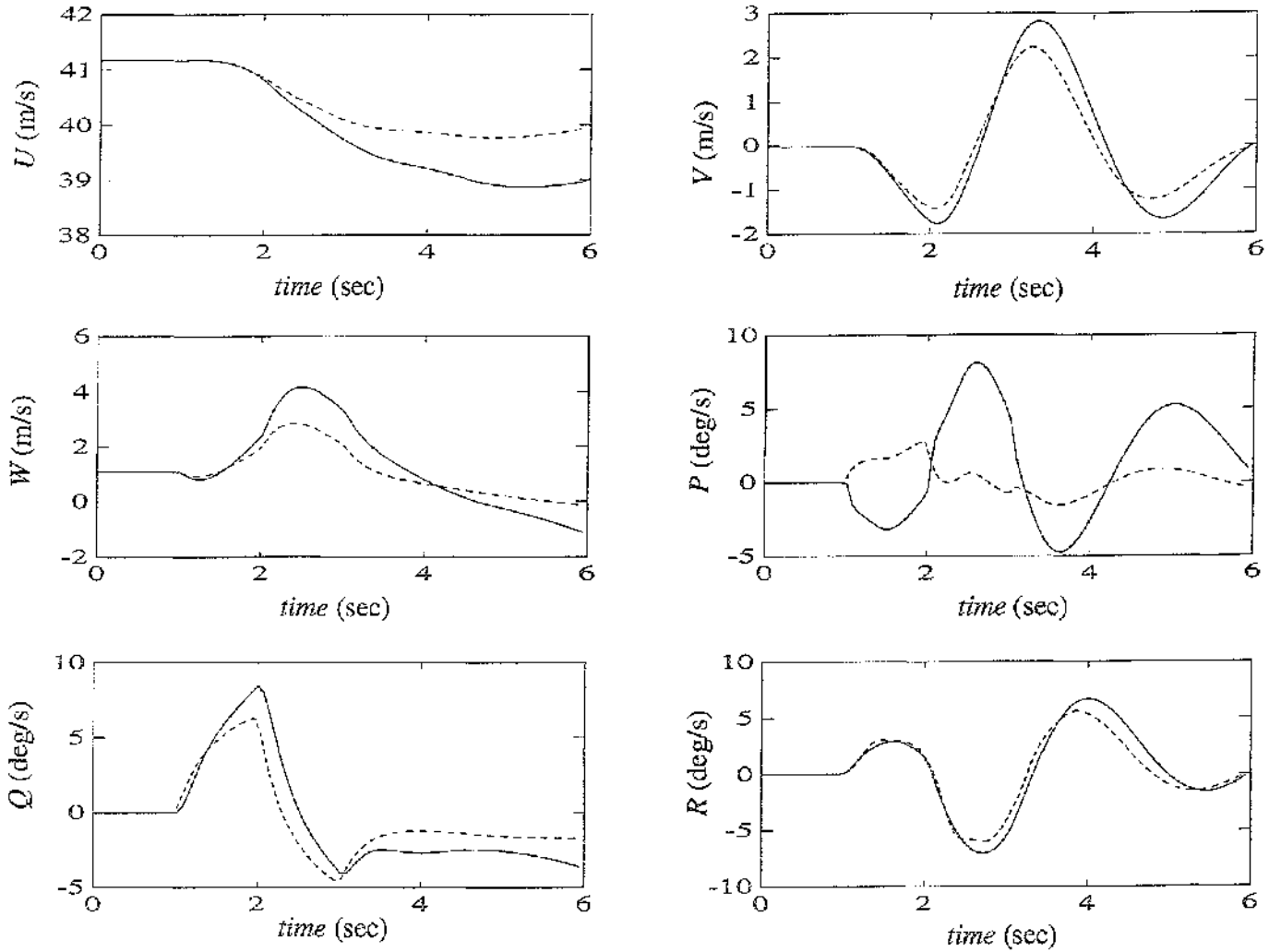

Figure 6.18 **Westland Lynx Open Loop Response to Doublet in Collective at 80 knots Forward Flight**

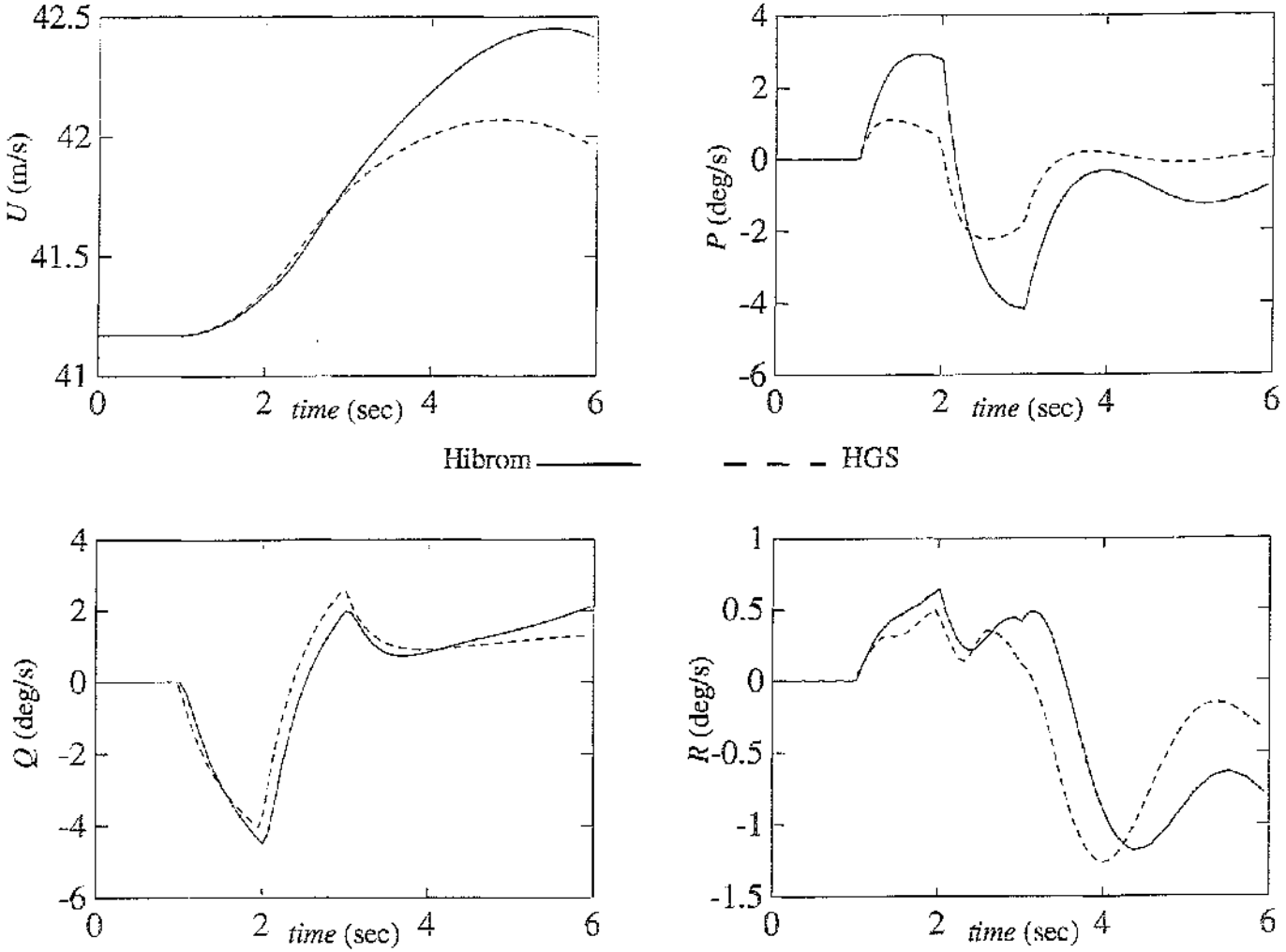

Figure 6.19 **Open Loop Response of Westland Lynx to Doublet in Longitudinal Cyclic from 80 knots Forward Flight**

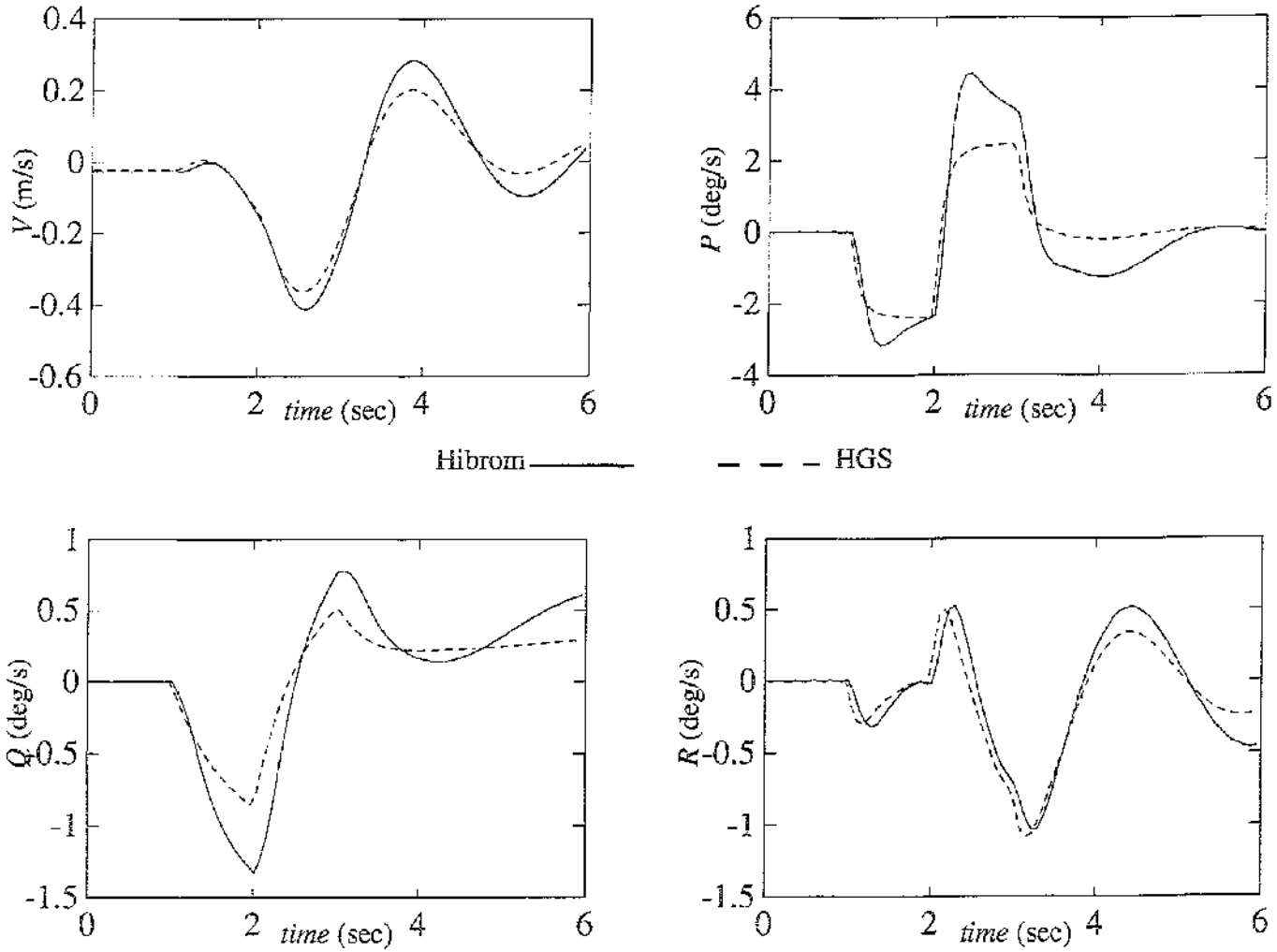

Figure 6.20 **Open Loop Response of Westland Lynx to Doublet in Lateral Cyclic from 80 knots Forward Flight**

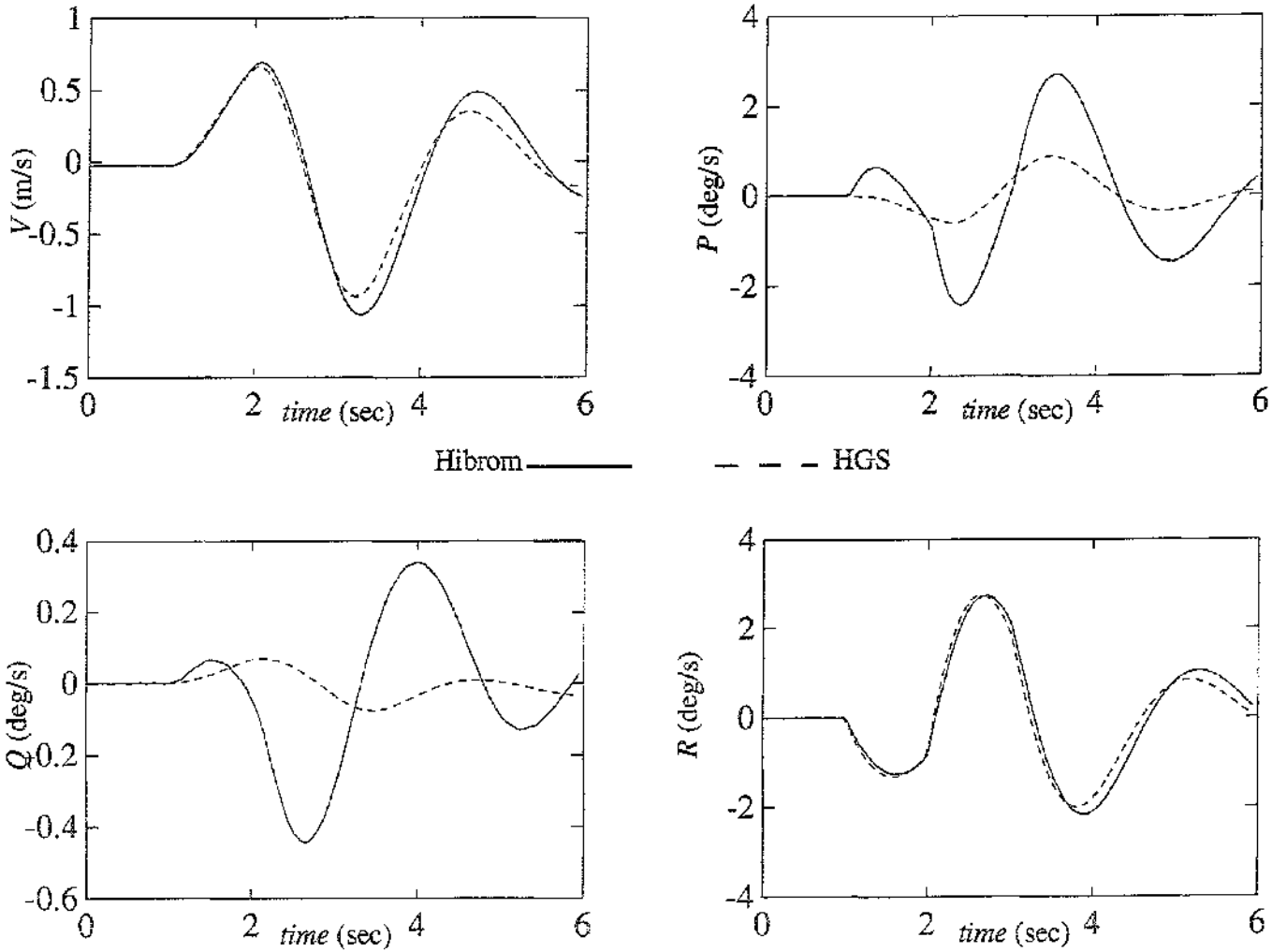

Figure 6.21 **Open Loop Response of Westland Lynx to Doublet in Tail Rotor Collective from 80 knots Forward Flight**

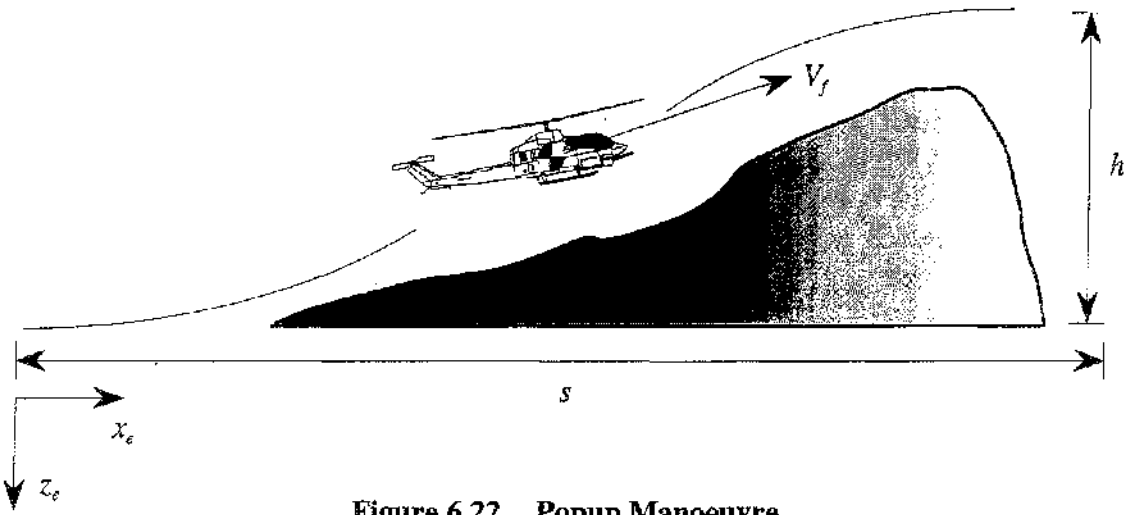

Figure 6.22 **Popup Manoeuvre**

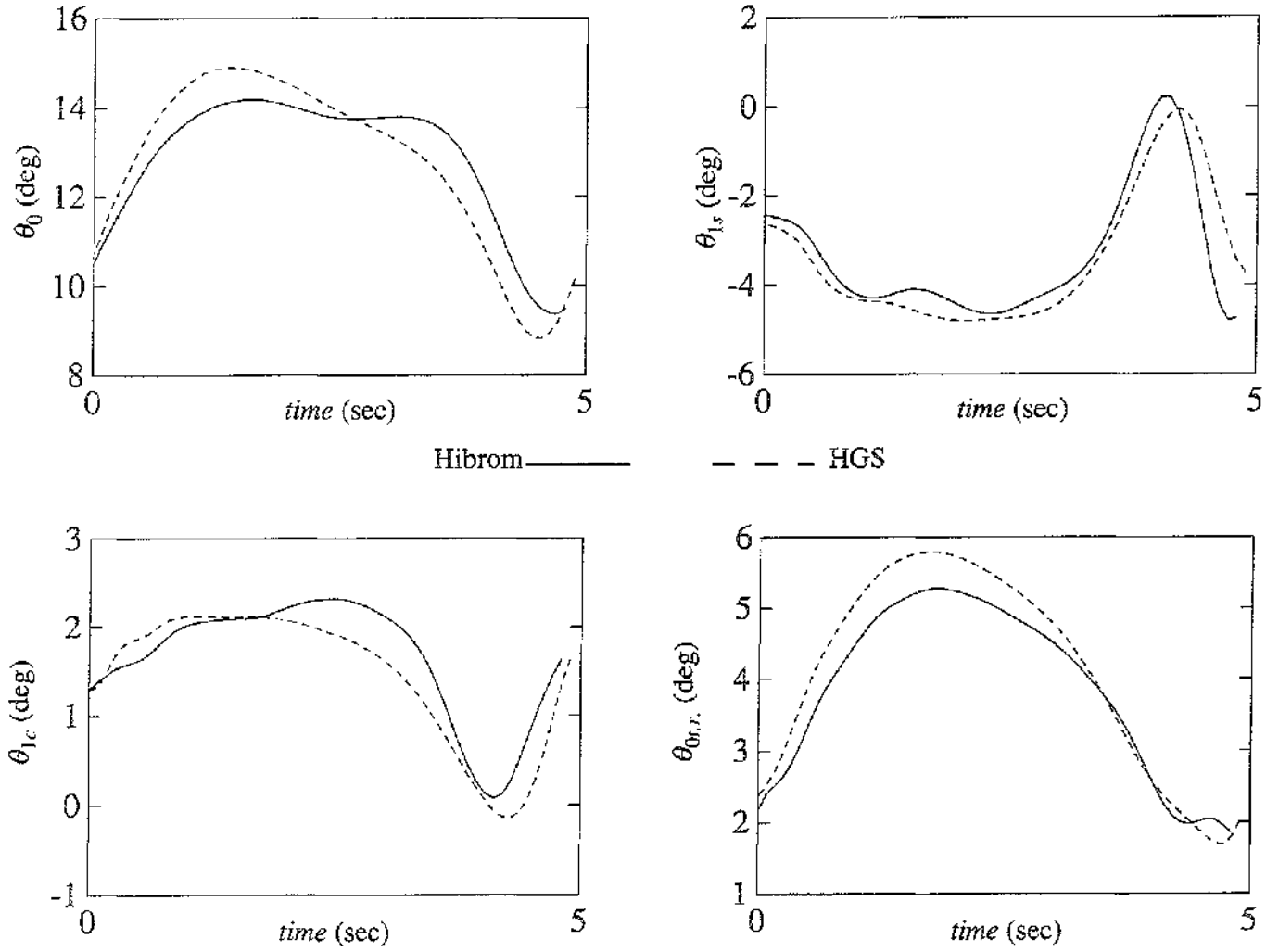

Figure 6.23 **Inverse Simulation Control Time Histories for a Pop-Up Manoeuvre (s=200m, h=25m, V_f=80kts) with Data for a Westland Lynx Helicopter**

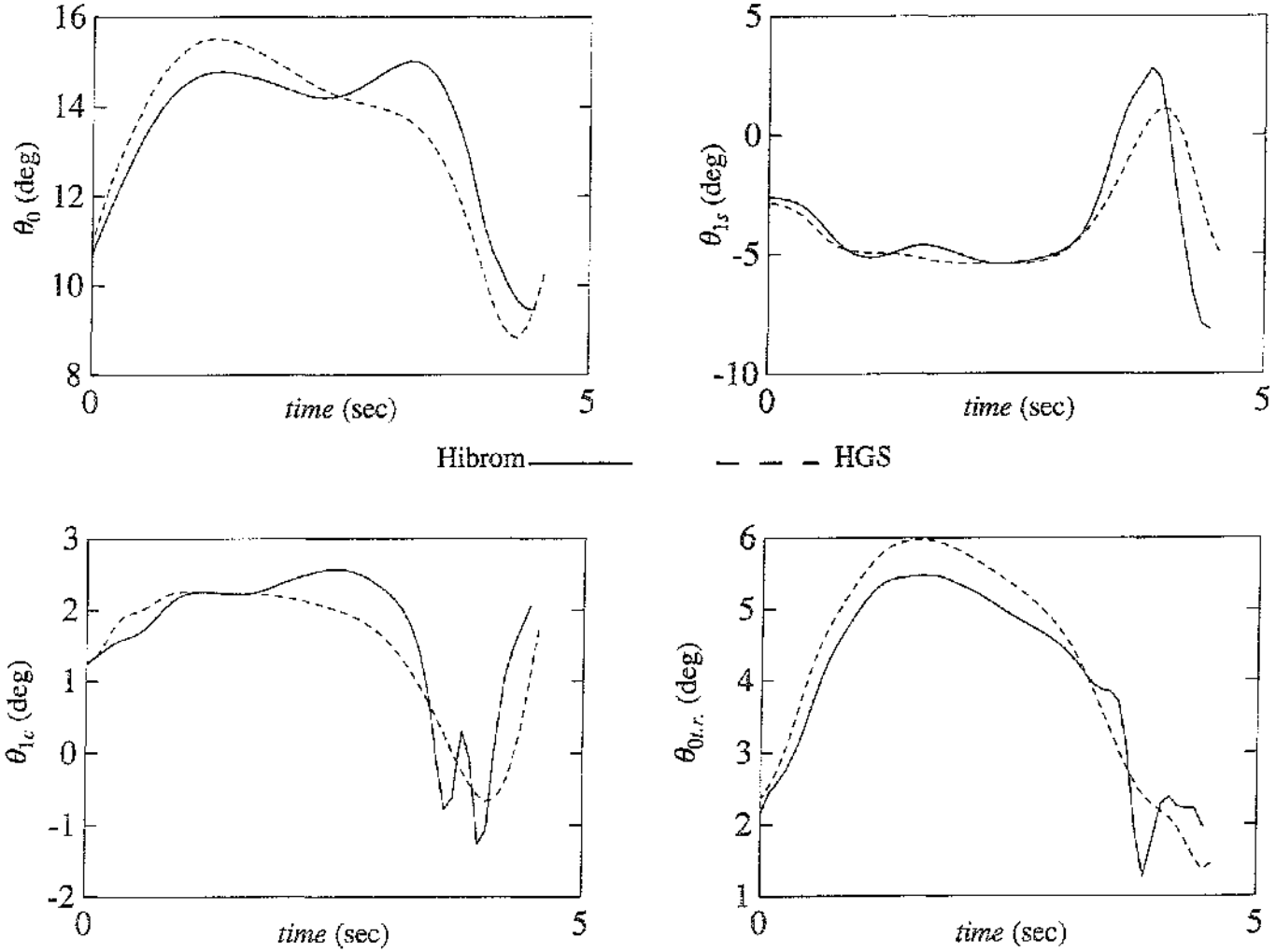

Figure 6.24 **Inverse Simulation Control Time Histories for a Pop-Up Manoeuvre (s=200m, h=25m, V_c=85kts) with Data for a Westland Lynx Helicopter**

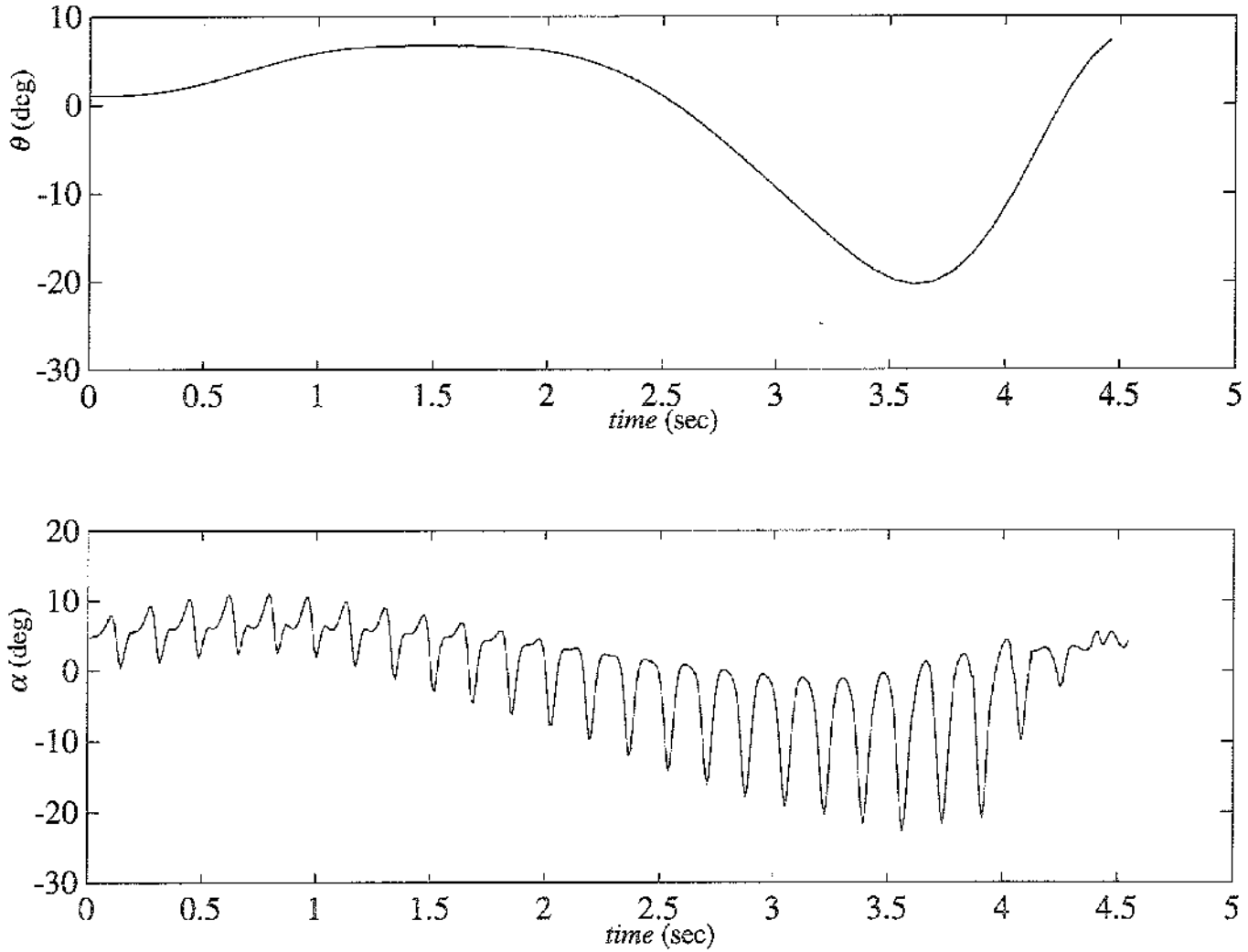

Figure 6.25 **Fuselage Pitch Angle and Blade Angle of Attack for a Pop-Up Manoeuvre (s=200m, h=25m, V_y=85kts) with Data for a Westland Lynx Helicopter**

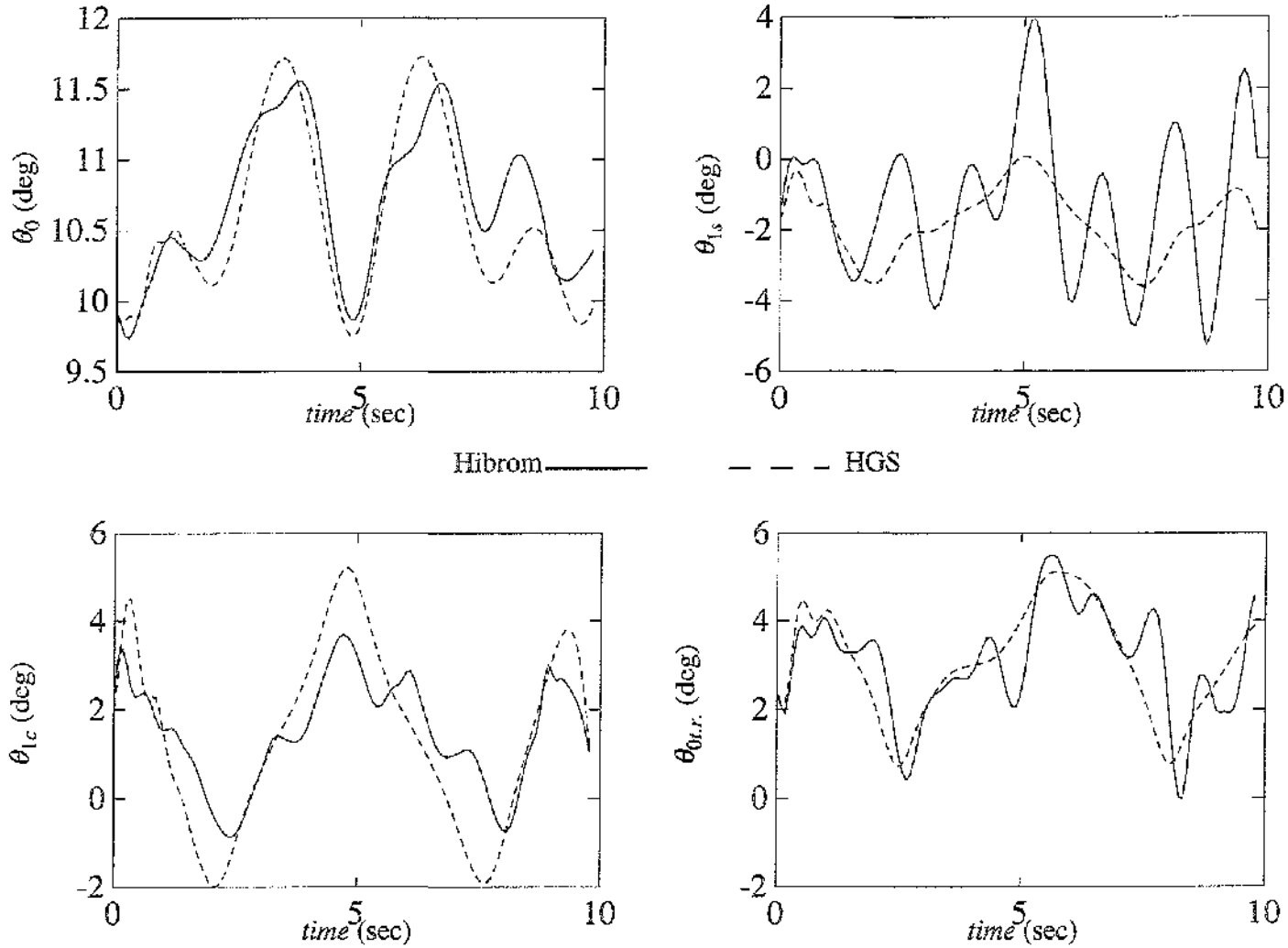

Figure 6.26 **Inverse Simulation Control Time Histories for a Slalom Manoeuvre (s=300m, h=10m, V_c=60kts, Δt=0.086sec) with Data for a Westland Lynx Helicopter**

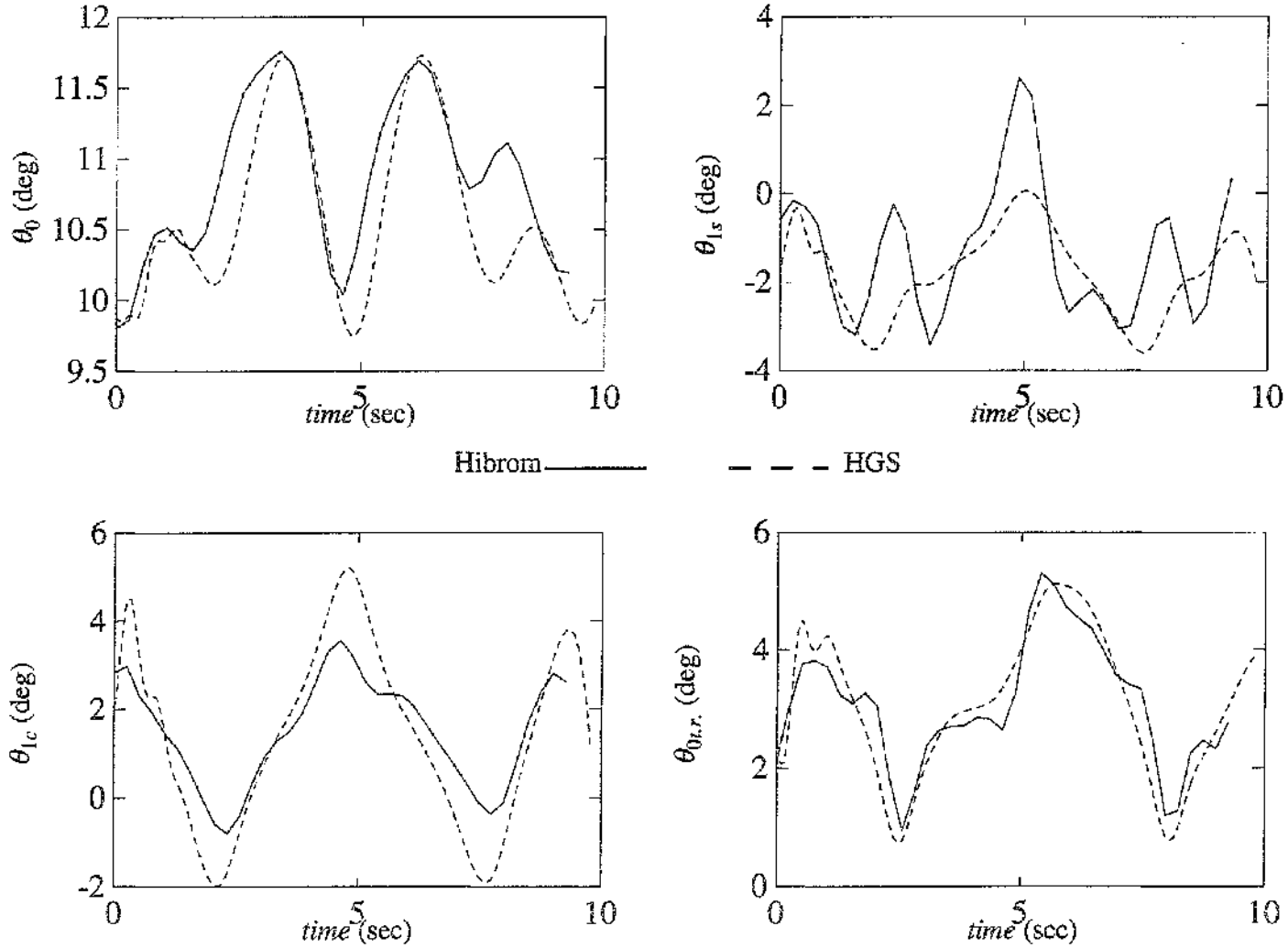

Figure 6.27 **Inverse Simulation Control Time Histories for a Slalom Manoeuvre (s=300m, h=10m, V_t=60kts, Δt=0.172sec) with Data for a Westland Lynx Helicopter**

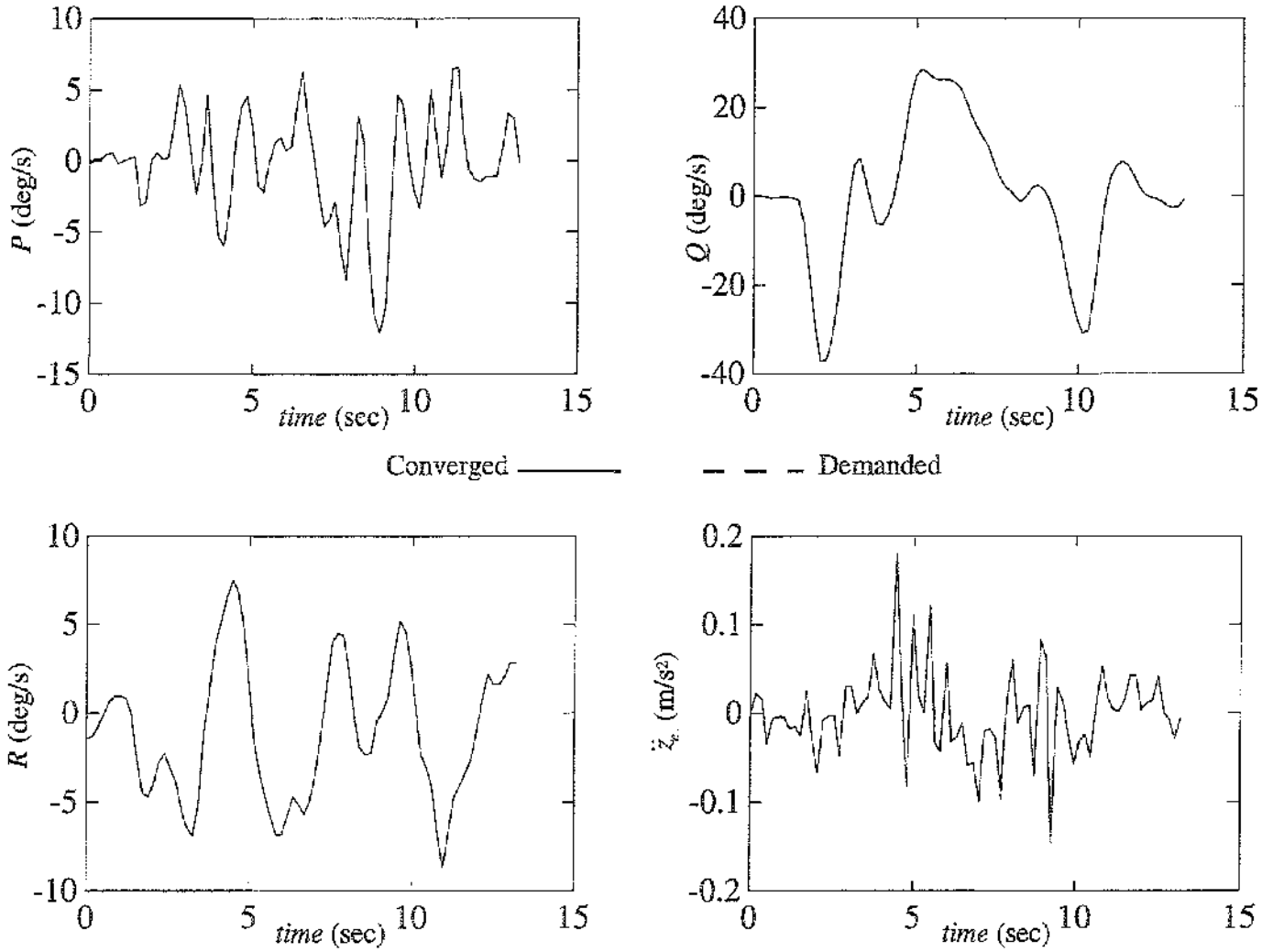

Figure 6.28 **Comparison Between Demanded Flight Path Parameters and Converged Values Calculated by Genisa**

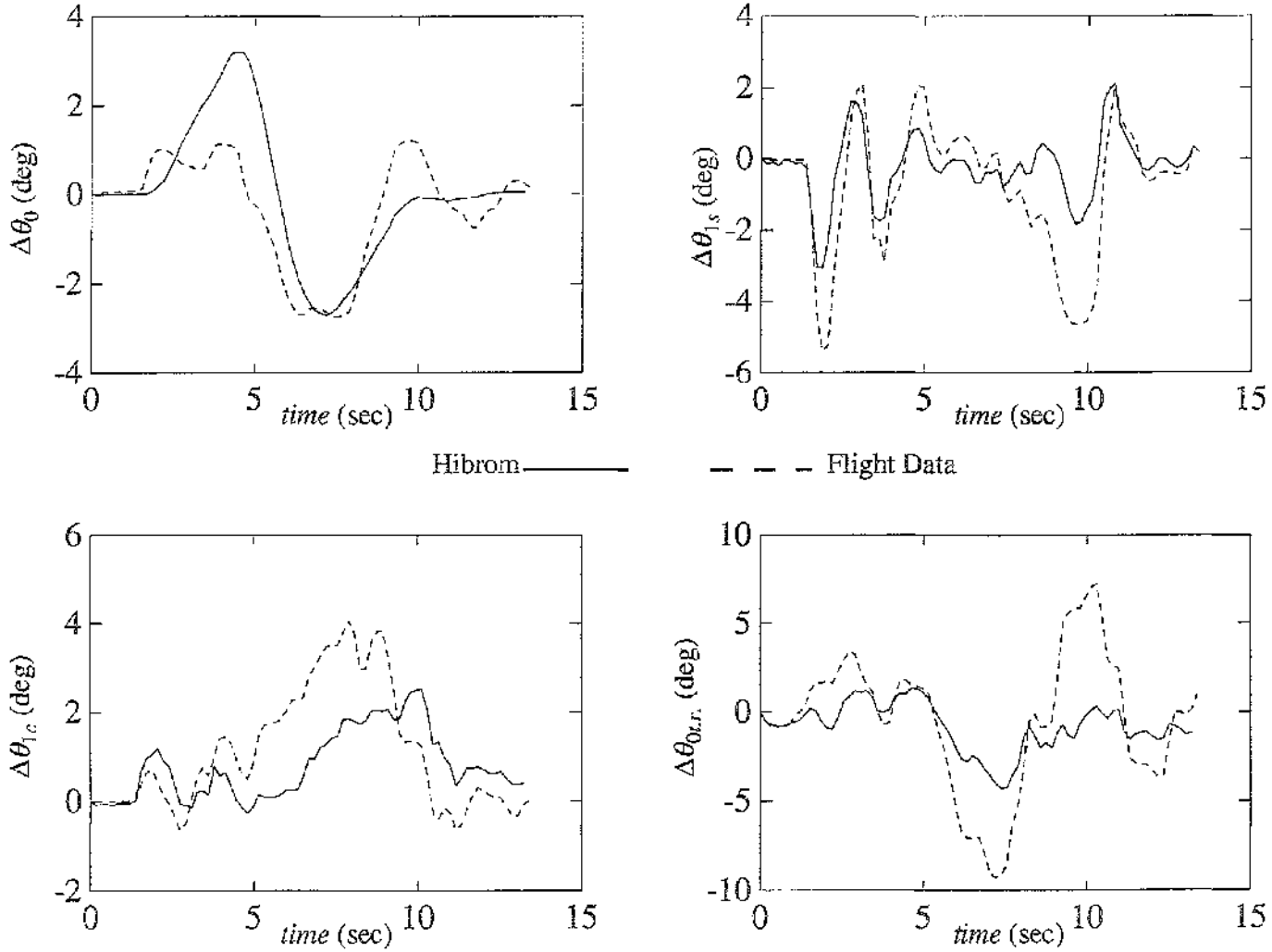

Figure 6.29 **Comparison Between Inverse Simulation Control Time Histories for a Quickhop Manoeuvre (*s*=91m) and Flight Test Data for a Westland Lynx Helicopter**

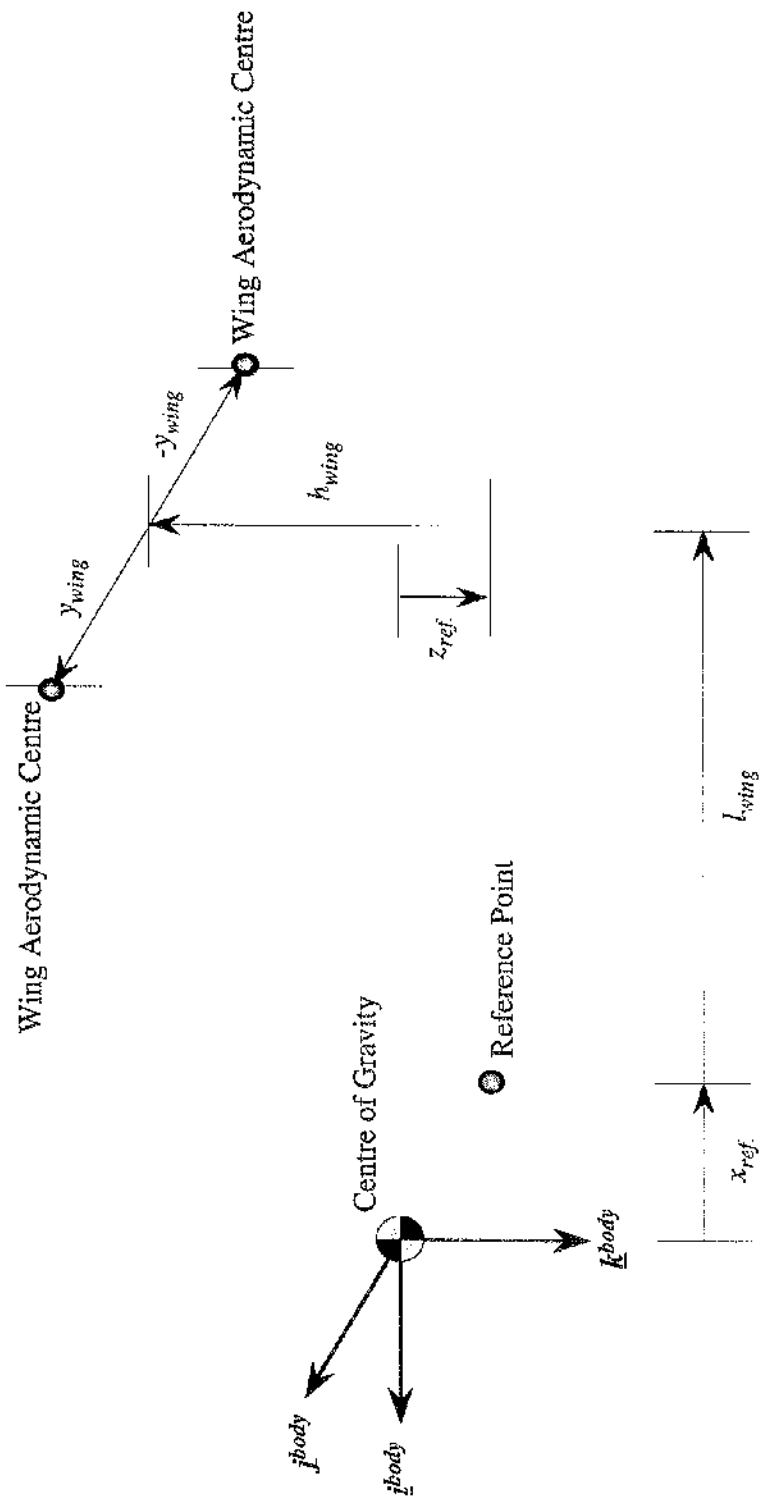

Figure 7.1 **Position of Wing Aerodynamic Centres in Body Axes**

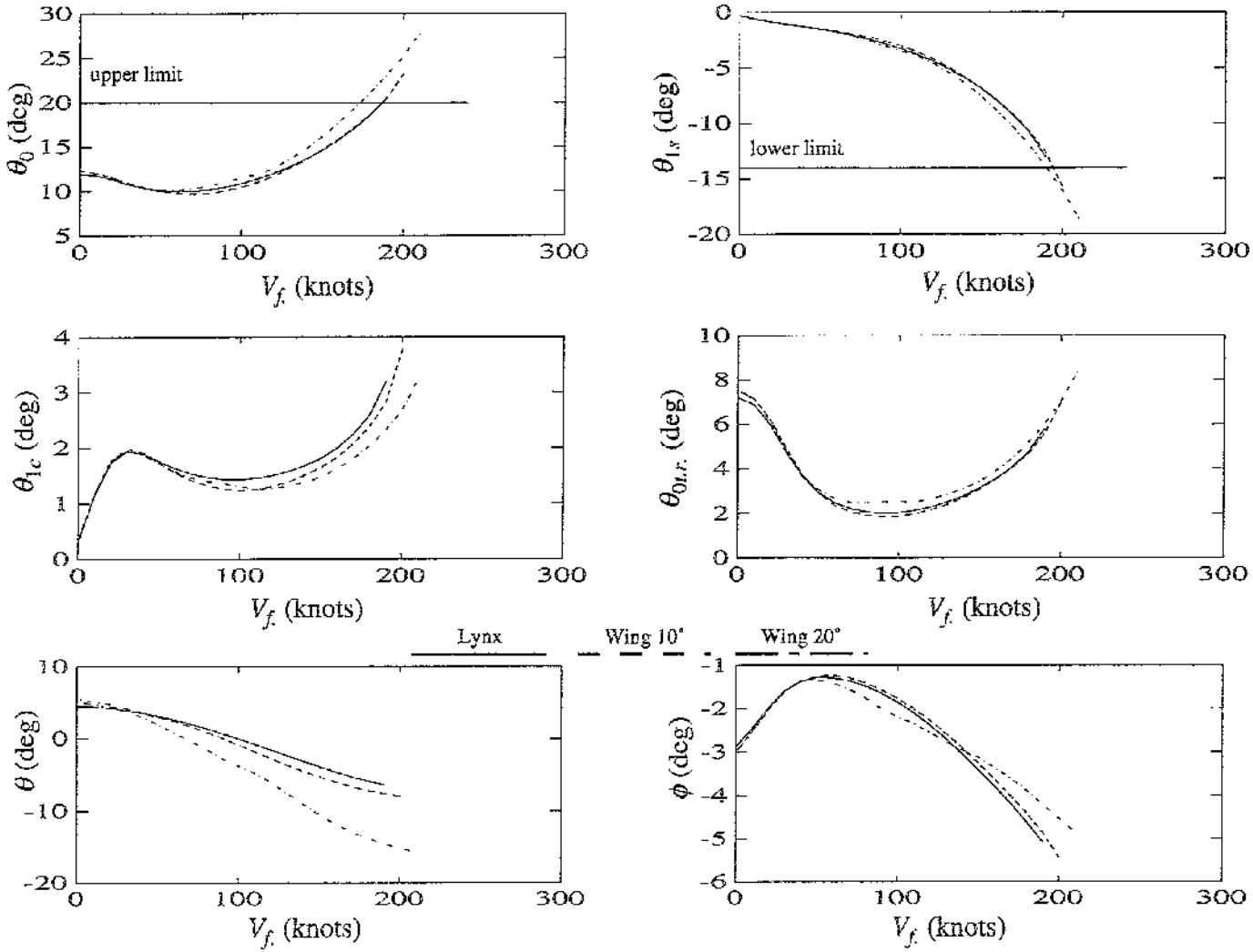

Figure 7.2 **Trim Controls and Attitudes for Westland Lynx without Wing and Wings Inclined at 10 and 20 Degrees**

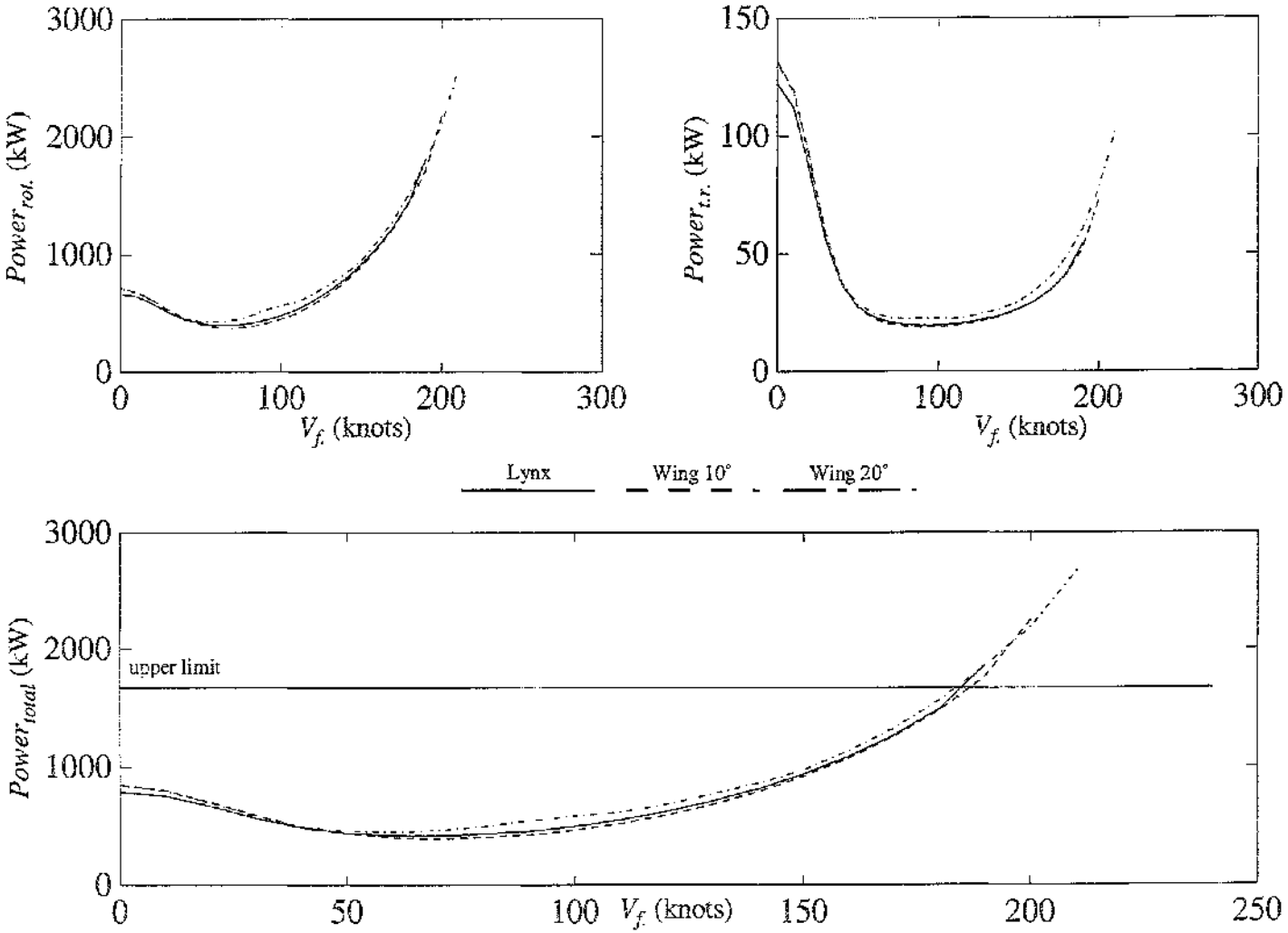

Figure 7.3 **Trim Rotor, Tail Rotor and Total Power for Lynx without Wing, and Wing Inclined at 10° and 20°.**

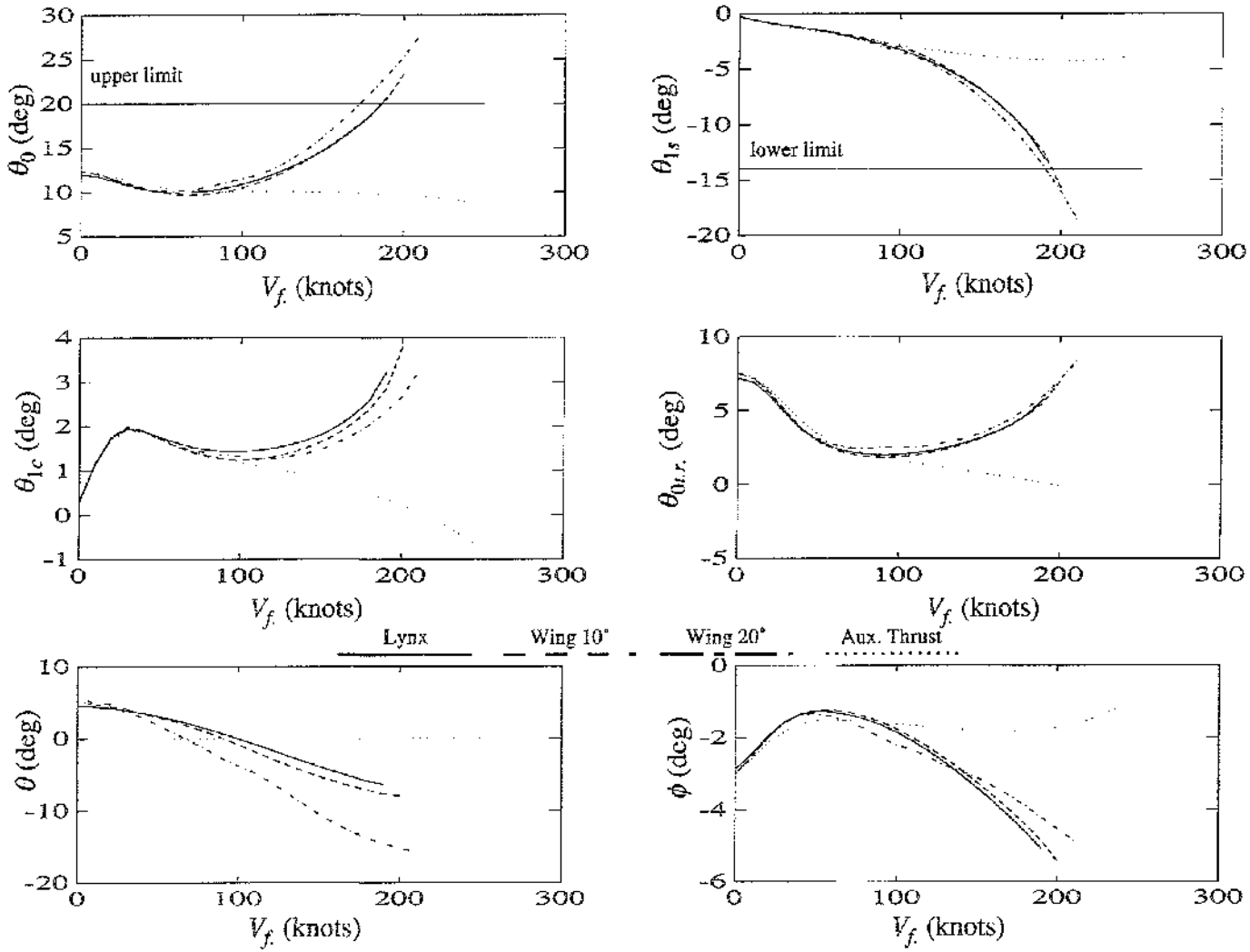

Figure 7.4 **Trim Controls and Attitudes for Westland Lynx without Wing, with Wing Inclined at 10 and 20 Degrees, and with Auxiliary Thrust**

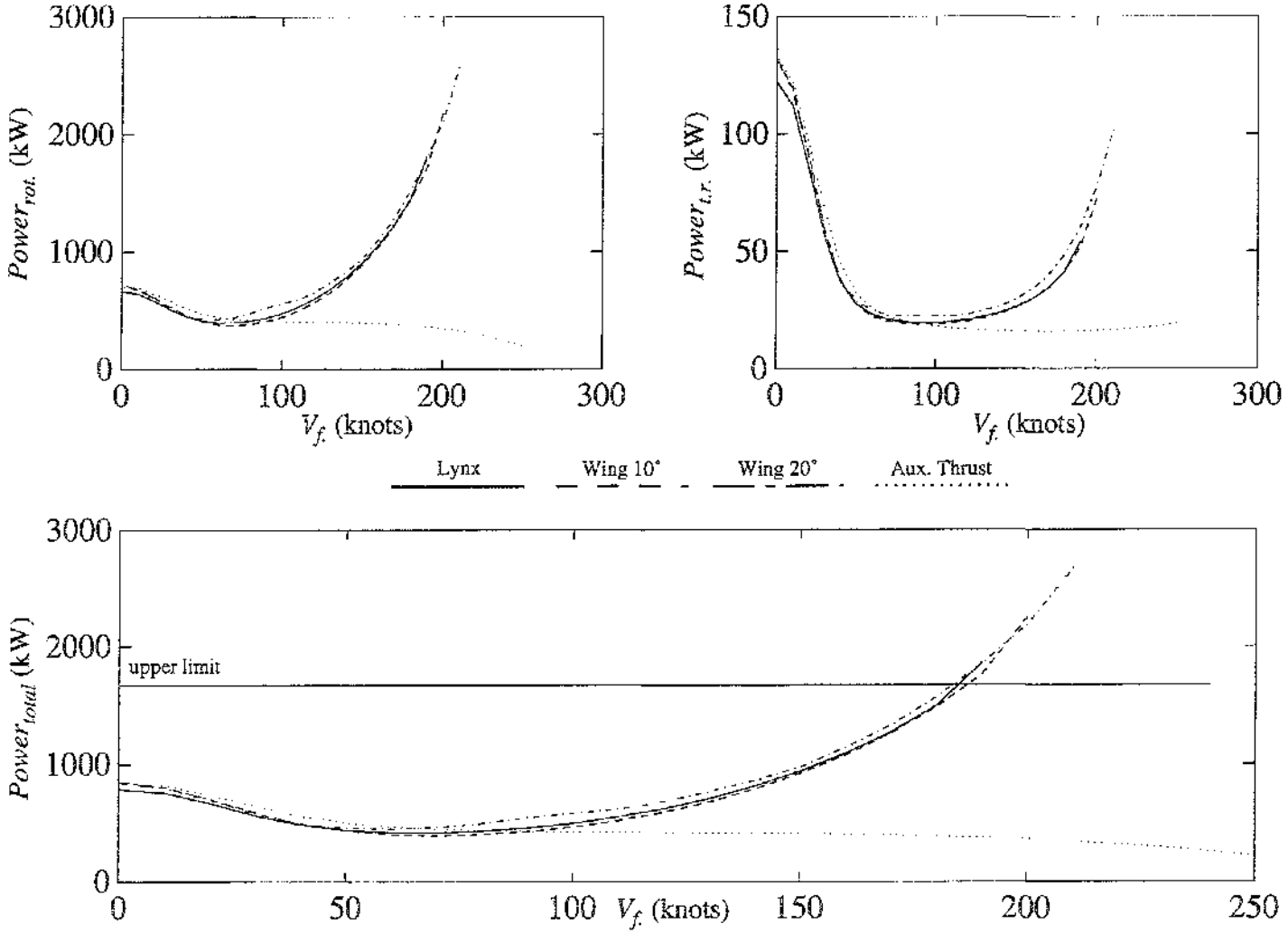

Figure 7.5 **Trim Rotor, Tail Rotor and Total Power for Lynx without Wing, with Wing Inclined at 10° and 20°, and with Auxiliary Thrust**

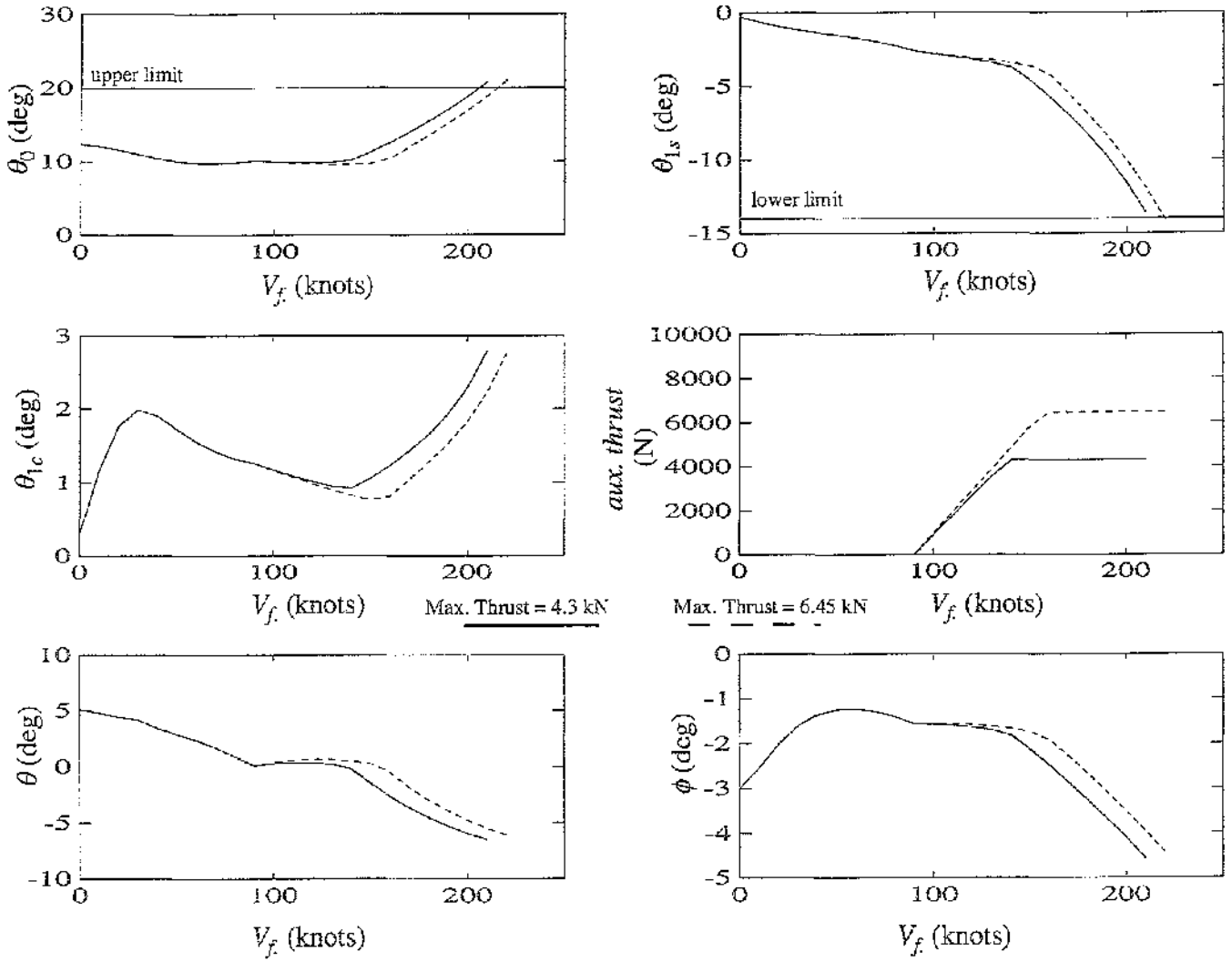

Figure 7.6 **Trim Controls and Attitudes for Westland Lynx with Prescribed Value of Auxiliary Thrust**

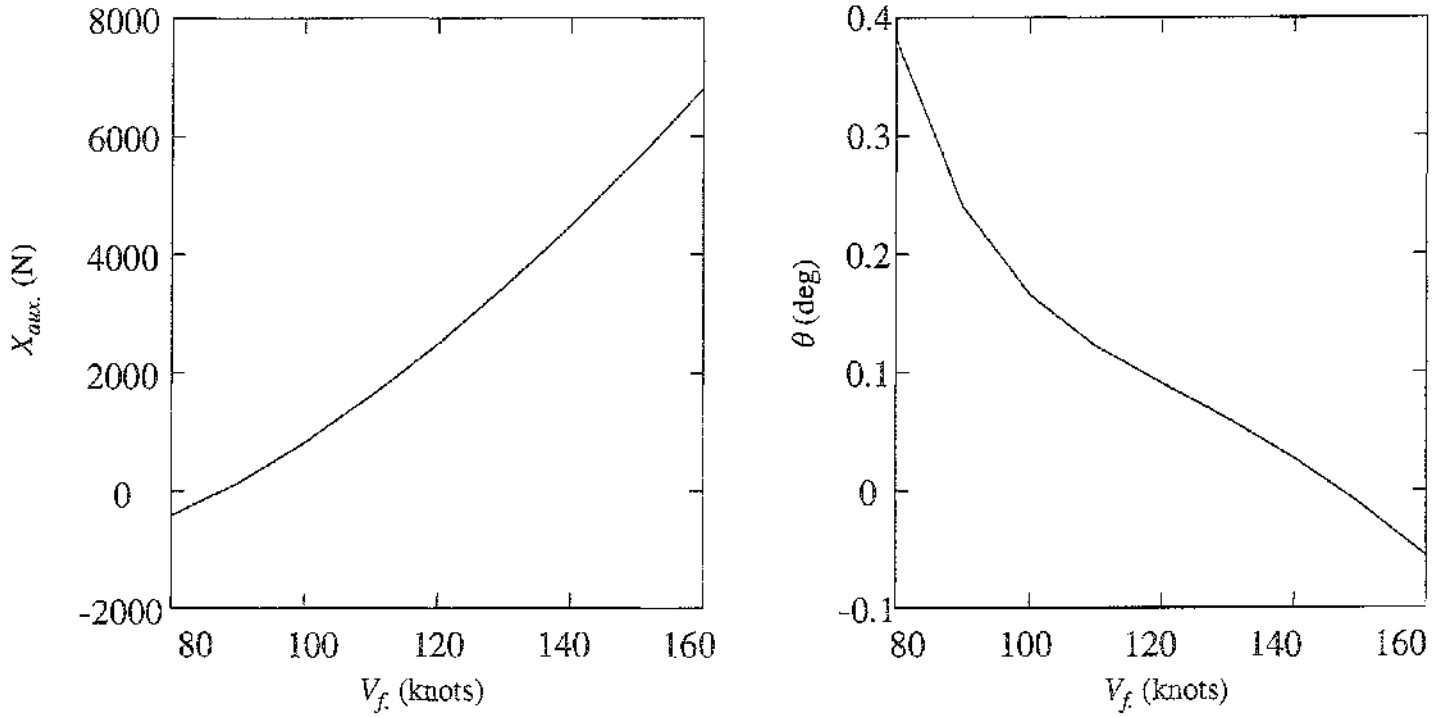

Figure 7.7 **Trim Auxiliary Thrust and Pitch Attitude for Collective Pitch Fixed to 10°**

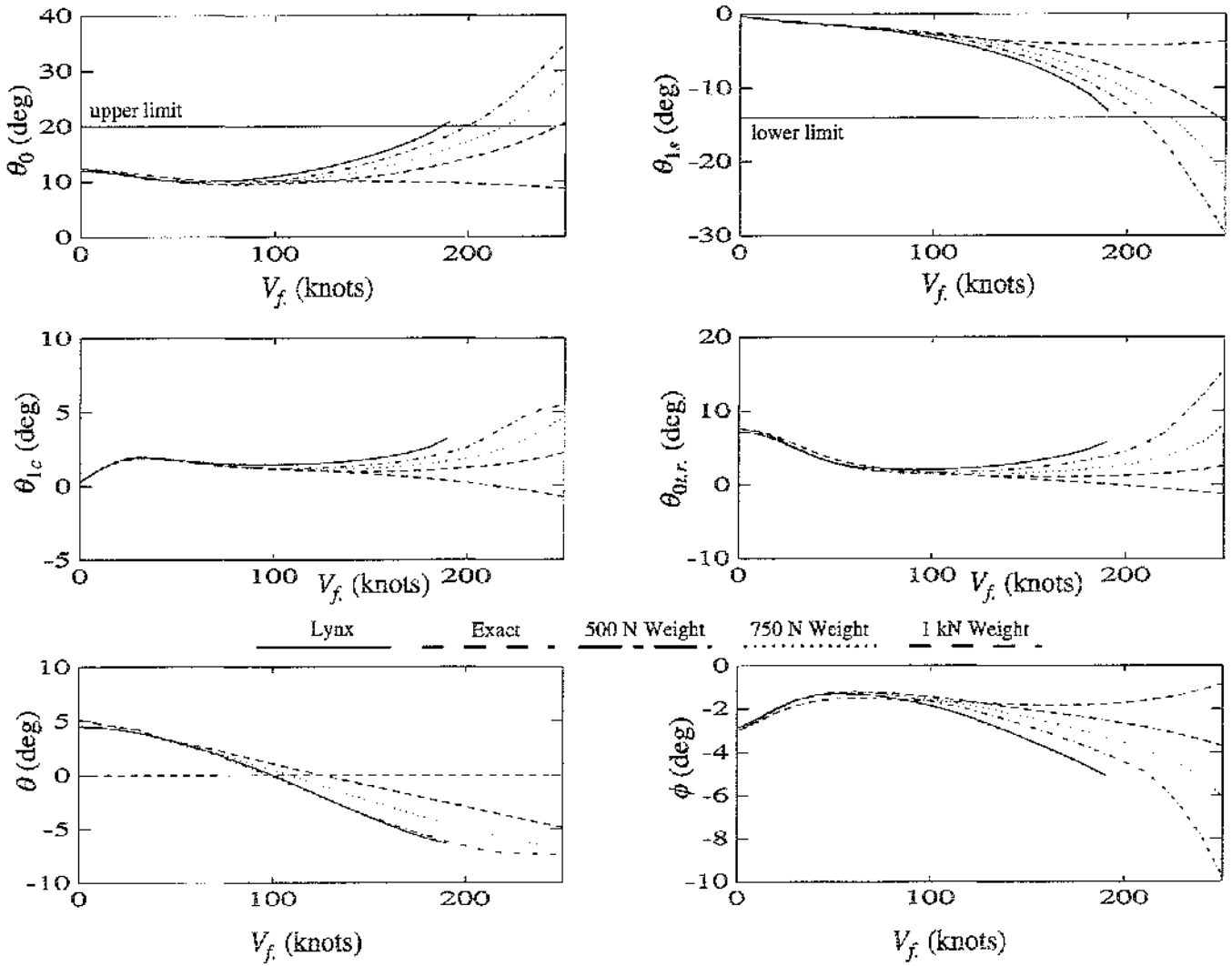

Figure 7.8 **Trim Controls and Attitudes for Westland Lynx, Exact Solution of Compound and Optimal for Different Weightings of Auxiliary Thrust**

Figure 7.9 **Body to Tail Rotor Blade Axis Set Transformations**

Figure 7.10 **Body to Propeller Blade Axis Set Transformations**

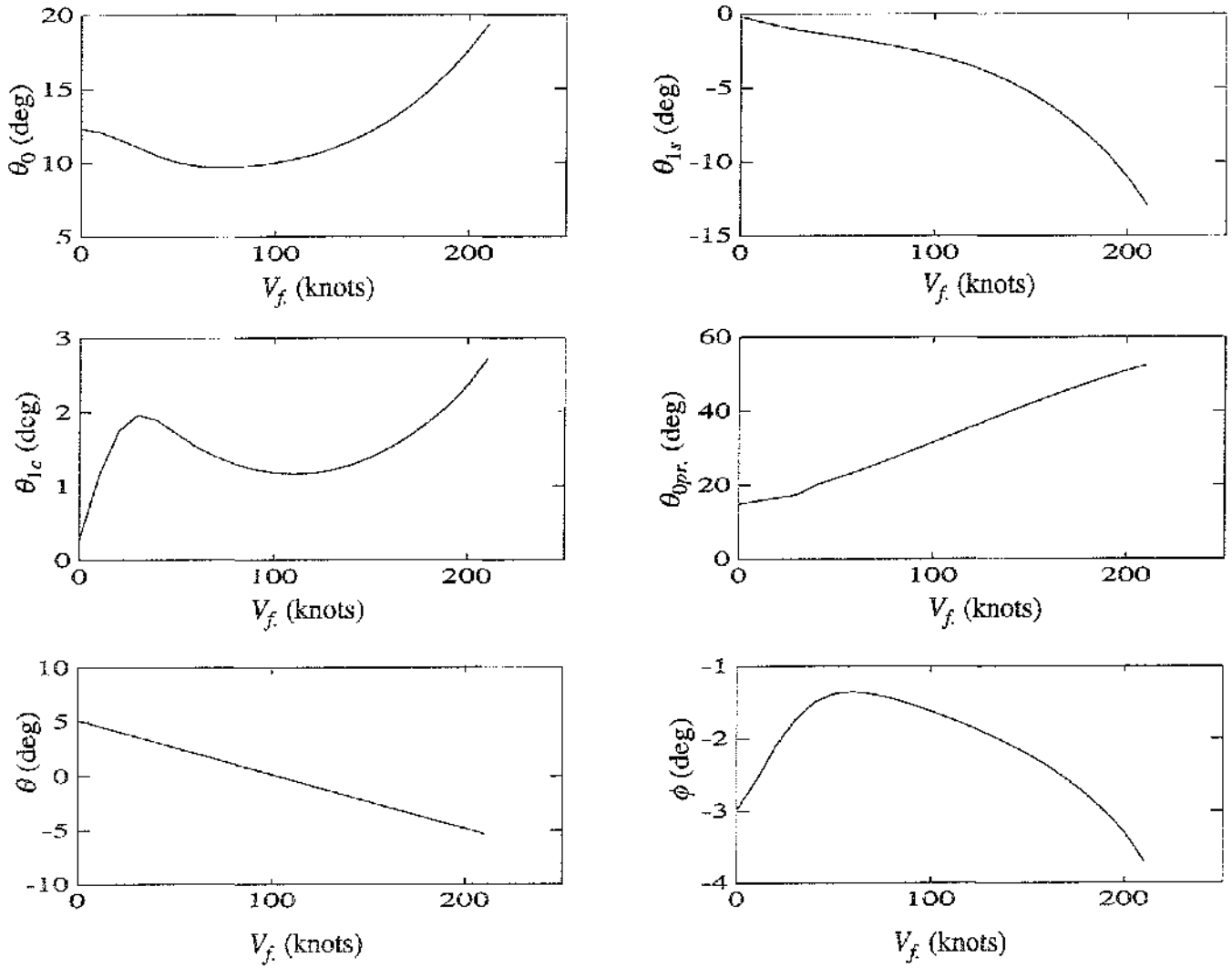

Figure 7.11 Trim Controls and Attitudes for Compound Lynx with Propeller

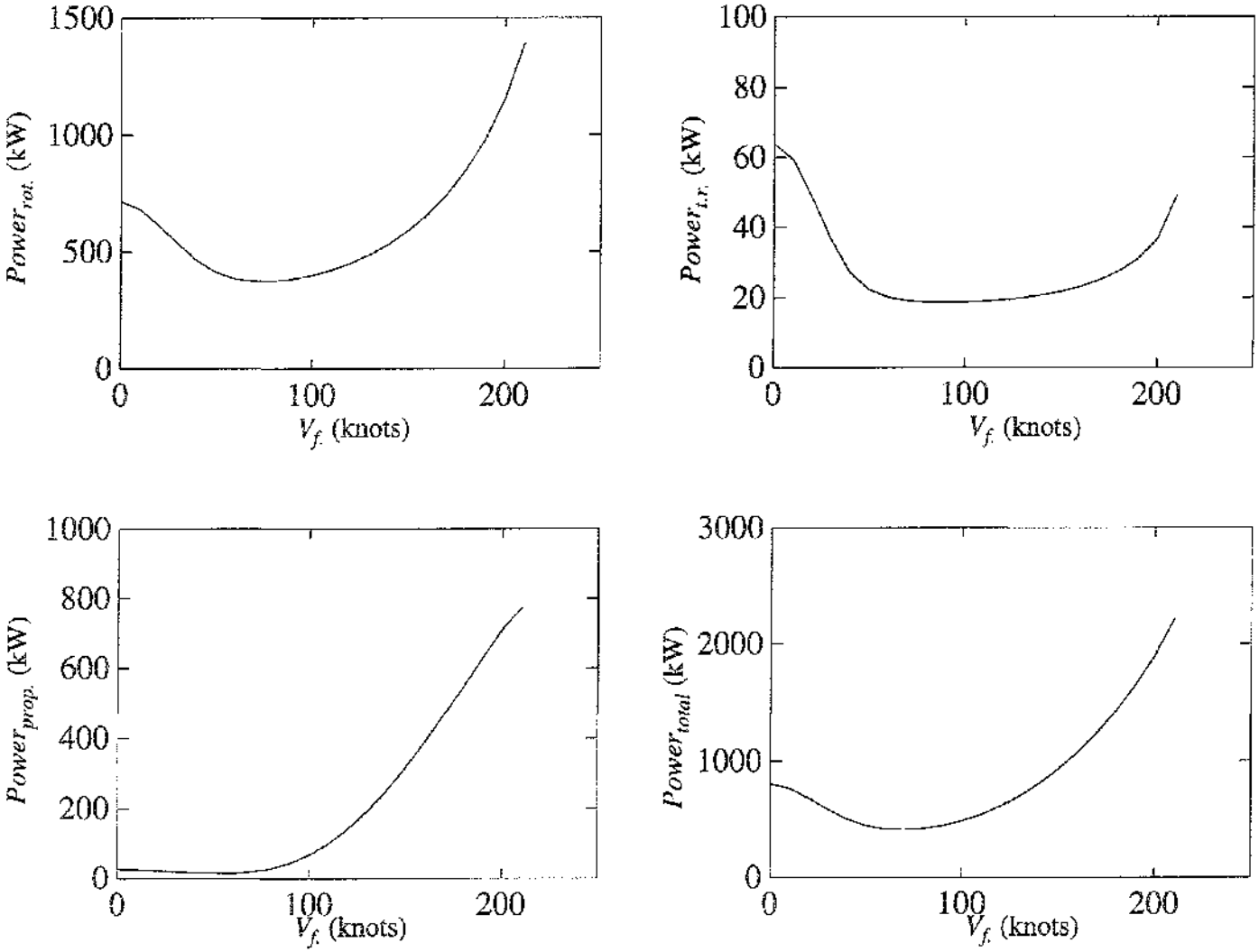

Figure 7.12 **Trim Rotor, Tail Rotor and Total Power for Compound Lynx with Propeller**

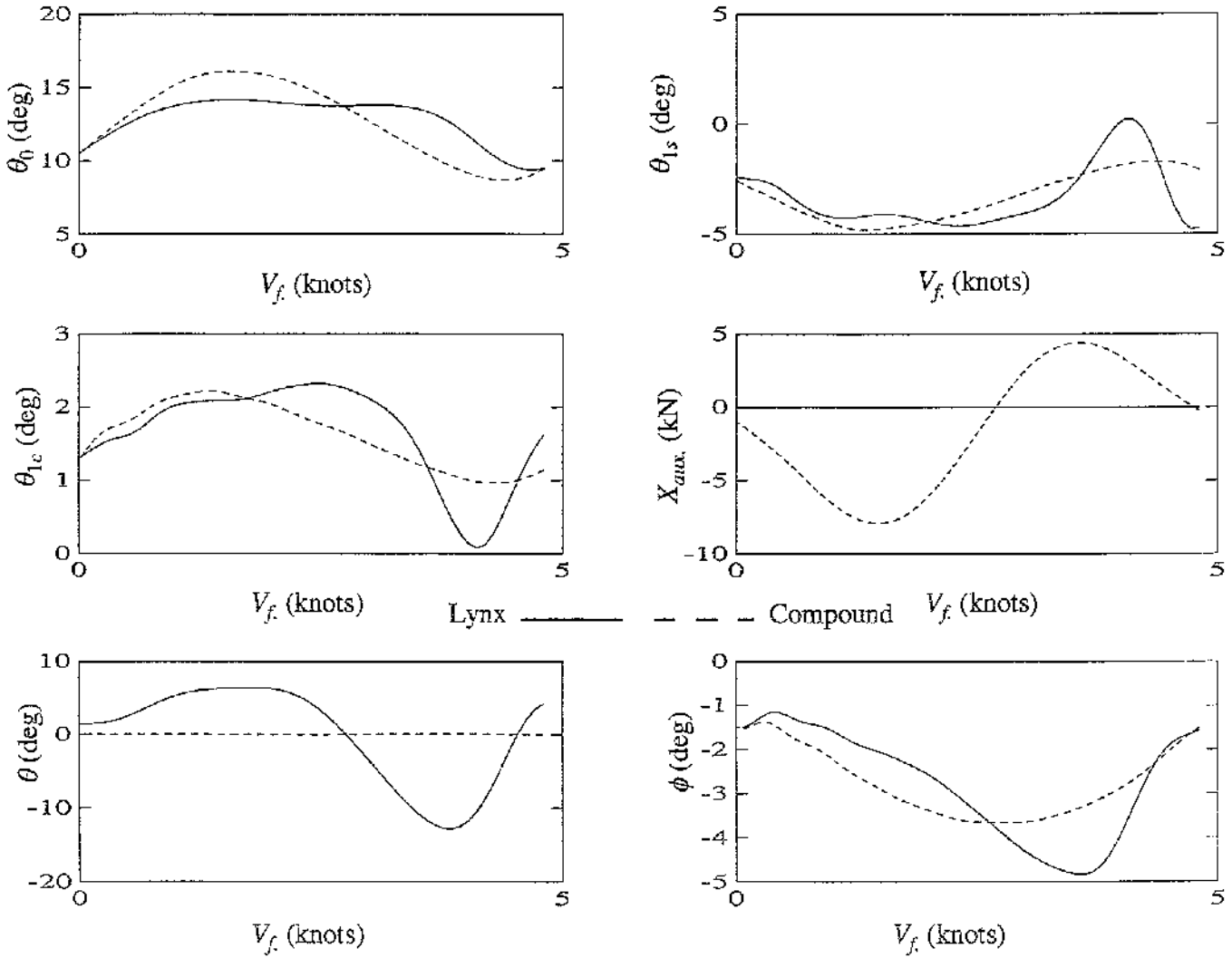

Figure 7.13 **Inverse Simulation Control Time Histories for a Pop-Up Manoeuvre (s=200m, h=25m, V_f=80kts) for Lynx and Compound Lynx**

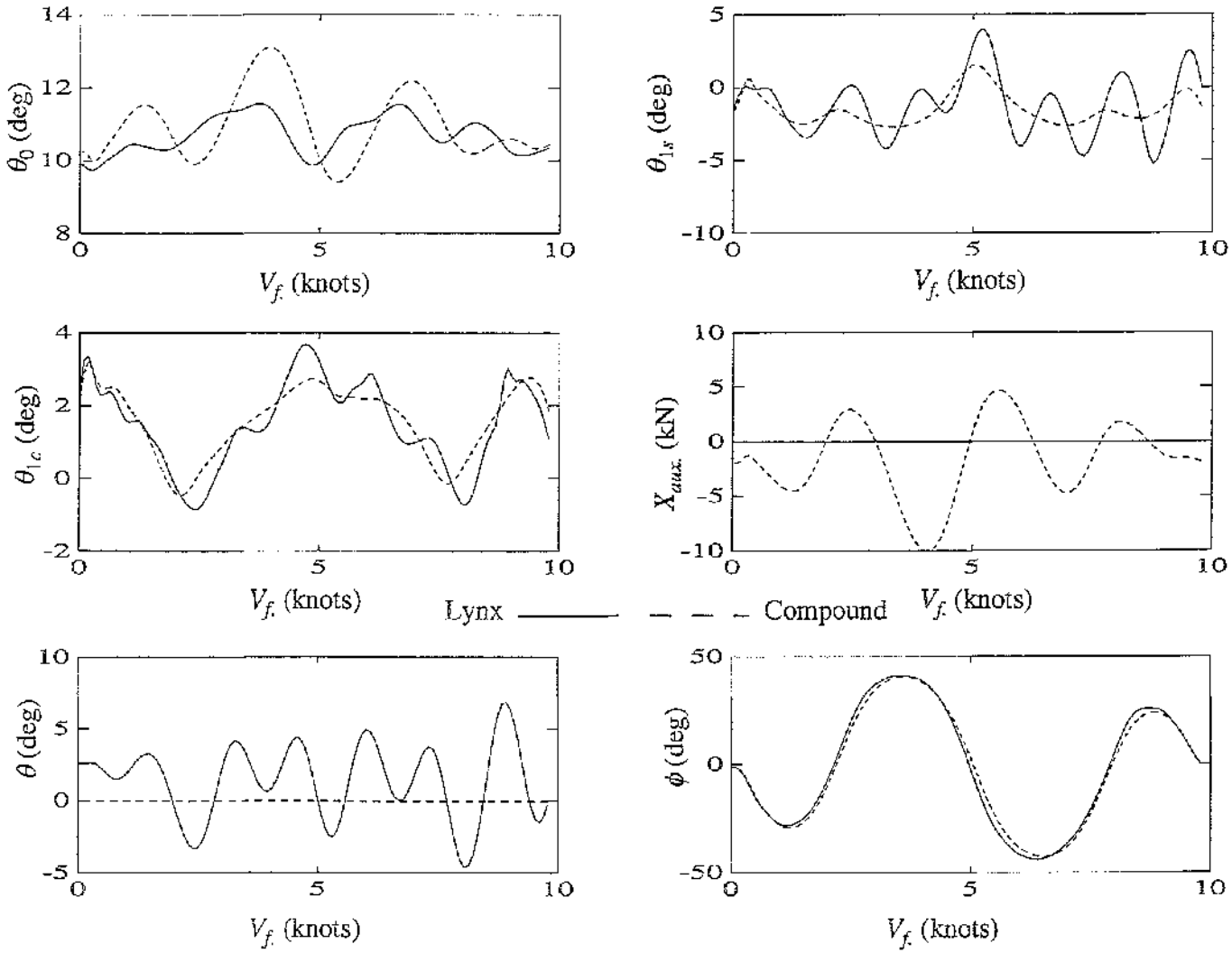

Figure 7.14 **Inverse Simulation Control Time Histories for a Slalom Manoeuvre (s=300m, h=-10m, V_f=60kts) for Lynx and Compound Lynx**

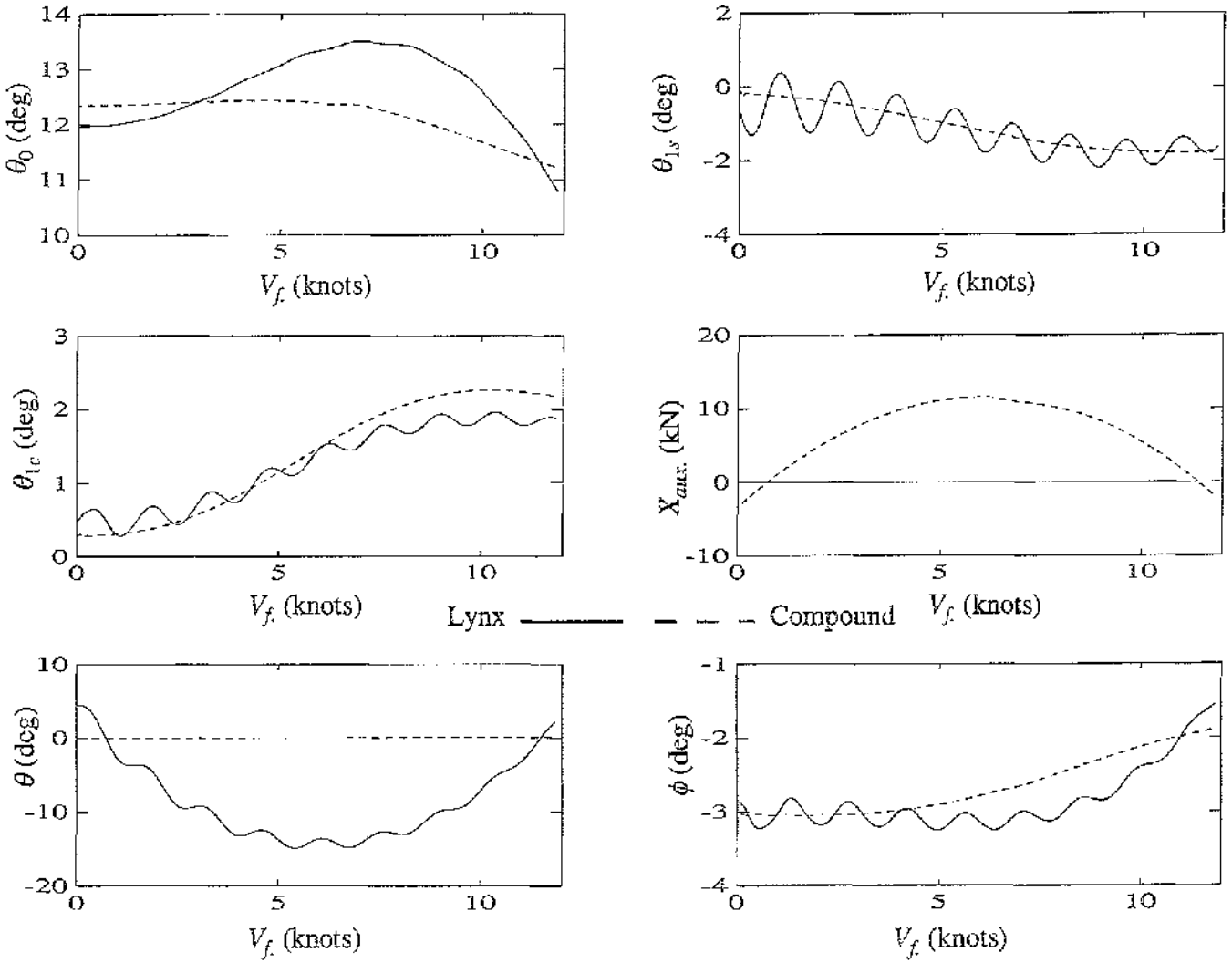

Figure 7.15 **Inverse Simulation Control Time Histories for Acceleration Manoeuvre (s=150m, V_f=0 to 50kts) for Lynx and Compound Lynx**

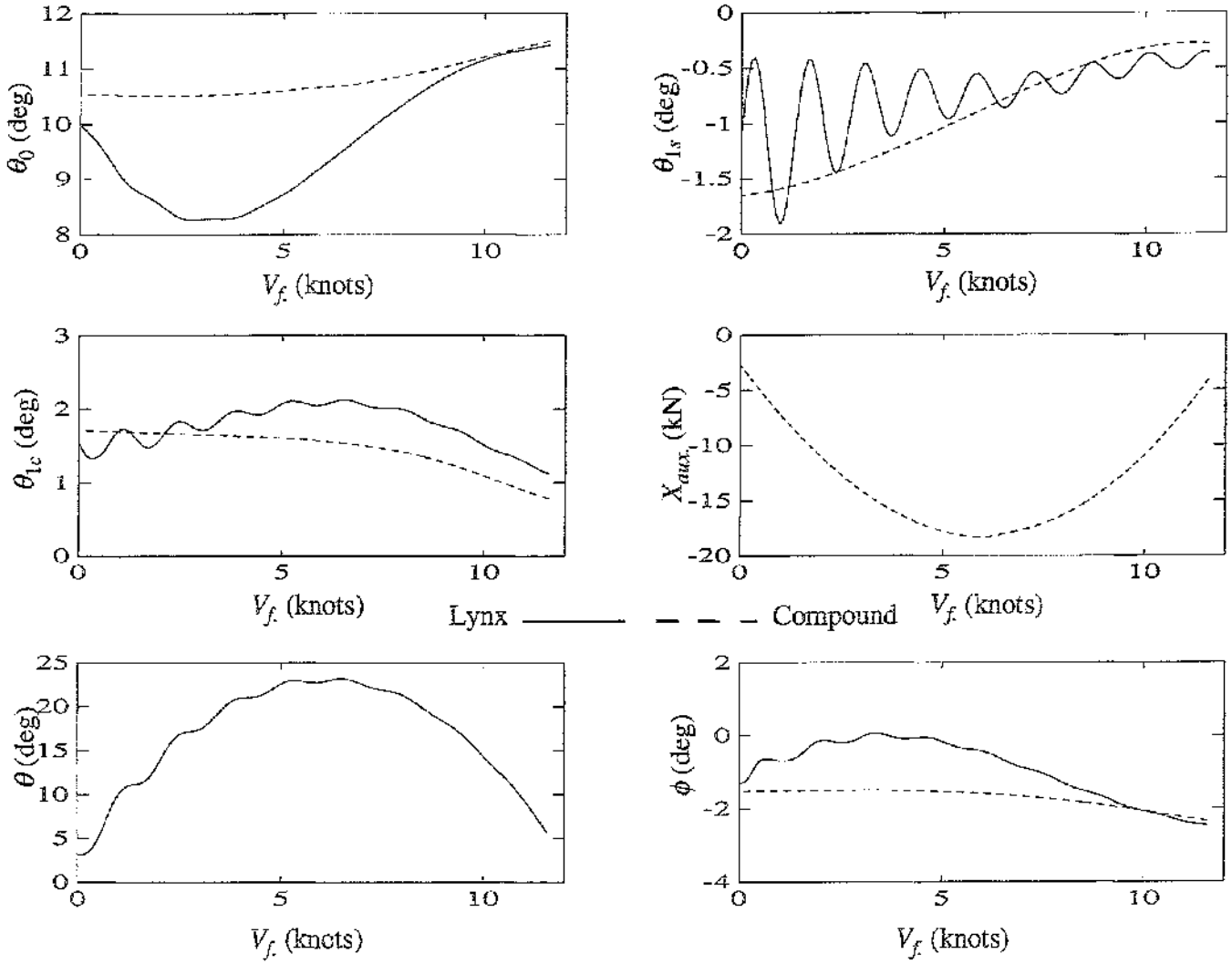

Figure 7.16 **Inverse Simulation Control Time Histories for Deceleration Manoeuvre (s=150m, V_f=50 to 0kts) for Lynx and Compound Lynx**

Figure A2.1 HGS Body to Blade Axis Set Transformations

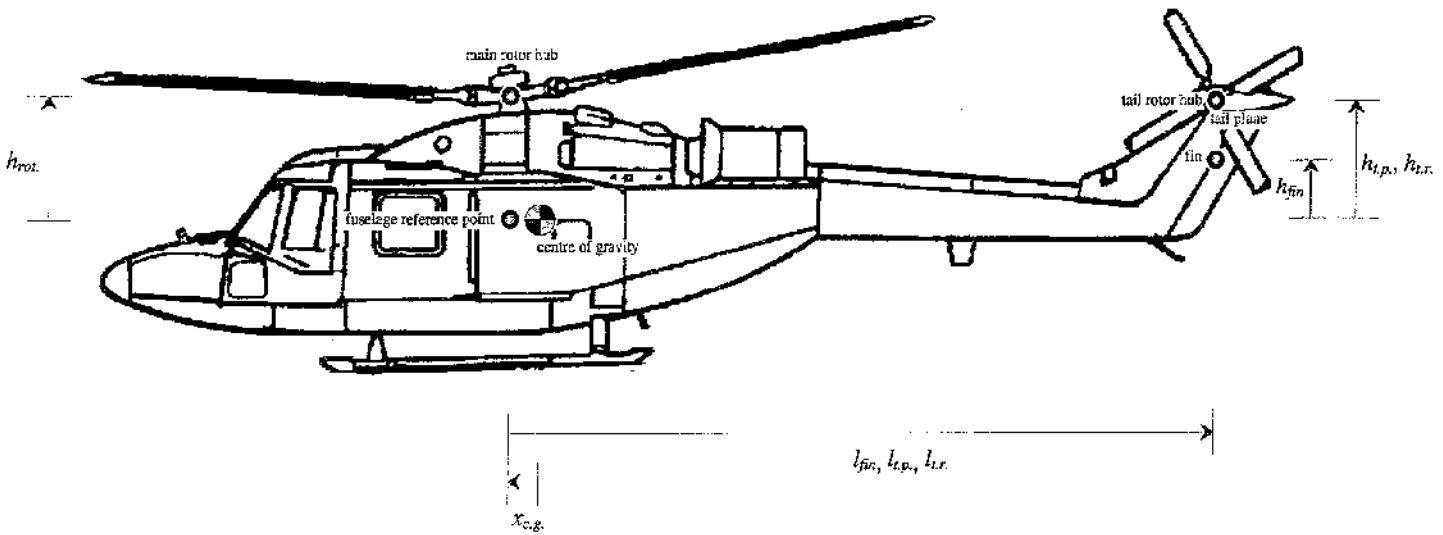

Figure A2.2 Relative Locations of Helicopter Components

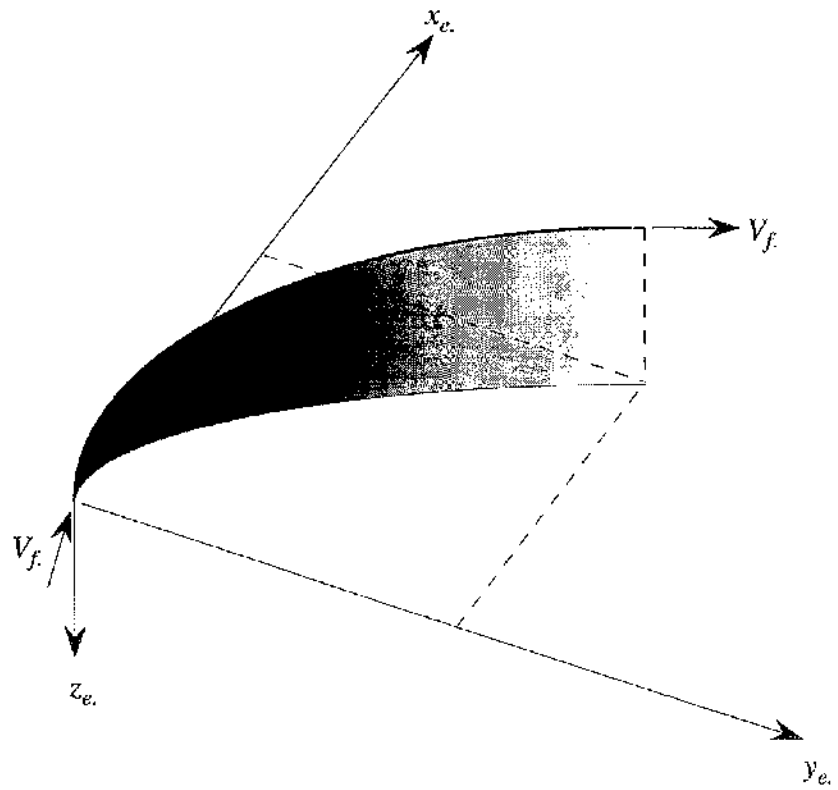

Figure A4.1 The 3D Manoeuvre

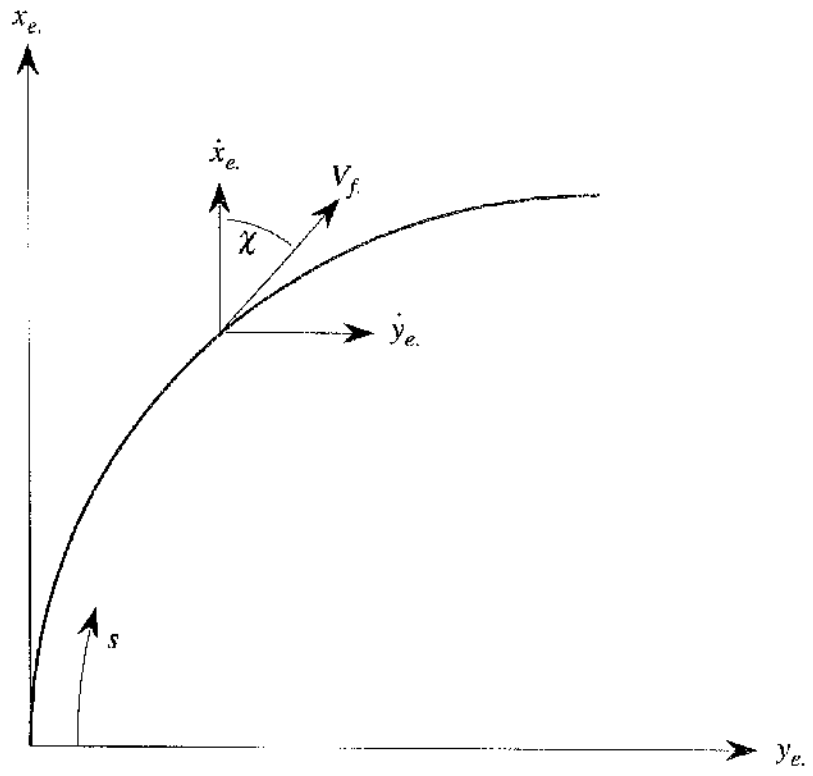

Figure A4.2 The Track

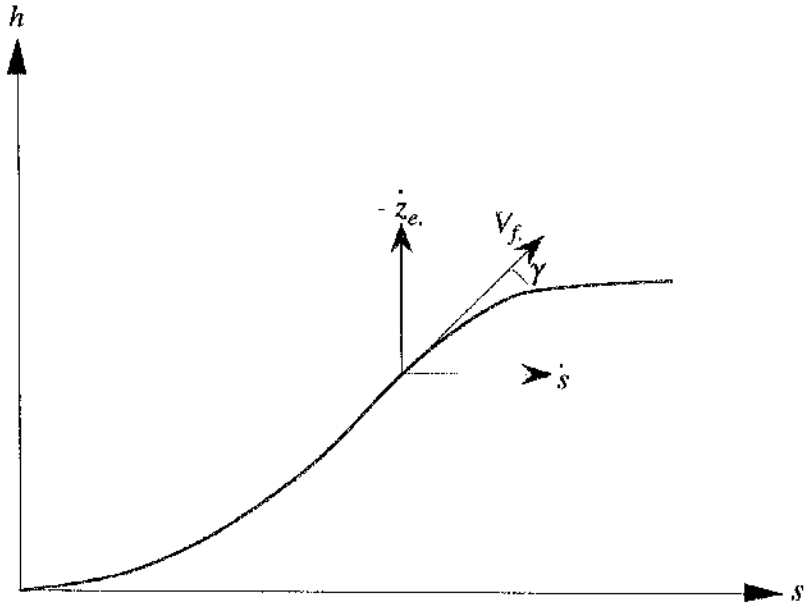

Figure A4.3 The Altitude

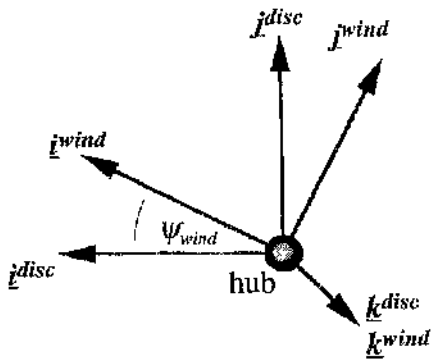

Figure A5.1 ***disc*** **to** ***wind*** **Axes Transformation**

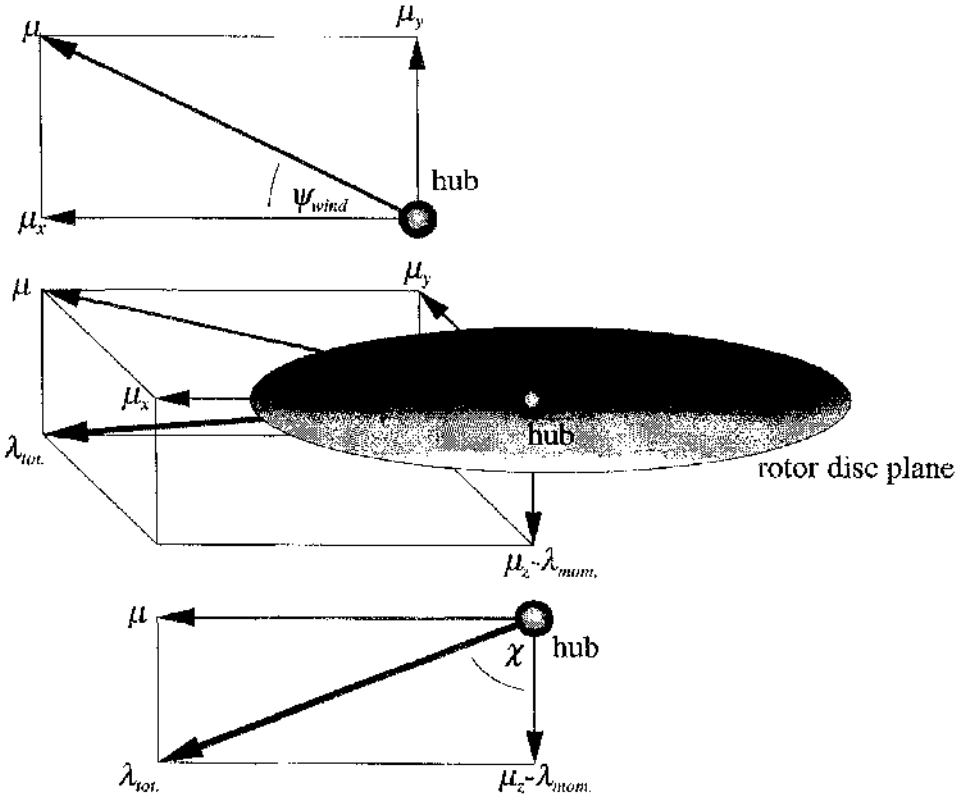

Figure A5.2 **Non-Dimensionalised Rotor Hub Velocities Referred to *disc* Axis Set**

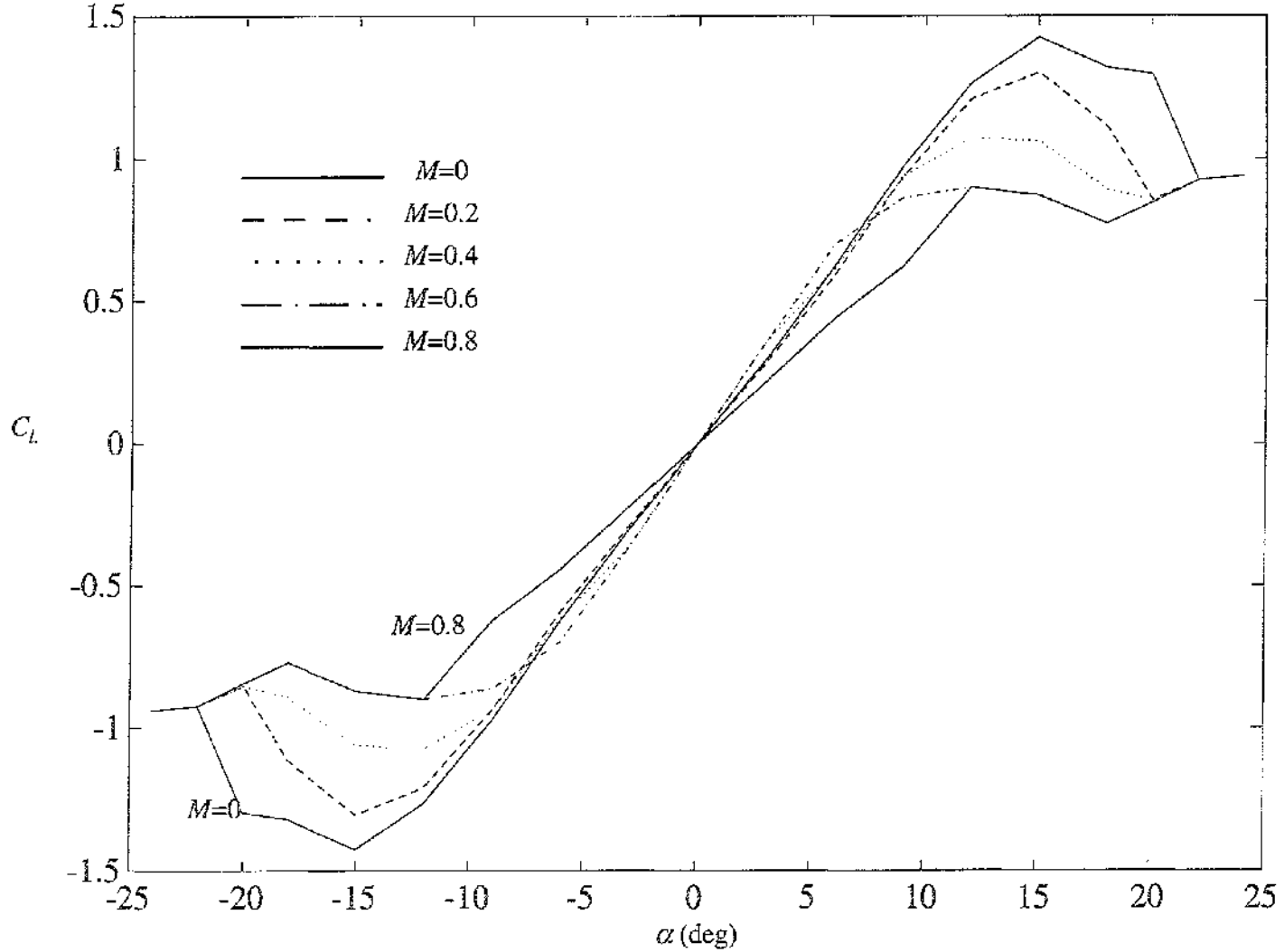

Figure A8.1 **Variation of Lift Coefficient for NACA 0012 Aerofoil with respect to Angle of Attack for Different Mach Numbers**

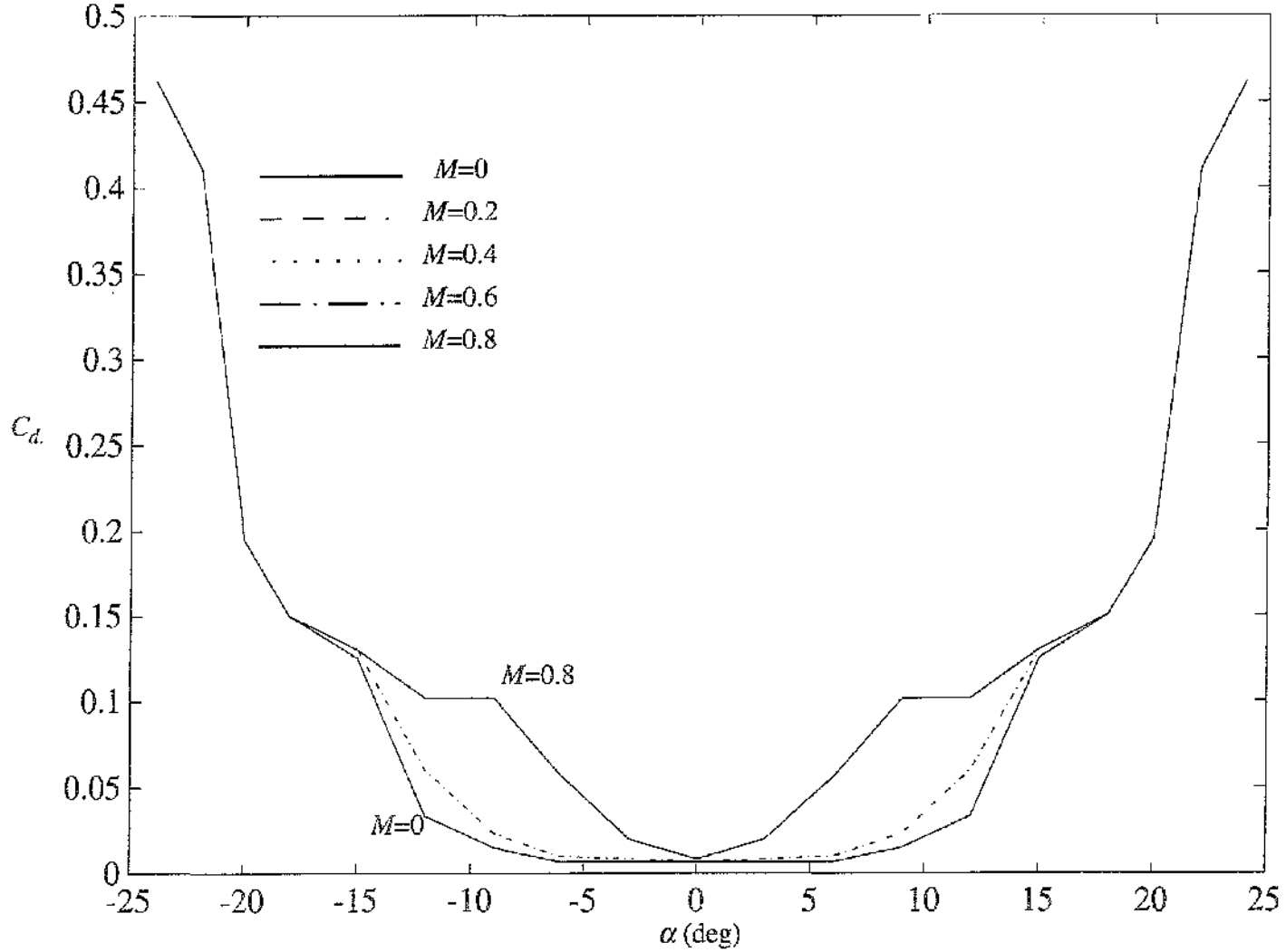

Figure A8.2 **Variation of Drag Coefficient for NACA 0012 Aerofoil with respect to Angle of Attack for Different Mach Numbers**

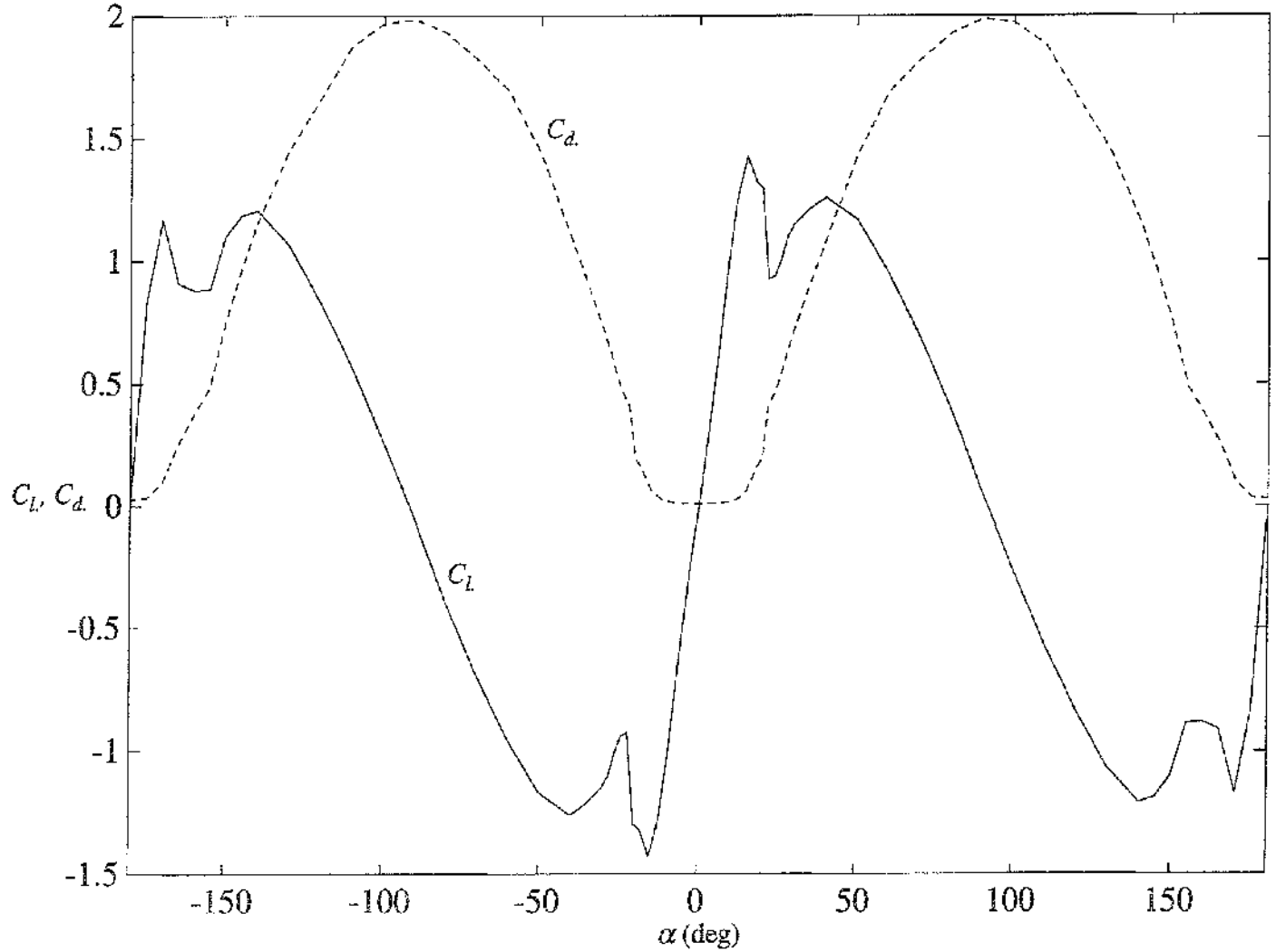

Figure A8.3 **Variation of Lift and Drag Coefficients for NACA 0012 Aerofoil with Respect to Angle of Attack (+/- 180°, M=0)**

References

Anderson, D.A., Tannehill, J.C., Pletcher, R.H., "Computational Fluid Mechanics and Heat Transfer", Hemisphere Publishing Corporation, 1984.

Anon., "Handling Qualities Requirements for Military Rotorcraft", Aeronautical Design Standard ADS-33D, United States Army Aviation and Troop Command, July 1994.

Arcidiacono, P.J., deSimone, G., Occhiato, J., "Preliminary Evaluation of RSRA Data Comparing Pure Helicopter, Auxiliary Propulsion and Compound Helicopter Flight Characteristics", Journal of the American Helicopter Society, Vol. 27, No. 1, January 1982.

Balke, R.W., Bennet, R.L., Gaffey, T.M., Lynn, R.R., "Tail Rotor Design Part 1: Aerodynamics", Journal of the American Helicopter Society, Vol. 15, No. 4, October 1970.

Bradley, R., Padfield, G.D., Murray-Smith, D.J., Thomson, D.G., "Validation of Helicopter Mathematical Models", Transactions of the Institute of Measurement and Control, Vol. 12, No. 4, 1990.

Bradley, R., Private Communication, May 1995.

Bramwell, A.R.S., "Helicopter Dynamics", Arnold 1976.

Bühler, M., Newman, S.J., "The Aerodynamics of the Compound Helicopter Configuration", The Aeronautical Journal, April 1996.

Busi, T., Cinquegrana, A., Parolini, M., "The Application of Advanced Techniques in the Design of the Flight Control Laws for Modern Fly-by-Wire Systems", Paper H7, 19th European Rotorcraft Forum, Como, Italy, September 1993.

Chen, R.T.N., "A Survey of Nonuniform Inflow Models for Rotorcraft Flight Dynamics and Control Applications", Paper 64, 15th European Rotorcraft Forum, Amsterdam, Netherlands, September 1989.

Cheney, W., Kincaid, D., "Numerical Mathematics and Computing. Second Edition", Brooks/Cole Publishing, 1985.

Diftler, M.A., "UH-60A Helicopter Stability Augmentation Study", Paper 74, 14th European Rotorcraft Forum, Milan, Italy, September 1988.

Dumond, R.C., Simon, D.R., "Flight Investigation of Design Features of the S-67 Winged Helicopter", American Helicopter Society 28th Annual Forum, May 1972.

Du Val, R.W., "A Real-Time Blade Element Helicopter Simulation for Handling Qualities Analysis", Paper 59, 15th European Rotorcraft Forum, Amsterdam, Netherlands, September 1989.

Etkin, B., "Charts for Evaluating Rolling Performance", NAE (Can.), Report No. 13, 1951.

Etkin, B., "Dynamics of Flight", John Wiley and Sons, New York, Chapter 11, 1959.

Ewing, D.H., Ph.D. Thesis, University of Glasgow, Department of Aerospace Engineering, to be submitted 1997.

Forman, B., "What Killed the Cheyenne?", Vertiflite, Vol. 42, No. 3, 1996.

Gao, C., Hess, R.A., "Inverse Simulation of Large-Amplitude Aircraft Maneuvers", Journal of Guidance, Control, and Dynamics, Vol. 16, No. 4, 1993.

Glauert, H., "A General Theory of the Autogyro", R&M No. 1111, British A.R.C., 1926.

Hansford, R.E., "Considerations In the Development Of the Coupled Rotor Fuselage Model", Journal of the American Helicopter Society, October 1994.

Haverdings, H. "A Control Model for Maneuvering Flight for Application to a Computer Flight Testing Program", Vertica, Vol. 7, No. 3, 1983.

Hess, R.A., Gao, C., "A Generalized Algorithm for Inverse Simulation Applied to Helicopter Maneuvering Flight", Journal of the American Helicopter Society, Vol. 16, No. 5, 1993.

Hess, R.A., Gao, C., Wang, S.H., "Generalized Technique for Inverse Simulation Applied to Aircraft Maneuvers", Journal of Guidance, Control, and Dynamics, Vol. 14, No.5, 1991.

Hill, G., Du Val, R.W., Green, J.A., Huynh, L.C., "A Piloted Comparison of Elastic and Rigid Blade-Element Rotor Models Using Parallel Processing Technology", Paper III.4.4, 16th European Rotorcraft Forum, Glasgow, U.K., September 1990.

Houston, S., "Rotorcraft Aeromechanics Simulation for Control Analysis - Mathematical Model Definition", University of Glasgow, Department of Aerospace Engineering, Internal Report No. 9123, 1991.

Houston, S., Caldwell, A.E., "A Computer Based Study of Helicopter Agility, Including the Influence of an Active Tailplane", 10th European Rotorcraft Forum, 1984.

Jane's All The World's Aircraft, 1994.

Johnson, W., "Helicopter Theory", Dover Publishing, 1980.

Jones, R.T., "A Simplified Application of the Method of Operators to the Calculation of Disturbed Motions of an Airplane", NACA TR 560, 1936.

Kaletka, J., "BO 105 Identification Results", AGARD-LS-178, Reference 9, October 1991.

Kato, G., Suguira, I., "An Interpretation of Airplane General Motion and Control as Inverse Problem", Journal of Guidance, Control and Dynamics, Vol. 9, No. 2, 1986.

Lane, S.H., Stengel, R.F., "Flight Control Design Using Non-Linear Inverse Dynamics", Automatica, Vol. 24, No. 4, July 1988.

Lewis, W.D., "An Aeroelastic Model Structure Investigation for a Manned Real-Time Rotorcraft Simulation", American Helicopter Society 47th Annual Forum, St. Louis, MO, May 1993.

Lin, K.C., Lu, P., Smith, M., "The Numerical Errors in Inverse Simulation", AIAA-93-3588-CP, 1993.

Lynn, R.R., Robinson, F.D., Batra, N.N., Duhon, J.M., "Tail Rotor Design Part 1: Aerodynamics", Journal of the American Helicopter Society, Vol. 15, No. 4, October 1970.

McCormick, B. W., "Aerodynamics Aeronautics and Flight Mechanics Second Edition", John Wiley and Sons, 1995.

McKillip, R.M. Jnr., Perri, T.A., "Helicopter Flight Control System Design and Evaluation for NOE Operations Using Controller Inversion Techniques", Proceedings of the 45th Annual Forum of the American Helicopter Society, Alexandria, VA, USA, pp. 669-680, May 1989.

McVicar, J. S. G., Bradley, R., "A Partial Periodic Trim Algorithm for Application to Advanced Mathematical Models of Rotorcraft Vehicles", Proceedings of the Kinematics and Dynamics Multi-Body Systems Seminar, Institution of Mechanical Engineers Headquarters, London, 1992.

Mansur, M.H., "Development and Validation of a Blade Element Mathamatical Model for the AH-64A Apache Helicopter", NASA-TM-108863, April 1995.

Mansur, M.H., Tischler, M.B., Chaimovich, M., Rosen, A., Rand, O., "Modeling Methods for High-Fidelity Rotorcraft Flight Mechanics Simulation", Paper III.11.2, 16th European Rotorcraft Forum, Glasgow, U.K., September 1990.

Meyer, G., Cicolani, L., "Application of Non-Linear Systems Inverses to Automatic Flight Control Systems Design", Paper No. 10, Theory and Applications of Optimum Control in Aerospace Systems, AGARDograph, 251, 1981.

Nannoni, F., Stabellini, A., "Simplified Inverse Simulation for Preliminary Design Purposes", 15th European Rotorcraft Forum, Amsterdam, September 1989.

Padfield, G.D., "A Theoretical Model of Helicopter Flight Mechanics for Application to Piloted Simulation", Royal Aircraft Establishment, TR 81048, April 1981.

Padfield, G.D., "SA 330 Puma Identification Results", AGARD-LS-178, Reference 10, October 1991.

Padfield, G.D., Du Val, R.W., "Application Areas for Rotorcraft System Identification: Simulation Model Validation", AGARD-LS-178, Reference 12, October 1991.

Padfield, G.D., Jones, J.P., Charlton, M.T., Howell, S.E., Bradley, R., "Where Does The Workload Go When Pilots Attack Manoeuvres? An Analysis Of Results From Flying Qualities Theory and Experiment", 12th European Rotorcraft Forum, Amsterdam, October 1994.

Padfield, G.D., "Helicopter Flight Dynamics", Blackwell Science Ltd., 1996

Peters, D.A., HaQuang, N., "Dynamic Inflow for Practical Applications", Journal of the American Helicopter Society, Technical Note, pp. 64-68, October 1988.

Pitt, D.M., Peters, D.A., "Theoretical Prediction of Dynamic Inflow Derivatives", Vertica, Vol. 5, pp. 21-34, 1981.

Press, W., Teukolsky, S.A., Vetterling, W.T., Flannery, B.P., "Numerical Recipes in Fortran. The Art of Scientific Computing. Second Edition", Cambridge University Press, 1986.

Prouty, R., Lecture, Aeromechanics and Simulation, Bedford, U.K., 1996.

Rieugnié, M., François, D., "Compound Helicopters A Parametric Approach", Paper No. III6, 21st European Rotorcraft Forum, St. Petersburg, September 1995.

Rutherford, S., Thomson, D.G., "Helicopter Inverse Simulation Incorporating an Individual Blade Rotor Model", Paper 3.6.3, ICAS Congress, Sorrento, Italy, September 1996.

Smith, G.A., Meyer, G., "Aircraft Automatic Flight Control System with Model Inversion", Journal of Guidance, Control and Dynamics, Vol. 10, No. 3, May 1987.

Stepniewski, W.Z., Keys, C.N., "Rotary-Wing Aerodynamics", Dover Publications, New York, 1984.

Sturisky, S.H., Schrange, D.P., "System Identification Validation of an AH-64 Aeroelastic Simulation Model", American Helicopter Society 47th Annual Forum, St. Louis, MO, May 1993.

Thomson, D.G., "An Analytical Method of Quantifying Helicopter Agility", Paper No. 45, 12th European Rotorcraft Forum, Garmisch-Partenkirchen, Sept. 1986.

Thomson, D.G., "Development of a Generic Helicopter Mathematical Model for Application to Inverse Simulation", University of Glasgow, Department of Aerospace Engineering, Internal Report No. 9216, June 1992.

Thomson, D.G., "The Helinv Numerical Algorithm", University of Glasgow, Department of Aerospace Engineering, Internal Report No. 9408, June 1994.

Thomson, D.G., Bradley, R., "An Investigation of the Stability of Flight Path Constrained Helicopter Manoeuvres by Inverse Simulation", Paper No. 7.7, 13th European Rotorcraft Forum, Arles, France, September 1987.

Thomson, D.G., Bradley, R., "Development and Verification of an Algorithm for Helicopter Inverse Simulation", Vertica, Vol. 14, No. 2, May 1990a.

Thomson, D.G., Bradley, R., "Modelling and Classification of Helicopter Combat Manoeuvres", Proceedings of ICAS Congress, Stockholm, Sweden, September 1990b.

Thomson, D.G., Bradley, R., "The Use of Inverse Simulation for Conceptual Design", Paper II.2.3, 16th European Rotorcraft Forum, Glasgow, U.K., September 1990c.

Thomson, D.G., Bradley, R., "Prediction of the Dynamic Characteristics of Helicopters in Constrained Flight", The Aeronautical Journal, December 1990d.

Thomson, D.G., Bradley, R., "The Contribution of Inverse Simulation to the Assessment of Helicopter Handling Qualities", Paper 7.3.2, Proceedings of the 19th ICAS Conference, Anaheim, U.S.A., September 1994.

Thomson, D.G., Talbot, N., Taylor, C., Bradley, R., Ablett, R., "An Investigation of Piloting Strategies for Engine Failures During Takeoff from Offshore Platforms", The Aeronautical Journal, January 1995.

Torres, M., "A Wing on the SA.341 Gazelle Helicopter and its Effects", Vertica, Vol. 1, pp. 67-73, 1976.

Turnour, S. R., Celi, R., "Modelling of Flexible Rotor Blades for Helicopter Flight Dynamics Applications", Journal of the American Helicopter Society, January 1996.

Whalley, M.S., "Development and Evaluation of an Inverse Solution Technique for Studying Helicopter Maneuverability and Agility", NASA TM 102889, 1991.

Wolfram, S., "Mathematica. A System for Doing Mathematics by Computer", 2nd. Edition, Addison-Wesley, ISBN 0-201-51502-4, 1991.

Wood, T.L., Ford, D.G., Brigman, G.H., "Maneuver Evaluation Program", USAAMRDL-TR-74-32, May 1974.

Young, M.I., "A Simplified Theory of Hingeless Rotors with Application to Tandem Helicopters", Proceedings of the 18th Annual National Forum of the American Helicopter Society, May 1962.